

# **Modelling sintering at particle scale using variational and molecular dynamic methods**

Thesis submitted for the degree of

Doctor of Philosophy

at the University of Leicester

by

**ANAS OBEED ALSHAMMERY**



UNIVERSITY OF  
**LEICESTER**

Department of Engineering

University of Leicester

**August 2018**

**ABSTRACT**

Sintering is the thermal process that uses powders to form a new dense product by increasing temperature but holding it under the melting point of the material in use. Modelling the sintering process is important for fundamental understanding the behaviour of the particles during the sintering process instead of through empirical experimental work.

In the first part of this thesis, a simplified method is developed to model the solid state sintering process which depends on the coupling between grain boundary and surface diffusion. A curve fitting method was developed to create a new relationship that relates the chemical potential at the junction of the grain-boundary and free surface to the neck size and the ratio of grain-boundary diffusivity over surface diffusivity. This relationship enables the de-coupling between the two diffusional processes when modelling the sintering process. The sintering process can, therefore, be separately modelled from the surface diffusion process, which greatly simplified the model for problems involving many particles such as those in a discrete element model. The results of the curve fitting method were first compared with the analytical Coblenz equations to allow for the validation and proofing of the new method in terms of modelling the sintering process; thereafter, comparisons were made with the full finite difference model using two parameters, namely diffusion coefficient ratio and applied stress. The curve fitting model matched well with the full finite difference model for the two parameters.

In the second part of this thesis, two stages were undertaken: firstly, the new method was used in a variational model to simulate the two copper particles, and was compared with a new curve fitting-finite difference method for two sintering ratios. The variational model results were in good agreement with the new curve fitting-finite difference method. Secondly, multiple particles of copper were used in a variational model to simulate selective laser sintering for 27 copper particles. Laser scan speed, laser power, and particle temperature were collected from the COMSOL model, after which the particle temperature was used in the variational model to calculate the neck growth and shrinkage ratios between particles for different particle sizes.

In the third part of this thesis, a molecular dynamics simulation code, LAMMPS, was used to investigate and understand the behaviour of nano-copper in the sintering process. Firstly, the melting temperature of nano-copper for different nanoparticle sizes was calculated and compared to four analytical models, after which neck size and shrinkage ratios were determined and compared with different diffusion mechanisms. The melting temperature numerical results matched well with the analytical nano-copper model. The hollow nano-copper improved the sintering process compared to solid nano-copper. Nanoparticle sintering has different behaviours comparing to micro-particle sintering. The nanoparticle sintering process is faster than for microparticle sintering; moreover, the melting temperature of the nanoparticles changed depending on size, when compared with microparticles where the melting point was constant.

**TABLE OF CONTENTS**

## Contents

<b>ABSTRACT</b> .....	<b>I</b>
<b>TABLE OF CONTENTS</b> .....	<b>III</b>
<b>LIST OF FIGURES</b> .....	<b>VII</b>
<b>LIST OF TABLES</b> .....	<b>XIV</b>
<b>LIST OF SYMBOLS</b> .....	<b>XV</b>
<b>LIST OF ABBREVIATIONS</b> .....	<b>XVIII</b>
<b>ACKNOWLEDGMENTS</b> .....	<b>XIX</b>
<b>LIST OF PUBLICATIONS</b> .....	<b>XX</b>
<b>1 CHAPTER ONE: Sintering Practice and Mechanisms</b> .....	<b>1</b>
1.1 Powder metallurgy.....	1
1.2 Sintering.....	2
1.2.1 Variables that control the sintering process .....	3
1.3 Solid state sintering processes .....	4
1.3.1 Spark plasma sintering process .....	6
1.3.2 Microwave sintering process .....	6
1.3.3 Electro sinter forging process .....	8
1.3.4 Selective laser sintering process.....	9
1.4 Driving Force of Sintering.....	11
1.5 Mechanisms of Solid State Sintering.....	12
1.5.1 Surface Diffusion .....	13
1.5.2 Volume Diffusion .....	15
1.5.3 Grain boundary diffusion .....	16
1.6 Stages of solid state sintering .....	17

---

1.6.1	The first stage of solid state sintering .....	19
1.6.2	The second stage of solid state sintering .....	19
1.6.3	The intermediate stage of solid state sintering .....	20
1.6.4	The final stage of solid state sintering .....	20
1.7	Measurement of the sintering process .....	21
1.8	Organization of thesis .....	21
2	CHAPTER TWO: A literature review on sintering models.....	23
2.1	Literature review of analytical models .....	23
2.1.1	Initial stage model .....	23
2.1.2	Viscous Flow model.....	26
2.1.3	Analytical model of sintering via grain boundary diffusion .....	27
2.1.4	Analytical model of sintering via surface diffusion .....	27
2.2	Literature review of numerical models for sintering .....	28
2.3	Literature review of selective laser sintering.....	51
2.4	Literature review of nanosintering modelling .....	53
2.5	Literature review of nanosintering modelling using molecular dynamics method ....	58
2.6	Unresolved issues in previous sintering models .....	62
2.7	Thesis Objective .....	63
3	CHAPTER THREE: Chemical potential at triple junction.....	65
3.1	Introduction.....	65
3.2	Governing equations for coupled grain boundary and surface diffusion .....	67
3.3	Numerical model for coupled grain boundary and surface diffusion .....	72
3.3.1	Curve-fitting equation method .....	75
3.4	Results and discussion .....	78
3.4.1	Effect of diffusion coefficient ratios in the sintering process .....	81

3.4.2 The influence of the diffusion coefficient ratio as compared between two methods	85
3.4.3 The influence of applied stress as compared between two methods:.....	90
3.4.4 Additional results .....	107
3.5 Summary.....	115
3.6 Conclusions.....	117
4 CHAPTER FOUR: Application of curvature fitting equation to SLS .....	118
4.1 Sintering of two particles based on the variational principle .....	118
4.1.1 Governing equations of the variational model for sintering two particles:.....	119
4.1.2 Variational model code .....	125
4.1.3 Validation of the VM curve fitting.....	126
4.2 A Model for Selective Laser Sintering of Multi-particles .....	127
4.2.1 SLS numerical model.....	128
4.2.2 Governing equations for the sintering model.....	128
4.2.3 Numerical model of sintering.....	135
4.2.4 Governing equations of thermal model in the COMSOL software .....	137
4.2.5 Governing equations for the laser beam in the COMSOL software .....	138
4.2.6 Materials used in this study .....	139
4.2.7 COMSOL software for laser beam and temperature distribution .....	140
4.2.8 Validation of the sintering model.....	143
4.2.9 Results and discussion .....	144
4.2.10 Grain boundary diffusion coefficient as affecting the movement of particles:	167
4.3 Summary.....	171
4.4 Conclusions.....	172
5 CHAPTER FIVE: Molecular Dynamics model for nanoparticles sintering.....	173

5.1	Introduction: .....	173
5.2	Methodology.....	174
5.2.1	Computational methods: .....	174
5.2.2	Analytical model .....	179
5.3	Calculation of nano-copper melting temperature .....	182
5.3.1	Analytical models of nanoparticle melting temperature .....	183
5.3.2	Numerical calculation of melting temperature of copper powder .....	185
5.3.3	Validation of melting temperature for nanocopper .....	188
5.4	Molecular dynamics simulation of solid-state sintering of nanocopper.....	189
5.4.1	Effect of crystal orientation on copper nanoparticle sintering .....	195
5.4.2	Surface area reduction.....	198
5.4.3	Mean square displacement (MSD).....	199
5.4.4	Hollow nanocopper sintering .....	201
5.4.5	Multiple copper nanoparticle sintering .....	207
5.4.6	Sintering of different nanoparticle sizes: .....	218
5.5	Summary.....	226
5.6	Conclusions.....	227
6	CHAPTER SIX: Conclusions .....	228
6.1	Overall Conclusions: .....	228
6.1.1	Chemical potential at triple junction conclusions .....	228
6.1.2	Application of curvature fitting equation to SLS Conclusions .....	228
6.1.3	Molecular Dynamics model for nanoparticles sintering Conclusions .....	229
	REFERENCES:.....	231
	Appendix A: .....	240

**LIST OF FIGURES**

Figure 1-1 General powder metallurgy stages [1].	1
Figure 1-2 The market for powder metallurgy parts [2].	2
Figure 1-3 Comparison between different processes for two terms material wastage and energy consumption per kg, (EPMA).	3
Figure 1-4 Three steps of solid state sintering [5].	4
Figure 1-5 Sintering process using a continuous furnace [1].	5
Figure 1-6 Spark plasma sintering process equipment [6].	7
Figure 1-7 Microwave sintering process equipment [7].	8
Figure 1-8 Electro sinter forging process equipment [8].	9
Figure 1-9 Components used in the SLS process and the movement of the laser [9].	10
Figure 1-10 Basis of the phenomena that occur during sintering [10].	11
Figure 1-11 Two types of mass transport [3].	13
Figure 1-12 Elements on the particle's surface [3].	14
Figure 1-13 Diffusion vacancy pathways [3].	15
Figure 1-14 Misorientation steps in a grain boundary [3].	17
Figure 1-15 Configuration of particles during the stages of sintering [11].	18
Figure 1-16 Configuration of pores at different stages of the sintering process [3].	19
Figure 1-17 Shape of particles in the intermediate stage of sintering [3].	20
Figure 1-18 Shape of particles in the final stage [3].	21
Figure 2-1 Relative density as a function of sintering time for four different cases [22].	30
Figure 2-2 Sintering of two particles of different sizes [5].	32
Figure 2-3 Particle diameter ratio for four styles [37].	34
Figure 2-4 Neck size ratio of copper and alumina powders [41].	36
Figure 2-5 Comparison of numerical results with analytical formulae [43].	37
Figure 2-6 Cracks inside a body with different viscous parameters [49].	39
Figure 2-7 Relative density with time for ZnO particles [50].	40
Figure 2-8 18,000 particle for three time scales [51].	40
Figure 2-9 Sintering process steps for two different particle sizes [52].	41

Figure 2-10 Porosity, normalized thickness, curvature, and stress due to sintering time [53].	42
Figure 2-11 Densification rate with relative density of matrix [55].	43
Figure 2-12 The densification as a function of time step [56].	44
Figure 2-13 The contact networks of copper powders [57].	45
Figure 2-14 Surface curvature for three diffusion coefficient ratios [58].	46
Figure 2-15 Critical time steps and sintering time at different mass factors: a) $10^{14}$ , b) $10^{16}$ [59].	47
Figure 2-16 Comparison between numerical methods and experimental data [60].	47
Figure 2-17 Comparison between two models and experimental data [65].	49
Figure 2-18 Comparison between two simulation models and experimental data [66].	50
Figure 2-19 Use of nanotechnology in industry [87].	54
Figure 2-20 Grain boundary and surface diffusion between particles [10].	56
Figure 2-21 Linear and nonlinear diffusion of different sized particles [10].	57
Figure 2-22 Comparison between microparticle and nanoparticle sintering for three particles [37].	59
Figure 2-23 Crystalline orientations between two nanoparticles (16 nm) [100].	59
Figure 3-1 Chemical potential between two particles	66
Figure 3-2 Geometry of two particles during the sintering process.	68
Figure 3-3 Details of neck between two particles [63].	70
Figure 3-4 FD-mesh of two of half surfaces for particles.	73
Figure 3-5 Flow chart of FD model.	74
Figure 3-6 Curvature $K_{n-1}$ as a function of the neck size ratio for three $D_S/D_g$ ratios of 0.1, 0.01, and 1.	76
Figure 3-7 Curvature $K_{n-1}$ as a function of neck size ratio for $D_S/D_g = 1-10000$ and stresses $\sigma_S = 25-100\text{MPa}$ .	77
Figure 3-8 Comparison of shrinkage ratio for numerical results and the analytical model.	79
Figure 3-9 Comparison of neck size ratio as used for numerical results and the analytical model.	80
Figure 3-10 Shrinkage ratio as a function of sintering time for different diffusion coefficient ratios.	82
Figure 3-11 Neck size ratio as a function of sintering time for different diffusion coefficient ratios.	83

Figure 3-12 Particle geometry change during the sintering process for different diffusion coefficient ratios. ....84

Figure 3-13 Particle geometry change during the sintering process for different sintering times.....85

Figure 3-14 Comparisons of the shrinkage ratio between curve-fitting FD and full FD results. ....86

Figure 3-15 Comparisons of the neck size ratio for curve-fitting FD and full FD results.....88

Figure 3-16 Comparisons of the shrinkage ratio between curve-fitting FD and full FD at 25 MPa. ....92

Figure 3-17 Comparisons of the shrinkage ratio between curve-fitting FD and full FD at 50 MPa. ....93

Figure 3-18 Comparisons of the shrinkage ratio for curve-fitting FD and full FD results at 75 MPa. ....95

Figure 3-19 Comparison of the shrinkage ratio for curve-fitting FD and full FD results at 100 MPa. ....96

Figure 3-20 Comparison of the neck size ratio for curve-fitting FD and full FD results at 25 MPa. ....98

Figure 3-21 Comparison of the neck size ratio between curve-fitting FD and full FD results at 50 MPa. ....99

Figure 3-22 Comparison of the neck size ratio between curve-fitting FD and full FD results at 75 MPa. .... 101

Figure 3-23 Comparison of the neck size ratio between curve-fitting FD and full FD results at 100 MPa. .... 102

Figure 3-24 Comparisons of the surface area reduction between curve fitting FD and full FD results at  $D_S/D_g = 1$ . .... 103

Figure 3-25 Shrinkage ratio rate as a function of tip curvature for different applied stresses. .... 104

Figure 3-26 Comparison of relative density between curve-fitting FD and full FD results at  $D_S/D_g = 1$ . .... 105

Figure 3-27 Curvature  $K_{n-1}$  as a function of diffusion coefficient ratio for different neck size ratios..... 107

Figure 3-28 A comparison of tip curvature  $K_{tip}$  at  $D_S/D_g = 1$  for different applied stresses.. 109

Figure 3-29. Tip curvature as a function of neck size ratio for different diffusion coefficient ratios..... 110

Figure 3-30 A comparison of  $K_{tip}$  at  $D_S/D_g = 0.1$  for different applied stresses. .... 111

Figure 3-31 A comparison of $K_{tip}$ at $D_s/D_g = 1$ for different applied stresses. ....	112
Figure 3-32 A comparison of $K_{tip}$ at $D_s/D_g = 50$ for different applied stresses. ....	113
Figure 3-33 A comparison of $K_{tip}$ at $D_s/D_g = 100$ for different applied stresses. ....	114
Figure 3-34 A comparison of $K_{tip}$ at $D_s/D_g = 1$ for different surface energies. ....	115
Figure 4-1 Geometry of two particles during the sintering process [26]. ....	120
Figure 4-2 Flowchart of the variational model describing the sintering process. ....	125
Figure 4-3 Comparison of the neck size ratio between the FD curve-fitting and VM curve-fitting models. ....	127
Figure 4-4 Diagram of the steps used in SLS modelling. ....	128
Figure 4-5. 27 Copper particle arrangement in three layers for use in the SLS model. ....	129
Figure 4-6 First layer for SLS model. ....	129
Figure 4-7 Second layer of the SLS model. ....	130
Figure 4-8 Third layer of the SLS model. ....	130
Figure 4-9 Flow chart describing the numerical model for the selective laser sintering process. ....	136
Figure 4-10 Snapshot of the FE mesh for the 27 copper particles. ....	141
Figure 4-11 Snapshot of the nine particles in the first layer. ....	142
Figure 4-12 Flow chart showing the validation method used for all particles. ....	143
Figure 4-13 Shrinkage ratio as a function of sintering time. ....	144
Figure 4-14 Neck size ratio as a function of sintering time. ....	145
Figure 4-15 A comparison between the two numerical models in terms of neck size ratio for a particle size of 1 $\mu\text{m}$ . ....	146
Figure 4-16 Sintering temperature as a function of laser scan speed for a particle size of 1 $\mu\text{m}$ . ....	148
Figure 4-17 Neck size ratio as a function of laser scan speed for three different laser powers and a particle size of 1 $\mu\text{m}$ . ....	149
Figure 4-18 Shrinkage ratio as a function of scan laser speed for three different laser powers and particle size 1 $\mu\text{m}$ . ....	151
Figure 4-19 Laser power as a function of laser scan speed for copper particles and a particle size of 1 $\mu\text{m}$ . ....	152
Figure 4-20 Neck size ratio between particles for four different particle sizes and a laser power of 8 W. ....	153
Figure 4-21 Laser scan speed as a function of particle size for a laser power of 8 W. ....	154

Figure 4-22 Neck size ratio as a function of particle size for a laser power of 8 W.....	155
Figure 4-23 Relative density as a function of sintering time. ....	156
Figure 4-24 Relative density as a function of neck size ratio. ....	157
Figure 4-25 Relative density as a function of a laser scan speed for different laser powers and a particle size of 1 $\mu\text{m}$ . ....	158
Figure 4-26 Surface area reduction as a function of sintering time. ....	159
Figure 4-27 Surface area reduction as a function of neck size ratio for different contact numbers, with a laser power of 8W, and a particle size of 1 $\mu\text{m}$ . ....	160
Figure 4-28 Surface area reduction as a function of laser scan speed for a particle size of 1 $\mu\text{m}$ . ....	161
Figure 4-29 Neck size ratio as a function of laser scan speed for a particle size of 1 $\mu\text{m}$ . ....	162
Figure 4-30 Shrinkage ratio as a function of scan laser speed for a particle size of 1 $\mu\text{m}$ . ...	163
Figure 4-31 The movements of the nine particles in the first layer for a particle size of 1 $\mu\text{m}$ . All dimensions are in microns. ....	164
Figure 4-32 Shrinkage ratio as a function of particle size. ....	165
Figure 4-33 Relative density as a function of particle size. ....	166
Figure 4-34 Neck size ratio as a function of particle size. ....	167
Figure 4-35 The movement of the nine particles in the second layer. ....	169
Figure 4-36 The movement of particle 18 to the front right due to the effects of grain boundary diffusion. ....	169
Figure 4-37 The movement of particle 18 to the left. ....	170
Figure 4-38 Shows the movement of particle 18 to the front. ....	171
Figure 5-1 Structure of the LAMMPS code. ....	177
Figure 5-2 Neck size ratio compared with different diffusion mechanisms. ....	182
Figure 5-3 Potential energy/atom as a function of temperature for different nanocopper diameters. ....	186
Figure 5-4 Full and surface melting temperatures. ....	187
Figure 5-5 Melting temperature of nanocopper comparison with models. ....	189
Figure 5-6 Neck size ratio for different nanoparticle sizes at a sintering temperature of 600 K. ....	190
Figure 5-7 Shrinkage ratio for different nanoparticle sizes at a sintering temperature of 600 K. ....	191

Figure 5-8 Snapshot of two half copper nanoparticles for crystal lattice (100-100) for a size of 5 nm and sintering temperature 600 K..... 192

Figure 5-9 “Relative density” for different nanoparticle sizes at a sintering temperature of 600 K..... 193

Figure 5-10 Neck size ratio with copper nanoparticle size for different sintering temperature. .... 194

Figure 5-11 Shrinkage ratio with copper nanoparticle size for different sintering temperatures. .... 195

Figure 5-12 Neck size ratio with time for different crystal orientations at 600 K..... 196

Figure 5-13 Neck size ratio with time for different crystal orientations at 1100 K..... 197

Figure 5-14 Surface area reduction with nanoparticle sizes for difference sintering temperatures..... 198

Figure 5-15 Mean square displacement of 5 nm for different sintering temperatures.....200

Figure 5-16 Diffusion coefficient for difference sintering temperature. ....201

Figure 5-17 A comparison of neck size ratio between solid and hollow nano-copper at 600 K. ....202

Figure 5-18 Shrinkage ratio with time for solid and hollow copper nanoparticles at 600 K. ....203

Figure 5-19 Snapshot of two hollow copper nanoparticles. ....204

Figure 5-20 MSD for solid and hollow copper nanoparticles at 600 K.....205

Figure 5-21 Comparison of MSDs for three solid types of particles at a fixed particle size of 5 nm at sintering temperature of 1000K. ....208

Figure 5-22 Comparison of MSDs for three solid types of particles at a fixed particle size of 5 nm at sintering temperature of 600 K. ....209

Figure 5-23 Comparison of MSDs for three hollow nanoparticles types at a sintering temperature of 600 K. ....210

Figure 5-24 Comparison of MSDs for three hollow types of nanoparticles at a sintering temperature of 1000 K. ....211

Figure 5-25 Comparison of MSDs for hollow and solid nanoparticles at 600 K. ....212

Figure 5-26 Potential energies per atom for hollow and solid nanoparticles at 1000 K.....218

Figure 5-27 MSD for two different nanoparticle sizes for different sintering temperatures. 219

Figure 5-28 Shrinkage ratio for a couple of different nanoparticles at different sintering temperatures.....220

Figure 5-29 Potential energies for a couple of different nanoparticles at different sintering temperatures.....221

Figure 5-30 Neck radii of solid and hollow nanoparticles at sintering temperature 600 K...223

Figure 5-31 Neck size radius for the solid nanoparticles at different sintering temperatures. ....224

Figure 5-32 Shrinkage ratio of two solid and hollow nanoparticles of differing size at 600 K. ....225

**LIST OF TABLES**

Table 1.1 Classification of mass transport mechanisms [3]. .....	12
Table 1.2 Main stages of sintering [3]. .....	18
Table 2.1 kinetic equations for different growth mechanisms [4]. .....	24
Table 2.2 Two exponents n, m and parameter B for different sintering mechanisms [3]. .....	25
Table 3.1 Comparison of the particle's geometry for four neck size ratios. ....	89
Table 3.2 Comparison of the particles' geometry for different diffusion coefficient ratios. ....	90
Table 4.1 Input parameters for copper powders used in the numerical model [30]. .....	139
Table 4.2 Laser parameters used as input to the COMSOL simulation.....	140
Table 5.1 Bulk activation energy for different diffusion coefficients [103]. .....	179
Table 5.2 Initial diffusion coefficients [132]. .....	180
Table 5.3 Diffusion coefficients at 600 K [132]. .....	180
Table 5.4 Parameters for copper nanoparticles.....	183
Table 5.5 Comparison between hollow and solid nanoparticles at a sintering temperature of 1000 K and nanoparticle size 5nm.....	206
Table 5.6 The number of atoms inside nanoparticles. ....	207
Table 5.7 Different systems of nanoparticles at various different temperatures. ....	213
Table 5.8 Different systems of hollow nanoparticles at different temperatures. ....	215
Table 5.9 Comparison between hollow and solid nanoparticles at a sintering temperature of 600 K.....	216
Table 5.10 Solid and hollow nanoparticles at different sintering temperatures. ....	222

---

**LIST OF SYMBOLS**

<b><u>symbols</u></b>	<b><u>Meaning</u></b>
$V_g$	Grain boundary velocity, m/s
$j_g$	Grain boundary flux, Kg/ m <sup>2</sup> s
$j_s$	Surface flux, Kg/ m <sup>2</sup> s
$a$	Neck radius, m
$\Psi$	Dihedral angle
$\theta$	Half of dihedral angle
$\gamma_s$	Surface energy, J/m <sup>2</sup>
$\gamma_g$	Grain boundary energy, J/m <sup>2</sup>
$D_{eg}$	Effective grain boundary diffusion coefficient, m <sup>2</sup> /s
$D_{es}$	Effective surface diffusion coefficient, m <sup>2</sup> /s
$D_g$	Grain boundary diffusion coefficient, m <sup>2</sup> /s
$D_s$	Surface diffusion coefficient, m <sup>2</sup> /s
$\delta_g$	Thickness of the grain boundary, m
$\Omega$	Atomic volume, m <sup>3</sup>
$B_z$	Boltzmann constant, <sup>23</sup> m <sup>2</sup> kg/(s <sup>2</sup> K)
$T$	Sintering temperature, K

$a_o$	Initial neck radius, m
R	Initial radius of particle, m
$F_a$	Applied force, N
$\sigma_s$	Applied stress, Pa
$a_m$	Maximum value of neck size radio
s	Radius of free surface curvature in the meridional plane just at the edge of the grain boundary
$K_{tip}$	tip curvatures at the edge of the grain boundary
$Q_g$	Activation energy for grain boundary diffusion, J/mol
$R_r$	Gas constant, J/mol K
$C_o$	Equilibrium vacancy concentration
$R_1$ and $R_2$	Radii of the particles, m
C	Vacancy concentration
$\mu$	Chemical potential
$\rho_r$	Relative density
$\rho_o$	Initial relative density
$C_a$	Atomic concentration
$d_p$	Pore size, m
f	Atomic jumping frequency

$F$	Atomic driving force
$A_a$	Atomic spacing, m
$D$	Particle diameter, m
$X$	Neck diameter, m
$N_c$	Particle coordination number
$\Delta S$	Change in surface area to a final surface area
$S_o$	Initial surface area
$D_V$	Lattice or volume diffusivity, $m^2/s$
$V_m$	Molecular volume, $m^3/mol$
$M$	Molecular weight, $Kg/mol$
$\eta$	Viscosity, $Pa.s$
$P_v$	Vapor pressure, $Pa$
$b$	Burgers vector, m
$\rho$	Theoretical density, $Kg/m^3$
$D_a$	Gas diffusivity, $m^2/s$

**LIST OF ABBREVIATIONS**

<b><u>Abbreviation</u></b>	<b><u>Definition</u></b>
FD	Finite difference method
FE	Finite element method
VM	Variational method
MD	Molecular dynamics method
DEM	Discrete element method
CF-FD	Curve fitting finite difference
CF-VM	Curve fitting Variational method
SLS	Selective laser sintering
NR	Neck size ratio
SR	Shrinkage ratio
MSD	Mean square displacement

## **ACKNOWLEDGMENTS**

I would like to express my deep thanks to Professor Jingzhe Pan, my supervisor, for his perfect guidance, keen encouragement and useful discuss of this dissertation. Again I want to express my gratitude to my supervisor, for his supporting to make my thesis. I have been very lucky to have a good supervisor who cared and encouraged so much about my research in PhD, and who responded to my questions and queries so instantly. I would also like to convey my gratitude all the members of engineering department staff at Leicester University.

I would like to express my gratitude my mother and my father Mr. Obeed Al balod for their undivided love. Without their supporting and encouragement, I could not complete my PhD. I would like to thank my family for their undivided love. Without their supporting and encouragement, I could not complete my PhD. I also want to acknowledge my officemates for their endless support during my PhD student.

I would also like to extend my thanks to the engineering department staff for offering service to support my research. I would like to thank the high performance computing ALICE staff in the Leicester University. I also want to acknowledge the Ministry of higher education and scientific research, Republic of Iraqi, for awarding me full scholarship for these four years' study.

I would also like to extend my thanks to the Comsol software group, for allowing me to use this software in my thesis under licence number (7074366).

Last, but not least, I would like to thank Lammps code software groups, for allowing me to utilize this software to solve my problems.

**ANAS ALSHAMMERY**

**UNIVERSITY OF LEICESTER**

## **LIST OF PUBLICATIONS**

### **Publication researches**

- 1- Alshammery A. & Pan J., 2018," A new method to model the changing in tip curvature between particles during sintering process", in preparation.
- 2- Alshammery A. & Pan J., 2018," A new theoretical model to simulate selective laser sintering", in preparation.
- 3- Alshammery A. & Pan J., 2018," The improving of neck growth between nanoparticles during sintering process", in preparation

## 1 CHAPTER ONE: Sintering Practice and Mechanisms

This chapter gives a background of the powder metallurgy process and sintering operation, focusing on the mechanism of sintering represented by mass transport between particles.

### 1.1 Powder metallurgy

Powder metallurgy is a manufacturing technology used to produce solid parts of different shapes and materials from metal powder. Generally, the powder metallurgy process can be divided into three stages: powder blending, powder compacting and sintering. Figure (1-1) shows the three stages of powder metallurgy. The first stage, which is known as powder blending in powder metallurgy and describes the mixing of powder [1].

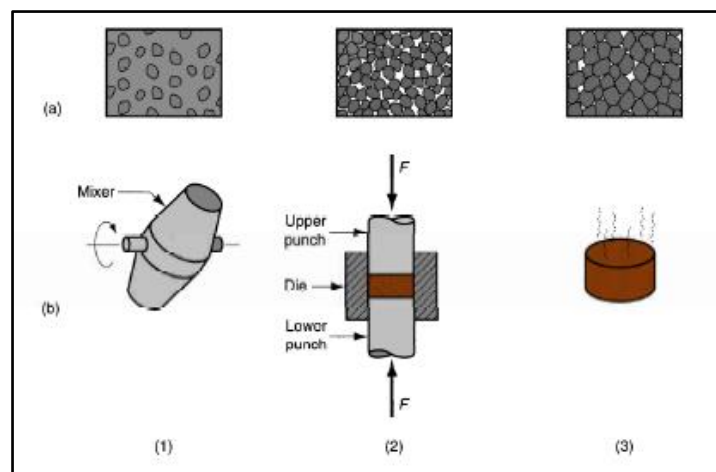


Figure 1-1 General powder metallurgy stages [1].

The second stage is the compacting stage. In this stage the mixed powders are pressed between two punches under uniform pressure to compress them into the

desired shape. As a result of this stage, the density of the product is increased during the second stage while sintering is the last stage of powder metallurgy in which the compressed product is heated to a temperature below its melting point in order to form bonds between the particles [1].

The chart in figure (1-2) shows the diversity of markets for powder metallurgical products. It can be seen from the chart that automotive applications take a 70% share the total of powder metallurgy products, while other industrial applications constitute about a quarter of the total [2].

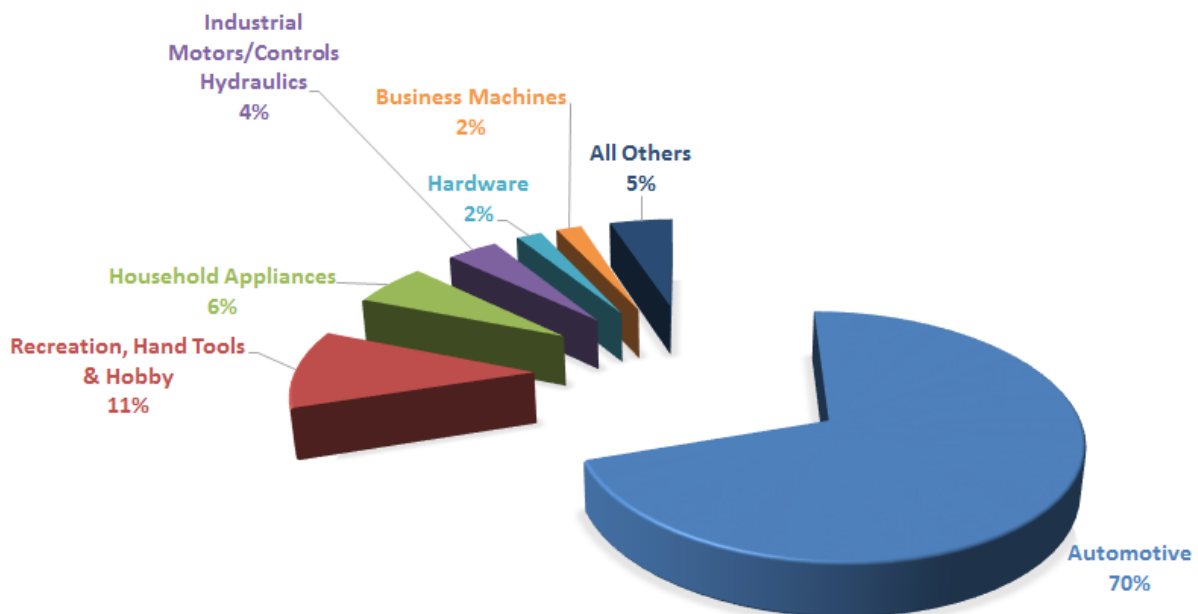


Figure 1-2 The market for powder metallurgy parts [2].

## 1.2 Sintering

Sintering is a technique used to produce a new product from the powder of different materials by supplying temperature and it represents the final stage of the powder metallurgy process. In the sintering process, the neck growth and densification between particles improve due to the increase in sintering temperature during the process. There are many parameters that can affect the sintering process, such as temperature, time, particle size, the geometrical structure of the particles, composition

of the powder mix, the density of the powder, composition of the protective atmosphere in the sintering furnace, etc. [3].

Generally, there are two types of sintering processes, i.e., solid state sintering and liquid phase sintering. Solid state sintering occurs between solid particles when the temperature is increased to the sintering temperature, while the liquid phase sintering uses particles in the liquid phase [4].

The chart shown in figure (1-3) illustrates a comparison of different processes in terms of material wastage and energy consumption per kilogram of product. Overall, it can be observed from the chart that sintering had the lowest material wastage and energy consumption.

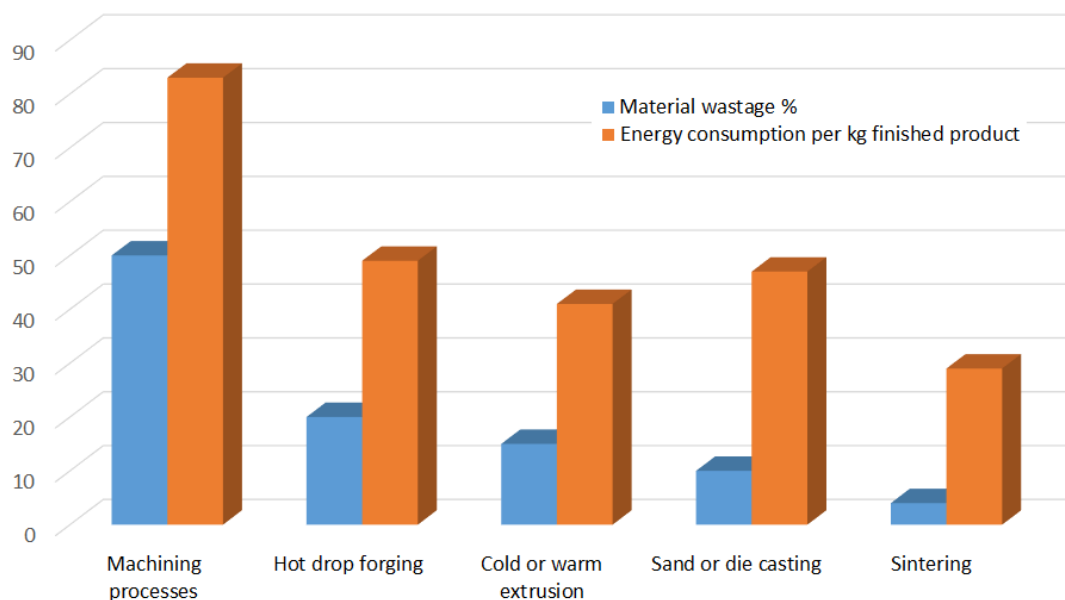


**Figure 1-3 Comparison between different processes for two terms material wastage and energy consumption per kg, (EPMA).**

### 1.2.1 Variables that control the sintering process

Variables play an important role in the sintering process. There are three types of parameters that can affect the sintering process, i.e., processing variables, material variables, and geometric variables [3]. For example, processing variables depend on

the sintering process, such as time, pressure, atmosphere, cooling rate and heating rate, relative density. Material variables depend on materials such as melting temperature, grain energy, surface energy, atomic volume, crystal orientation, and diffusion coefficient, density. Geometric variables depend on the geometric of the particles such as surface area, particle size, pore size and pinning.

### 1.3 Solid state sintering processes

Solid state sintering is a densification process that occurs between solid particles at solid phase temperatures, and the neck construction occurs by diffusion. Figure (1-4) shows the three steps of sintering between particles which are initial contact between particles, neck growth, and densification [5].

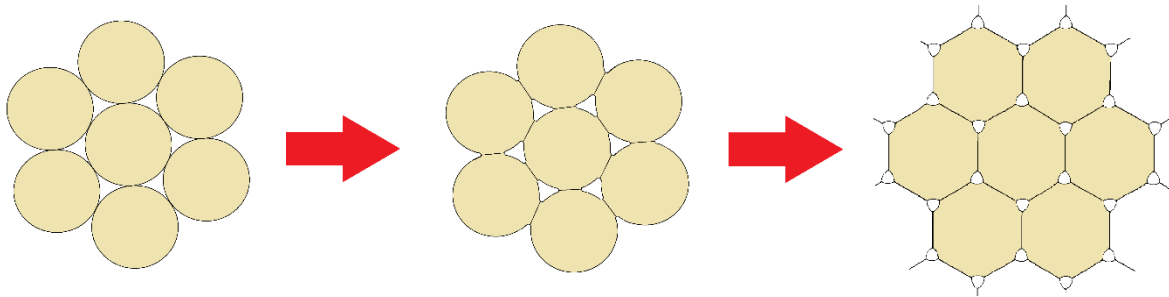


**Figure 1-4 Three steps of solid state sintering [5].**

Sintering temperature is one of the important factors in sintering process, and typically ranges between 0.7 and 0.9 times the powder's melting point. Another important factor is that sintering time is dependent on the size of the mechanical part being manufactured. Tungsten is an example of a material that requires a long sintering time [1].

The furnace atmosphere is another important factor in the sintering process because it controls chemical reactions such as carburization and decarburization. In addition, the furnace atmosphere is used to prevent oxidation and remove existing oxides, prevent undesirable chemical reactions and facilitates the burning off of additives. Carbon monoxide, disassociated ammonia, hydrogen, argon, and helium are generally used for industrial sintering processes. A vacuum system is sometime used

to control the atmosphere during the sintering process, especially in the sintering of stainless steel [1].

There are three efficient zones to complete the sintering process of a metal, namely the pre-heat zone “De-Lubrication”, the hot zone and cooling zone (see figure (1-5)) [1].

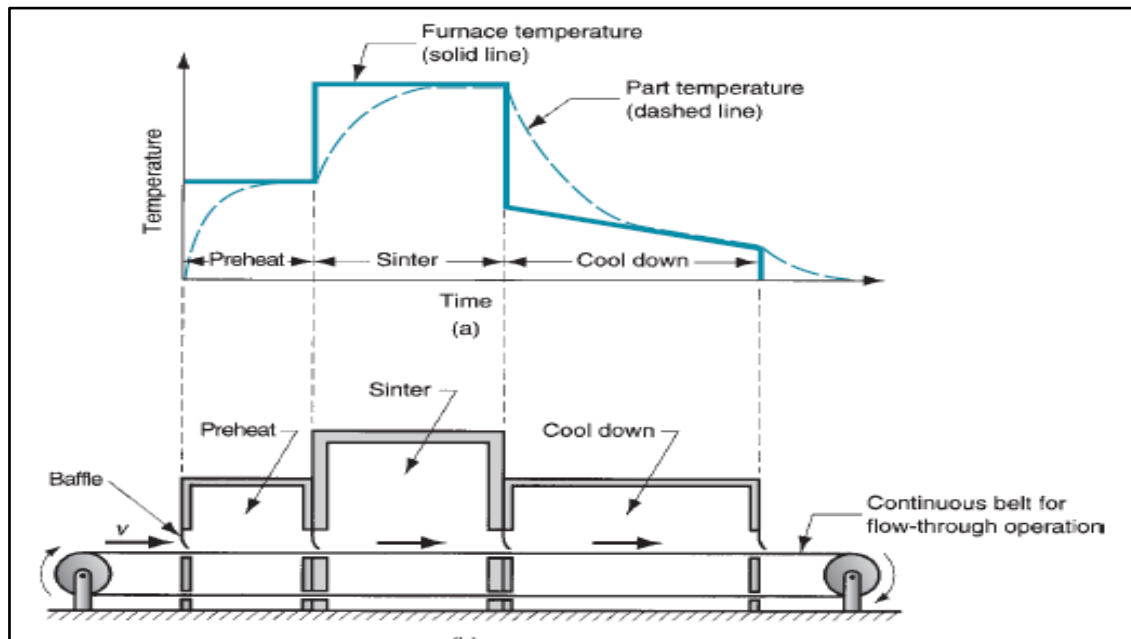


**Figure 1-5 Sintering process using a continuous furnace [1].**

First of all, the compressed powder is exposed to preheating. The preheating stage will only heat the part to a low temperature to burn off binders and lubricants. The temperature is increased to the sintering temperature in the second stage and maintained for the desirable duration necessary for the chosen amount of bonding between the powder particles to occur. In the third stage, the temperature is decreased to allow the part to cool. Furnace atmosphere is important at this stage and there is a particular need to control the atmosphere during the cooling down of the part to prevent unwanted chemical reactions between the part and the environment [1]. There are many types of solid state sintering processes, for example, spark plasma sintering, electro-sinter-forging, microwave sintering, selective laser sintering, etc.

### 1.3.1 Spark plasma sintering process

Spark plasma sintering is a new sintering technology which is based on the phenomenon of spark discharge. This process depends of the two actions of pulsed direct electrical current (DC) and uniaxial force under conditions, of either low atmospheric pressure, or with the addition of gas to accelerate powder consolidation. The mechanism of SPS is that the gap between powder particles carries a micro-spark discharge that results in the sintering itself.

The advantages of the SPS process are a decreased sintering time and temperature; for example, the SPS process can operate at high sintering rates and give a high heating rate. SPS proceeds via three stages: plasma heating, to produce surface heating; joule heating, to increase the diffusion of atoms within the neck between particles; and plastic deformation, to increase the densification between particles. SPS is consequently considered to be a rapid, high efficiency process that is easy to complete and can be used with a wide range of different materials.

Figure (1-6) shows the various components of the spark plasma sintering process equipment. The load on the punch in the SPS process can be up to 100 MPa, whilst the voltage is generally very low, with a DC pulse time of around 1-10 ms.

### 1.3.2 Microwave sintering process

Microwave sintering is different to conventional sintering because microwave sintering includes radiation and conductive heating components for the transfer of thermal energy, where the heat of the microwave comes from converting the electromagnetic energy into thermal energy in a highly efficient and rapid process.

The advantages of microwave sintering are: saving energy and time, a reduced process temperature and cycle time, rapid heating rate, enhanced mechanical properties, and reduced impact on the environment. Aluminium, tungsten, tin, copper, nickel, cobalt, iron, and steel powders can be used in microwave sintering as raw powders. The largest microwave sintered products are gears which are produced from steel powders for dimensions of 10 cm in diameter and 2.5 cm in height.

Figure (1-7) shows the components of the microwave sintering process equipment. The power and frequency used in microwave sintering are 1-6 kW and 2.45 GHz, respectively. The sample is placed inside an insulated ceramic chamber to keep the heat generated within the sample. Gases are provided for the atmosphere of the microwave chamber in order to increase the temperature of the process to 1600°C. N<sub>2</sub>, H<sub>2</sub>, and Ar are examples of the gases used for the atmosphere.

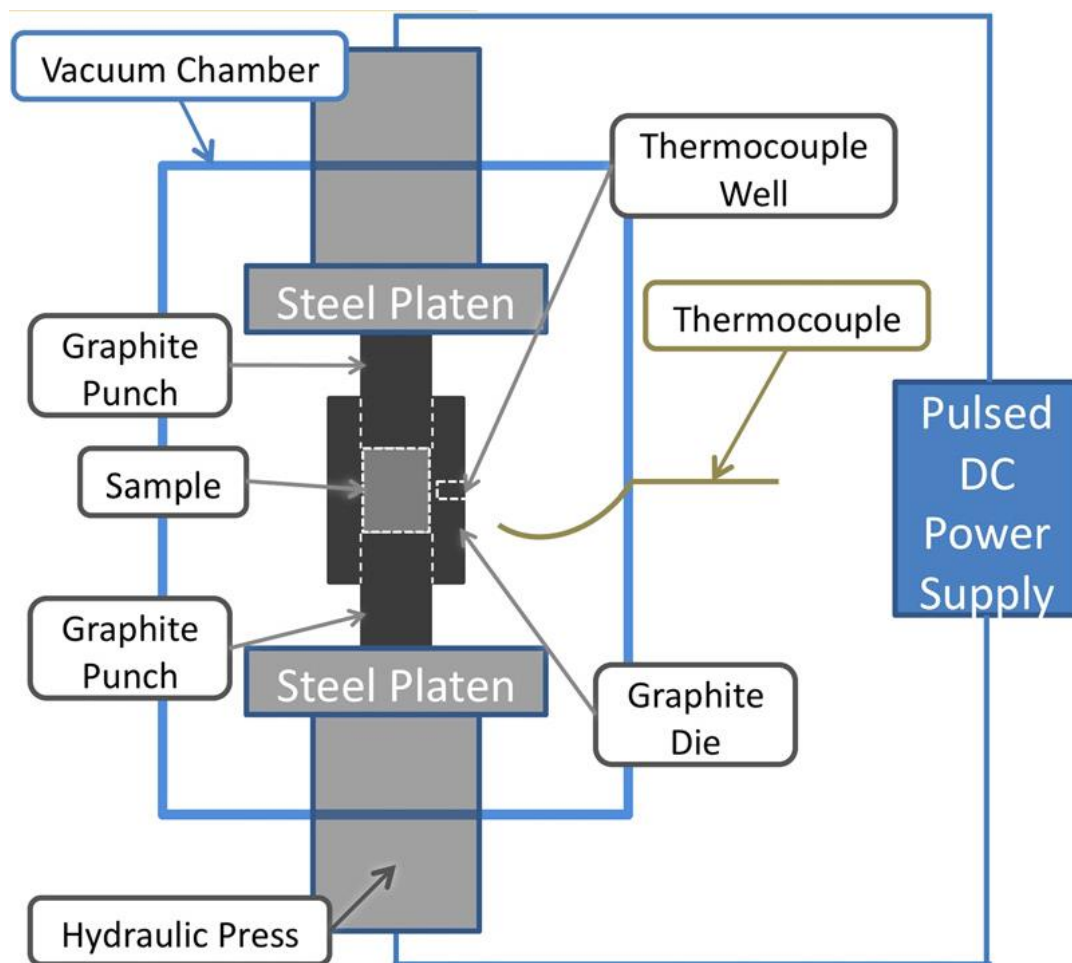


Figure 1-6 Spark plasma sintering process equipment [6].

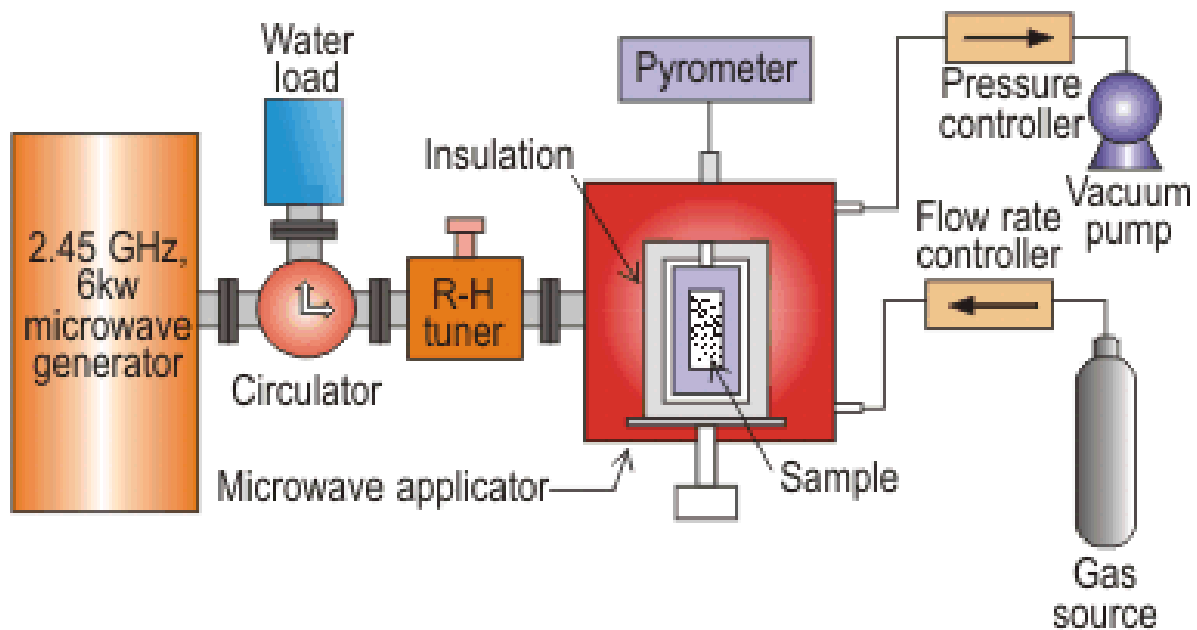


Figure 1-7 Microwave sintering process equipment [7].

### 1.3.3 Electro sinter forging process

Electro sinter forging (ESF) is a new, faster sintering technique which combines electromagnetic energy with compression load. This process does not require vacuum, only a tiny amount of energy, it can accommodate a new range of different materials and alloys, and has a process time cycle of less than 29 mins. Figure (1-8) shows the electro sinter forging process equipment.

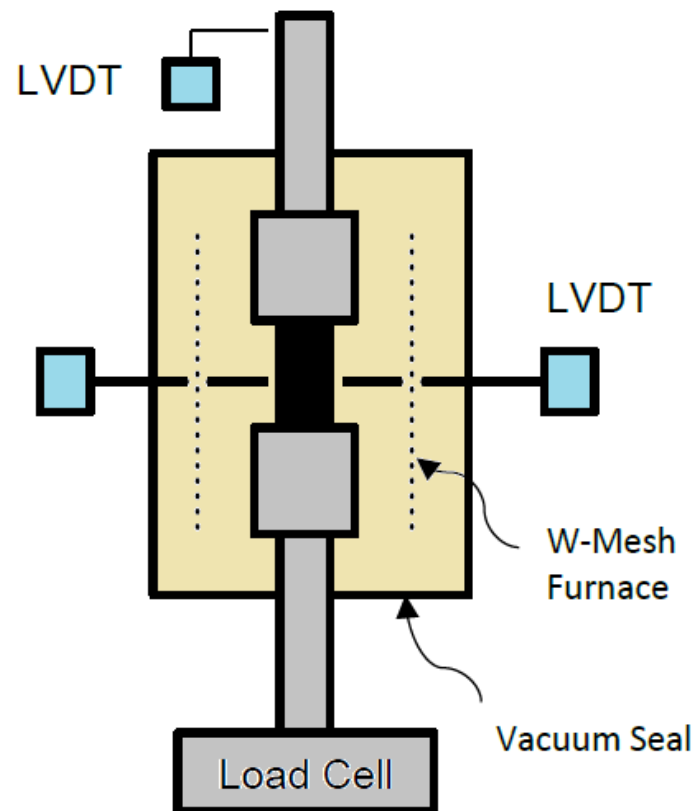


Figure 1-8 Electro sinter forging process equipment [8].

### 1.3.4 Selective laser sintering process

Selective laser sintering is a new technique that uses a laser as a source for heating in the sintering process. This method is a type of additive manufacturing process that first converts CAD drawing files to the STL format. Then the next and final stage of SLS process is making a 3D object using a 3D laser printer. Metals, plastics, ceramics, composite materials, and glass powders are utilized in the SLS process. The material powders are heated using a CO<sub>2</sub> laser to induce the sintering process between particles and to ultimately create the product. There are four steps to the SLS process, as shown below.

The first step: a piston containing the powder is raised to the top of the powder level. In the second step: the roller will start to move the powders about to ensure complete

coverage and levelling of all surface powders. The third step: the laser beam starts scanning and focussing on the design shape within the powders. The fourth step is started by moving the product piston down with the scanned powders. The SLS process will continue until the final product shape is complete. These four steps are repeated for each layer, so, for example, if the product has 1000 layers, then the SLS process will perform 4000 steps for one product. The factors that affect the SLS process are the: SLS laser stages, laser scanning direction, and powders. The laser scanning process is shown in Figure (1-9).

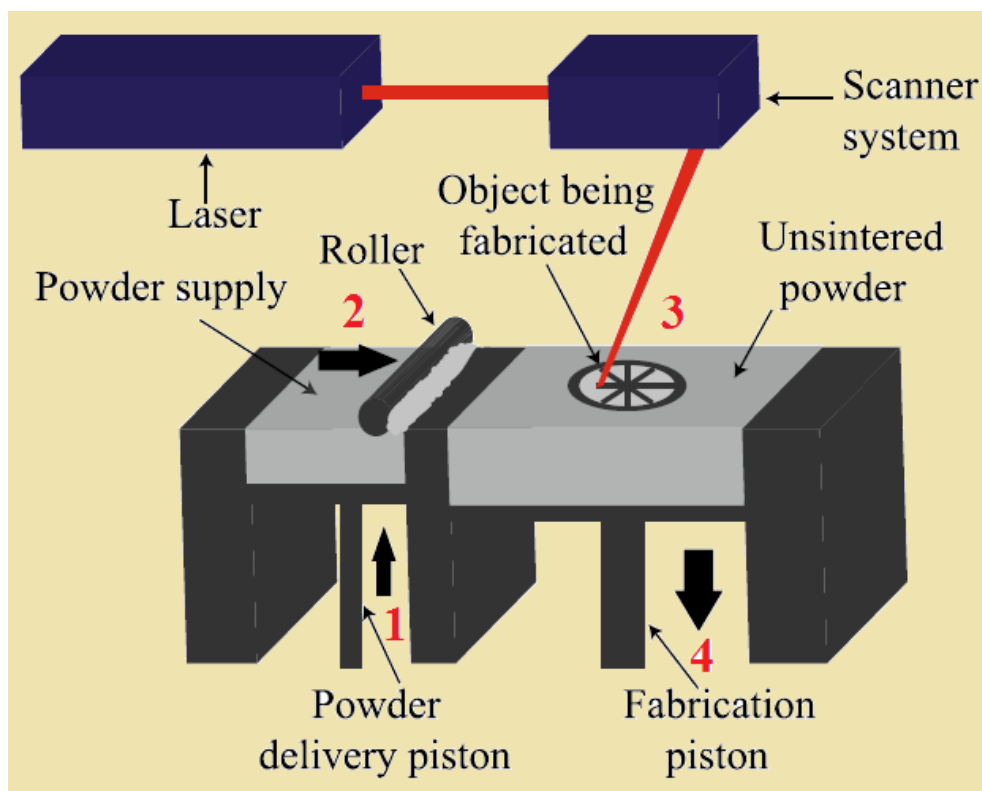


Figure 1-9 Components used in the SLS process and the movement of the laser [9].

Selective laser sintering represents the movement of the laser beam over the powders to make connections between particles during the rapid sintering period, while the other methods depend on supplying a thermal process directly, with or without the use of pressure. There are many advantages to using selective laser sintering such as the ability to produce complex designs and also produce designs rapidly. It can use a

wide range of materials and a variety of mechanical properties. It is an easy method to use (direct method) and has a low cost compared with other methods (time-saving).

#### 1.4 Driving Force of Sintering

The contact between solid particles is induced when temperatures are increased, from the outcome of this contact, a neck forms between each of the particles during which they will bond; this process is known as sintering (see figure 1-10) [10].

The driving force of sintering can be defined as the total interfacial energy, which is equal to the total free energy of the particles, and the transport of two surfaces to the grain boundary, which is shown in figure (1-10). Thus, the full interfacial energy of a compressed powder is given by  $\Delta E$ , where  $\gamma_s$  is the surface energy,  $\gamma_g$  is grain boundary energy, and  $A$  is the surface area of the compact [10]. The decrease in the total energy is shown in equation (1.2).

$$\gamma_s \cdot 2A \rightarrow \gamma_g \cdot A \quad (1.1)$$

$$\Delta E = \gamma_g \cdot A - \gamma_s \cdot 2A = (\gamma_g - 2\gamma_s)A \quad (1.2)$$

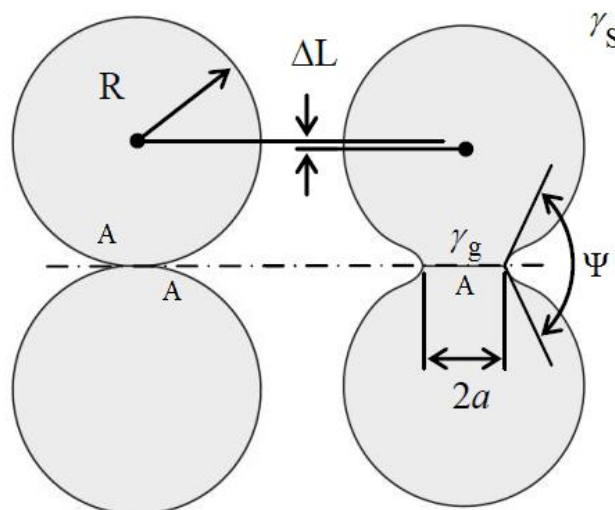


Figure 1-10 Basis of the phenomena that occur during sintering [10].

## 1.5 Mechanisms of Solid State Sintering

Mass transport represents the mechanisms within sintering which can be used to explain the flow of atoms in response to the driving force of sintering. The movement of atoms and vacancies depend on the type of diffusions, such as grain boundary diffusion, surface diffusion, volume diffusion, and evaporation-condensation.

The mass movement may take place via various different transport mechanisms along various paths; however, there are two general types of mass transport, namely surface transport and bulk transport. Each type constitutes several mass transport mechanisms at the atomic level, which are summarised in table (1.1). The basic difference between surface and bulk transport is the shrinkage or densification of the particles, which does not occur during surface transport mechanisms, as shown in Figure (1-11) [3].

**Table 1.1 Classification of mass transport mechanisms [3].**

<b>Type of Mass Transport</b>	<b>Mechanisms Involved</b>
Bulk Transport	Plastic Flow Grain Boundary Diffusion Volume Diffusion
Surface Transport	Evaporation-Condensation Surface Diffusion Volume Diffusion

Surface transport can be categorised in one of three ways: surface diffusion, volume diffusion, and evaporation-condensation. The neck growth between particles occurs during surface transport due to the movement of atoms from the surface of the

particles to the surface of the neck. Because the atoms move from the surface, and not the interior of the particles, there is no shrinkage or densification (without overlap between particles). Most metal mass transport mechanisms are dominated by surface diffusion at low temperature during sintering. Evaporation-condensation does not occur in metals; whilst volume diffusion can occur, the movement of mass is extremely slow compared to other transport mechanisms because the atoms transport through the inside of the particle not via its surface [3].

Bulk transport includes the three categories: plastic flow, grain boundary diffusion and volume diffusion. Neck growth occurs during the bulk transport processes, but results in the densification of the particles due to the atoms originating from inside the particles and diffusing to the neck. Grain boundary diffusion is significant in the densification of materials which have crystalline structures, while plastic flow usually occurs early in the heating operation. Generally, the bulk transport mechanisms are more effective at elevated temperatures because of the faster transport of atoms inside the particles. The mass transport theory of sintering is to be discussed below [3].

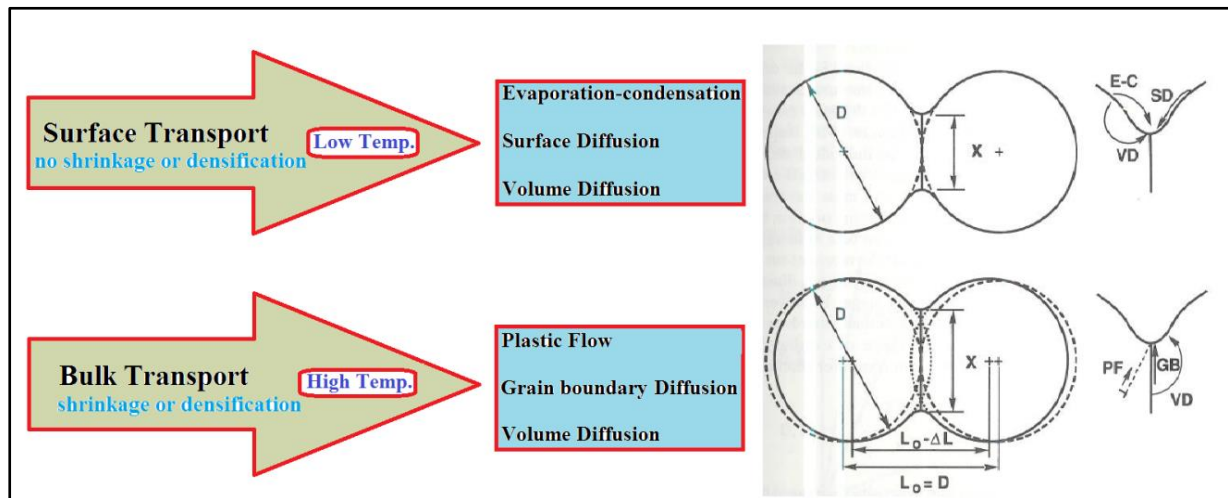
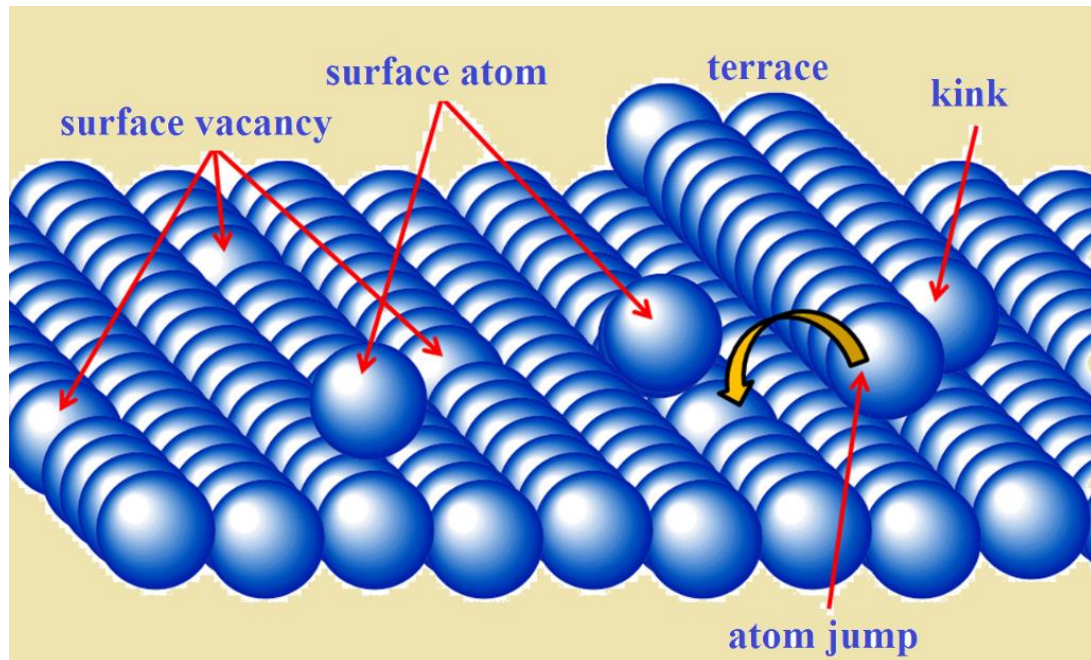


Figure 1-11 Two types of mass transport [3].

### 1.5.1 Surface Diffusion

Sintering by surface diffusion occurs through atom transport on the surface of the particles, and the movement is from the particle surface to the neck surface. Temperature and crystal orientation are significant factors in surface diffusion. The

surface of a solid particle is usually rough but consists of defects that contain elements such as kinks, adatoms, ledges and vacancies, as shown in figure (1-12), and atoms can move easily between these elements [3].



**Figure 1-12 Elements on the particle's surface [3].**

There are three stages in surface diffusion: the first is the breaking of atomic bonds, especially at a kink; the second is the movement of atoms across the surface; and the last stage is the reattachment of atoms to the new region of the surface. The transport of atoms across the surface of the particles is very rapid. The surface diffusion activation energy is associated with the rate of the slowest step, and changes with temperature. Surface diffusion increases due to the increase of curved surfaces and temperature, also the surface defects increase, which leads to additional surface diffusion.

Heating to the sintering temperature makes surface diffusion an active process, where the activation energy for surface diffusion is lower than for other diffusion processes. In addition, surface diffusion occurs at lower temperatures in comparison with other sintering mechanisms. Atomic transport occurs from one surface position to another position during surface diffusion. Therefore, surface diffusion does not result in densification. If densification is important, this means surface diffusion is undesirable.

Rapid heating to the sintering temperature is one method of reducing mass transport due to surface diffusion which can be used when densification is desired [3].

### 1.5.2 Volume Diffusion

Volume diffusion, or lattice diffusion, is the transport of vacancies through the lattice structure between particles. Figure (1-13) shows the volume diffusion between three particles. There are three factors that can affect the rate of volume diffusion, which are the composition of the particles, the temperature, and the pressure. There are three major paths by which vacancy diffusion can contribute to sintering. The first vacancy path is from the surface of the neck, through the inside of the particle, and then onto the particle surface. A net consequence of this path is that of mass transport to the neck surface, so there is no associated shrinkage or densification. This path is known as volume diffusion adhesion in order to distinguish it from the densification process [3].

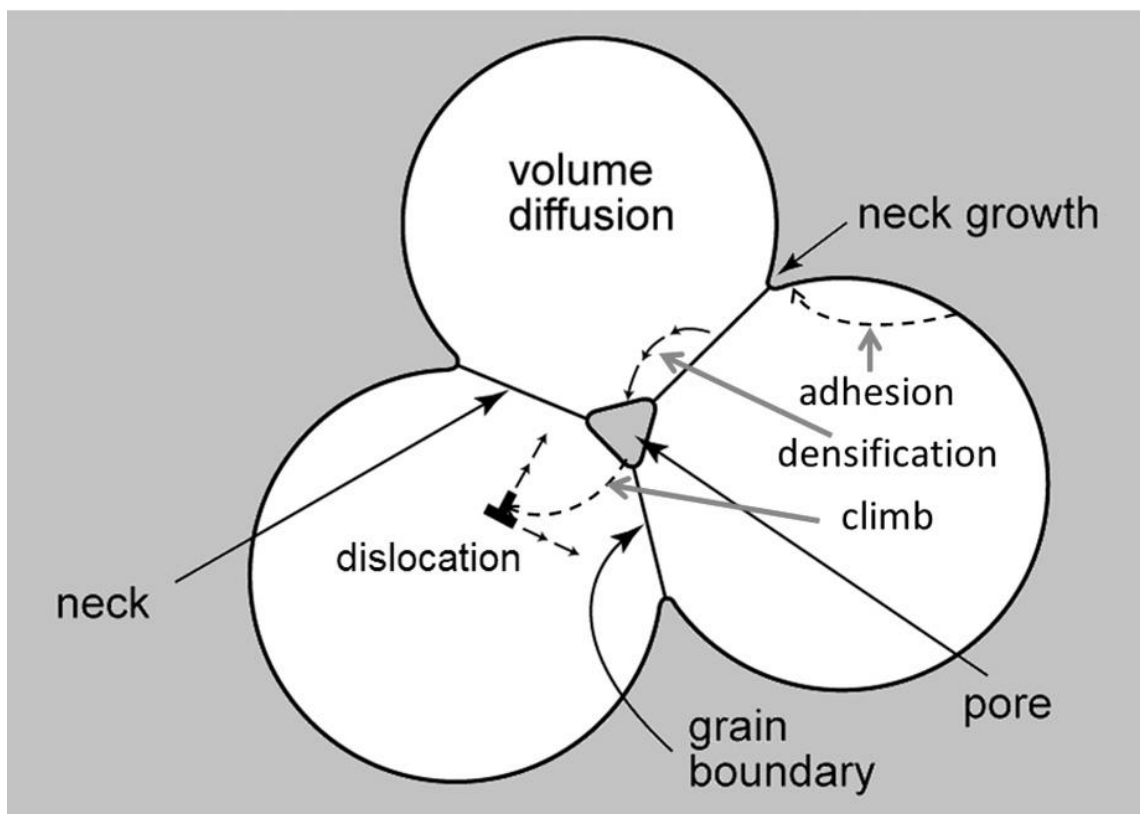


Figure 1-13 Diffusion vacancy pathways [3].

The flow of vacancies to the interparticle grain boundary from the surface of the neck represents the second volume diffusion path. Two consequences of this path are densification and shrinkage, because the vacancy is removed from the grain boundary and replaced by an atom. In addition, the distance between the centres of the neighbouring particles is decreased by the second diffusion path. This is the best method by which gain densification occurs as it decreases the distances between the centres of the particles. The third and last volume diffusion path is known as dislocation climb, because vacancies are annihilated by this path. The direction of the vacancy path opposes the direction of the atoms' movement, therefore vacancies disappear from inside the particle to the surface during this path.

The concentrations of vacancies in the particles are affected by temperature and curvature, and the vacancy concentration can be determined from the curvature. The vacancy concentration is lower for a convex surface and greater for a concave surface. This means that the direction of mass transport is from the surface of the particles (convex) to the neck between particles (concave). The activation energy of volume diffusion is higher than for other diffusion mechanisms (surface and grain boundary diffusion) [3].

### **1.5.3 Grain boundary diffusion**

Grain boundary diffusion is one of the basic mechanisms of bulk transport between particles at high temperature. Grain boundaries are the interface between particles with different crystal directions. Figure (1-14) illustrates a group of misorientation steps between particles, where the angle of misorientation between the two grain boundaries is  $36^{\circ}.52'$  [3].

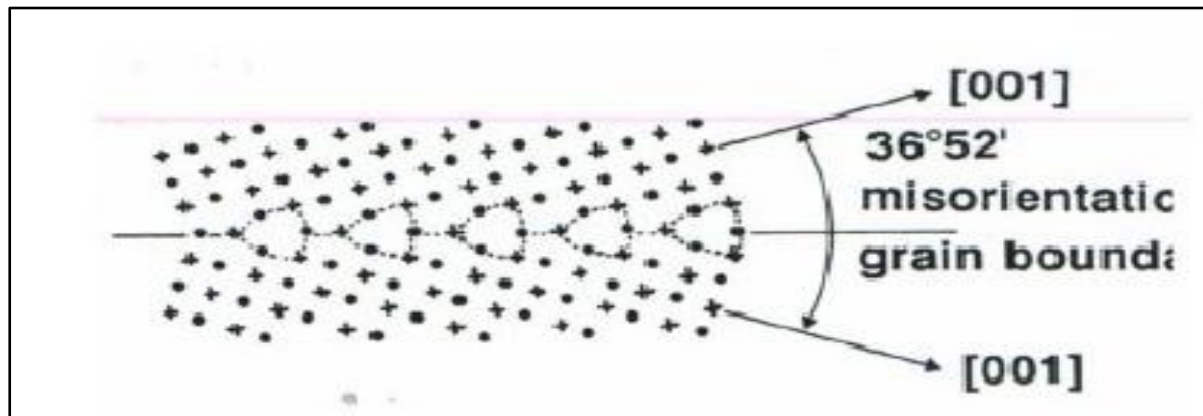


Figure 1-14 Misorientation steps in a grain boundary [3].

The activation energy required for grain boundary diffusion is between the amount required for surface and volume diffusion. The distance between grain boundaries is small, but the mass transport path is still effective. The vacancies transport in the opposite direction to the mass, where the mass is removed along with the grain boundary and into the sintered bond. Grain growth and the space between particles are the limiting factors in the grain boundary diffusion process. Finally, there are several factors that can affect grain boundary diffusion, namely grain size, grain shape and distribution [3].

## 1.6 Stages of solid state sintering

The stages of sintering are a series of physical processes that occur between particles causing them to bond together, whilst removing the porosity between them. There are four principal stages to reach an equilibrium of the sintering process. Table (1.2) illustrates the sintering stages and the processes associated with each stage.

Figure (1-15) shows the four stages of sintering, starting with the first stage, which is known as the loose powder stage, and after transforming to the initial stage (neck growth), and to the intermediate stage which is known as densification. Lastly, in the final stage, the pore size decreases with grain growth.

Table 1.2 Main stages of sintering [3].

Stage	Process	Densification	Coarsening
Adhesion	Initial contact	None	None
Initial	neck formation between particles	Initial densification	Minimum
Intermediate	Densification between particles, and cylindrical pore on particle edges	Effective	Grain and pore size Increasing
Final	Spherical and closed pore on particle corners	Slow process	Grain growth

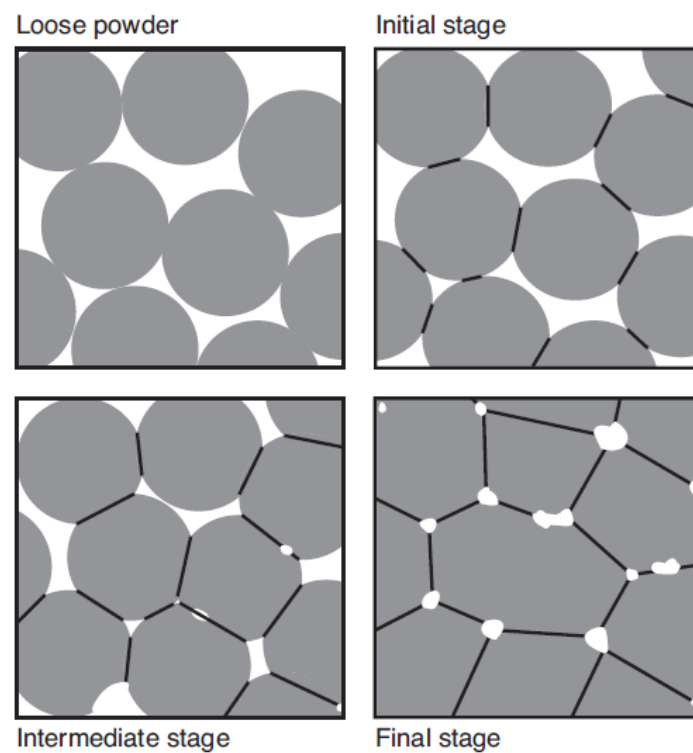


Figure 1-15 Configuration of particles during the stages of sintering [11].

Figure (1-16) illustrates the changes in pore size during the various stages of sintering. The pores start as a group of linked spaces between the grains and close off with the particles' densification to finally become isolated from each other [3].

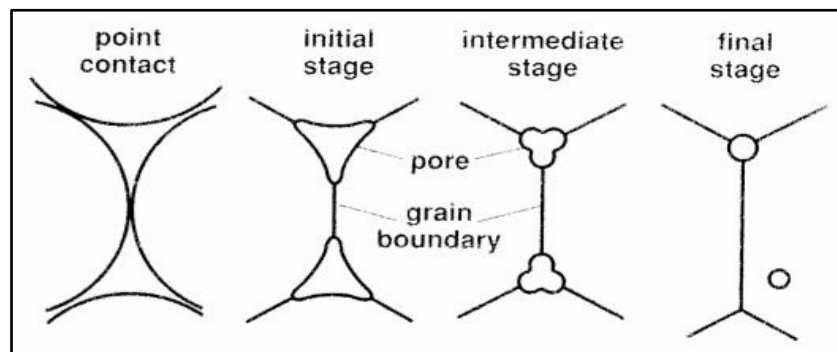


Figure 1-16 Configuration of pores at different stages of the sintering process [3].

### 1.6.1 The first stage of solid state sintering

The adhesion, rearrangement, and repacking of particles occur in the first stage of sintering which is known as the loose powder stage. In this stage, the particles gain a higher green density and accompanied by a reduction in the energy of the grain boundary structure by rotation and repacking, which results in unstable surface energies, diverse crystallographic orientations, and inhomogeneous packing coordination. The primary coordination number of each particle is typically seven with an approximately 64% a green density, and the coordination number rises to a maximum of 14 as shrinkage and densification occur [3].

### 1.6.2 The second stage of solid state sintering

The initial stage is the second stage of sintering which is known as neck growth. In this stage, the neck between the particles grows to form a disc. The growths of the necks are independent of each other during the initial stage, as the necks are extremely tiny. The end of this stage is reached when the ratio of the neck size is around 0.3, and neck size ratio is equal to the neck radius to particle radius ratio. The neck growth stage is significant because it can be connected to other factors such as shrinkage, density, and surface area [3].

### 1.6.3 The intermediate stage of solid state sintering

The intermediate stage plays an important role in densification. Simultaneous pore rounding, particle grain growth, and densification occur during this stage. In addition, the shape and colour of the grains are changed to a tetrakaidecahedron and dark. The grain growth at the end of this stage is rapid because the effect of pore pinning decreases as the pores change from a cylindrical shape to a spherical shape [3]. Figure (1-17) shows the grains in the intermediate stage.



**Figure 1-17 Shape of particles in the intermediate stage of sintering [3].**

### 1.6.4 The final stage of solid state sintering

The density is increased and the pores become closed in the final stage of sintering. In addition, the percentage of open pores reduces, which start to close at around 15% porosity and are fully closed by 5%. Ostwald ripening can occur in the final stage, where the smaller pores contribute to the growth of larger ones. All three earlier stages

occur more rapidly than the final stage. Figure (1-18) shows a tetrakaidecahedron grain with spherical pores [3].

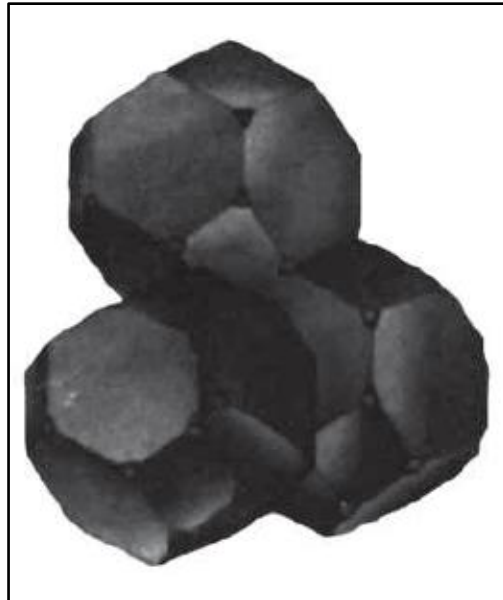


Figure 1-18 Shape of particles in the final stage [3].

### 1.7 Measurement of the sintering process

There are several parameters that can be affected during the sintering process which can be measured experimentally using specific equipment. Good examples of such parameters are the measurement of density or the shrinkage of the powder with time or temperature during the compacting operation, and measuring density as a function of sintering time or temperature. The Dilatometer test is one of the best tests by which to measure the density or the shrinkage of a compact powder [3].

### 1.8 Organization of thesis

This thesis is divided into six chapters, which describe the extent of knowledge about the mathematical modelling of the sintering process between particles. Chapter one gives an introduction to sintering, which contains the definition and history of sintering,

and the mechanisms which describe the sintering process and gives a discussion of different mechanisms of mass transport. Chapter two presents a literature review of sintering models which focusses on the variational method, Finite Difference method, and the molecular dynamics method that is used to model nanosintering. Also, this chapter summarises the analytical solutions to different transport mechanisms.

Chapter three focusses on making a new sintering model depending on the curve fitting equation used to connect the curvature of the particles' surfaces and neck size ratio considering two spherical particles. The finite difference method is used in the code to create a new curve fitting method for different diffusion coefficient ratios. Also, the different applied stresses are used in model to validate the new method with a full FD method for different diffusion coefficient ratios. Surface reduction area and relative density are used in the validation of the new method. Chapter four focusses on applying the curve fitting equation via the variational method to create a selective laser sintering model for 27 copper particles. Also, the COMSOL software is used in chapter four to simulate the movement of a laser beam over copper powder during the SLS process; moreover, the sintering temperature is also determined from this simulation. Chapter five focusses on nanoparticle sintering using molecular dynamics methods, using the LAMMPS code to simulate solid-state sintering between nanocopper particles, and to calculate the full and surface melting temperatures for different nanoparticle sizes. Also, the LAMMPS code is used to simulate multiple nanoparticles of copper in two cases: hollow and solid nanoparticles. The last chapter, chapter six, gives a number of concluding remarks regarding the results of the thesis.

## 2 CHAPTER TWO: A literature review on sintering models

This chapter gives a literature review of the analytical formulae and modelling of solid-state sintering used by many researchers. There are different forms of numerical solutions such as the Finite element method (FE), the Finite difference method (FD), Discrete element method (DEM), Molecular dynamics (MD), variational method (VM), and Monte Carlo simulations; all of these can be used to model solid-state sintering.

### 2.1 Literature review of analytical models

Sintering modelling is the simplest way to examine the behaviour of particles during the sintering process, for instance the connection and movement between particles can be studied without using a lab to access these parameters. Experimental sintering processes are expensive and time consuming compared with modelling the sintering process, which is a relatively fast way by which to collect sintering parameters.

#### 2.1.1 Initial stage model

The initial stage of sintering is the second stage, which is known as neck growth. In this stage, the neck between particles grows to form a disc. Table (2.1) illustrates the kinetic equations that represent different mechanisms for this growth, giving a physical description of both neck growth and shrinkage at the initial stage of sintering [4].

Another sintering model used to represent the sintering transport mechanism uses the neck size ratio ( $X/D$ ), that is, the ratio of the neck diameter to the particle diameter, as per equation (2.1); this equation is a function of sintering time under conditions of constant temperature. Table (2.2) gives a list of two exponents,  $n$  and  $m$ , and parameter  $B$ , where the exponent  $m$  is dependent on particle size [12].

Table 2.1 kinetic equations for different growth mechanisms [4].

Sintering mechanism	Neck growth	Shrinkage	Scale exponent
1-Lattice diffusion from grain boundary to neck	$a^4 = \frac{16D_V \gamma_S V_m R}{R_r T} t$	$\frac{\Delta l}{l} = \left( \frac{D_V \gamma_S V_m}{R_r T R^3} \right)^{1/2} t^{1/2}$	3
2-Grain-boundary diffusion from grain boundary to neck	$a^6 = \frac{48D_g \delta_g \gamma_S V_m R^2}{R_r T} t$	$\frac{\Delta l}{l} = \left( \frac{3D_g \delta_g \gamma_S V_m}{4R_r T R^4} \right)^{1/3} t^{1/3}$	4
3-Viscous flow	$a^2 = \frac{4 \gamma_S R}{\eta} t$	$\frac{\Delta l}{l} = \frac{3 \gamma_S}{8\eta R} t$	1
4-Surface diffusion from particle surface to neck	$a^7 = \frac{56D_s \delta_s \gamma_S V_m R^3}{R_r T} t$		4
5-Lattice diffusion from particle surface to neck	$a^5 = \frac{20D_V \gamma_S V_m R^2}{R_r T} t$		3
6-Gas phase transport			
6.1 Evaporative-condensation from particle surface to neck	$a^3 = \sqrt{\frac{18 P_V \gamma_S}{\pi \rho^2}} \left( \frac{M}{R_r T} \right)^{3/2} R t$		2
6.2 Gas diffusion from particle surface to neck	$a^5 = 20 P_V D_a \gamma_S \left( \frac{V_m}{R_r T} \right)^2 R^2 t$		3

$$\left( \frac{X}{D} \right)^n = \frac{Bt}{D^m} \quad (2.1)$$

The parameter B depends on the temperature, which is given by equation (2.2), whilst equations (2.1) and (2.2) represent the end of the initial sintering stage.

$$B = B_0 \exp\left(-\frac{Q}{R_r T}\right) \quad (2.2)$$

Shrinkage occurs when overlap between particles occurs. Equation (2.3) represents the sintering shrinkage,  $\Delta L/L_0$ , which is the change in distance between two particles' centres as a ratio of the original distance.

$$\left(\frac{\Delta L}{L_0}\right)^{\frac{n}{2}} = \frac{Bt}{D^m} \quad (2.3)$$

A useful initial solid state sintering model is represented by equation (2.4), as developed by Coblenz et al. [13] This model depends on time and temperature. The neck size ratio ( $X/D$ ) is used in equation (2.4) to determine the type of the sintering stage. The result from the Coblenz model fits a range  $0.03 < X/D < 0.3$ .

$$\frac{X}{D} = \left(\frac{225t}{\tau_s}\right)^{\frac{1}{5}} \quad (2.4)$$

Where  $\tau_s$  is given by equation (2.5)

$$\tau_s = \frac{kTR^4}{\Omega\delta_s D_s \gamma_s} \quad (2.5)$$

**Table 2.2 Two exponents n, m and parameter B for different sintering mechanisms [3].**

<b>Mechanism</b>	<b>n</b>	<b>m</b>	<b>B</b>
Surface diffusion	7	4	$\frac{56D_s \gamma_s \Omega^{4/3}}{R_r T}$

Lattice(volume) diffusion	5	3	$\frac{80D_V \gamma_S \Omega}{R_r T}$
Grain-boundary diffusion	6	4	$\frac{20D_g \gamma_S \delta \Omega}{R_r T}$
Plastic flow	2	1	$\frac{9\pi D_V \gamma_S b}{R_r T}$
Viscous flow	2	1	$\frac{3 \gamma_S}{\eta}$
Evaporation-condensation	3	2	$\left(\frac{3P_V \gamma_S}{\rho^2}\right) \left(\frac{\pi}{2}\right)^{1/2} \left(\frac{M}{R_r T}\right)^{3/2}$

### 2.1.2 Viscous Flow model

The initial model of sintering occurs between particles undergoing viscous flow whilst ignoring grain boundary diffusion, was proposed by Frenkel [14]. This model consists of two spherical particles from amorphous materials in contact with each other, whilst ignoring the effects of grain boundary diffusion. This contact starts neck growth to ultimately form a disc between particles, the neck is seen to be very smooth because it does not have a grain boundary. When the temperature of the amorphous materials is increased, the viscosity is reduced, and the rate of sintering is thus increased. Equation (2.6) represents Frenkel's viscous flow sintering model; Frenkel assumed that densification occurred through surface diffusion. This equation depends in particular on the neck size ratio ( $X/D$ ) and time.

$$\left(\frac{X}{D}\right)^2 = \frac{3\gamma t}{D\eta} \quad (2.6)$$

### 2.1.3 Analytical model of sintering via grain boundary diffusion

The first model of sintering between particles involving grain boundary diffusion was proposed by Coble (1958) [15], whose model was subsequently corrected by Coblenz et al. [13]. Equation (2.7) represents the corrected model of grain boundary sintering.

$$\frac{a}{R} = \left( \frac{192t}{\tau_g} \right)^{\frac{1}{6}} \quad (2.7)$$

And equation (2.8) gives  $\tau_g$

$$\tau_g = \frac{kTR^4}{\Omega\delta_g D_g \gamma_s} \quad (2.8)$$

Finally, equation (2.9) represents the Coblenz shrinkage ratio

$$\frac{w}{R} = \left( \frac{3t}{\tau_g} \right)^{\frac{1}{3}} \quad (2.9)$$

### 2.1.4 Analytical model of sintering via surface diffusion

A robust model of sintering via surface diffusion was developed by German (2014) [3]. Equation (2.10) represents the German model of surface sintering.

$$\left( \frac{a}{R} \right)^7 = \frac{9tM_s h_s \gamma_s}{R^4 \beta_s} \quad (2.10)$$

Analytical models use the first concept of the theoretical model of the sintering process, thus, they represent an approximated solution of the sintering process. This is because the analytical solutions are collected using approximation factors in the grain geometry and the mechanism of diffusion flow. Analytical models do not take into account all of the factors that occur in experimental sintering. This is due to assumptions about the shapes and packing configurations in these models. In addition, these models cannot combine multiple sintering mechanisms, this is opposed to the real sintering process where the process depends on the use of more than one mechanism; for instance, the sintering between two particles depends on surface diffusion on the particles' surfaces and the grain boundary diffusion in the neck boundary between particles.

Another issue, the analytical formulae have application conditions, such as the sintering stage condition. For example, the application condition of the Coble and Coblenz analytical formula is valid for the initial stage of the sintering process only, that means the Coble and Coblenz analytical formula cannot be used during the initial sintering stage (maximum neck size ratio was set to 0.3 in the initial sintering stage). In addition, the surface diffusion formula did not include essential parameters such as the surface diffusion velocity, surface mobility, and the change in curvature of particles' surface. Finally, all analytical formulae represent a weak solution to the model of the sintering process.

## **2.2 Literature review of numerical models for sintering**

The first model to simulate the solid-state sintering process was used in 1955, and major publications on the kinetics of sintering were published in 1960. Basically, sintering time was considered to be the main focus of the whole sintering process, as was the calculation of significant sintering parameters such as the neck radius and the shrinkage between particles. Sintering simulations showed different stages of development, as discussed below:

The first stage (1960-1970): simulation of the sintering process which represented the neck radius growth between two particles. The second stage (1970-1980): simulation

of the different diffusion mechanisms using the shrinkage ratio between two particles. The third stage (1980-1990): simulation to calculate the density during sintering processes conducted under high pressure. The fourth stage (1990-2000): simulation using different numerical methods, for example, finite difference method, finite element method, and continuum mechanics. The final stage (2000-2018): simulation using new methods, for example, Monte Carlo Simulation, Discrete Element Method, and Molecular Dynamics Method. The modelling of the overlap between contacting particles and neck growth between perfect particles via surface and grain boundary diffusion has been the topic of study of a large number of authors [3].

Frenkel (1945) [14] and Kucsyński (1949) [16] developed successful theoretical approaches to sintering mechanisms by modelling two spherical particles at various stages of the sintering process. Ashby (1974) [17] and Swinkels et al. (1981) [18] studied and developed analytical relationships for the size of the neck between particles and their approach velocity in terms of geometric variables and powder properties. These formulae are dependent on assumptions about the geometry of the neck between particles and the shapes of the particles. Moreover, the very early stages of sintering limited the models when the contact size and the radius of curvature of the neck between particles was very small compared to the radius of the particle. Cannon et al. (1989) [19] calculated the equilibrium shapes of a row of sintering particles, where only surface diffusion was active. They also calculated the surface curvatures of the equilibrium shapes as a function of dihedral angle.

Lippmann et al. (1997) [20] used the finite element model to simulate densification between particles during compaction. They used Shima and Oyane model [21] to calculate relative densities during the sintering process simulation, moreover, they used grain boundary diffusion in the sintering calculation, using a numerical model. They concluded that the distribution of relative density in the model was affected by the impact of the sintering process.

Mori et al. (1998) [22] used a granular element method to model circular elements of particles for different particle sizes to calculate the densification between particles during compaction. They calculated the viscoplastic deformation with shrinkage

between particles during the sintering process; moreover, they concluded that the shape of particles changed during the simulation. In addition, they used a random mixture of particles in the simulation model, and discovered that the relative density of the mixture ratio, 1:4, was higher than the relative density of the same sized particles, as shown in figure (2-1).

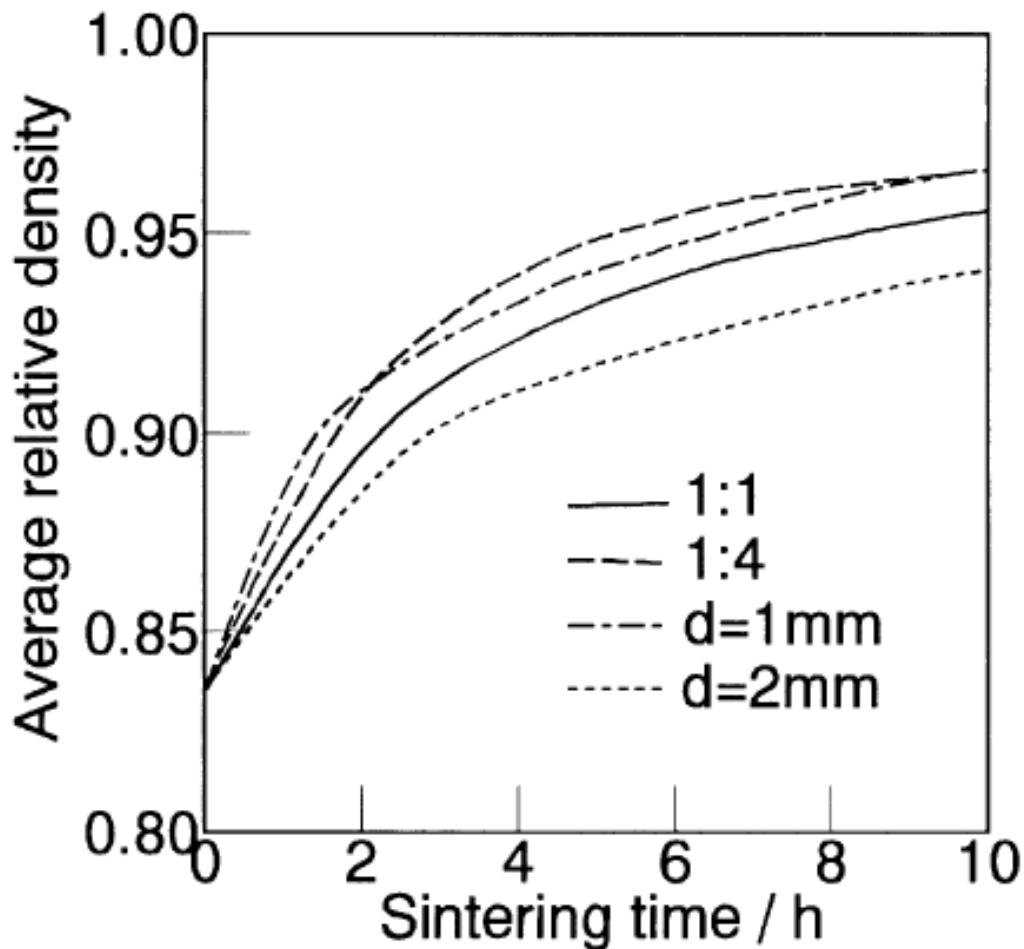


Figure 2-1 Relative density as a function of sintering time for four different cases [22].

Svoboda and Riedel (1995) [23] used the rate of dissipation with the Gibbs free energy for two particles through a grain boundary and surface diffusion. They produced results for the growth of overlapping necks between particles of the same size. The above

studies did not expect the equilibrium shape for two or a row of same particles when small perturbations in geometry produced no variation in the free energy of the system. Zhang and Schneibel (1995) [24] calculated the growth of circular prisms into their stability shapes.

Pan et al. (1995) [5] used a numerical formula to simulate two different particle sizes by coupling the grain boundary and surface diffusion with a focus on the triple junction between the free surface and the grain boundary. They combined two methods, the finite element and finite difference methods, by simulating grain boundary diffusion via the finite element method and surface diffusion via the finite difference method. They noted from the sintering of two cylindrical particles that the smaller particle in sintering process vanished after the total sintering time, while the two cylindrical particles became a single cylindrical particle, as shown in figure (2-2).

Bouvard and McMeeking (1996) [25] studied and solved the resulting equation using a numerical solution for the particle shape. This solution relaxed the limitation of requiring a small contact radius and radius of curvature of the neck; moreover, the approach allowed for a more precise solution to the development of neck size, particle shape, and shrinkage between particles during sintering.

Pan et al. (1997) [26] used finite element code to simulate two particles using coupling between surface and grain boundary diffusion by employing grain boundary migration. They offered a numerical solution to the velocities of each particle, migrating surfaces and grain boundaries. They used the new technique of combined the finite element formula with integration over time; this technique can be used in various physical problems such as the sintering process, grain growth, and void growth. Kryuchkov (1997) [27] used various structural models of ceramic materials to estimate the sintering efficiency. He concluded that the Voronoi polyhedra remained unchanged with respect to the porosity of the system, whereas the pore volume decreases with increasing particle diameter.

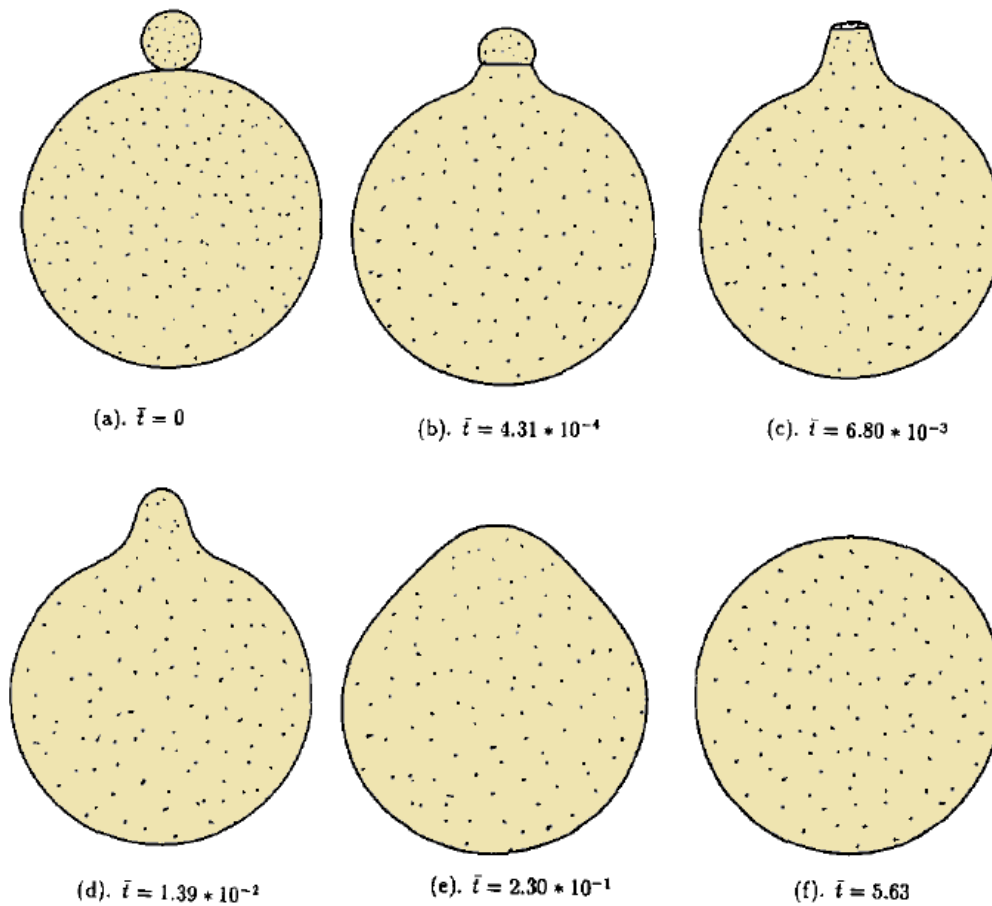


**Figure 2-2 Sintering of two particles of different sizes [5].**

Zhang et al. (1998) [28] applied surface and grain boundary diffusion as a model for the sintering of two particles in three dimensions, and also studied the effects of joining conditions. They used a simple formula to represent grain boundary diffusion. They conclude that the model could be used to represent the sintering of a cluster of particles. Pan et al. (1998) [29] used a numerical model (by Pan et al. (1995) [5]) to model the co-sintering of two spherical particles of different sizes using the combined of two diffusion methods: surface diffusion and grain boundary diffusion. Concluding that the difference in particle size did not affect the shrinkage between particles;

moreover, they created a new empirical formula describing the co-sintering time and the shrinkage rate for the two particles.

Parhami and McMeeking (1999) [30] created interparticle contacts and neck growth by application of a grain boundary and surface diffusion to model rows of spherical particles. Also, they investigated the effects of dihedral angles, diffusivities, initial particle sizes, and applied forces. Their results agreed with Coble's analytical treatment (Coble, 1958) [15] for intermediate configurations. Moreover, the larger particle was found to absorb the smaller particle, and a large dihedral angle leads to an increased neck radius.

Hooper et al. (2000) [31] applied the finite element method to model viscoelastic sintering. They solved mass conservation and momentum in the creeping flow using the upper-converted Maxwell constitutive equation. They concluded that the descriptions of viscoelastic flow in models of polymer sintering did not realistically describe the behaviour of such systems. Martin et al. (2003) [32] used the discrete element method to simulate the closed die compaction and cold isostatic of powders. They also studied the effects of particle rearrangement by comparing simulations that used a homogeneous strain to include the local rearrangement, and simulations that did not include the local rearrangement. It was concluded that local rearrangement affects the average coordination, macroscopic stress and the average contact area.

Pan et al. (2005) [33] investigated the kinetics of sintering for large pores in a dense polycrystalline solid using an appropriate computer model. Two types of diffusion were used in these computer models, namely grain boundary and surface diffusion. They concluded that the numerical solution supports the analytical formula developed by Ma (1997) [34]. Martin et al. (2006) [35] investigated the free sintering of metallic powders using a discrete element method to introduce a simple coarsening model. They compared simulated densification rates with experimental data from Hwang et al. (1991) [36]. They also studied the anisotropic shrinkage of green compacts. Pan et al. (2007) [37] used a computer program to simulate the effects of particle size on two cylindrical particles. They compared four styles, where the distance between two particle centroids was considered a function of dimensionless time using a larger

particle size of 2  $\mu\text{m}$ , a mobility ratio of 50, an energy ratio of 3, and  $Mm = 10000$ ; also, they discovered that the configuration of two unequal particles resulted in the maximum value of  $(1-d/d_0)$  compared to all other configurations, as shown in figure (2-3).

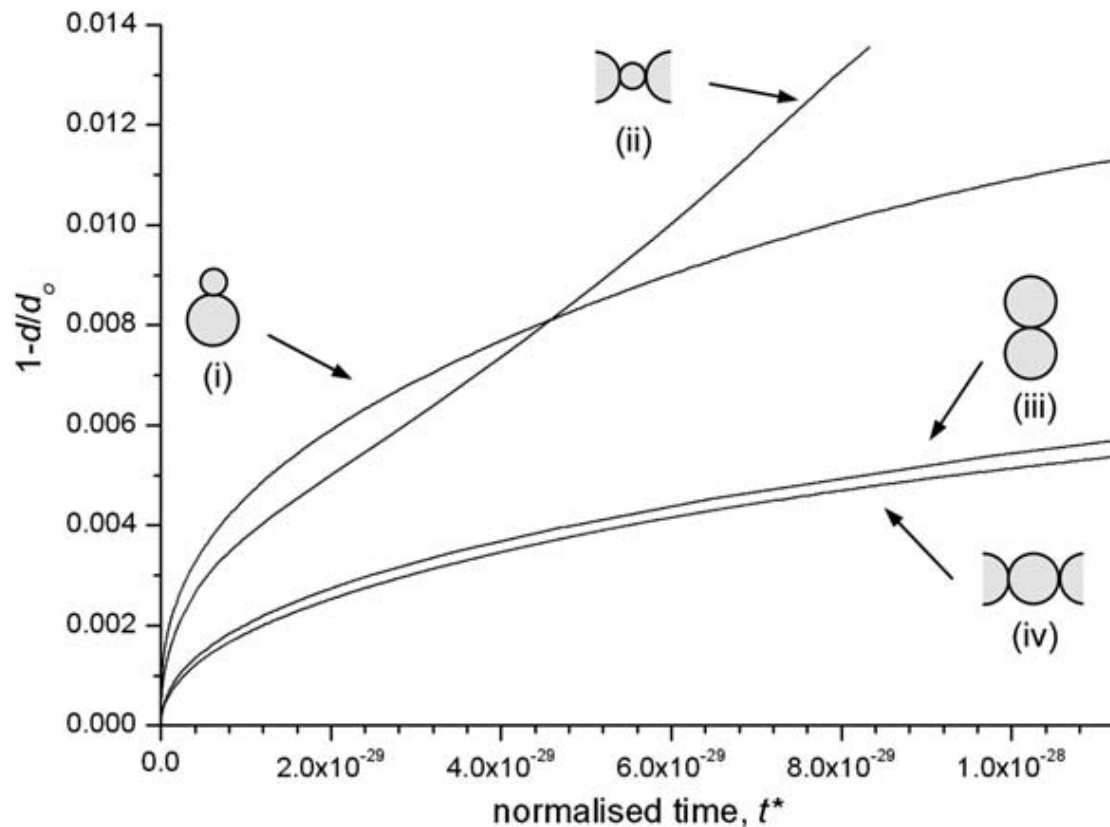


Figure 2-3 Particle diameter ratio for four styles [37].

Chen et al. (2008) [38] studied the effects of temperature and force between particles using the discrete element method to simulate pressure sintering. They used two particles for the first time and, later, used ten particles arranged in a 'V' shape. They concluded that the result of the simulation agreed with the experimental results of Exner (1979) [39] for free sintering, and the rate of neck growth was very low at temperatures in the range 25-150  $^{\circ}\text{C}$ , but the rate of neck growth was increased by increasing the temperature by applying an external compression force (1 N at 700  $^{\circ}\text{C}$ ).

Henrich et al. (2007) [40] used the discrete element method to perform a three-dimensional simulation of 1800 particles using an initial relative density of 0.64. They observed that the densification is affected by initial mass scale, where if the mass scale decreases then the densification increases. In addition, the coordination number is affected during the sintering process, where it was found to depend on the relative density; thus the comparison between analytical and simulated results using a relative density of 0.64, showed a good agreement between the curves at a coordination number of 7.3.

Olmos et al. (2009) [41] used a mixture of powders, i.e., copper and alumina, to estimate the efficiency of a mixture of powders when sintering experimentally, and to allow a comparison with a simulated model. They used different volume fractions of the two powders. They discovered that the mixture of copper with a 30% volume fraction of alumina obtained the maximum relative density compared with different volume fractions. In addition, they discovered that the contact of copper-copper is higher than the copper-alumina and alumina-alumina contacts, as shown in figure (2-4). Olevsky et al. (2002) [42] modelled a ceramic composite to calculate the development of damage in the initial stages of the sintering process, especially at the junctions between particles. They proposed a new criterion of fracture of damage, concluding that the damage is clear at  $\zeta > 0.15$  and, moreover, that the factor  $\zeta$  increases with increasing sintering temperature. Also, the model was used to understand the effective damage of the free sintering process.

Tikare et al. (2003) [43] used a Monte Carlo model to simulate two dimensional layouts of three identical particles. They used several sintering mechanisms in two dimensions to model three circular particles, namely short-range grain boundary diffusion for grain growth, long range grain boundary diffusion from powder to pore, and surface diffusion at the surface of particles. They compared the numerical results of shrinkage with the analytical formula  $y_1 = Br^{-1.32}t^{0.33}$ , and found that the numerical results were in good agreement with the analytical result,  $y_1$ , especially in the initial stage of time 7000 MCS,

but used another formula,  $y_2 = (R_0^2 - (R_0^4 - Ct)^{1/2}) / (R_0^2)$ , to compare to simulation for the stage after times of 10000 MCS. They noted that the simulation results were indeed in good agreement with analytical  $y_2$  after a time of 10000 MCS, as shown in figure (2-5).

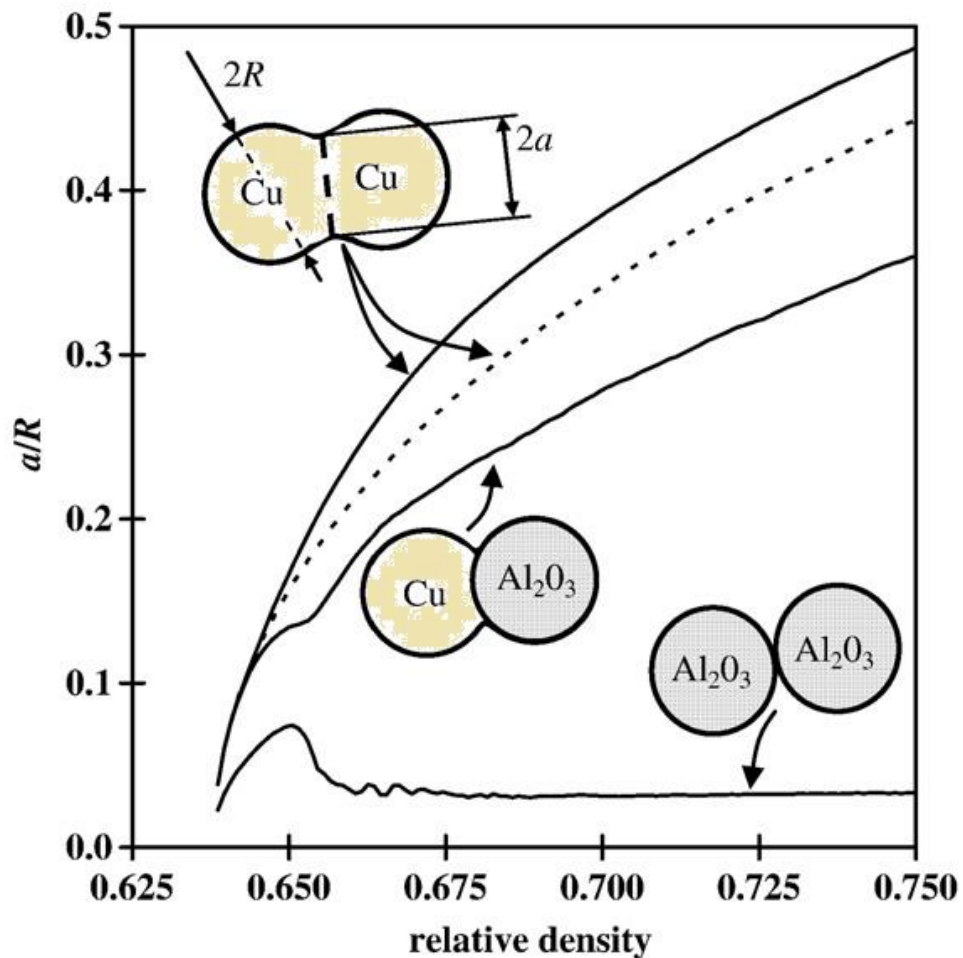


Figure 2-4 Neck size ratio of copper and alumina powders [41].

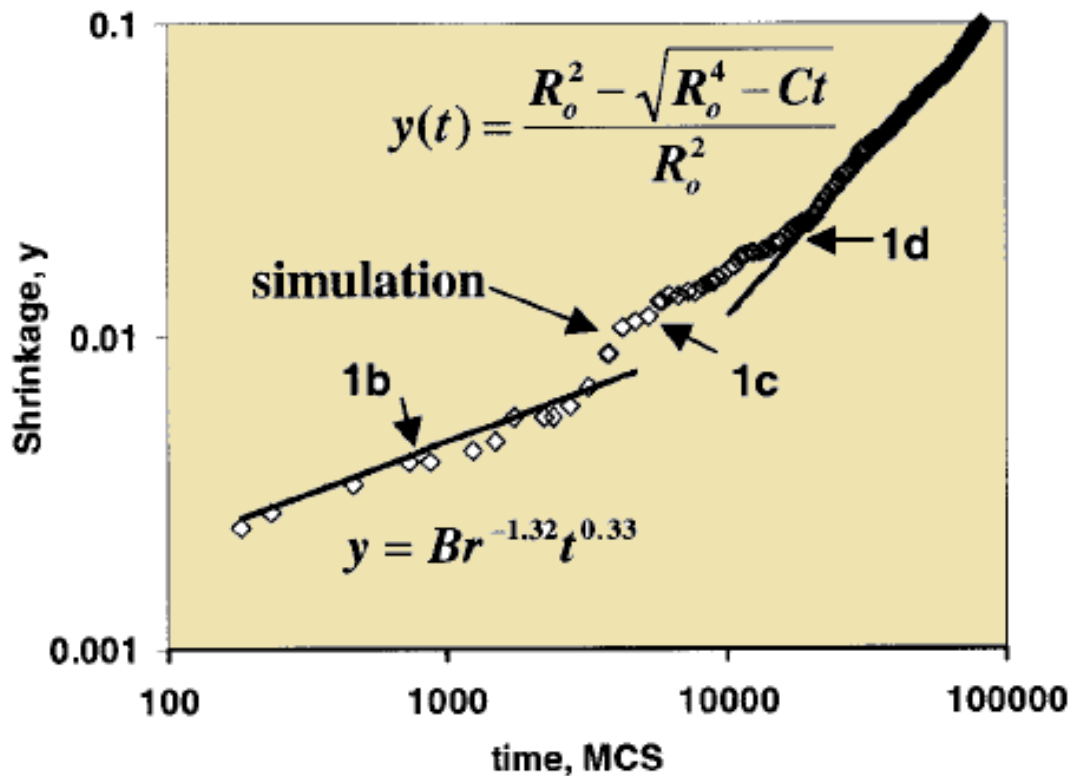
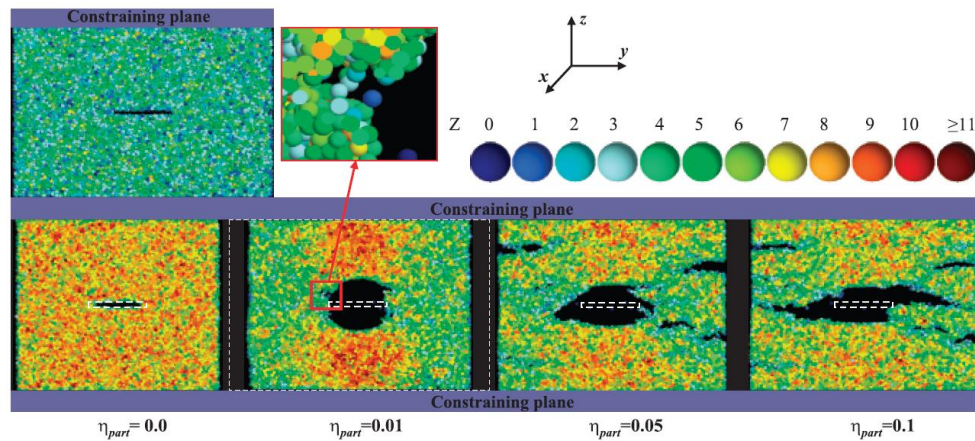


Figure 2-5 Comparison of numerical results with analytical formulae [43].

Demirskyi et al. (2010) [44] investigated neck growth kinetics for the microwave sintering of copper powder. They applied the sphere-to-sphere approach for long-soaking sintering times, and discovered anomalous neck growth in the initial stage of microwave sintering. Kiani et al. (2007) [45] used the finite element method using densification data to illustrate the sintering process under zero-pressure conditions, via a method that became known as the densification-based finite element method (DFEM). They used the case study of a dumb-bell shaped from alumina powders, with an initial relative density of 0.4, to check and compare the results of DFEM with the experimental data from the two cases. They concluded from these comparisons that DFEM gave a closer representation to the experimental data than from the finite element method.

Andrey et al. (2004) [46] used numerical methods to simulate the neck growth rate between two identical particles. They used three types of diffusion: volume, surface, and grain boundary diffusion, in their sintering model over two stages. They pointed out that the diffusion coefficients were different for the two sintering parameters in each of the two stages, the effective diffusion coefficient of the neck ratio is different to the shrinkage rate, especially in the first stage. They calculated the dimensionless chemical potential as a function of the distance from the neck using the two different diffusion coefficient ratios. Wakai et al. (2005) [47] used the Surface Evolver program to simulate the grain growth to be coarser during the solid-state sintering process using two particles of different sizes. They discovered that the small particle disappeared after only a short time with an increased grain boundary energy to surface energy ratio, and the final shape of the two particles looked essentially like one particle; moreover, the grain boundary was found to be flat when the mobility of the grain boundary was larger than the mobility of the surface, thus the grain boundary of the small particle disappeared in a relatively short time.

Olmos et al. (2009) [48] used copper powders of different sizes, specifically 14, 20, 24, and 63  $\mu\text{m}$ , when making artificial pores to study the behaviour of particles in experimental sintering processes. They compared with simulated DEM, using the coordination number, strain, and particle movement, concluding that the experiment curve was close to simulated curve. Martin et al. (2009) [49] used the discrete element method-dp3D code to simulate a crack between the particles in the sintering process. They used 54,000  $\text{Al}_2\text{O}_3$  particles with an initial relative density of 0.5, and considered different viscous parameters of 0.00, 0.01, 0.05, and 0.10. They concluded that a defect grows in two directions, nominally the y- and z-directions, during the sintering process with increasing viscous parameter and, moreover, that a decrease in relative density and strain occurs due to an increasing viscous parameter. Figure (2-6) illustrates crack growth with viscous parameters.



**Figure 2-6 Cracks inside a body with different viscous parameters [49].**

Olevsky et al. (2006) [50] combined a kinetic Monte Carlo model with continuum theory to simulate the evolution of particles during the sintering process. They used two styles of bilayered structures for ZnO particles such as different initial porosity with the same powder, and two types of powders. Also, they used a particle size  $0.2 \mu\text{m}$ , a heating rate of  $5^\circ\text{C}/\text{min}$ , and an initial relative density of 0.47. They concluded that the relative density determined by the model and its experimental analogue were closely matched, as shown in figure (2-7).

Martin et al. (2009) [51] used the discrete element method to simulate 18,000  $\text{Al}_2\text{O}_3$  particles using contact law for the two cases of particle-particle and particle-substrate contacts. They modelled two geometries, rectangular and cylindrical pillars, where the number of particles inside the two geometries were different, and particle size was  $0.1 \mu\text{m}$  in each case. The effect of different sintering times, as scaled to 18,000 particles, is shown in figure (2-8).

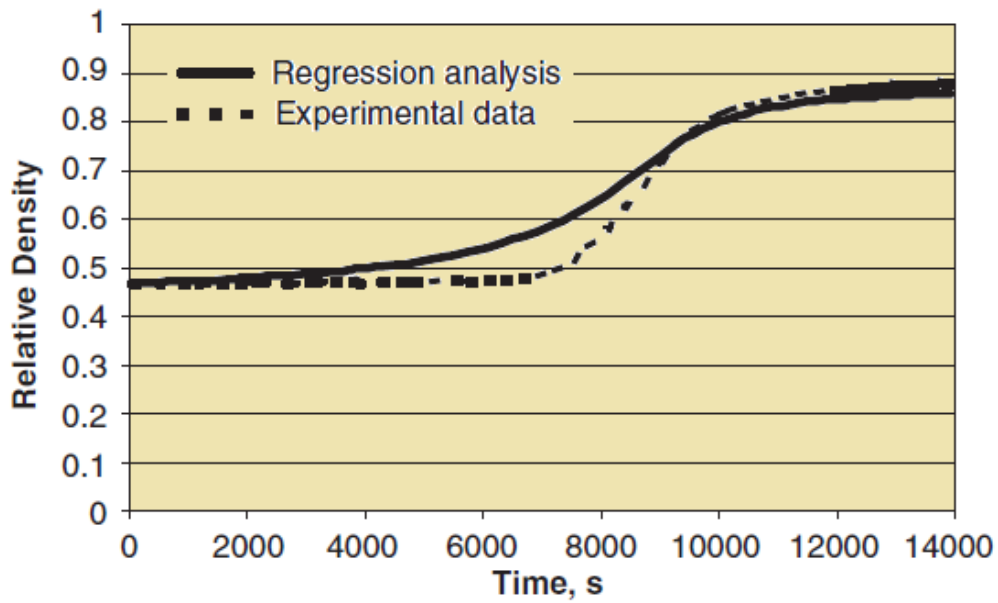


Figure 2-7 Relative density with time for ZnO particles [50].

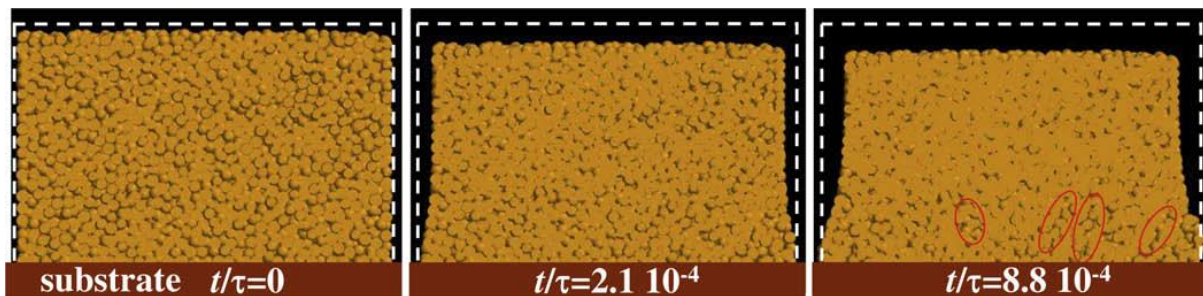
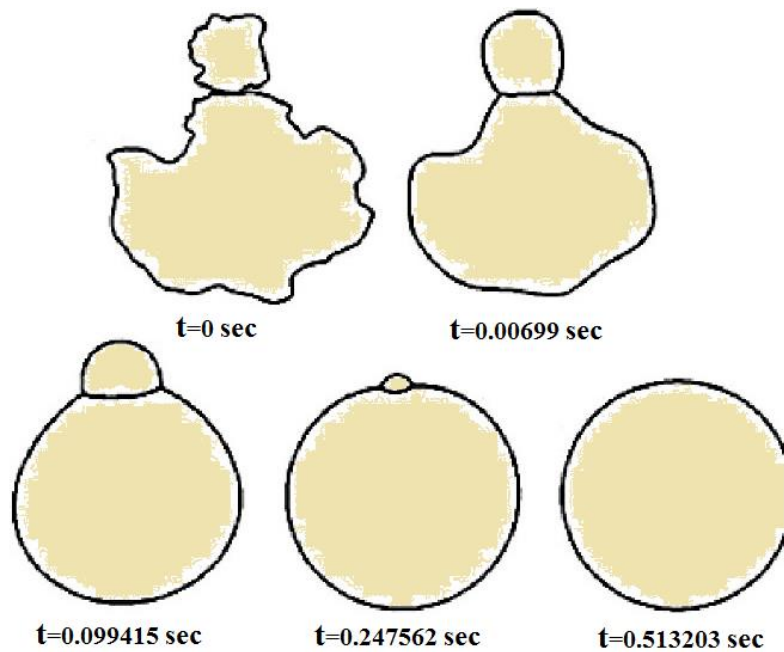


Figure 2-8 18,000 particle for three time scales [51].

Galakhov (2009) [52] used the boundary element method to simulate the sintering process of two different particle sizes for alumina at a sintering temperature of 1600°C. Galakhov found that smaller particles disappeared at a sintering time of 0.513 s, and the two particles became one large particle as shown in figure (2-9). He used four particle diameter ratios, 0.2, 0.4, 0.6, and 0.8, for two different-sized particles to show

the effects of these ratios on neck size ratio and the specific surface of the sintering process.



**Figure 2-9 Sintering process steps for two different particle sizes [52].**

Olevsky et al. (2013) [53] used a theoretical model to solve the sintering problem for two- and three-layered porous systems under isothermal conditions. Two types of solutions were suggested using linear and uniform strain distributions across the thickness of each layer. They concluded that the two solutions agreed well, as shown in figure (2-10).

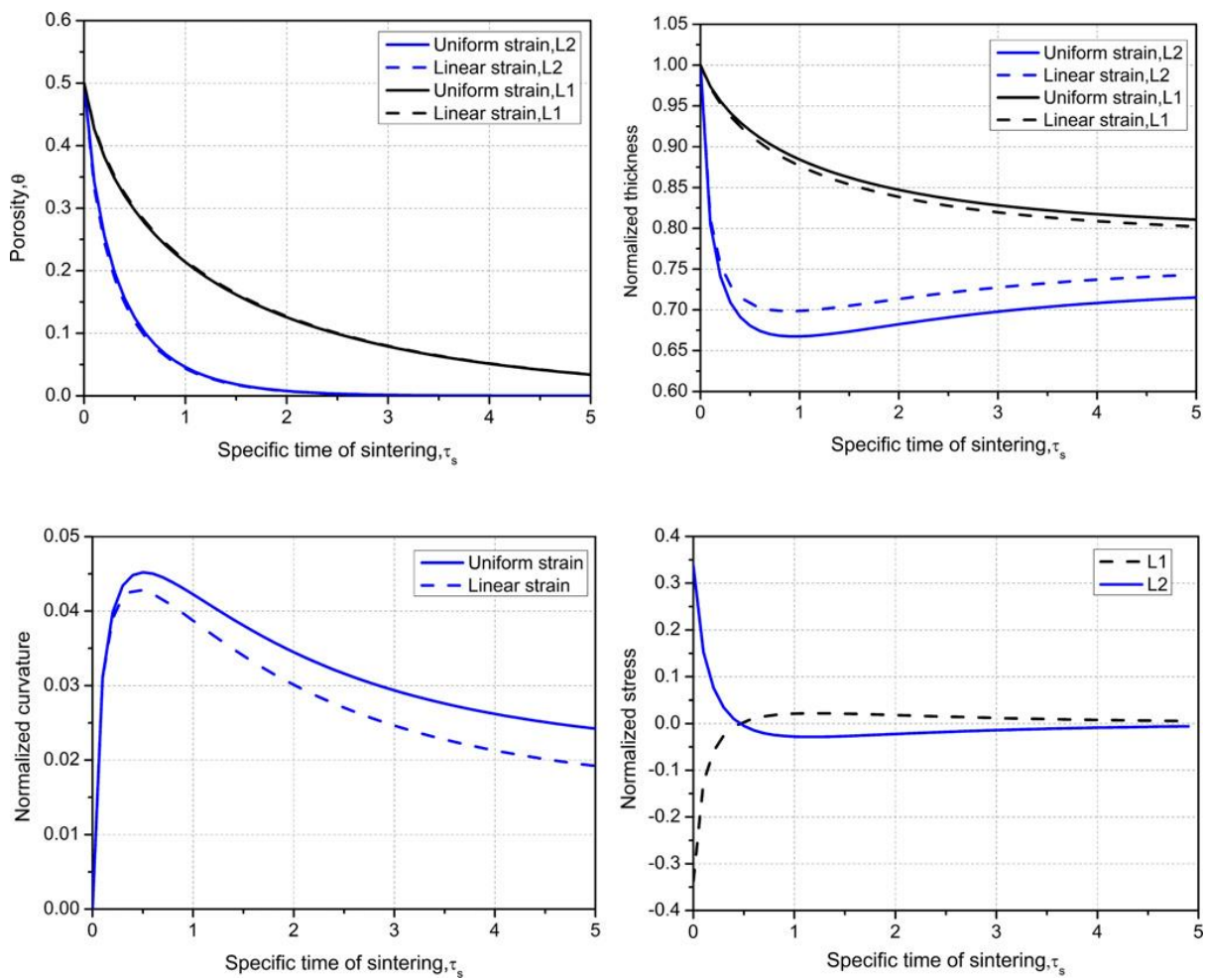


**Figure 2-10 Porosity, normalized thickness, curvature, and stress due to sintering time [53].**

Wakai et al. (2012) [54] developed the mechanics behind the sintering of a single grain boundary using fabricated specimens in which a three-dimensional computer simulation was used to analyse the associated rotation and shrinkage. They concluded that the grain boundary diffusion coefficient and grain boundary energy influenced the translational motion and rotation of the particles during sintering. In addition, the grain boundary diffusion coefficient and grain boundary energy were also found to be dependent on crystallographic orientation. Yan et al. (2013) [55] used the discrete

element method to simulate a group of 1000 spherical composite powders including different volume fractions (5, 10, 15, 20%), to study the effect of size, volume fraction and homogeneity on the densification rate of the matrix. The researchers used different-sized particles (300, 180, 100, and 60nm) in the matrix to show the effects of inclusion size on the sintering process. They observed that a decreasing inclusion size and increasing volume fraction of inclusion, led to a decrease in the densification of the matrix, as shown in figure (2-11). They were also able to enhance the dispersion of the inclusions by giving their volume fraction and size.

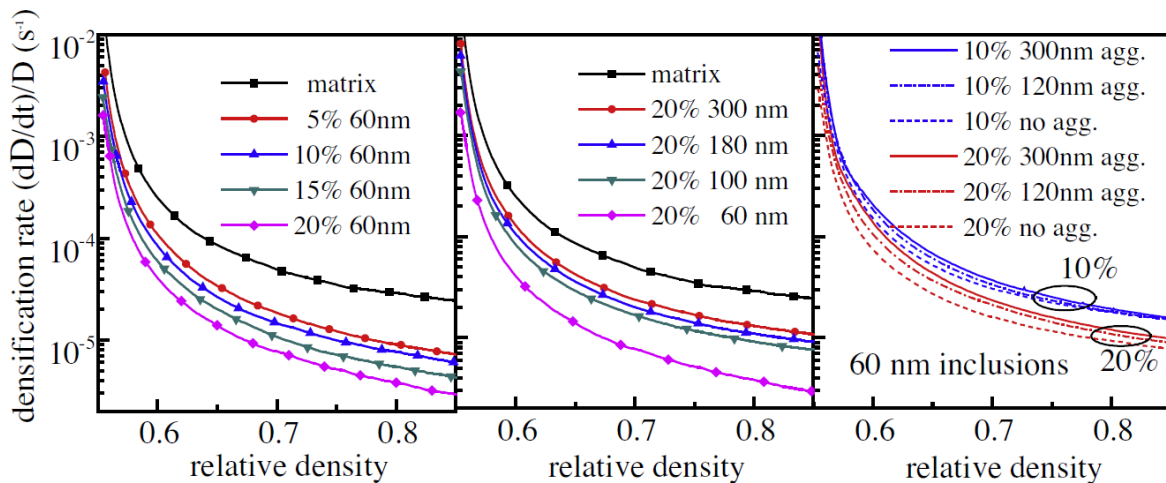


**Figure 2-11 Densification rate with relative density of matrix [55].**

Wang et al. (2012) [56] used the discrete element method to simulate the sintering of copper particles in two dimensions. They used 500 identical particles inside a circle 50 times the particle's diameter, and considered two cases: one with a particle size of 25  $\mu\text{m}$  at a sintering temperature of 1223 K to allow validation against experimental data, whilst the second used a particle size of 127  $\mu\text{m}$  at a sintering temperature of 1300 K. They concluded that the number of agglomerates increases sharply due to the increase in sintering time at first sintering stage, but that afterwards this number decreases dramatically until reaching a constant at 65; moreover, the densification

during the sintering of all particles with agglomerates became higher than the densification without agglomerates, as shown in a figure (2-12). Wang et al. (2013) [57] used the discrete element method for a complex network of 500 copper particles with diameters of 254  $\mu\text{m}$ . They considered the contact and force networks for a random circular group with a diameter of 6.35 mm at a sintering temperature of 1300 K in a solid-state sintering process. They concluded that the size and shape of the particles' network affected the evolution of the particles' microstructure. Figure (2-13) displays the contact networks for the sintering of 500 copper particles; there are eight polygons inside the network.

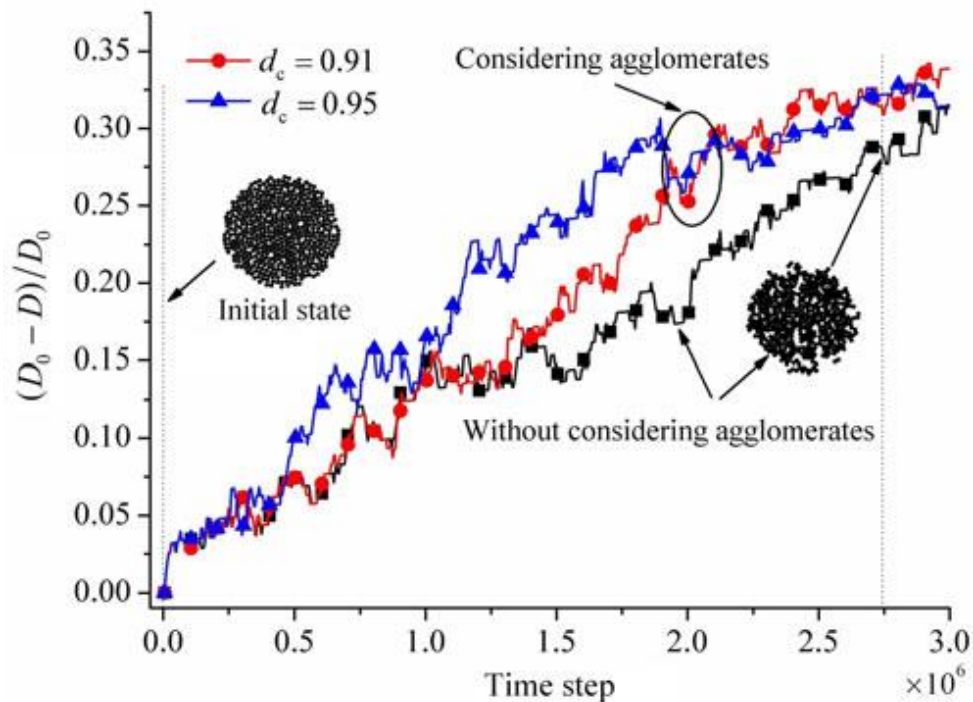
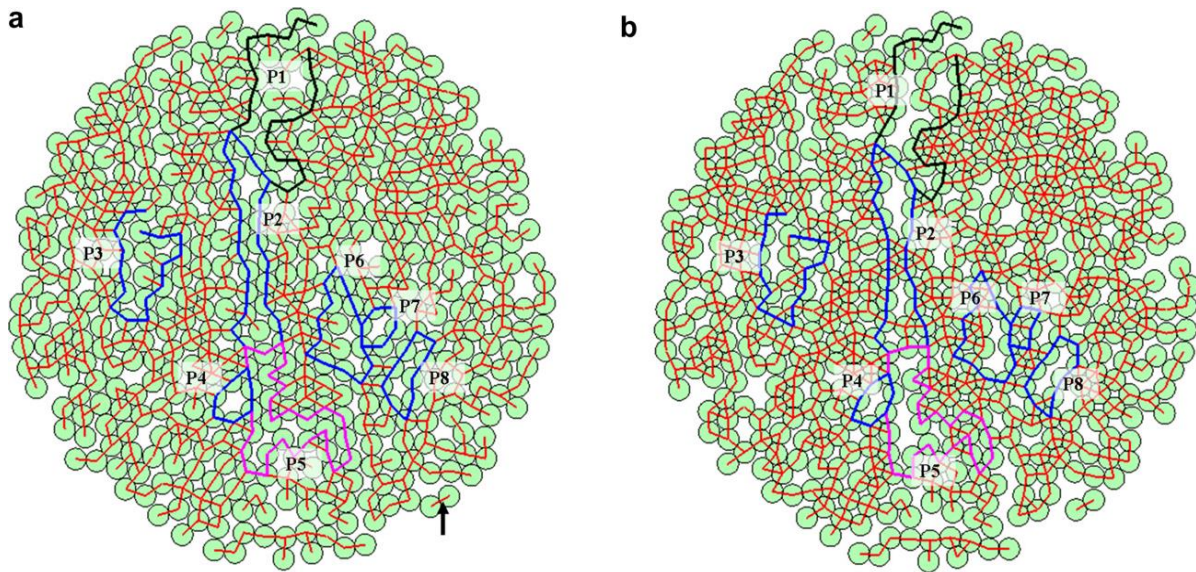
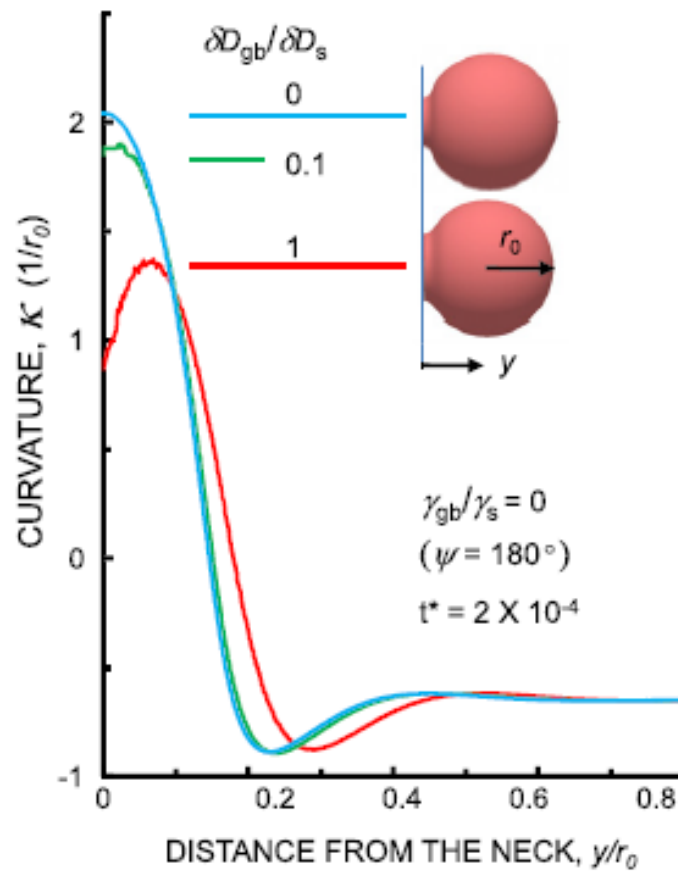


Figure 2-12 The densification as a function of time step [56]



**Figure 2-13** The contact networks of copper powders [57].

Wakai et al. (2011) [58] used the discrete element method to simulate two spherical particles where there was coupling between the surface and grain boundary diffusion. Also, they calculated the sintering force and mobility during the sintering process until equilibrium was achieved. They concluded that the shrinkage ratio increases due to the increase in diffusion coefficient ratio and decrease in energy ratio,  $Y_r$ . In addition, they discovered that  $K_{tip}$  decreases due to the increased diffusion coefficient ratio  $D_g/D_s$  at the beginning of the sintering process. They also found that the minimum surface curvature of two particles is at a distance from neck  $y/r_o = 0.2$  using three diffusion coefficient ratios, while the maximum surface curvature of two particles is at the neck between them, under the same conditions of the diffusion coefficient ratio being equal to zero, as shown in a figure (2-14).



**Figure 2-14 Surface curvature for three diffusion coefficient ratios [58].**

Nosewicz et al. (2013) [59] used two copper particles in DEM with a viscoelastic model to simulate solid-state sintering, and to compare with a viscous model for different mass scales. They found that the viscous model had higher critical time steps than the viscoelastic model at the beginning of the initial sintering stage, and the effect of the viscosity coefficient was as presented in a figure (2-15).

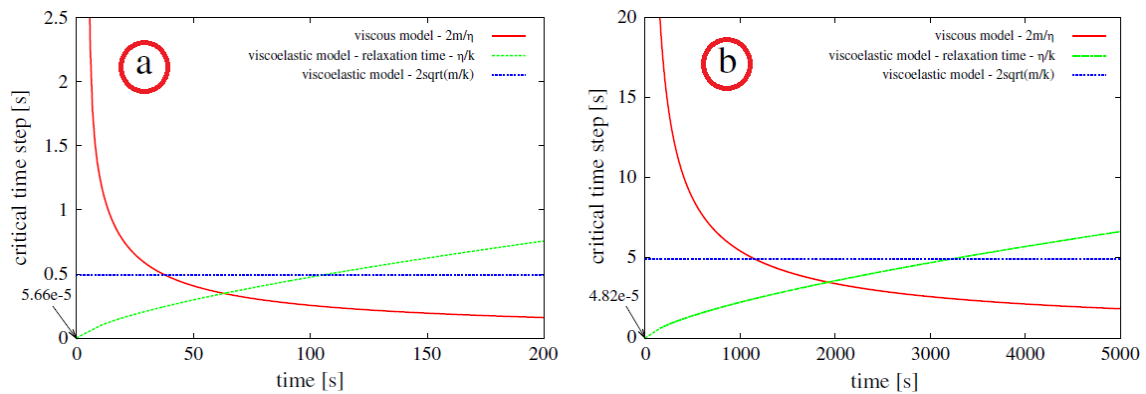


Figure 2-15 Critical time steps and sintering time at different mass factors: a)  $10^{14}$ , b)  $10^{16}$  [59].

Martin et al. (2014) [60] used a non-smooth technique of the discrete element method for 18,000 copper powders of different particle sizes in a method known as contact dynamics. From a comparison of the simulation with experimental and numerical data determined by previous researchers, they concluded that contact dynamics gives a better description of the experiment than with the use of smooth dynamics, where figure (2-16) shows the numerical curve is close to the experimental curve, indicating that the non-smooth method and experiment were in good agreement.

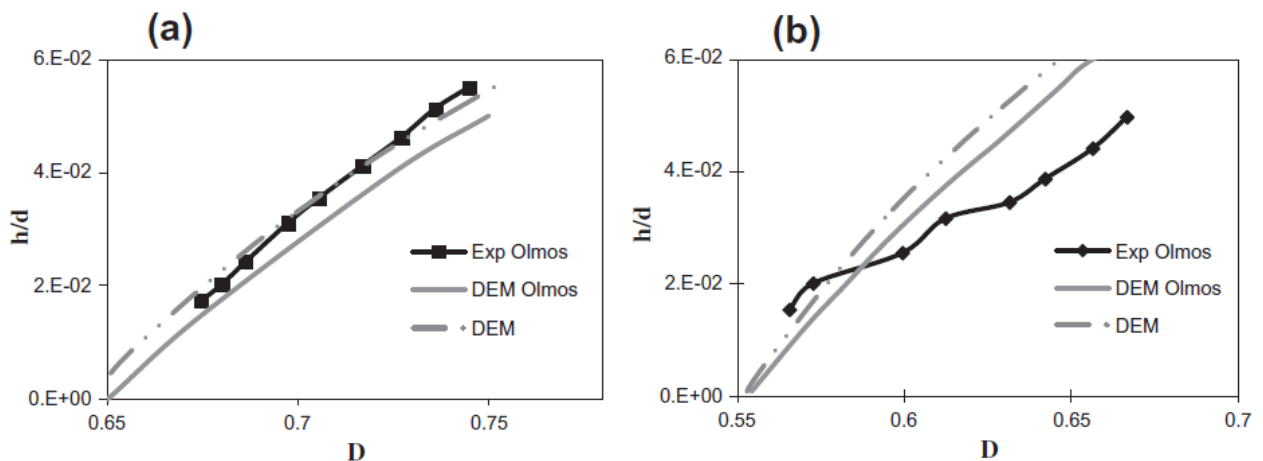


Figure 2-16 Comparison between numerical methods and experimental data [60].

Ou et al. (2014) [61] used finite element simulations to describe sintering during Powder Injection Moulding. Also, they studied sintering behaviour using dilatometer experiments, where micro-bi-material components were used with the thermoelasto-viscoplastic model. They concluded that the numerical simulation results represented by shrinkage and relative density are matched well with the experimental data. Martin et al. (2015) [62] used a discrete element method to study the sintering of bimodal powders. The effect of the type of connection between small, large, and other sized groups of particles in terms of their macroscopic behaviour was also studied. They concluded that a connection type did not only depend on the associated probability of connection but also on the particle radius. Moreover, the densification with a small group of connection was slower.

Luo and Pan (2015) [63] used a finite difference model to simulate two spherical alumina particles. They used different ranges of diffusion coefficient ratios and applied stresses to show the impact of these parameters with different heating rates. They found that the shrinkage rate decreases, and the neck growth rate increases due to increasing surface diffusion. Martin et al. (2016) [64] used a discrete element method to simulate ceramic particles during the sintering process while introducing an artificial defect between particles using a particle size of 2  $\mu\text{m}$ . They pointed out that the simulation of the last stage of sintering by DEM is seemingly no better than using FEM or Monte Carlo methods, or in other words the FE and MC methods are better at simulating the last stage of the sintering process than DEM.

Nosewicz et al. (2017) [65] used linear and nonlinear elastic models of the Hertz formula in DEM to simulate the sintering process of two NiAl particles using a particle size of 20  $\mu\text{m}$ . They compared the relative density and particle penetration determined by numerical results and experimental data at different pressures in order to validate the numerical models. They observed that the Hertz model results were closer to the experiential relative density than the linear model, as shown in figure (2-17).

Rojek et al. (2017) [66] used molecular dynamics methods to calculate the diffusion coefficient, followed by the discrete element method to simulate the sintering of 1751 particles of a nickel aluminide alloy for a range of particle sizes (3.97-200  $\mu\text{m}$ ). They

compared the relative densities obtained with DEM and MD-DEM with experimental results to verify the effectiveness of each method. They found that the MD-DEM curve, matched the experimental curve more accurately than that found for DEM, as shown in figure (2-18). In addition, they calculated the relative densities for three uniaxial compressions of 5, 15, and 30 MPa at a temperature of 1673 K, and recorded the relative density with increasing pressure.

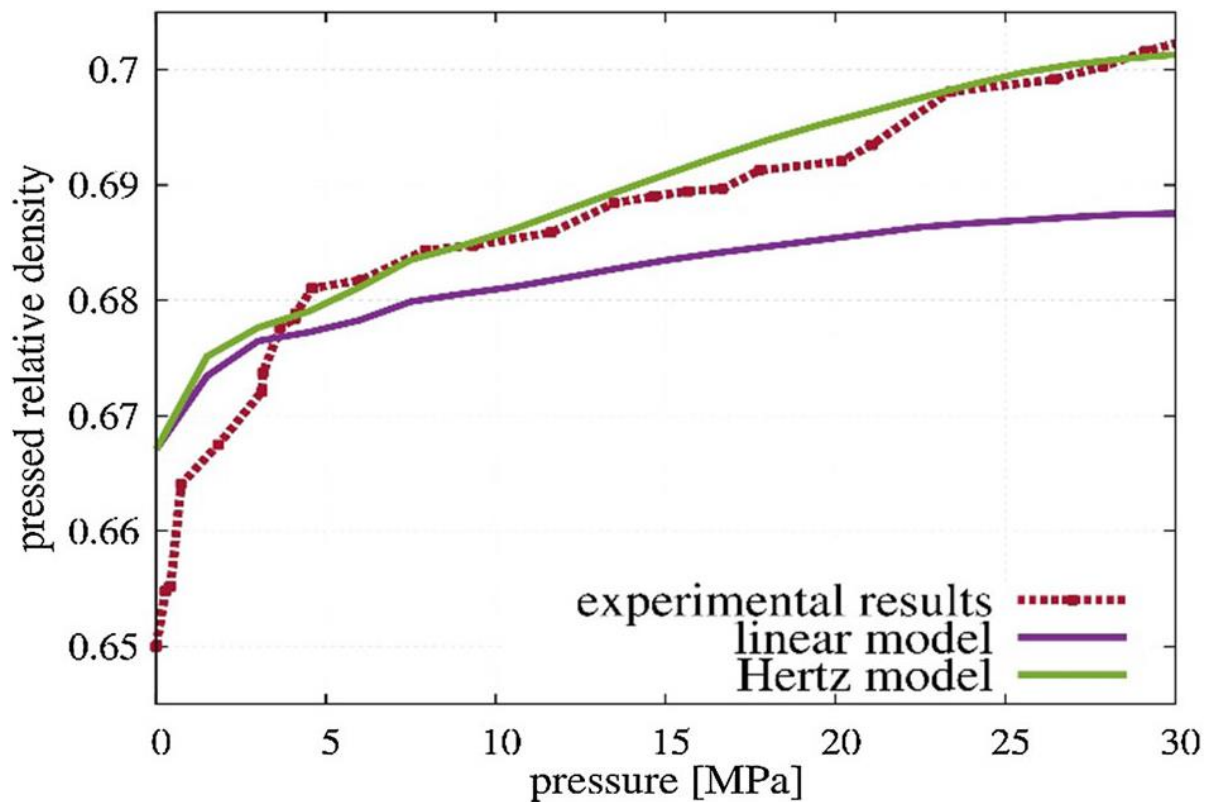


Figure 2-17 Comparison between two models and experimental data [65].

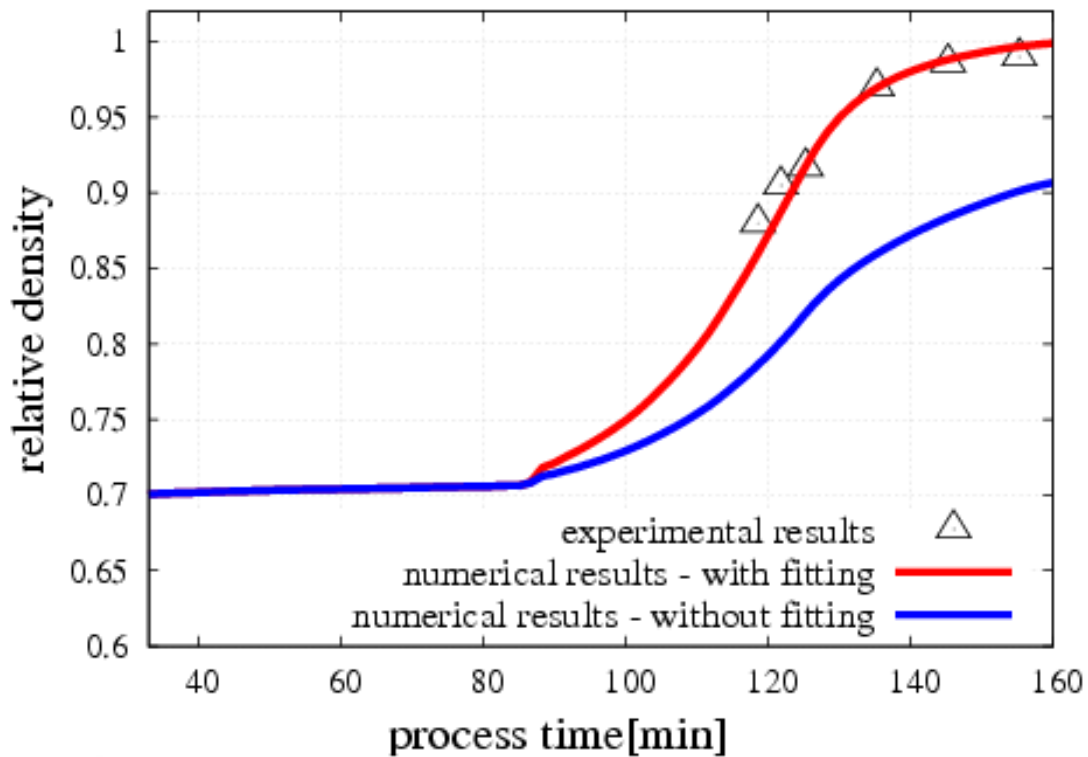


Figure 2-18 Comparison between two simulation models and experimental data [66].

Wang et al. (2017) [67] used a spark plasma sintering process for titanium-aluminium alloy powders at different sintering temperatures and stresses. They found that the relative density increases with increasing temperature, and also noted the temperature and pressure affect the grain boundary diffusion; they also discovered that the fracture strength and plastic strain increased with increasing relative density.

The surface diffusion mechanism plays an important role in the transport of atoms on particle surfaces during the sintering process. The neck growth depends on the movement of the curvatures of the particles' surfaces, which is dependent on the surface diffusion mechanism. Thus, the improvement in the sintering process depends on the increase in neck growth which is used as a parameter to describe the sintering process between particles.

Previous researchers solved the sintering process model problem by introducing a coupling between the surface and grain boundary diffusion mechanism via numerical methods, where the surface diffusion model depends on the change in the curvature of the particles' surface. The curvature is a significant parameter in the sintering process because it makes the connection between the edge of the neck boundary (grain boundary diffusion) and pore surface (surface diffusion). However, solving the sintering process using the surface diffusion mechanism makes the solution difficult because the surface diffusion numerical model depends on the change in the curvature of particles' surfaces; moreover, the model of the sintering process for multiple particles has a complication because it needs to solve the full coupling problem, which is impossible for multiple particles. There has been no previous considerations in the literature to solve the solid state sintering model using the grain boundary diffusion mechanism without using the surface diffusion mechanism in the modelling of the sintering process.

### **2.3 Literature review of selective laser sintering**

Selective laser sintering (SLS) is the one of the best manufacturing processes for the rapid prototyping of complex geometries using a wide range of material powders [68, 69] and a high-powered laser [70]. Laser power, powder size, layer thickness, spot size, scan spacing, part-bed temperature, scan speed, ratio of the powders in the mixture, pulse frequency, laser energy, pulse size, and powder density are all effective parameters in the SLS process [71]. SLS can make functional products for use in the automotive industry, aerospace, and biomedical applications. Texas University, Austin, was the first to develop selective laser sintering. In 1992, the first experimental SLS system was built, and currently uses several systems worldwide [72]. Maeda and Childs et al. (2004) [73] produced parts using hard metal powders (WC-Co) using selective laser sintering to make a hard metal coating that showed especially good resistance to abrasion. Romer et al. [74] constructed a new theoretical method to find the surface temperature of particles during laser processes, which depends on various

parameters, such as scan speed of the laser beam, different spot geometries, laser power, laser spot intensity on the surface, etc.

A number of researchers created the thermal numerical model to simulate the SLS process, and Dong et al. (2009) [75] built a 3D model using the finite element method to determine temperature during SLS, that also allowed densification to be calculated. Loh et al. (2015) [76] used aluminium alloy 6061 powder in SLS to produce sintered parts. They used temperature and density as parameters for scan speed and laser power to develop a thermal numerical model. They found that the resultant temperature predictions were in good agreement with experiment when considering a single scan line. Ganeriwala and Zohdi (2014) [77] simulated the SLS process using the discrete element method for one layer of particles. They concluded that the particles were hotter for small sizes and in the surface of the layer. Ganci et al. (2017) [78] developed a three-dimensional model using the DEFORM package for comparison with previous experimental results. They concluded that the numerical results were in good agreement with previous experimental results. Miranda et al. [70] used a high-powered fibre laser (8 kW) to produce a cylindrical shape. They concluded that the high power of this laser was especially beneficial, particularly in terms of the laser's flexibility, and the cost of maintaining the laser equipment being low.

Singh et al. [79] used a CO<sub>2</sub> laser over a range of laser powers and a polyamide powder in their SLS experiments, determining the mechanical properties of the product parts after testing. Velu et al. (2014) [80] used polymethylmethacrylate (PMMA) powder to produce complex shapes for use in biomedical applications. Peyre et al. (2015) [81] used both experiment and numerical models to determine the fusion depths and thermal cycles of two types of polymers during SLS. They showed that accurate fusion depths, and heat cycles for the two types of polymers could be effectively determined using both diffusion and laser absorption in the powder bed.

Cheng et al. (2015) [82] used copper nanoparticles in a femtosecond laser sintering process at a wavelength of 800 nm and a pulse duration of 100 fs, and further built a theoretical 1D model to describe the process. They concluded that the numerical results using a multi-shot laser model for two temperatures showed good agreement

with the experimental data. Moser et al. (2016) [83] simulated the thermal conductivity of the powder using the discrete element method. The numerical model results were in good agreement with results from previous experiments on powder beds.

## 2.4 Literature review of nanosintering modelling

The term “nano” is derived from the Greek word “nanos”, which means extremely small, and can be used in different SI units to describe a billionth of that unit; for example, a nanosecond represents one-billionth of a second, and a nanometre represents one-billionth of a metre. A nanoparticle is defined as a solid particle which ranges in size from about 1 nm to about 100 nm, and any process relating to nanoparticles is referred to as nanotechnology. The International Organization for Standardization (ISO) (2008) [84] defines nanoparticles as separate nano-objects that measure less than 100 nm [85].

In recent times, there has been significant increase interest in the function of metal nanoparticles (NP), the best example of which is laser sintering when used to make electrical circuit patterns. Nanoparticles can be used to make tiny mechanical parts such as molecular computers or very strong materials. A very large surface area compared to volume is one of the most significant properties of nanoparticles, thus they are allowed to react and rapidly effect any given process. Another property of nanoparticles is that they have different properties to the same material in bulk, the best example of which is gold [86]. The pie chart in figure (2-19) displays the share the nanotechnology industry has in different fields. As can be seen from the chart, the materials industry has a significantly greater share than any other field, while their lowest use is found in the aerospace industry, which means that the focus of interest in terms of nanotechnology is in the materials fields [87].

There has been considerable research into the development of nanoparticle applications such as in medicine (Sahoo and Labhasetwar, 2003 [88]; Silva, 2004 [89]), electronics (Tsukagoshi, Yoneya et al., 2002 [90]), electrochemistry (Gooding, 2005 [91]) and aerospace (Laurvick and Singaraju 2003) [92].

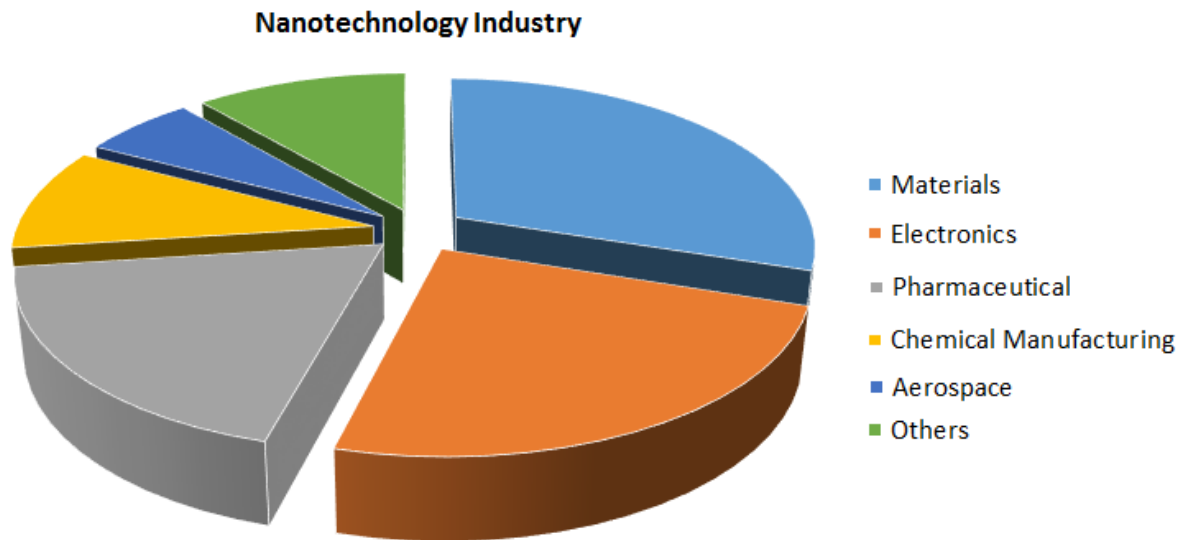


**Figure 2-19 Use of nanotechnology in industry [87].**

Pan developed a model for nanosintering which is outlined later in this section [10]. The effect of nanoscale particles on sintering can be represented by an analytical equation which describes atomic movement. At this point, the diffusive flux ( $j$ ) is used to model solid-state sintering, which is a parameter that represents the number of atoms crossing through a unit area per second. The atomic driving force ( $F$ ) represents the flux, which is equal to the gradient of the chemical potential. Equation (2.11) gives the total atomic flux during the sintering process as related to the atomic drift velocity ( $V$ ) and atomic concentration ( $C_a$ ) [10].

$$j = C_a V \quad (2.11)$$

The atomic drift velocity ( $V$ ) is equal to the atomic jumping frequency ( $f$ ) and the atomic spacing ( $A_a$ ), allowing us to rewrite equation (2.11) as equation (2.12).

$$j = C_a A_a f \quad (2.11)$$

The diffusion is then driven by the atomic driving force (F) and the jumping frequency is reliant on the hyperbolic sine of (F), and thus we have:

$$j = \frac{2D}{aa\Omega} \sinh\left(\frac{A_a F}{2kT}\right) = \frac{2D}{aa\Omega} \sinh\left(-\frac{A_a}{2kT} \nabla\mu\right) \quad (2.13)$$

The diffusion coefficient (D) depends on the two material constants and temperature. Assume  $A_a F \leq kT$  in classical sintering theory, which leads to the linearization of  $\sinh\left(\frac{A_a F}{2kT}\right)$  and  $\left(\frac{A_a F}{2kT}\right)$ . The linear diffusion law can be rewritten in a simpler manner:

$$j = \frac{DF}{\Omega kT} = -\frac{D}{\Omega kT} \nabla\mu \quad (2.14)$$

Equations (2.13) and (2.14) can be solved by an expression involving the chemical potentials ( $\mu$ ), where the chemical potential can measure the energy difference when one atom when placed in a particular location. The chemical potential will be affected by local excess energies that will lead to diffusion [10]. Figure (2-20) illustrates two different types of diffusion, surface and grain boundary diffusion, which both play a significant role in the sintering process. The grain boundary and surface diffusion is given by flux  $j_g$  and flux  $j_s$ , as per figure (2-20) [10].

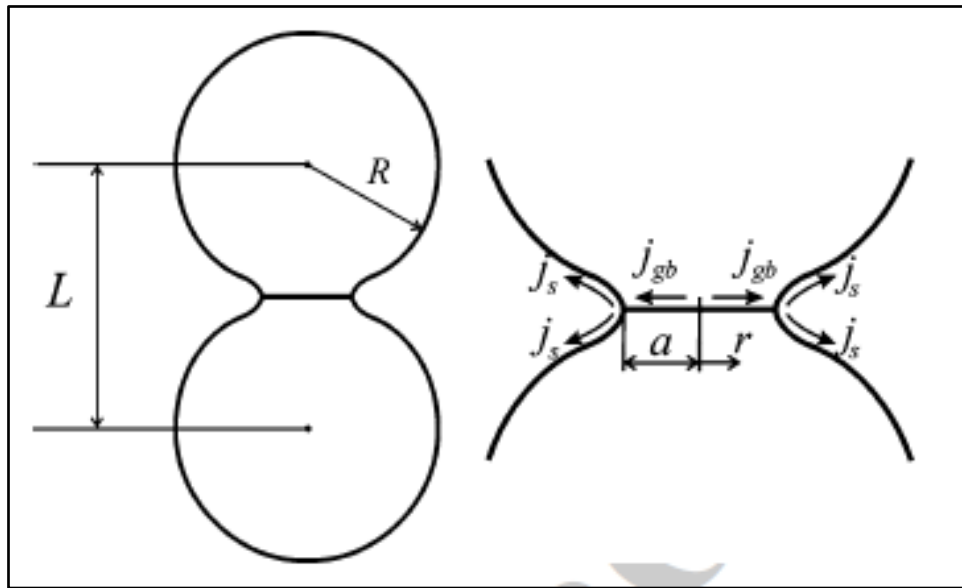


Figure 2-20 Grain boundary and surface diffusion between particles [10].

The chemical potential is shown in equation (2.15) [15]:

$$\mu = -\Omega\sigma \quad (2.15)$$

The stress ( $\sigma$ ) is normal to the grain boundary, which is equal to principal curvature of the free surface ( $K$ ) and specific surface energy ( $\gamma_s$ ).

$$\mu = -\Omega\gamma_s K \quad (2.16)$$

Figure (2-21) illustrates the comparison between linear and nonlinear diffusion laws of sintering alumina with different sized particles [10]. When both particle size ( $R$ ) and neck size ( $a$ ) are small, this leads to greater relative errors in the linearization process when the driving force is calculated. However, when a particle of  $R \geq 100$  nm is used, the linearization is generally quite acceptable.

Equation (2.17) describes the main curvature at the tip of the contact area.

$$K_{r=a} = \frac{1}{\rho} - \frac{1}{a} = \frac{4R}{a^2} - \frac{1}{a} \quad (2.17)$$

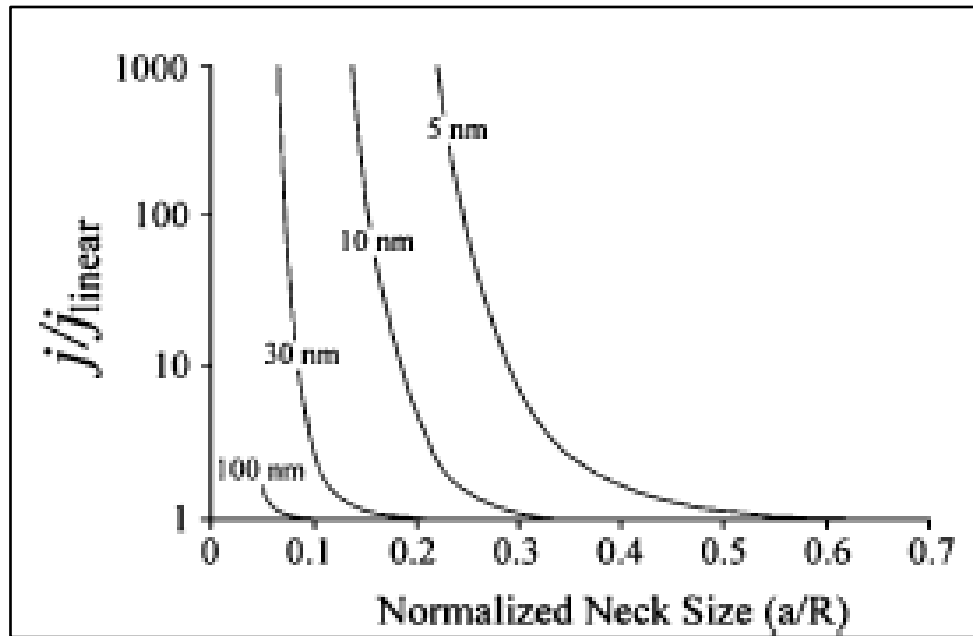


Figure 2-21 Linear and nonlinear diffusion of different sized particles [10].

Equation (2.18) refers to the driving force at the edge of the grain boundary

$$F = \nabla\mu = \frac{\nabla\mu}{\nabla r} \approx \frac{\mu_{r=a} - \mu_{r=0}}{\frac{a}{2}} = 2\gamma_s(4R - a) \frac{\Omega}{a^3} \quad (2.18)$$

Where simplification of equation (2.18) gives equation (2.19)

$$F = 2\gamma_s \left(4 - \frac{a}{R}\right) \frac{\Omega}{(a/R)^3 R^2} \quad (2.19)$$

It can be seen from equation (2.19) that the particle size ( $R$ ) decreases with increasing driving force ( $F$ ). As a result, the small value of nanoparticle size will generate a high driving force value in the nanosintering process. If this is in fact true, equation (2.14),

as describing the linearization, can be re-examined, and the estimate  $A_a F \leq kT$  might not be set to the same conditions [10].

## **2.5 Literature review of nanosintering modelling using molecular dynamics method**

Molecular dynamics method is a significant tool to study the nanoparticle sintering process. As a proof of concept, the molecular dynamics technique has been employed to study and understand the mechanism of neck growth between nanoparticles during the solid-state sintering process [93-95]. Face centre cubic metals have been previously simulated as models for the nanosintering process by molecular dynamics, for example, gold [93], silver [96], and copper [97], as have body centre cubic metals. Tungsten has been used to investigate the neck formation mechanism of two tungsten nanoparticles at sintering temperatures ranging from 2000-3500 K [98]. Kazuhide Nakao et al. (2014) [99] combined molecular dynamics simulations with a master sintering curve approach to study the change in sintering activation energy with temperature and particle size for porous materials. The researchers concluded that the sintering activation energies obtained from simulation had a good match with experimental results.

Chng et al. (2007) [37] used a computer simulation of the sintering between three different particle sizes to compare microparticle sintering and nanoparticle sintering, and to show the coarsening in behaviour between the two cases. They showed that the small particle was invaded by large particles during the sintering process between microparticles, whereas there was a difference in sintering between nanoparticles as the small particles resisted invasion by larger ones (see figure 2-22) [37].

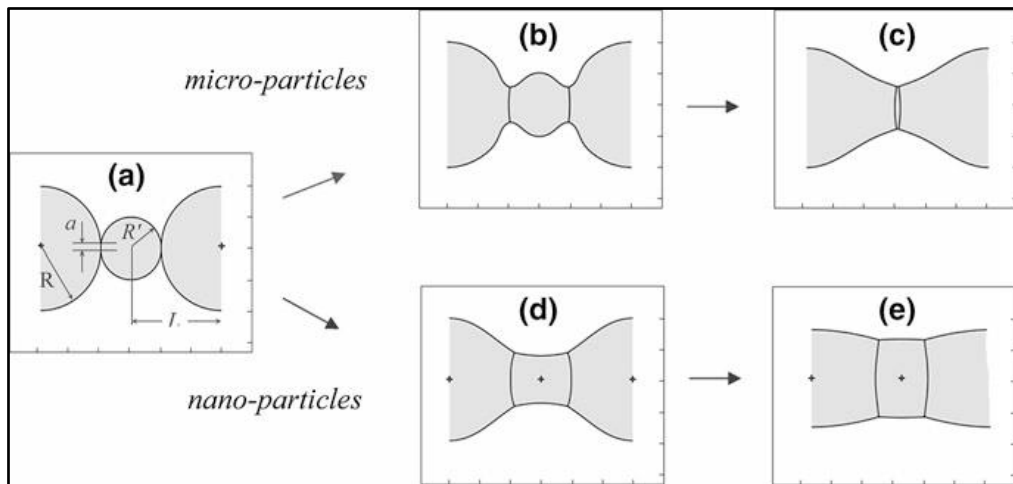


Figure 2-22 Comparison between micro-particle and nanoparticle sintering for three particles [37].

Ding et al. (2009) used a molecular dynamics model to examine the sintering between two particles with diameters of 16 nm to show crystalline orientations in the contact area between the two particles. Also, they compared their molecular dynamics model with the continuum model, demonstrating that the continuum model was not capable of capturing the action of nanoparticle sintering. Moreover, the crystalline orientations were found to be reoriented by particles in the primary sintering process, which leads to the creation of a new type of neck between particles, as shown in figure (2-23) [100].

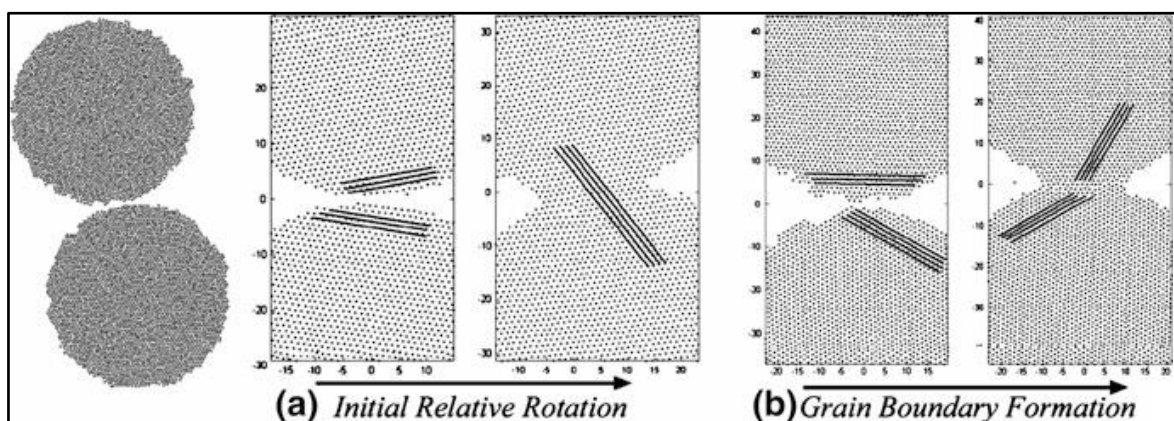


Figure 2-23 Crystalline orientations between two nanoparticles (16 nm) [100].

Yang et al. (2012) used molecular dynamics methods to simulate the neck growth of gold nanoparticles using laser sintering; they also used different heating rates with different gold nanoparticle sizes, with diameters ranging from 4 to 20 nm. They showed that solid-state sintering occurred at room temperature, and the stable neck size increased with increasing nanoparticle size [101].

Buesser et al. (2016) [102] used molecular dynamics to simulate two silver nanoparticles with different diameters (2.5, 3.0, 3.5 and 4.0 nm), and using temperatures ranging from 400-1000 K. They concluded that the melting temperature of silver nanoparticles depended on nanoparticle size, which was found to increase with increasing melting temperature; also, they showed the relationship between melting temperature and nanoparticle size, and subsequently compared experimental and molecular dynamics results. Seong et al. (2015) [103] used molecular dynamics (via the LAMMPS code) to simulate two copper nanoparticles with a range of sizes from 2.8 to 5.4 nm under free sintering conditions and at different sintering temperatures (1000, 1100, 1200, 1300 K). They concluded that shrinkage ratio and densification increase with increasing sintering temperature; moreover, the shrinkage ratio and the densification could decrease as a result of an increase in misorientation angles, using 60°, 30°, and 0°. They also noted that shrinkage ratio and densification increased with decreasing nanoparticle size.

Wang et al. (2016) [104] used molecular dynamics simulations to investigate solid-state sintering between two Ag-Cu core-shell nanoparticles with different geometries over a range of temperatures (300-1000 K). They concluded that there were three separated steps in the shrinkage ratio curve. Zhang et al. (2016) [96] used the LAMMPS code to investigate solid-state sintering between two silver nanoparticles at low temperature and using a nanoparticle of 6 nm in diameter because the sintering temperature of nanosilver ink can proceed at low thermal temperatures, and also using intense pulsed-light sintering. They concluded that the initial sintering stage shows a rapid decrease in resistivity because of the rapid neck formation between particles. In addition, they demonstrated that increasing the temperature of the sintering process

led to a decrease in resistivity. They compared these results with the equivalent experimental and analytical results, and found good agreement in all cases.

Alarifi et al. (2013) [105] used molecular dynamics simulations with the embedded atom method to model two silver nanoparticles during solid-state sintering with a range of different nanoparticle sizes (4-20 nm); they further modelled three and four silver nanoparticles with 4 nm diameters. They found that the nanosilver sintering process had three clear stages. In addition, densification during the sintering of three nanoparticles occurred during the first stage, but for four nanoparticles the same occurred during the second stage for the same sized silver nanoparticles. Yousefi [106] used molecular dynamics to simulate two different nanoparticles, copper and nickel, at a sintering temperature of 300 K and with various crystallographic structures. They found that surface diffusion was the dominant mechanism in the sintering process; it was noted that the copper nanoparticles started to rotate when sintering, whilst the nickel nanoparticles remained in the same position.

In the past few decades, solid nanoparticles have been investigated extensively by researchers who are interested in the nanosintering process, where solid nanoparticles were used in the modelling of the nanosintering process. This process was utilized to simulate two or more nanoparticles of different materials. A number of parameters have been investigated, such as the driving force of the nano-sintering process, heating rates, different powder metals, effective conductivity, nanoparticle size, sintering temperature, atomic transport mechanisms, and different crystallographic structures, etc. However, there is a lack of research into the understanding of the effect of hollow nanoparticles on improving neck growth between particles, according to the best of our knowledge. There are a number of parameters that can be employed to improve neck growth, for instance nanoparticle size and sintering temperature. In addition to these parameters, hollow nanoparticles and crystal orientations are proposed as a new way to resolve the lack of contact between nanoparticles.

Another issue, the melting temperature is an important parameter in the nanosintering process because it changes depending on nanoparticle size; moreover, the sintering

temperature depends on the melting temperature of the nanoparticles, which is ( $T_{\text{sintering}} = 0.95T_{\text{melting}}$ ). However, there is a general lack of knowledge in investigating the melting temperature of nanoparticles, especially nanoparticles of copper, which affects the nanosintering process. The nanosintering process can be improved by increasing the neck size between nanoparticles using smaller nano-copper particles which have a lower melting temperature and thus a lower sintering temperature. In addition, previous studies have not considered the use of MD simulations to calculate the melting temperature for the surface and centre of the nano-copper particles, which affects the nanosintering process.

## 2.6 Unresolved issues in previous sintering models

Three unresolved issues can be identified through the literature review:

Firstly, a numerical solution for the coupled surface and grain-boundary diffusion problem is computationally intensive. This is mostly due to the surface diffusion part of the problem. The complexity occurs due to the movement of the particle surface is controlled by the gradient of the surface curvature, i.e. the very high order of derivatives for the surface profile. Extremely small time steps have to be used to make the numerical solution stable. Numerical computation becomes untenable if one wants to simulate the sintering process involving thousands of particles.

Secondly, there has been very little research work in the literature on a fundamental understanding of the selective laser sintering process (SLS), despite various numerical methods being readily available for such theoretical studies. SLS has become an important technology in additive manufacturing; however quality control is poor, which leads to poor mechanical properties in any subsequently manufactured parts. Computer models for SLS can help to resolve the issue.

Thirdly, there is a major gap in the understanding of nano-sized particles. Issues such as the melting temperature of nanoparticles and their dependence on particle size are poorly understood. There is also a need to understand the sintering behaviour of

hollow nanoparticles because of their potential applications in engineering and medicine.

Overall, this thesis is set out to resolve these issues.

## **2.7 Thesis Objective**

The objective of this thesis is to make a numerical model of the sintering process between particles using grain boundary diffusion and surface diffusion mechanisms. The major objective is realized through the following:

- 1- To make a simple numerical model of the sintering process by creating new equations describing the curvatures of particles' surfaces depending on the neck growth ratio for different coefficient ratios using a finite difference numerical method.
- 2- To validate a new method by comparing with results of full the FD method for different diffusion coefficient ratios and different applied stress using two sintering parameters with known neck size and shrinkage ratios.
- 3- To build a new numerical model of the sintering between two particles via a variational method using a new tip curvature equation to make sure that the new method describes other models accurately.
- 4- To validate the results from VM-CF by comparison with FD-CF.
- 5- To make a new numerical code for VM-CF to simulate the selective laser sintering process for 27 copper particles, and to validate the SLS process using VM-CF results with FD-CF results.
- 6- To create a thermal model of the laser beam via the COMSOL multiphysics software, from which temperatures of particles during illumination by the laser beam will be collected and used in the sintering model.
- 7- To build a new numerical model to calculate melting temperature for each nanoparticle size via molecular dynamics methods - LAMMPS code.
- 8- To build a new numerical model of the sintering between nanoparticles via molecular dynamics method - LAMMPS code to simulate the behaviour of

nanoparticles during the sintering process, and lastly comparing the micro- and nanosintering processes.

### 3 CHAPTER THREE: Chemical potential at triple junction

Chapter three focusses on the simulation of a new method to model the sintering process between particles using the Finite Difference model. The new method focusses in curvature deformation between particles during the sintering process, and thus on the change in the curvature of particles' surfaces during sintering. The Finite Difference model is used to model the movement and change of curvature of the particles during the neck growth process. The curvature in a triple junction between two particles',  $K_{tip}$ , depend on two curvatures, whilst the neck growth between two particles depends on the change in the tip curvature,  $K_{tip}$ . The curve fitting equations for curvatures for different diffusion coefficient ratios are used in the FD model to calculate the neck size and shrinkage ratios instead of the full calculation of  $K_{tip}$ . Diffusion coefficient ratios and applied stresses are used in the FD model to compare the curve-fitting and the full FD methods so as to show that the former is useful for modelling the solid-state sintering process between particles.

#### 3.1 Introduction

For solid-state, diffusion-controlled sintering, matter transport is first achieved from inside any contact area to the edge of the contact by grain boundary diffusion, and second from the edges to the pore surface by surface diffusion. The chemical potential where the grain boundary meets the pore surface provides the boundary conditions for both the grain boundary and surface diffusion processes. Pan et al. [5] referred to this chemical potential as "tip curvature", or  $K_{tip}$ , although a curvature does not exist for the "pore tip" which is shown in figure (3-1).

The curvature,  $K_{tip}$ , is defined as the curves at the junction between particles, which are modified and changed during the sintering process. The curvature,  $K_{tip}$ , depends on two curves: the first represents the curvature near the neck between particles; and the second represents the neck radius.

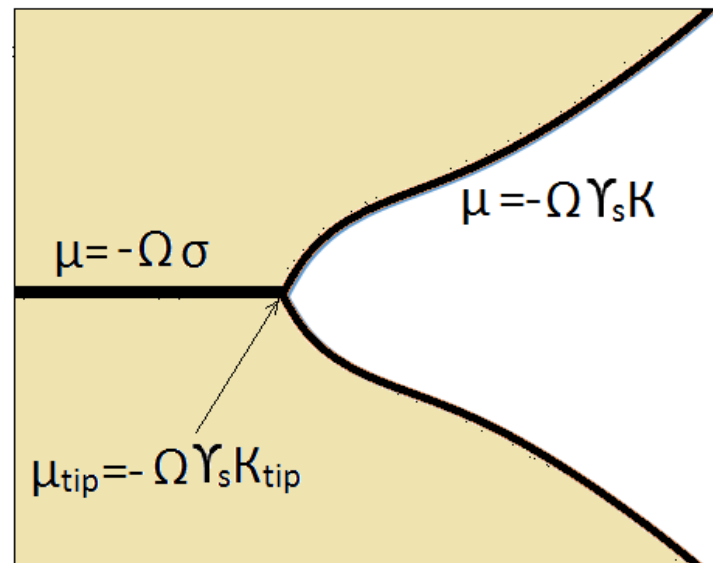


Figure 3-1 Chemical potential between two particles

The change in curvature depends on the very fast of the movement of atoms from one position on the particles' surface to another during the sintering process; these movements start from a convex surface, which is the particle surface, and flow to a concave surface, which is neck between the particles. Atom movement depends on sintering temperature, which means that the movement of atoms between surfaces increases due to the increase in sintering temperature, consequently accelerating the sintering process itself. Thus, the curvature,  $K_{tip}$ , participates in the neck growth process between particles because of the movement of atoms between surfaces. This movement depends on particle size; for example, movement of atoms is faster when using a smaller particle during the sintering process [3, 11].

The stress in the neck depends on two parameters: surface energy and tip curvature,  $K_{tip}$ . Equation (3-1) shows the tip stress while equation (3-2) shows the chemical potential in the junction between particles which is dependent on tip curvature [11].

$$\sigma_{tip} = \gamma_s K_{tip} \quad (3 - 1)$$

$$\mu_{tip} = -\gamma_s \Omega K_{tip} \quad (3 - 2)$$

The curvature contains two curved surfaces, which are concave and convex; by convention, the sign of the concave surface is negative because it is under tension stress, while the sign of convex surface is positive because of compressive stress. A saddle-shaped surface can result for the sintering neck between the particles. The neck growth depends on tip stress; for example, a small neck between particles has a large tip stress, while a large neck between particles has little tip stress. The sintering process continues until the change in tip stress reaches zero, which means that the sintering process reaches equilibrium, and all concave and convex curvatures have flattened (in the last stage of the sintering process) [3, 11].

### 3.2 Governing equations for coupled grain boundary and surface diffusion

A two spherical particles with the same radius are assumed to be in contact, as shown in figure (3-2). The basic equation of diffusion flux is considered by Fick's law, which is dependent on the gradient of the chemical potential,  $\mu$ , of the diffusing atoms:

$$j = -\frac{D\delta}{KT} \frac{\partial \mu}{\partial s} \quad (3 - 3)$$

The chemical potential in the grain boundary is dependent on normal stress,  $\sigma$ , and atom volume,  $\Omega$ :

$$\mu = -\sigma\Omega \quad (3 - 4)$$

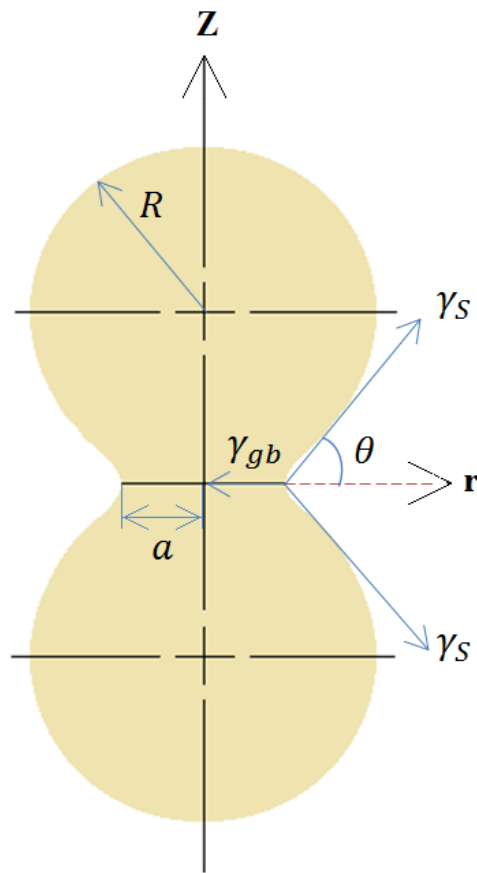


**Figure 3-2 Geometry of two particles during the sintering process.**

And effective grain boundary diffusivity:

$$D_g = \frac{D_g \delta_g \Omega}{KT} \quad (3 - 5)$$

The chemical potential on the particle surface is dependent on surface energy, the atomic volume,  $\Omega$ , and the principal curvature, K.

$$\mu = -\Omega \gamma_s K \quad (3 - 6)$$

The surface diffusivity is shown in equation (3-7):

$$D_s = \frac{D_s \delta_s \Omega \gamma_s}{KT} \quad (3 - 7)$$

From figure (3-2), the equilibrium of the grain boundary energy and the surface energy in the triple junction can be found by the equation (3-8).

$$\gamma_g = 2\gamma_s \cos \theta \quad (3 - 8)$$

From figure (3-3), the equilibrium flux in the triple junction can be found by equation (3-9).

$$j_g - 2j_s = 0 \quad (3 - 9)$$

The chemical potential during sintering must be continuous from the grain boundary to the tip of the two surfaces between the particles, and the chemical potential of the grain boundary in the tip should be equal the chemical potential of the surface.

$$\mu_{tip} = -\Omega\sigma_{tip} = -\Omega\gamma_s K_{tip} \quad (3 - 10)$$

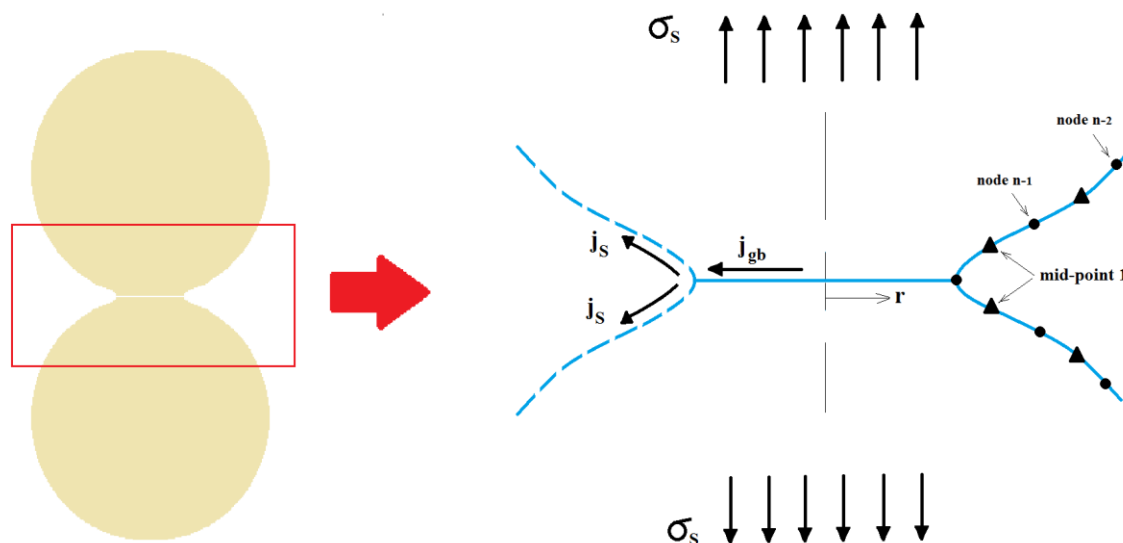


Figure 3-3 Details of neck between two particles [63].

Rewriting equation (3-10):

$$\sigma_{tip} = \gamma_s K_{tip} \quad (3 - 1)$$

Basically, the principle curvature,  $K_{tip}$ , can be defined as the sum of the all principle curvatures in the tip of the neck between particles, and also represents two curvatures. The first curvature is positive because the centre of curvature is outside the particle, which is known as a positive curvature, whilst the second curvature is negative because the centre of curvature is inside the particle [25].

The principle curvature,  $K_{tip}$ , cannot be calculated using the finite difference method because it is dependent on two curvatures which are caused by the tangential discontinuity of the free surface. Pan and Cocks [5] gave some of the details of the general solution that can be applied to the simple problem of the sintering of two particles. Figure (3-3) shows the surface flux at mid-point 1 near to the tip between the

two particles, which can be calculated using the finite element method, as per equation (3-11).

$$j_s = D_{es} \frac{K_{n-1} - K_{tip}}{\Delta S_{n-1}} \quad (3 - 11)$$

Equation (3-12) was derived by Luo et al. [63].

$$K_{tip} = \frac{\left[ 2D_{eg} \left( \frac{\sigma_s}{a} - \frac{2\gamma_s \sin \theta}{a^2} \right) + D_{es} \gamma_s \left( \frac{K_{n-1}}{\Delta S_{n-1}} \right) \right]}{\left( \frac{2\gamma_s D_{eg}}{a} + \frac{D_{es} \gamma_s}{\Delta S_{n-1}} \right)} \quad (3 - 12)$$

Where  $\sigma_s$  is the applied stress,  $K_{n-1}$  is a principle curvature of finite difference for the node before the junction between the particles, and  $\Delta S_{n-1}$  is the arc distance between node n-1 and the tip of the neck.

Adding further details to the effective grain boundary diffusion equation and the effective surface diffusion equation, as shown in equations (3-13) and (3-14), respectively, gives:

$$D_{eg} = \frac{\Omega (D_{go} \delta_g) \exp(-Q_g/R_r T)}{B_z T} \quad (3 - 13)$$

$$D_{es} = \frac{\Omega \gamma_s D_{so} \delta_s \exp(-Q_s/R_r T)}{B_z T} \quad (3 - 14)$$

### 3.3 Numerical model for coupled grain boundary and surface diffusion

In this study, a finite difference code [5] is improved to simulate the curvatures of surface particles as might be found in solid-state sintering. The FD code has been developed to investigate the influence of the grain boundary and surface diffusion between two particles during the sintering process. Before starting the simulation, the input to the FD code had to be prepared, such as mesh, position of particle centre etc., the latter being important to the simulation because it defines the position of the mesh of the two half surfaces of the particles; figure (3-4) shows the FD mesh for the two half surfaces for the particles used in the simulation, where this mesh contains a multitude of points (x and y coordinates) around the surface of the particles to represent the change in geometry of the particles and the neck growth between them during the sintering process. An FD mesh was used as input to the FD code to represent the change in curvature between particles during the sintering process in this instance.

The flow chart for the FD code for two particles is shown in Figure (3-5), where this chart contains the steps implemented in the FD code to simulate the sintering process between two particles, and these steps represent the calculation of grain boundary velocity, tip curvature, etc. The output of this code is the sintering parameters such as neck radii and shrinkage ratio and the change in curvature of two particles during the sintering process.

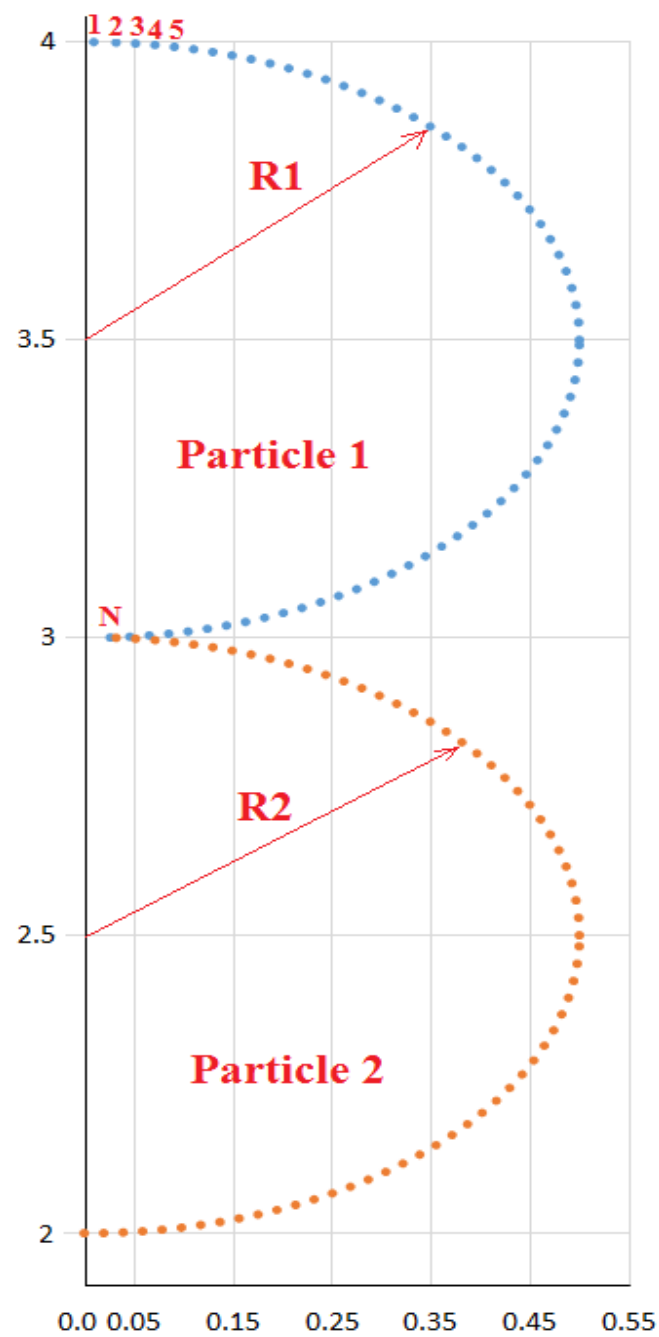


Figure 3-4 FD-mesh of two of half surfaces for particles.

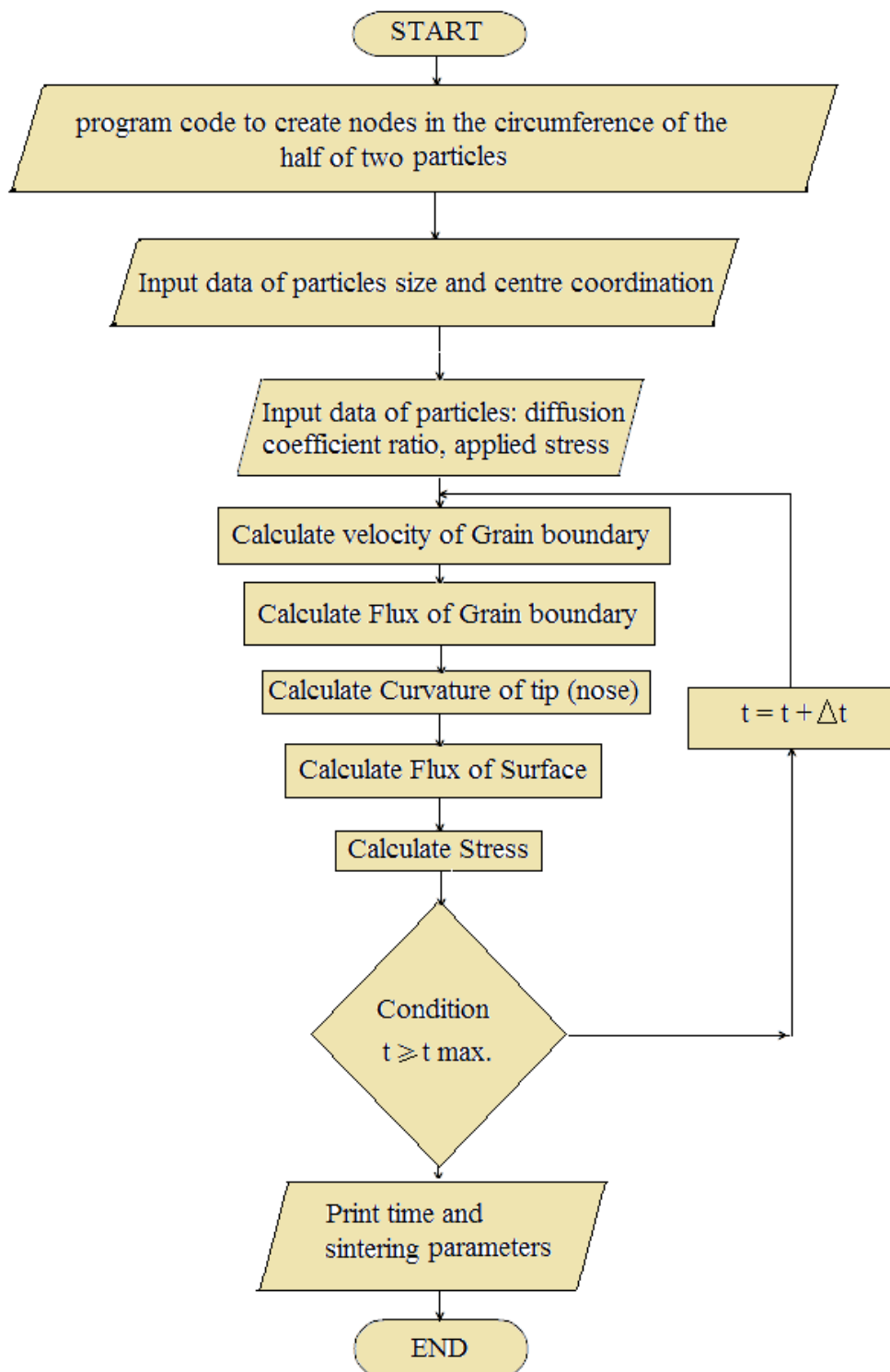


Figure 3-5 Flow chart of FD model.

### 3.3.1 Curve-fitting equation method

The curve-fitting equation method is a new method designed to simplify the solution of the curvatures of surfaces of particles which is used to simulate the sintering process.

The curve-fitting equation method comprises four steps. Firstly, the curve-fitting equation for the curvature  $K_{n-1}$  was created from a full FD simulation, where the location of curvature  $K_{n-1}$  was between the point next to the neck and the point of the junction between the particles. Thus, the curvature  $K_{n-1}$  will participate with tip curvature  $K_{tip}$  to form a simple solution to sintering between particles.

Figure (3-6) illustrates a comparison of curvature  $K_{n-1}$  between the curve-fitting FD and the full FD method. Thus, this figure shows two types of curves: the first curve represents the fluctuating curvature,  $K_{n-1}$ , obtained from the full FD method for three different diffusion coefficient ratios,  $D_S/D_g = 0.01, 0.1, \text{ and } 1$ , while the second curve represents the curve fitting of curvature  $K_{n-1}$  for the three diffusion coefficient ratios. Overall, the difference between curves can be seen from the figure: the curves for the full FD method fluctuated due to small numerical errors that arose during the determination of the numerical solution when the coordination of nodes was updated to change to a new curvature, where these errors increased due to updating the coordination of the nodes. While the curves of curve fitting FD method is smooth without fluctuating. The fitting equations for three diffusion coefficient ratios will be used in simulation via  $K_{tip}$  equation, and three fitting equations for three different diffusion coefficient ratios  $D_S/D_g = 0.01, 0.1, \text{ and } 1$  are shown in equations (3-15), (3-16), and (3-17) respectively.

$$K_{n-1} = 381.54 \left(\frac{a}{R}\right)^2 - 370.39 \left(\frac{a}{R}\right) + 99.5 \quad \text{for } \frac{D_S}{D_g} = 0.01 \quad (3-15)$$

$$K_{n-1} = 455.7 \left(\frac{a}{R}\right)^2 - 370.73 \left(\frac{a}{R}\right) + 79.5 \quad \text{for } \frac{D_S}{D_g} = 0.1 \quad (3-16)$$

$$K_{n-1} = 127.24 \left(\frac{a}{R}\right)^2 - 100.57 \left(\frac{a}{R}\right) + 18.846 \quad \text{for } \frac{D_S}{D_g} \geq 1 \quad (3-17)$$

The three equations (3-15), (3-16), and (3-17) collected from curve fitting of fluctuating curve for curvature  $K_{n-1}$  which is calculated from finite difference code for different diffusion coefficient ratios.

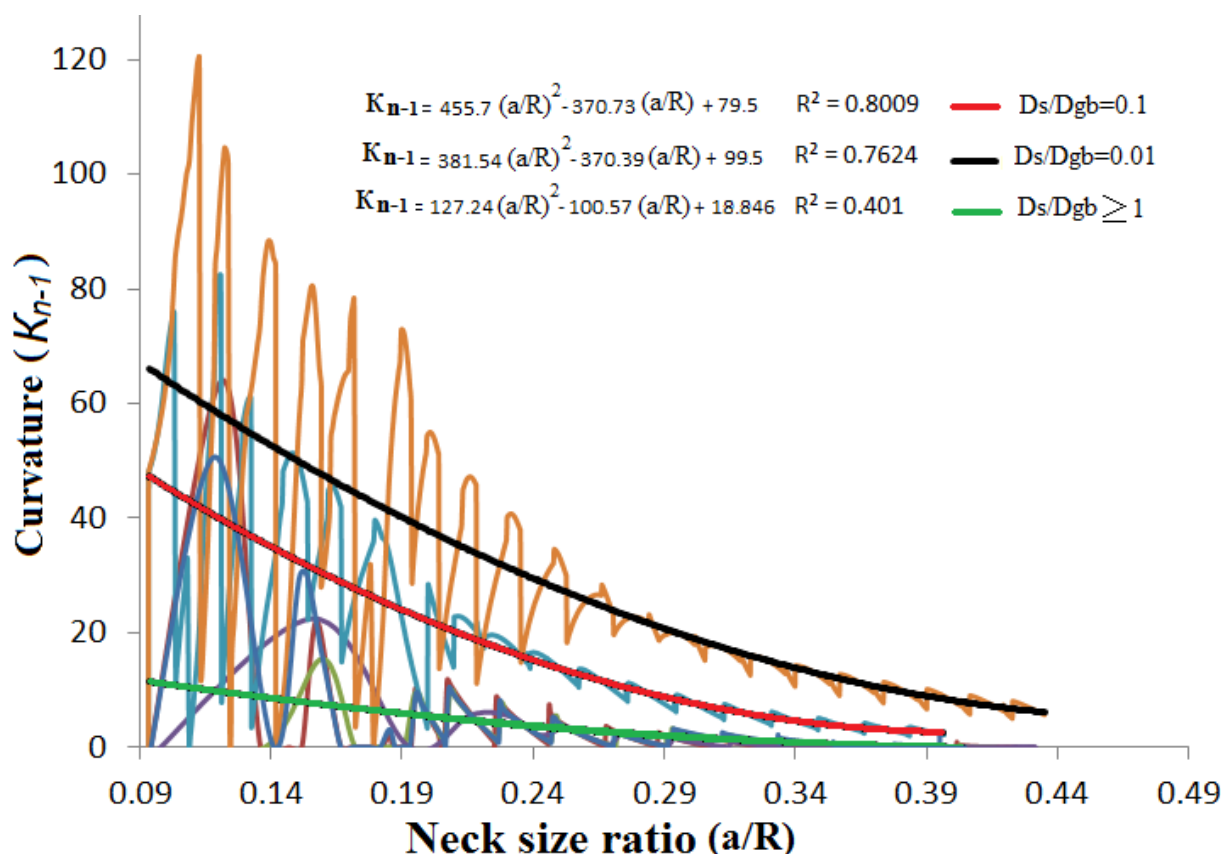


**Figure 3-6 Curvature  $K_{n-1}$  as a function of the neck size ratio for three  $D_S/D_g$  ratios of 0.1, 0.01, and 1.**

Figure (3-7) illustrated curvature  $K_{n-1}$  for diffusion coefficients ratios  $D_S/D_g = 1-10000$  and for applied stresses  $\sigma = 25-100$  MPa, obtained from a full FD simulation. Also, the figure shows the curve-fitting equation for curvature  $K_{n-1}$  using a ratio  $D_S/D_g = 1$ , and diffusion coefficient ratios  $D_S/D_g = 1-10000$  for applied stresses  $\sigma = 25-100$  MPa. Overall, it can be seen from this figure that the curve-fitting equation is the same for all  $D_S/D_g = 1-10000$  and  $\sigma = 25-100$  MPa, and can be used to simulate sintering process between particles for all cases mentioned before. In addition, all curves

obtained from the full FD model fluctuated at the start of the simulation from high to low, and continued fluctuating until the last stage of sintering; moreover, the maximum curvature  $K_{n-1}$  is 64 at a neck size ratio of 0.08, while the maximum curvature  $K_{n-1}$  is 1.5 at neck size ratio 0.45.

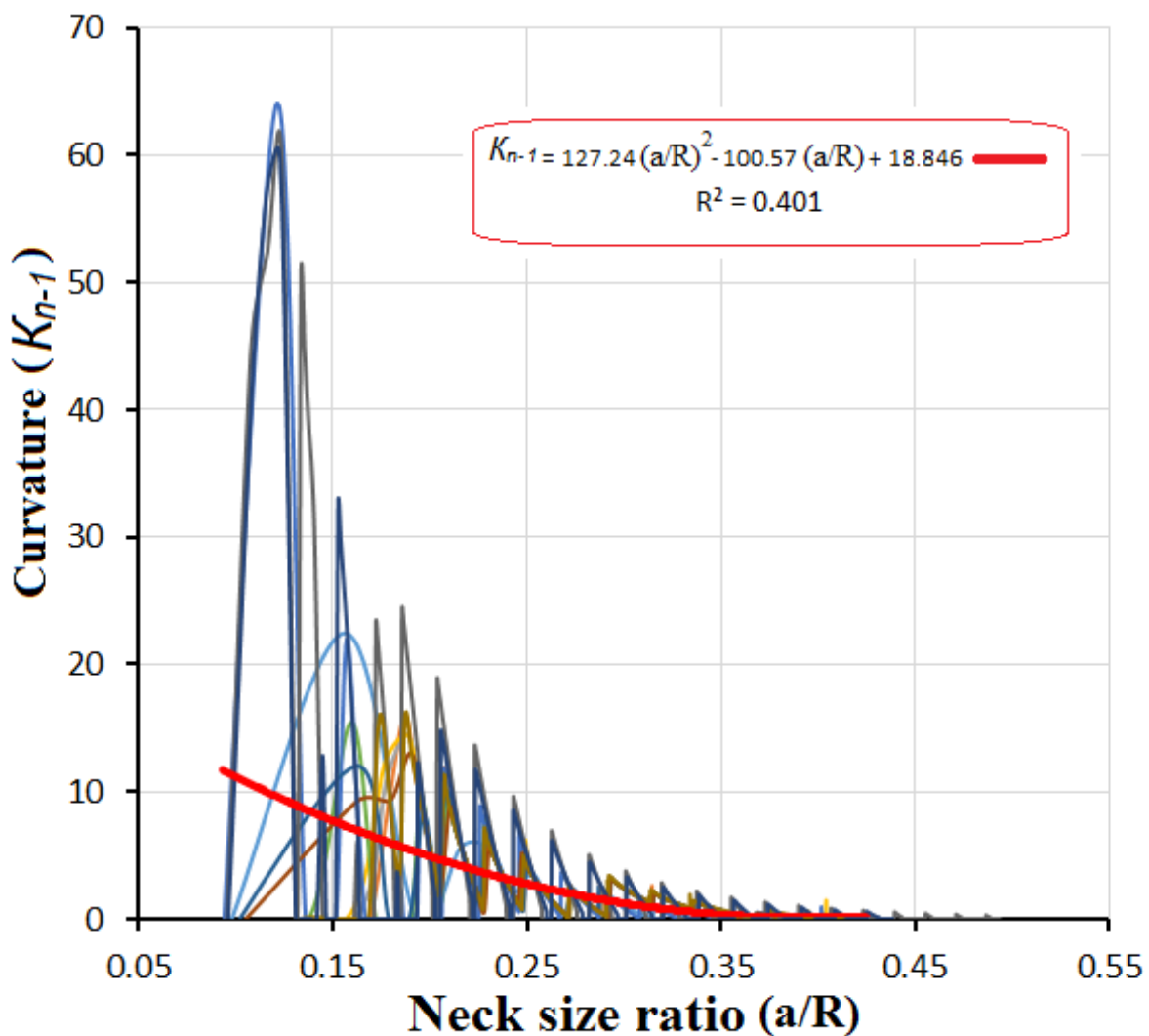


Figure 3-7 Curvature  $K_{n-1}$  as a function of neck size ratio for  $D_s/D_g = 1-10000$  and stresses  $\sigma_s = 25-100\text{MPa}$ .

Secondly, equation (3-12) was normalized by dividing this equation by certain parameters, as shown below.

$$\dot{K}_{tip} = \frac{\left[ 2 \left( \frac{\sigma_s}{a} - \frac{2 \sin \theta}{a^2} \right) + \frac{D_s}{D_g} \left( \frac{K'_{n-1}}{\Delta S'_{n-1}} \right) \right]}{\left( \frac{2}{a} + \frac{D_s}{D_g} * \frac{1}{\Delta S'_{n-1}} \right)} \quad (3 - 18)$$

Where

$$\dot{K}_{tip} = K_{tip} * R ,$$

$$a = \frac{a}{R}$$

$$K'_{n-1} = K_{n-1} * R ,$$

$$\Delta S'_{n-1} = \Delta S_{n-1} / R , \text{ and}$$

$$\sigma_s = \frac{\sigma_s}{\gamma_s / R}$$

Thirdly, equation (3-18) is run in FD code instead of full method of FD to calculate  $K_{tip}$  by assuming  $\Delta S'_{n-1}$  to be a constant of 0.008 for all calculation, and also assuming that R is 1.

Lastly, 354 nodes of FD mesh were constructed as input data on the surface of the two half-particles, as shown in figure (3-4).

### 3.4 Results and discussion

The numerical results needed to be compared to analytical models for validation purposes. To validate the curve fitting FD model, the simulation results (neck size and shrinkage ratios) were compared to the analytical model provided by Coblenz et al.

(1980) [13]. Shrinkage ratio is defined as the linear dimensional change,  $\Delta L/L_o$ , which means that the change in the initial length to the final sintered length is given as  $\Delta L$ , compared to the original length,  $L_o$ . Figure (3-8) shows a comparison of the shrinkage ratio between curve-fitting FD results and analytical Coblenz model. Overall, it can be seen from this diagram that the curve-fitting FD curves are close to the analytical model, in particular the C-F curve with a diffusion coefficient ratio of  $D_s/D_g=1$  in the final stage of the sintering process. This is because the Coblenz model is an analytical formula intended only for grain boundary diffusion; moreover, the conditions for the Coblenz analytical formula are used in the initial stage of sintering only.

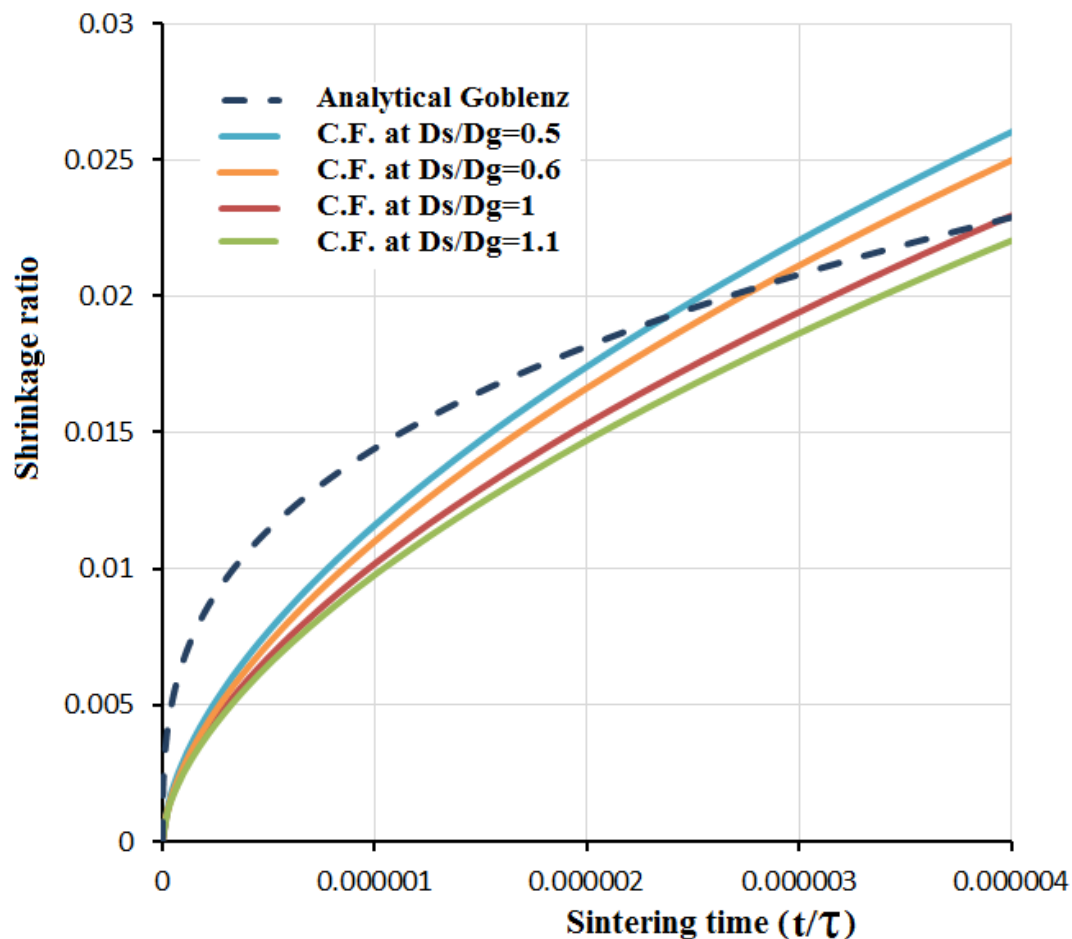


Figure 3-8 Comparison of shrinkage ratio for numerical results and the analytical model.

Neck size ratio is significant in the sintering process because of the dependence of various stages of the sintering process on this factor. A comparison of neck size ratio in the curve-fitting FD and analytical Coblenz models are shown in figure (3-9). Overall, it can be seen from the diagram that the curve-fitting FD model is close to the Coblenz analytical model, especially for the CF curve at  $D_s/D_g=3$  in the final stage of the sintering process.

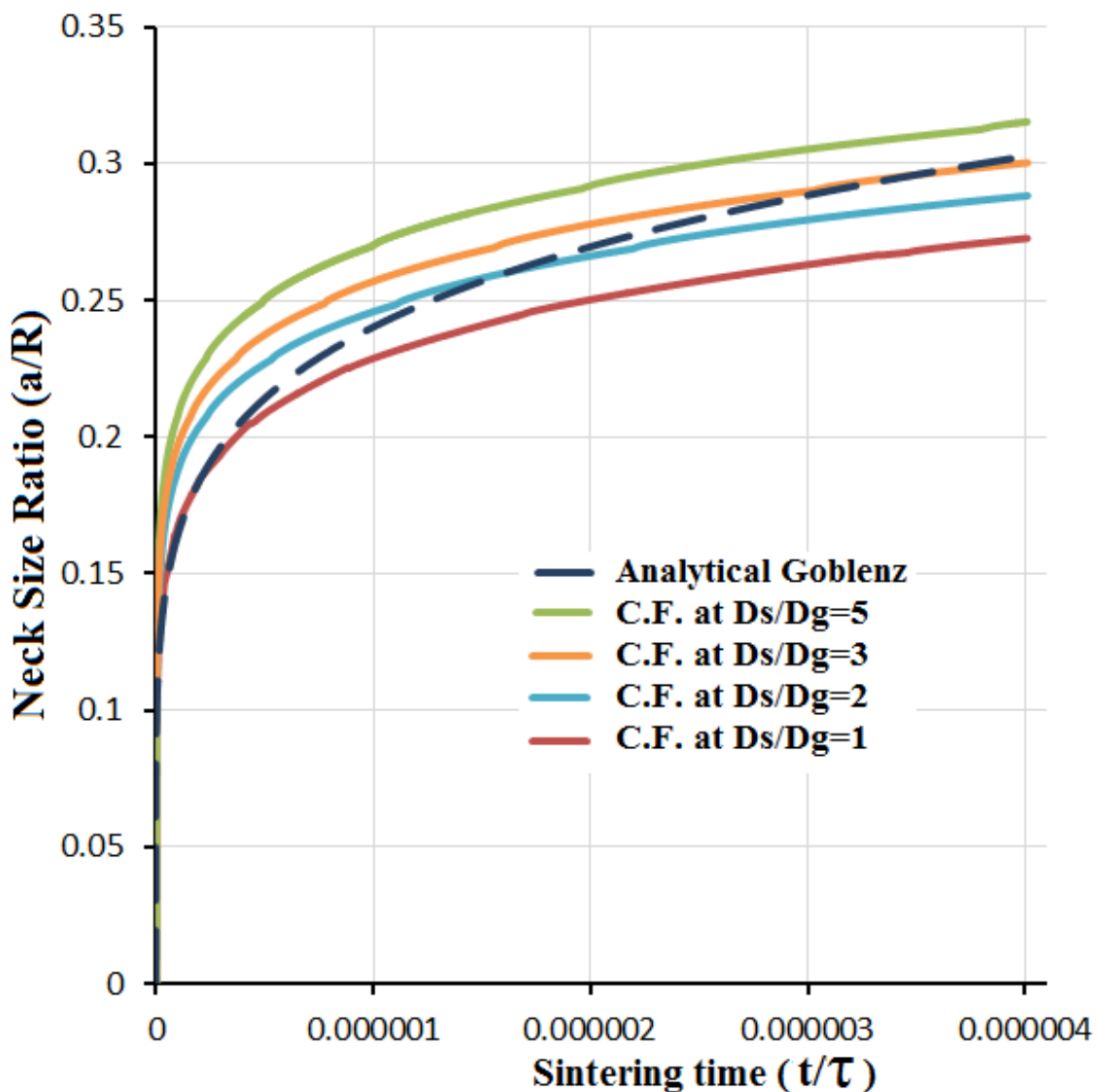


Figure 3-9 Comparison of neck size ratio as used for numerical results and the analytical model.

### 3.4.1 Effect of diffusion coefficient ratios in the sintering process

Diffusion coefficient ratio is a significant parameter in terms of describing the sintering process, and is defined as the ratio of surface diffusion to grain boundary diffusion ( $D_s/D_g$ ) rates.

Figure (3-10) shows a comparison of shrinkage ratios for different diffusion coefficient ratios. Seven different diffusion coefficient ratios, i.e.,  $D_s/D_g = 0.01, 0.1, 1, 5, 50, 100,$  and 1000 were used in this study to understand the effect of the diffusion coefficient ratio on the shrinkage ratio during the sintering process. Overall, it can be seen that the shrinkage ratio increases with decreasing diffusion coefficient ratio, especially in the final stage of the sintering process, whereas all curves are close together at the beginning of sintering process. Also, the maximum shrinkage ratio in the last step of the sintering process is 0.078 at a diffusion coefficient ratio  $D_s/D_g = 0.01$  while the minimum shrinkage ratio is 0.0025 at a diffusion coefficient ratio  $D_s/D_g = 1000$ . Finally, the shrinkage ratio between particles was improved by grain boundary diffusion because the activation of grain boundary diffusion increases with increasing sintering temperature, and lastly the increase in grain boundary velocity with increasing grain boundary diffusion will be accelerated the shrinkage between particles during the sintering process.

Figure (3-11) illustrates neck size ratio as a function of sintering time for different diffusion coefficient ratios. Seven diffusion coefficient ratios,  $D_s/D_g = 0.01, 0.1, 1, 5, 50, 100,$  and 1000, were used in this study to investigate the effect of diffusion coefficient ratio on neck size ratio during the sintering process. Overall, it can be observed from the comparison that the neck size ratio increases with increasing diffusion coefficient ratio, which means that the surface diffusion coefficient accelerates neck growth during the sintering process. This is because the activation of the movement of atoms from the particles' surface to the neck between particles increases with increasing surface diffusion without shrinkage between particles. Additionally, the neck size ratio increases due to the increased sintering time. Neck size ratio curves at  $D_s/D_g = 50-1000$  are close together, especially in the final stage of

the sintering process. In addition, the maximum neck size ratio at a diffusion coefficient ratio of 1000 is 0.415, while the minimum neck size ratio at a diffusion coefficient ratio of 0.01 is 0.16.

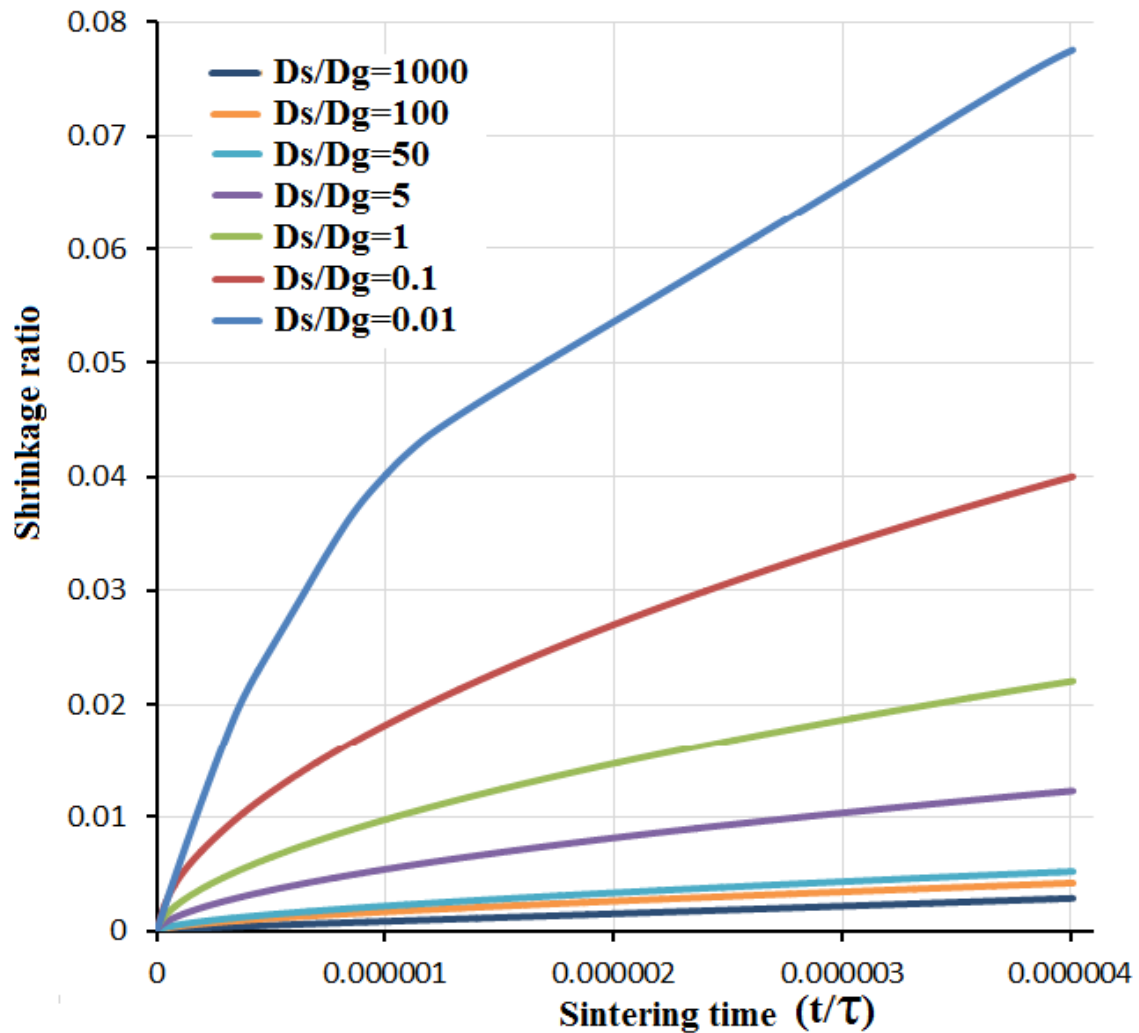


Figure 3-10 Shrinkage ratio as a function of sintering time for different diffusion coefficient ratios.

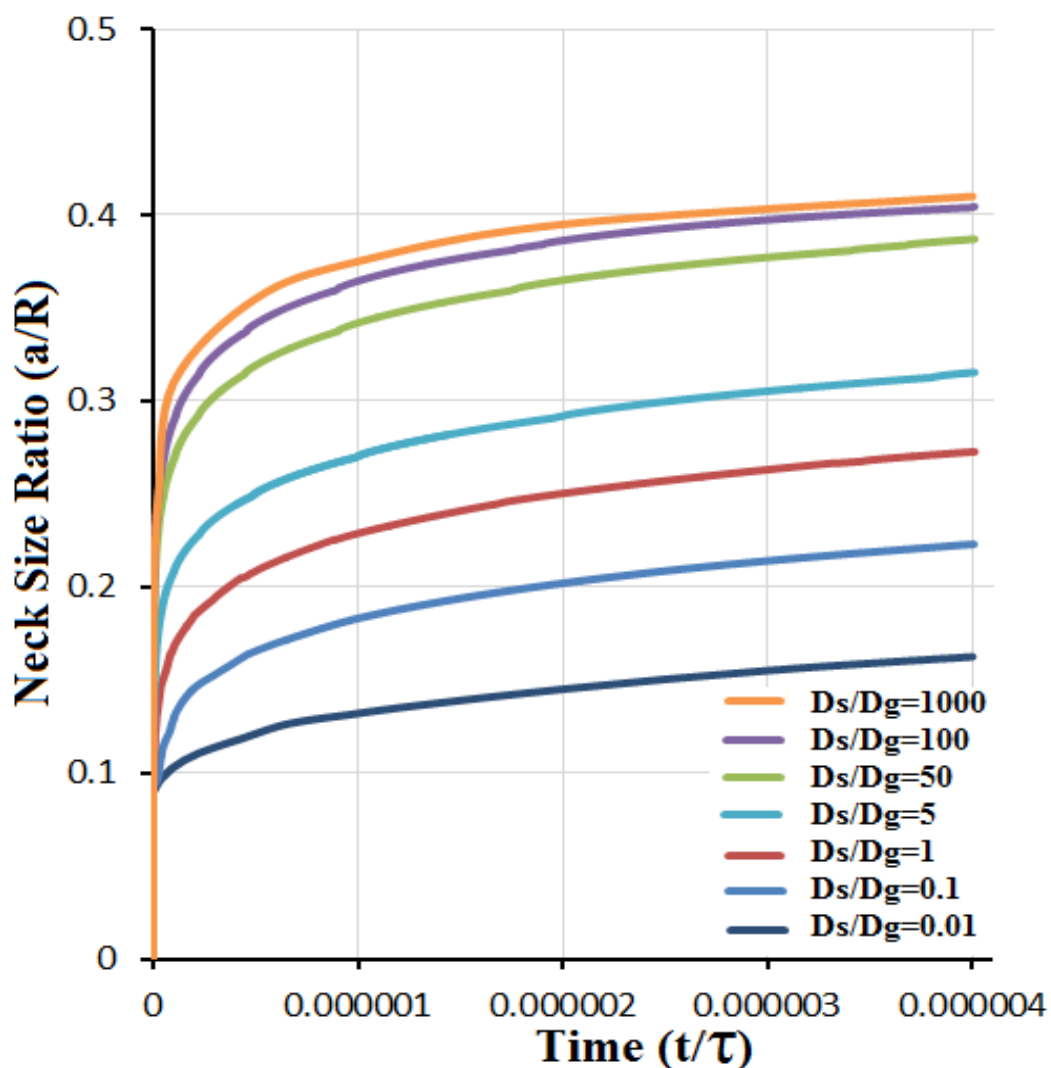
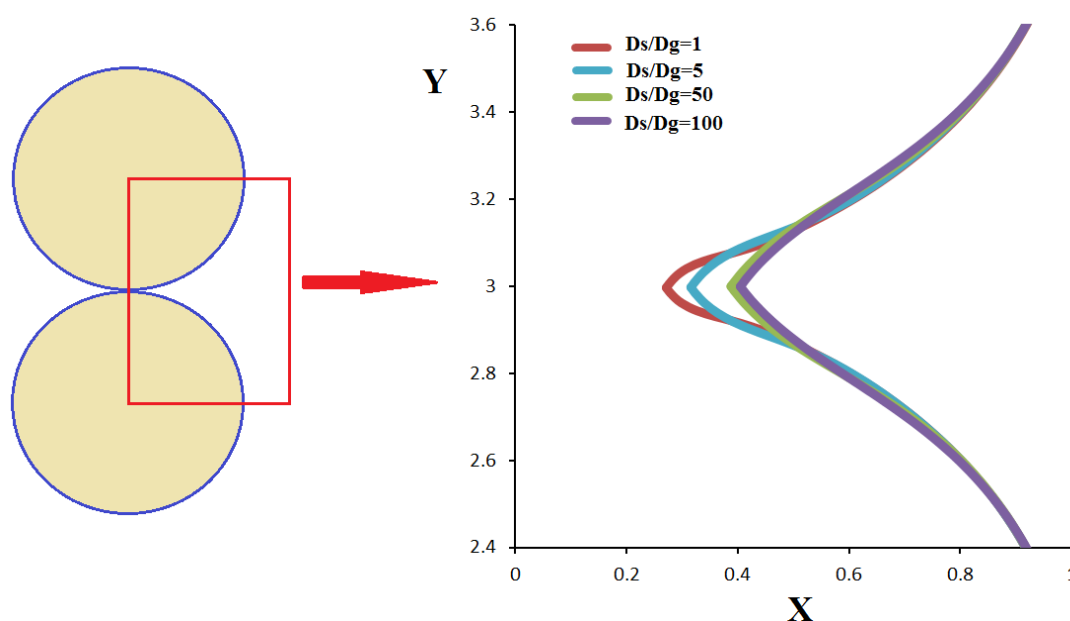


Figure 3-11 Neck size ratio as a function of sintering time for different diffusion coefficient ratios.

Figure (3-12) displays the effects of the diffusion coefficient ratio on the triple junction between particles for a total sintering time  $t/\tau = 4 \times 10^{-6}$ . Four different diffusion coefficient ratios,  $D_s/D_g = 1, 5, 50,$  and  $100$ , were used in this study to investigate the effect of diffusion coefficient ratio on the triple junction between particles. Generally, the geometry of the junction between the particles is changed during the sintering process. It can be seen that the neck between the particles grows outwards, which

means that the neck radius increases due to the increase in diffusion coefficient ratio. This is because an increased rate of neck growth ratio depends on the grain boundary velocity, and increases with increasing grain boundary velocity. In addition, the tip of the neck between the particles at  $D_s/D_g = 100$  matches the tip of the neck at  $D_s/D_g = 50$ , which means that the effect of diffusion coefficient ratio on the triple junction between particles is essentially insignificant when  $D_s/D_g > 50$ .



**Figure 3-12 Particle geometry change during the sintering process for different diffusion coefficient ratios.**

Figure (3-13) displays the effects of sintering time on the triple junction between the particles for a diffusion coefficient ratio of  $D_s/D_g = 1$ . Three different sintering times,  $t/\tau = 4 \times 10^{-6}$ ,  $2 \times 10^{-4}$ , and  $3.58 \times 10^{-3}$ , were used to investigate these effects. Generally, the geometry of the junction changes shape during the sintering process. Overall, it can be seen from this figure that the neck between particles grows outwards, which means that the neck radius increases with increasing sintering time for a given diffusion coefficient ratio. This is because the neck growth rate and the densification

rate increase with increasing sintering time. In addition, the neck on tip between particles at time  $t/\tau = 3.58 \times 10^{-3}$  moved outward and down to another position, which means that the neck growth and shrinkage between particles improves during this [dimensionless] time.

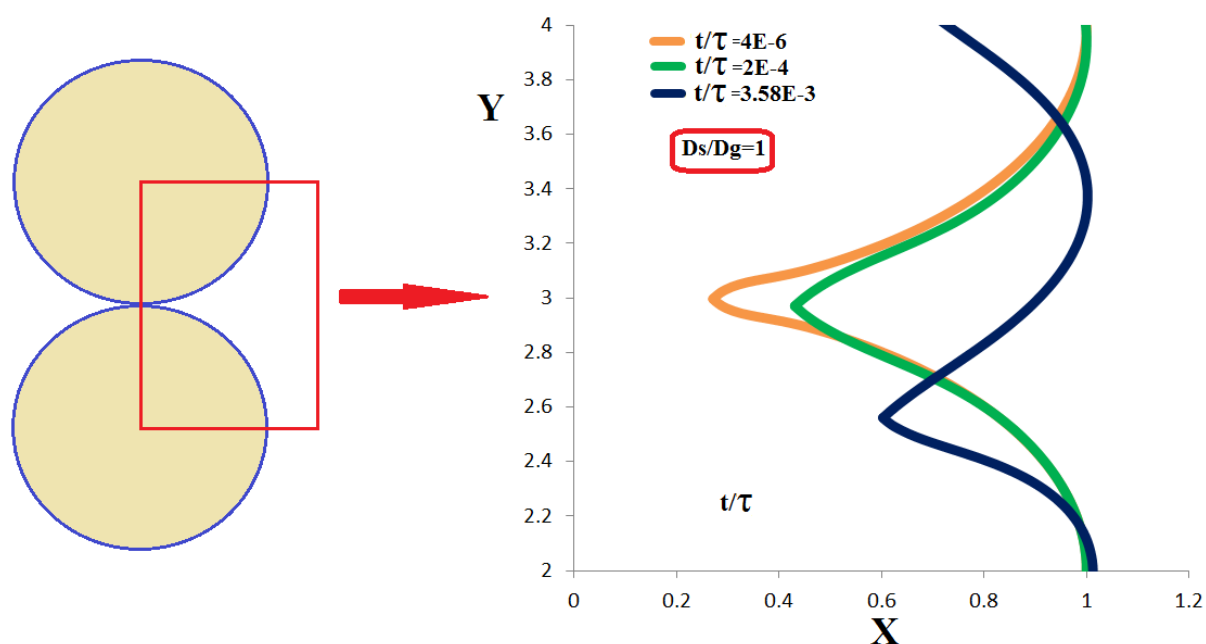


**Figure 3-13 Particle geometry change during the sintering process for different sintering times.**

### 3.4.2 The influence of the diffusion coefficient ratio as compared between two methods

The six graphs in figure (3-14) show comparisons of the shrinkage ratio between curve-fitting FD and full FD results for different diffusion coefficient ratios. Six different diffusion coefficient ratios,  $D_s/D_g = 0.01, 0.1, 1, 5, 50,$  and  $100$ , were used in this study to simulate the influence of diffusion coefficient ratios on shrinkage ratio, as per the comparison between the curve-fitting FD and full FD curves. Overall, it can be seen

that the curves for  $D_S/D_g = 100, 50$  and  $5$  are in good agreement for the two methods, while the curves for  $D_S/D_g = 0.01, 0.1$  and  $1$  show notable differences.

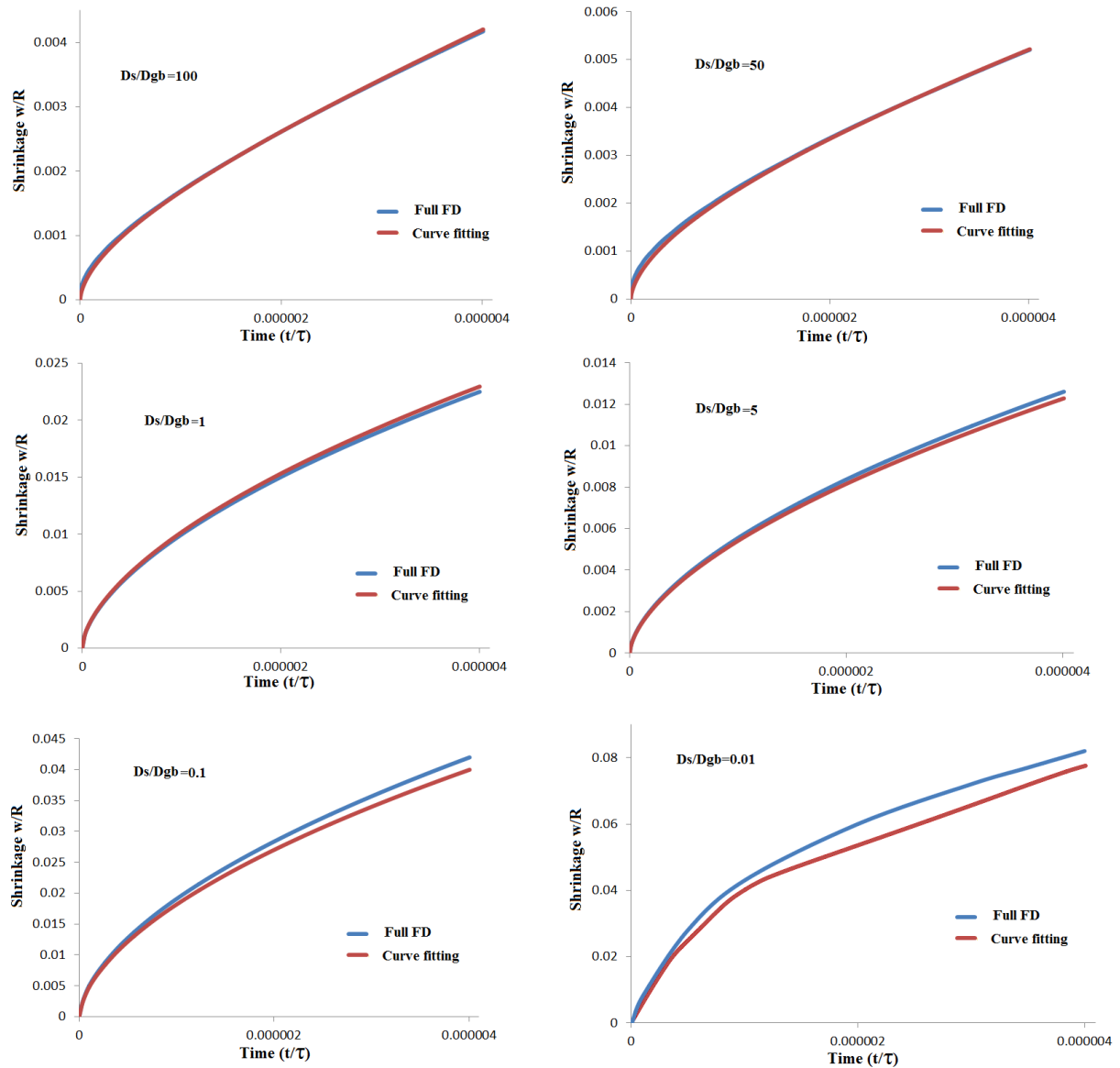


**Figure 3-14 Comparisons of the shrinkage ratio between curve-fitting FD and full FD results.**

A comparison of the neck size ratio between the curve-fitting FD and full FD results for different diffusion coefficient ratios are shown in figure (3-15). Six different diffusion coefficient ratios,  $D_S/D_g = 0.01, 0.1, 1, 5, 50, \text{ and } 100$ , were used to simulate the influence of diffusion coefficient ratios on neck size ratio as per the comparison between the curve-fitting FD and full FD curves. Overall, it can be seen that the curves for  $D_S/D_g = 100, 50, 5, \text{ and } 1$  are in good agreement for the two methods, while the curves fitting FD for  $D_S/D_g = 0.1 \text{ and } 0.01$  show slight differences with the full FD curves.

The twelve graphs in table (3-1) give a comparison of the evolution of two particles' geometries between curve-fitting FD and full FD results for three diffusion coefficient ratios of  $D_S/D_g = 1, 100, \text{ and } 1000$ . Four different neck size ratios were used in this table to study the impact of diffusion coefficient ratios on particles' geometries during the sintering process. Overall, it can be seen that the particles' geometries change due to increasing neck size ratio, which is shown in the junction between the particles in the figure. Furthermore, the curve-fitting FD curves match the full FD curves. In addition, the curvatures of the particles are the same for all diffusion coefficient ratios ( $D_S/D_g = 1, 100, \text{ and } 1000$ ) for each neck size ratio, whereas the curvatures between particles are changed due to the increase in neck size ratio.

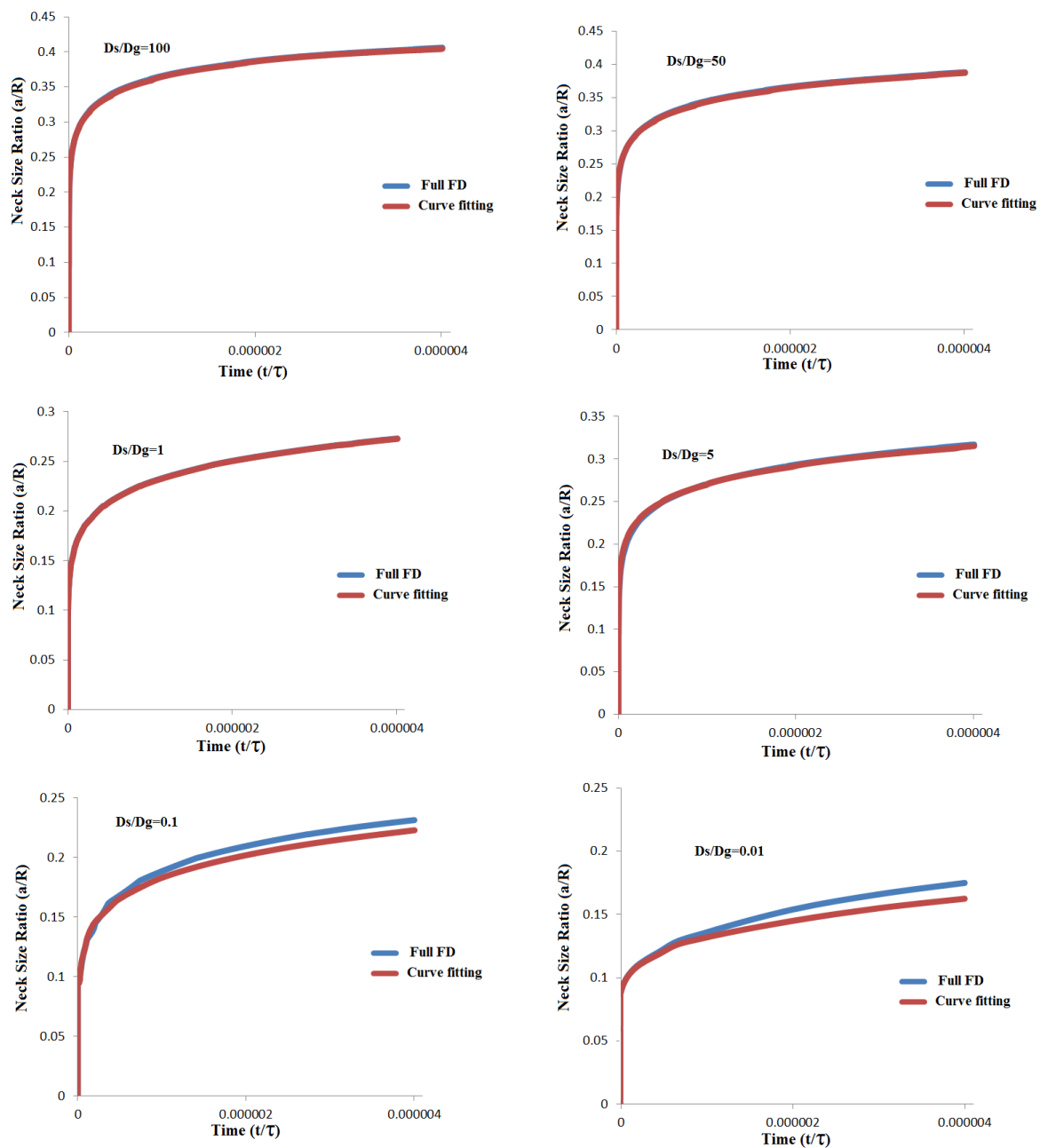
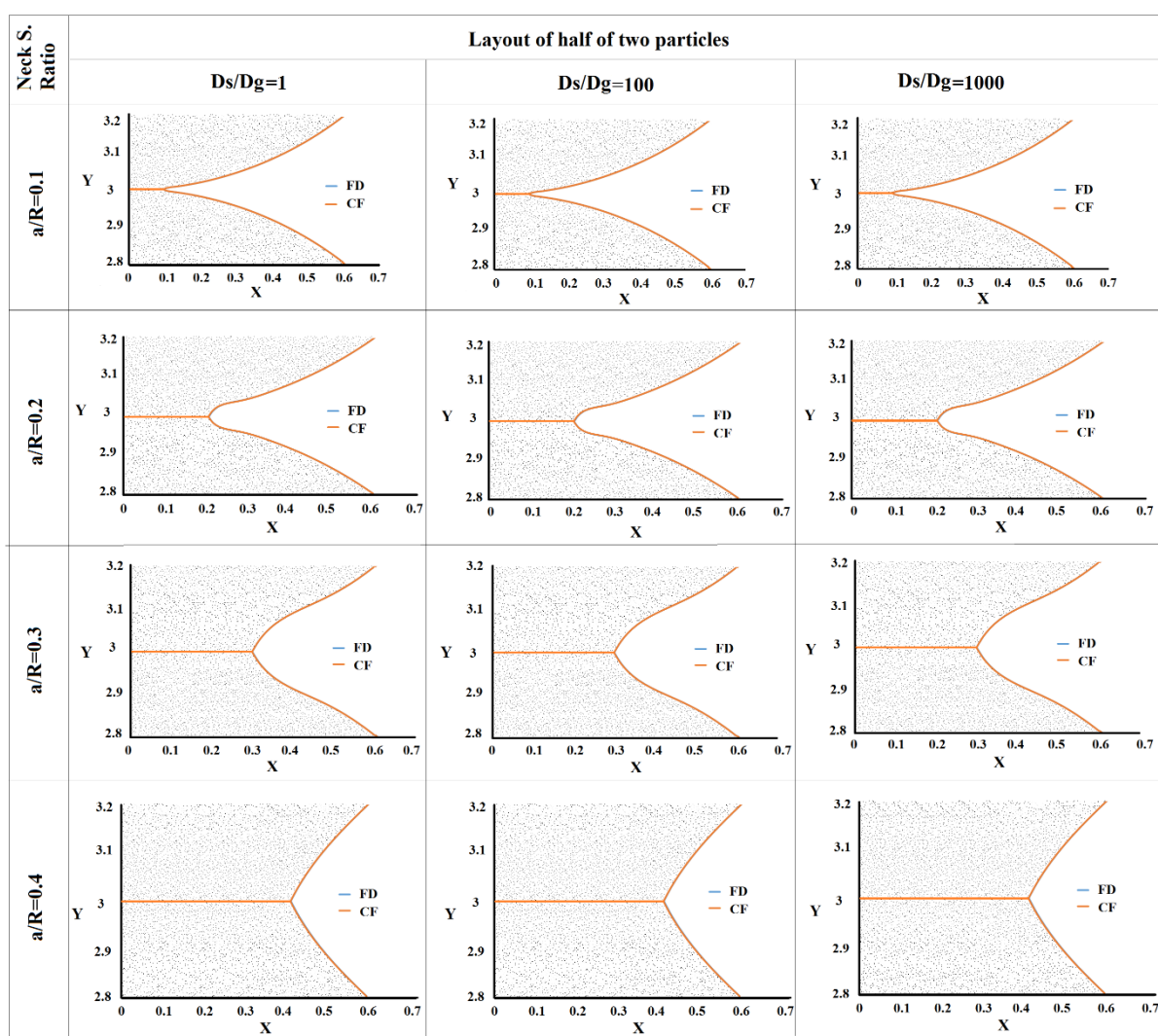


**Figure 3-15 Comparisons of the neck size ratio for curve-fitting FD and full FD results.**

The eight graphs in table (3-2) show a comparison of the particles geometry between curve-fitting FD and full FD results for two diffusion coefficient ratios of  $D_S/D_g = 0.1$ , and 1. Four different neck size ratios were used in this table to study the effect of

diffusion coefficient ratios on the neck growth process. Overall, it can be seen from this table that the densification between particles of diffusion coefficient ratio  $D_S/D_g=0.1$  was greater than for the particles of diffusion coefficient ratio  $D_S/D_g=1$ , especially when neck size ratio is larger than  $a/R=0.1$ . In addition, the curve-fitting FD curves were a good match to the full FD curves for each diffusion coefficient ratio.

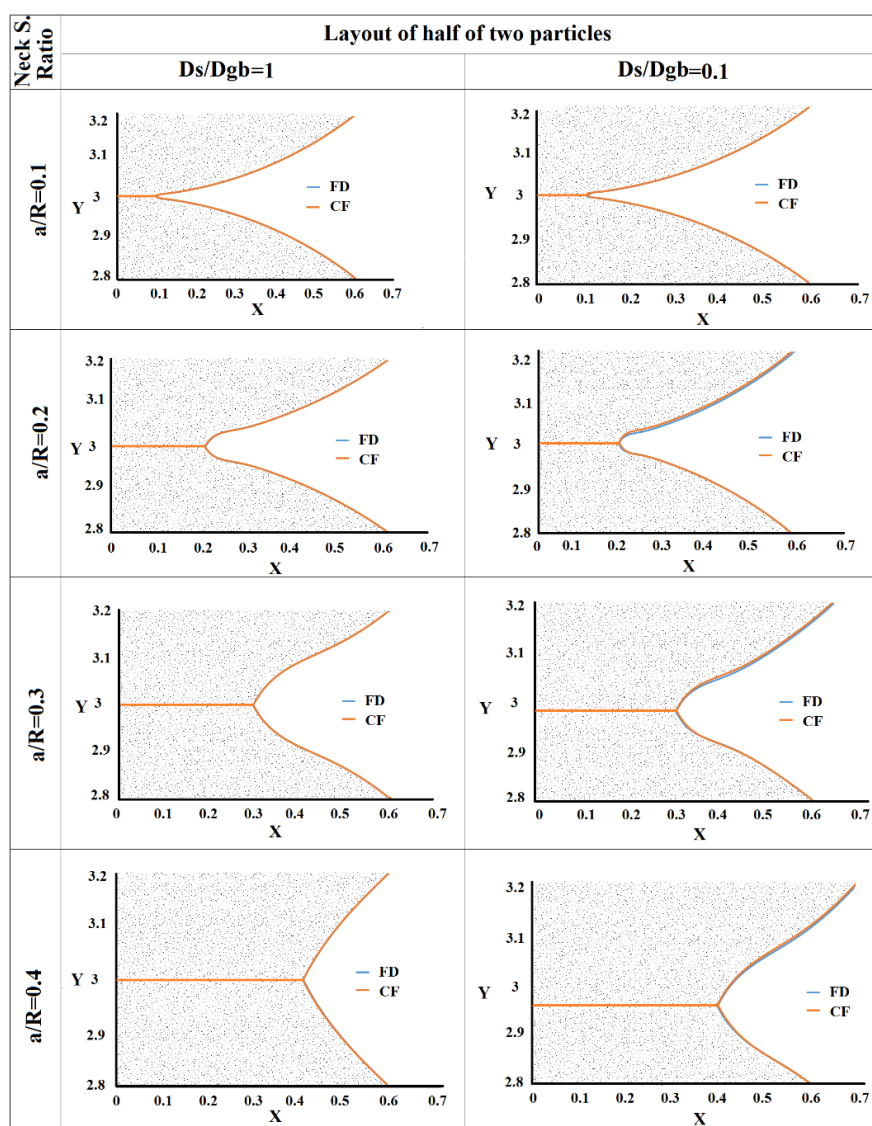
**Table 3.1 Comparison of the particle's geometry for four neck size ratios.**



### 3.4.3 The influence of applied stress as compared between two methods:

Shrinkage and neck size ratio were used to study the effect of applied stress in the comparison between the curve-fitting FD and full FD models, and thus the shrinkage ratio is the first factor to show, from comparison, that curve fitting is appropriate for use in simulating the sintering process.

**Table 3.2 Comparison of the particles' geometry for different diffusion coefficient ratios.**



The six graphs in a figure (3-16) show the comparisons of the shrinkage ratio between curve-fitting FD and full FD results for different diffusion coefficient ratios at an applied stress of 25 MPa. Six different diffusion coefficient ratios,  $D_S/D_g = 0.01, 0.1, 1, 5, 50,$  and 100, were used in this study to investigate the influence of applied stress (at a fixed 25 MPa) in the comparison between the curve fitting FD and full FD curves for different diffusion coefficient ratios. Overall, it can be seen that the curves for  $D_S/D_g = 100, 50$  and 5 for the curve-fitting FD matched well with the full FD curves, while the curves for  $D_S/D_g = 0.01, 0.1$  and 1 for the curve-fitting FD are the same, though they show some slight differences with the full FD curves.

The six graphs in a figure (3-17) compare the shrinkage ratio between curve-fitting FD and full FD results for different diffusion coefficient ratios at an applied stress of 50 MPa. Six different diffusion coefficient ratios,  $D_S/D_g = 0.01, 0.1, 1, 5, 50,$  and 100, were used to investigate the influence of applied stress (fixed at 50 MPa) to compare the curve-fitting FD and full FD curves for different diffusion coefficient ratios. Overall, it can be seen that the curves for  $D_S/D_g = 100, 50, 5$  and 1 for the curve-fitting FD are in good agreement with the full FD curves, while the curves for  $D_S/D_g = 0.01$  and 0.1 for curve-fitting FD are the same, though they show some slight differences with the full FD curves.

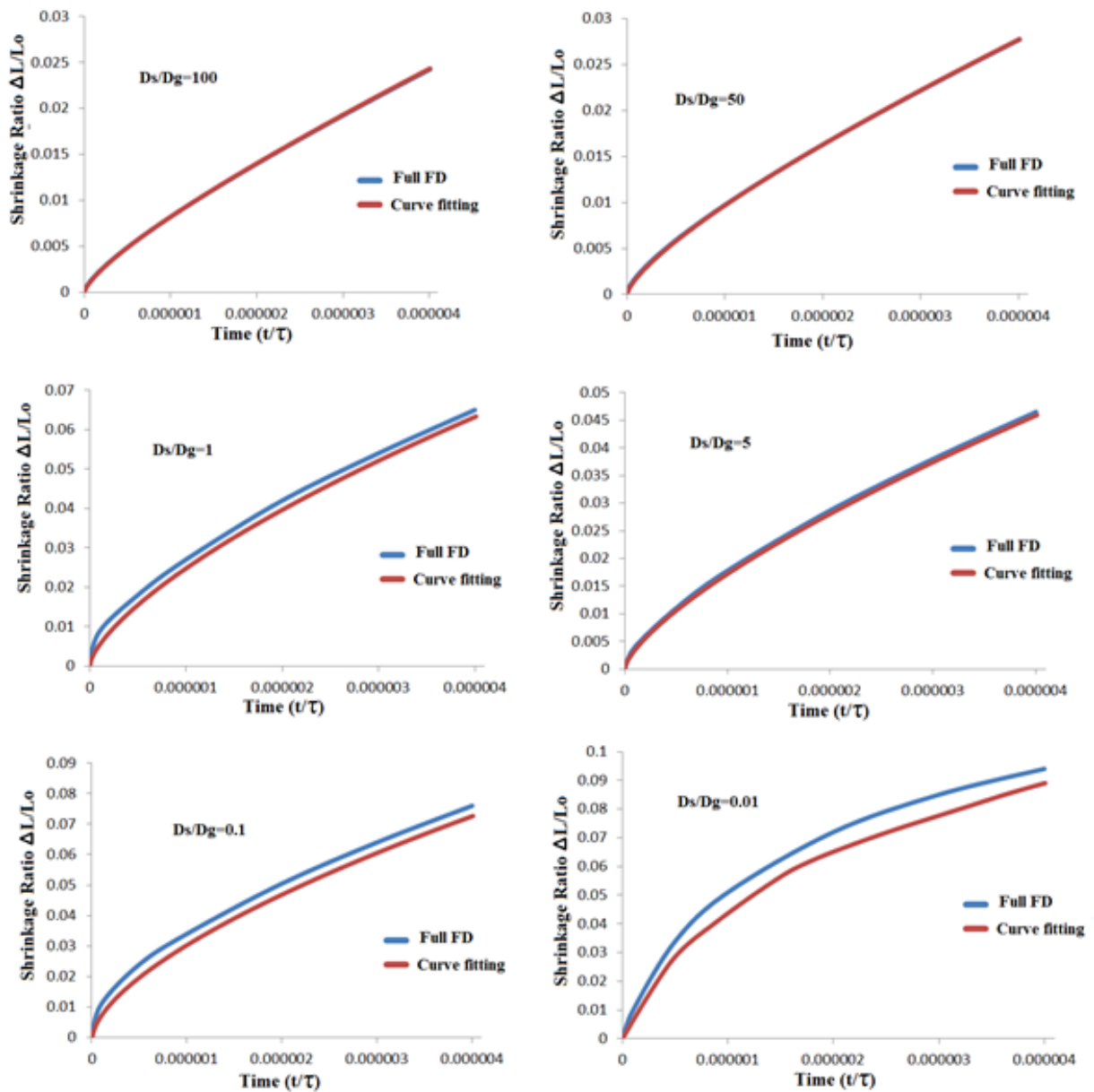


Figure 3-16 Comparisons of the shrinkage ratio between curve-fitting FD and full FD at 25 MPa.

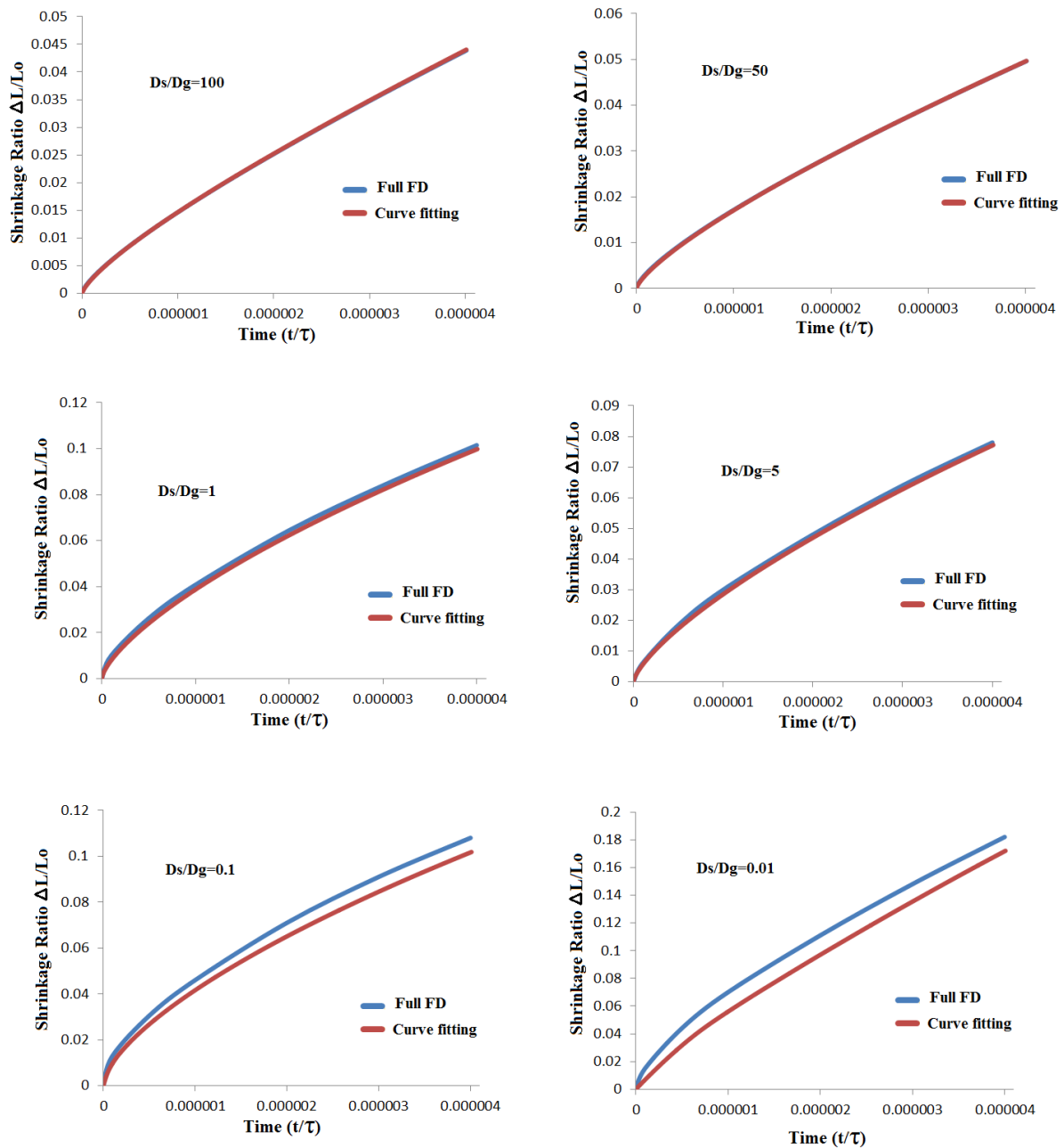


Figure 3-17 Comparisons of the shrinkage ratio between curve-fitting FD and full FD at 50 MPa.

The six graphs in figure (3-18) compare shrinkage ratios for curve-fitting FD and full FD results for different diffusion coefficient ratios at an applied stress of 75 MPa. Six

different diffusion coefficient ratios,  $D_S/D_g = 0.01, 0.1, 1, 5, 50,$  and  $100,$  were used to investigate the influence of an applied stress of  $75 \text{ MPa}$  in the comparison between curve-fitting FD and full FD curves for different diffusion coefficient ratios. It can be seen that the curves for  $D_S/D_g = 100, 50, 5$  and  $1$  for curve-fitting FD and full FD curves match up well against each other, whereas the curves for  $D_S/D_g = 0.01$  and  $0.1$  for the curve-fitting FD and full FD curves differ slightly but have a similar difference between them. As can be observed in figure (3-18), when increasing the surface diffusion coefficient the two curves continue to converge which results in them perfectly matching at higher surface diffusion coefficients.

The six graphs in figure (3-19) compare the shrinkage ratios for curve-fitting FD and full FD results for different diffusion coefficient ratios at an applied stress of  $100 \text{ MPa}$ . Six different diffusion coefficient ratios,  $D_S/D_g = 0.01, 0.1, 1, 5, 50,$  and  $100$  were used to investigate the influence of applied stress of  $100 \text{ MPa}$  on the comparison between curve-fitting FD and full FD curves for different diffusion coefficient ratios. It can be seen that the curves for  $D_S/D_g = 100, 50, 5$  and  $1$  for curve-fitting FD and full FD curves match up well against each other, whereas the curves for  $D_S/D_g = 0.01$  and  $0.1$  for the curve-fitting FD and full FD curves differ slightly but have a similar difference between them. All of the curves in figure (3-19) are higher than the curves in figure (3-18). This is because the applied stress is  $25 \text{ MPa}$  more than in the previous figure.

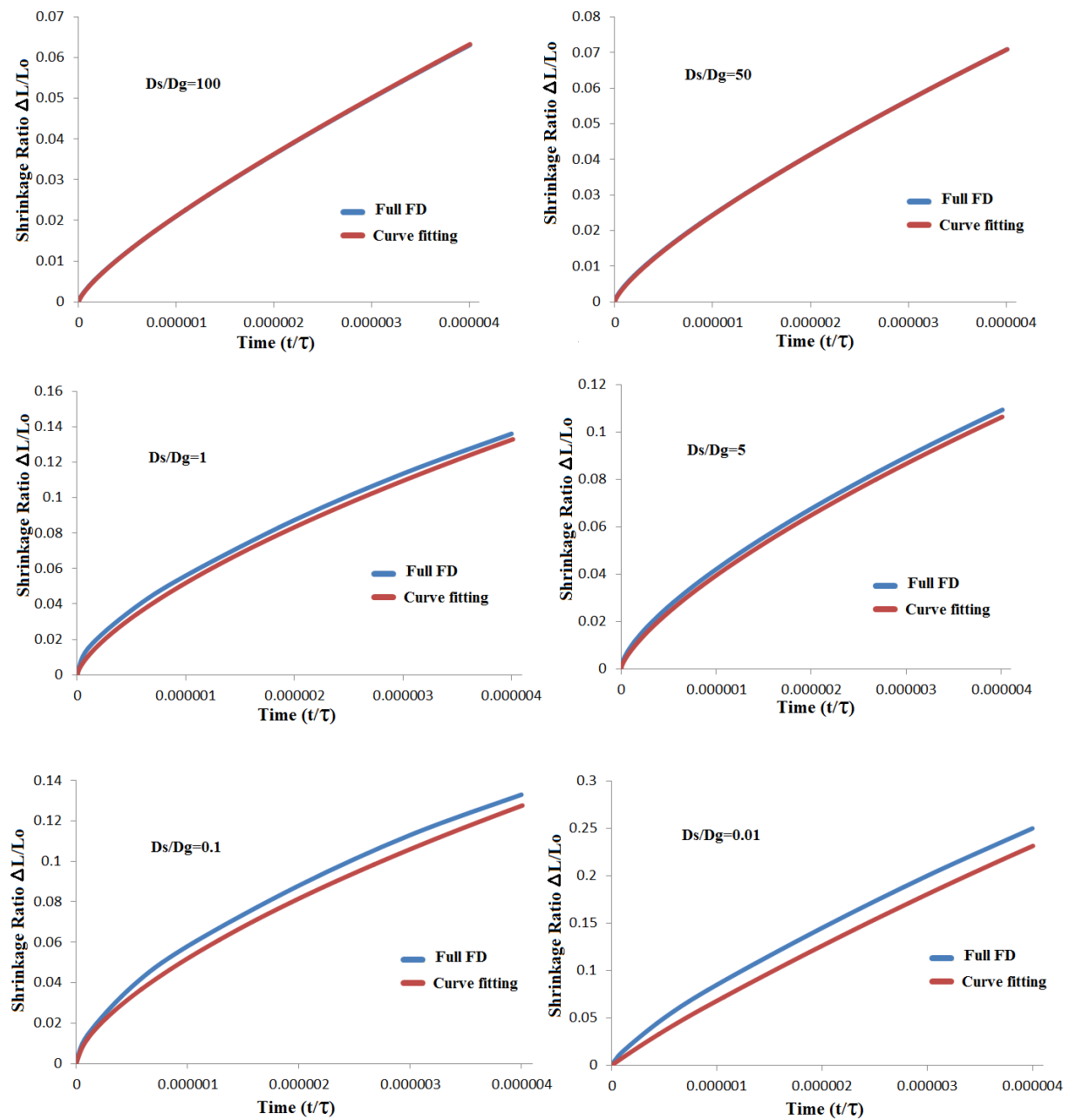
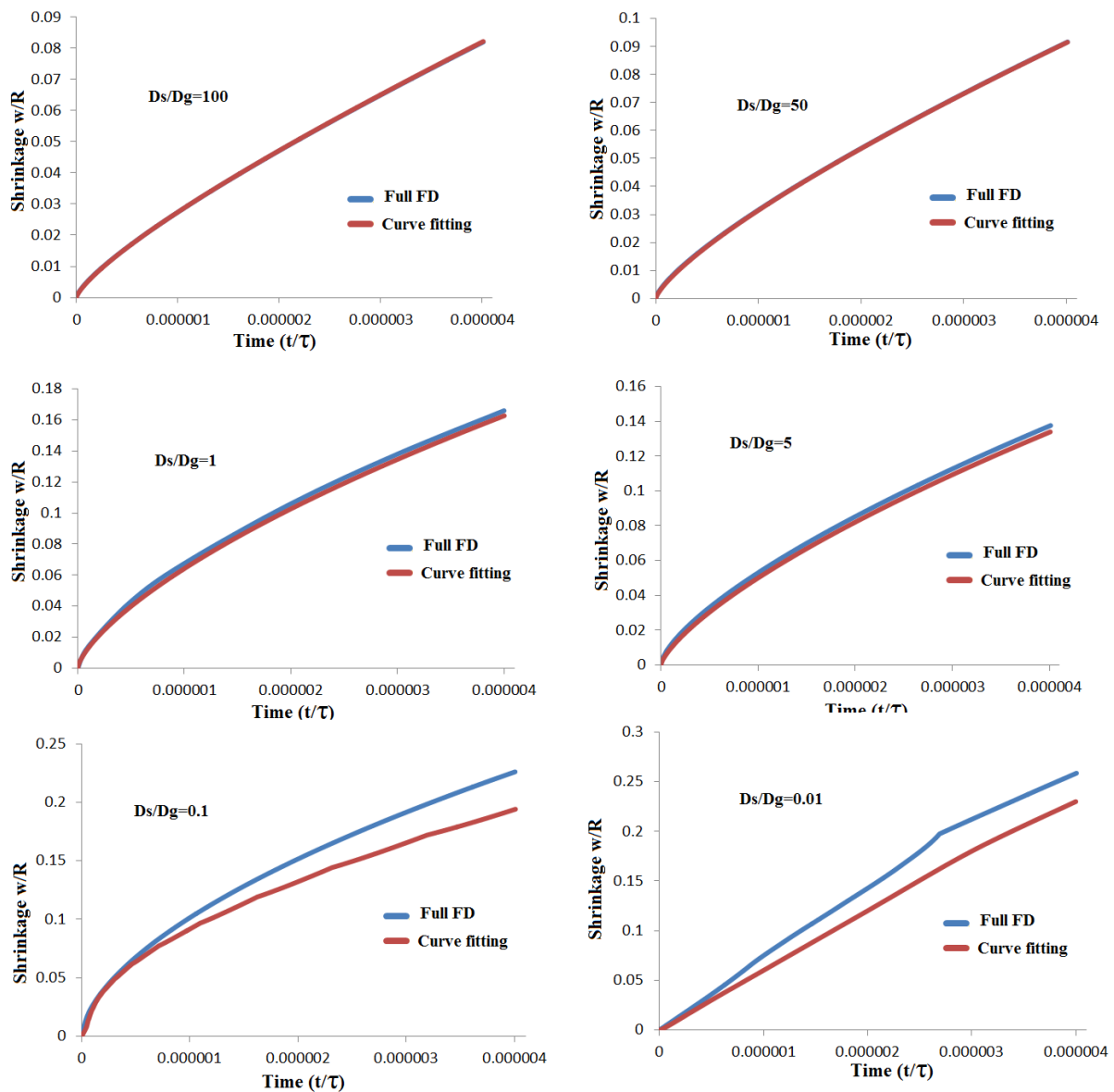


Figure 3-18 Comparisons of the shrinkage ratio for curve-fitting FD and full FD results at 75 MPa.



**Figure 3-19 Comparison of the shrinkage ratio for curve-fitting FD and full FD results at 100 MPa.**

The six graphs in a figure (3-20) compare neck size ratios between curve-fitting FD and full FD results for different diffusion coefficient ratios at an applied stress of 25 MPa. Six different diffusion coefficient ratios,  $D_s/D_g = 0.01, 0.1, 1, 5, 50,$  and  $100$  were used to investigate the influence of applied stress at a fixed value of 25 MPa, in the

comparison between the curve-fitting FD and full FD curves. It can be seen that the curves for  $D_S/D_g = 100, 50, 5$  and  $1$  for curve-fitting FD and full FD curves match up well against each other, whereas the curves for  $D_S/D_g = 0.01$  and  $0.1$  for the curve-fitting FD and full FD curves differ notably but have a similar difference between them. The six graphs in figure (3-21) compare the neck size ratios between curve-fitting FD and full FD results for different diffusion coefficient ratios at an applied stress of 50 MPa. Six different diffusion coefficient ratios,  $D_S/D_g = 0.01, 0.1, 1, 5, 50,$  and  $100$ , were used to investigate the influence of an applied stress of 50 MPa in the comparison between curve-fitting FD and full FD curves for different diffusion coefficient ratios. It can be seen that the curves for  $D_S/D_g = 100, 50, 5$  and  $1$  for curve-fitting FD and full FD curves match up well against each other, whereas the curves for  $D_S/D_g = 0.01$  and  $0.1$  for the curve-fitting FD and full FD curves differ slightly but have a similar difference between them.

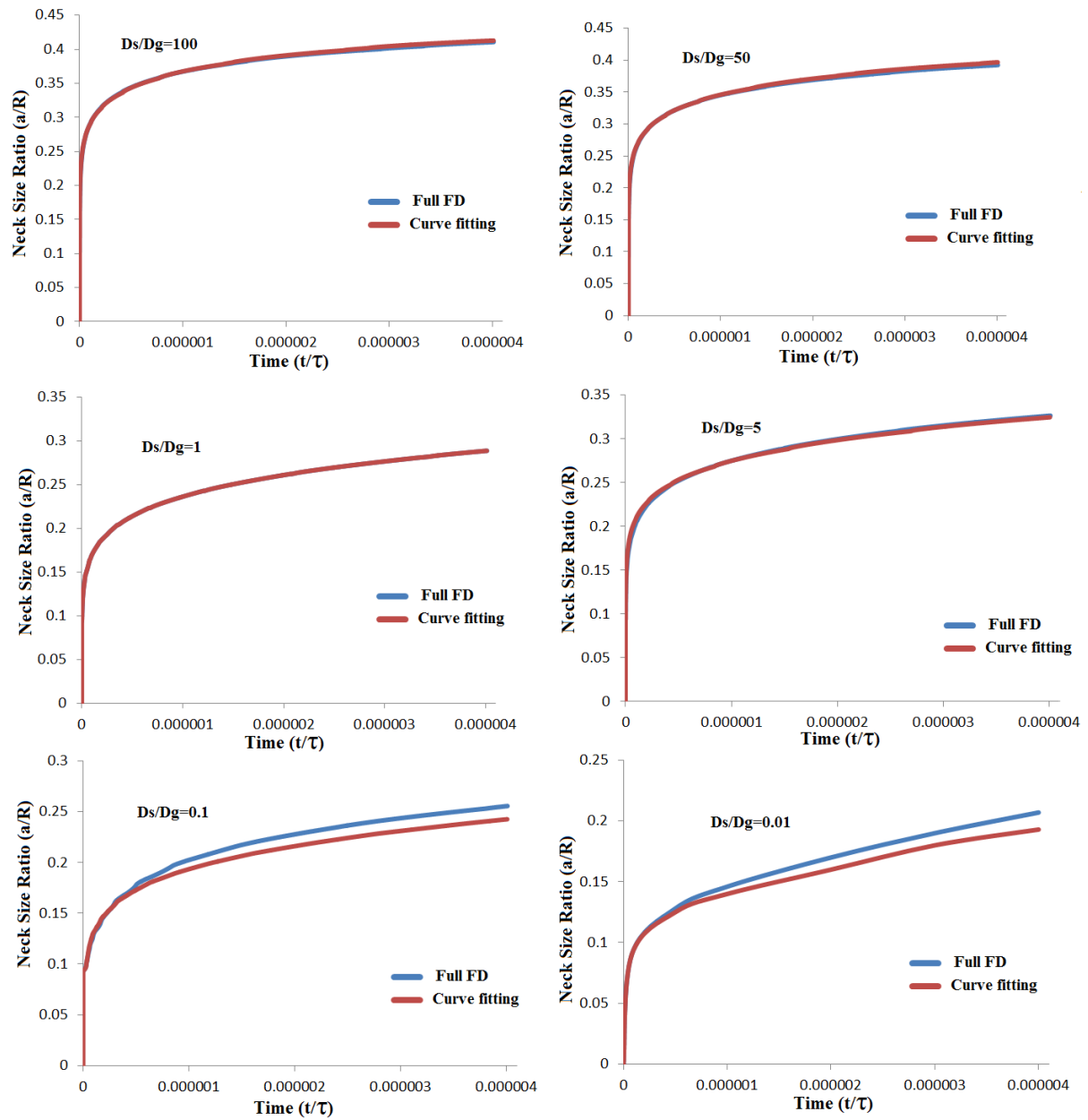
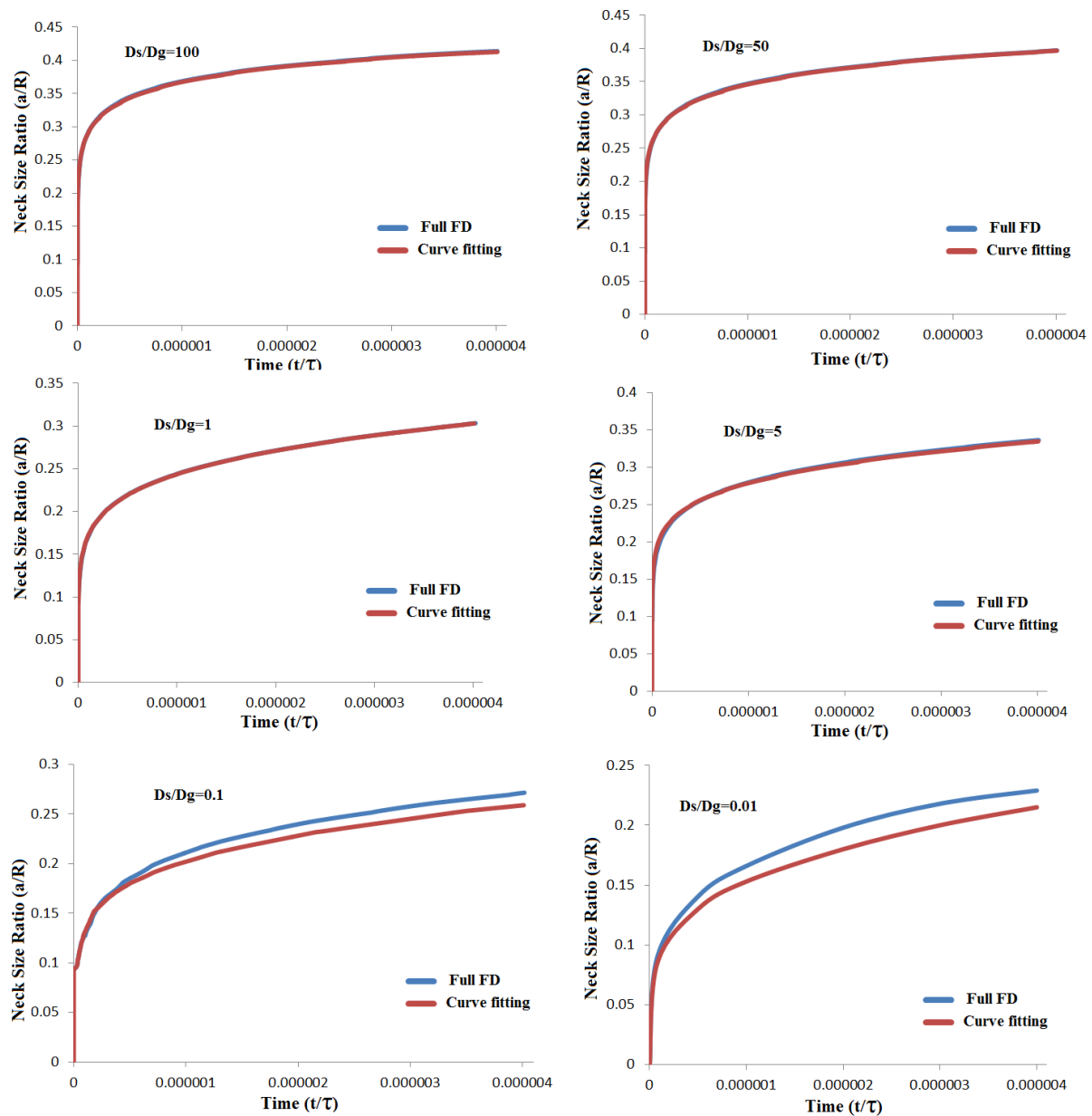


Figure 3-20 Comparison of the neck size ratio for curve-fitting FD and full FD results at 25 MPa.



**Figure 3-21 Comparison of the neck size ratio between curve-fitting FD and full FD results at 50 MPa.**

The six graphs in a figure (3-22) compare the neck size ratios between curve-fitting FD and full FD results for different diffusion coefficient ratios at an applied stress of 75 MPa. Six different diffusion coefficient ratios,  $D_s/D_g = 0.01, 0.1, 1, 5, 50,$  and  $100$  were

used to investigate the influence of an applied stress of 75 MPa in the comparison between curve-fitting FD and full FD curves for different diffusion coefficient ratios. It can be seen that the curves for  $D_s/D_g = 100, 50, 1, \text{ and } 5$  for curve-fitting FD are in good agreement with the full FD curves while the curves for  $D_s/D_g = 0.01$  and  $0.1$  for curve-fitting FD are the same, with only small differences between them. As can be observed in figure (3-22), when increasing the surface diffusion coefficient the two curves continue to converge which results in them matching perfectly at higher surface diffusion coefficients.

The six graphs in a figure (3-23) compare the neck size ratios between curve-fitting FD and full FD results for different diffusion coefficient ratios at an applied stress of 100 MPa. Six different diffusion coefficient ratios,  $D_s/D_g = 0.01, 0.1, 1, 5, 50, \text{ and } 100$ , were used in this study to investigate the influence of applied stress of 100 MPa in the comparison between curve-fitting FD and full FD curves for different diffusion coefficient ratios. It can be seen that the curves for  $D_s/D_g = 100, 50, 5 \text{ and } 1$  for curve-fitting FD match well with the full FD curves, while the curves for  $D_s/D_g = 0.01$  and  $0.1$  for curve-fitting FD don't match well but are seen to have the same difference between them. All of the curves in figure (3-23) are higher than the curves in figure (3-22). This is because the applied stress is 25 MPa more than in the previous figure.

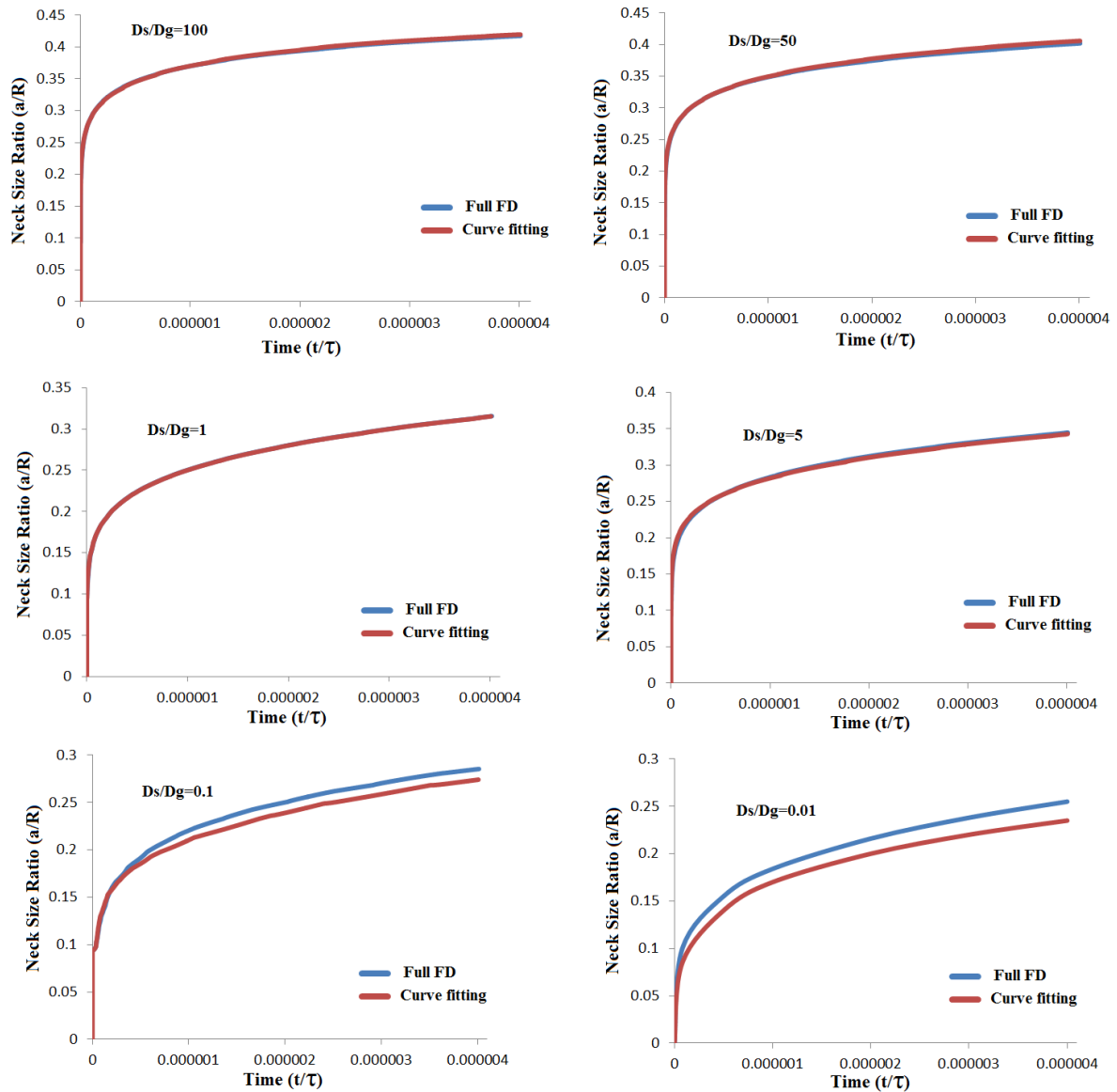
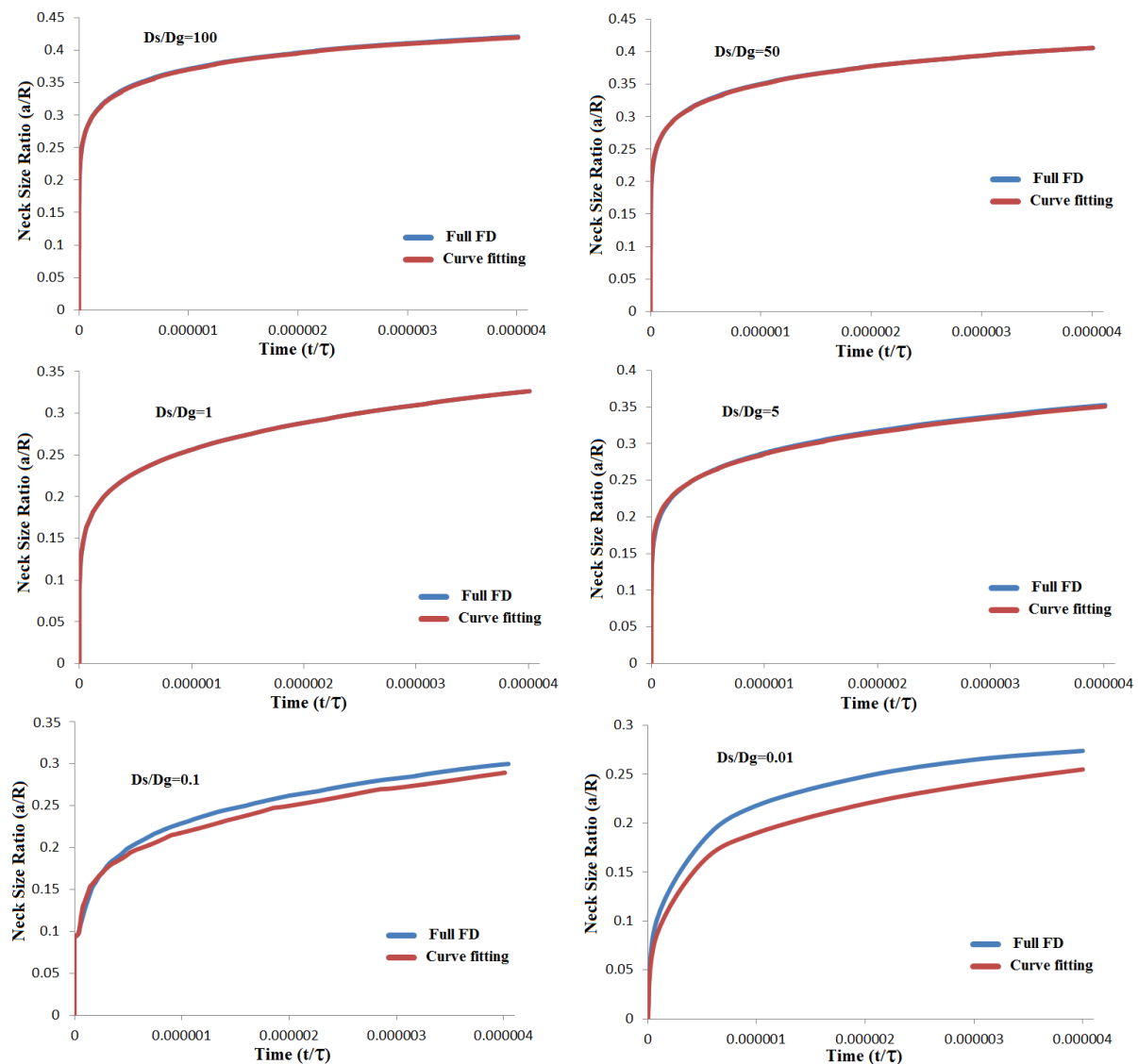


Figure 3-22 Comparison of the neck size ratio between curve-fitting FD and full FD results at 75 MPa.



**Figure 3-23 Comparison of the neck size ratio between curve-fitting FD and full FD results at 100 MPa.**

The surface area reduction is defined as the reduction in surface area,  $\Delta S/S_0$ , which is the change in the initial surface area to the final sintered surface area, given as  $\Delta S$ , where the original surface area is  $S_0$ . Equation (3-19) was used in the numerical model program to determine the surface area reduction, whilst a particle coordination number,  $N_c$ , of 2 was used as input in the computer program [107].

$$\frac{\Delta S}{S_0} = \frac{N_C}{4} \left(\frac{a}{R}\right)^2 \quad (3 - 19)$$

Figure (3-24) gives a comparison of the surface area reduction determined by curve-fitting FD and full FD for a diffusion coefficient ratio  $D_S/D_g = 1$ . Overall, it can be seen that the curve for the curve-fitting FD is a good match with the full FD curve; furthermore, the surface area reduction for the two methods increases with increasing sintering time, which is due to neck growth between particles. Also, the maximum surface area reduction is 0.0365 at a sintering time of  $4 \times 10^{-6}$ , while the minimum surface area reduction is 0.005 at a sintering time of  $1 \times 10^{-7}$ .

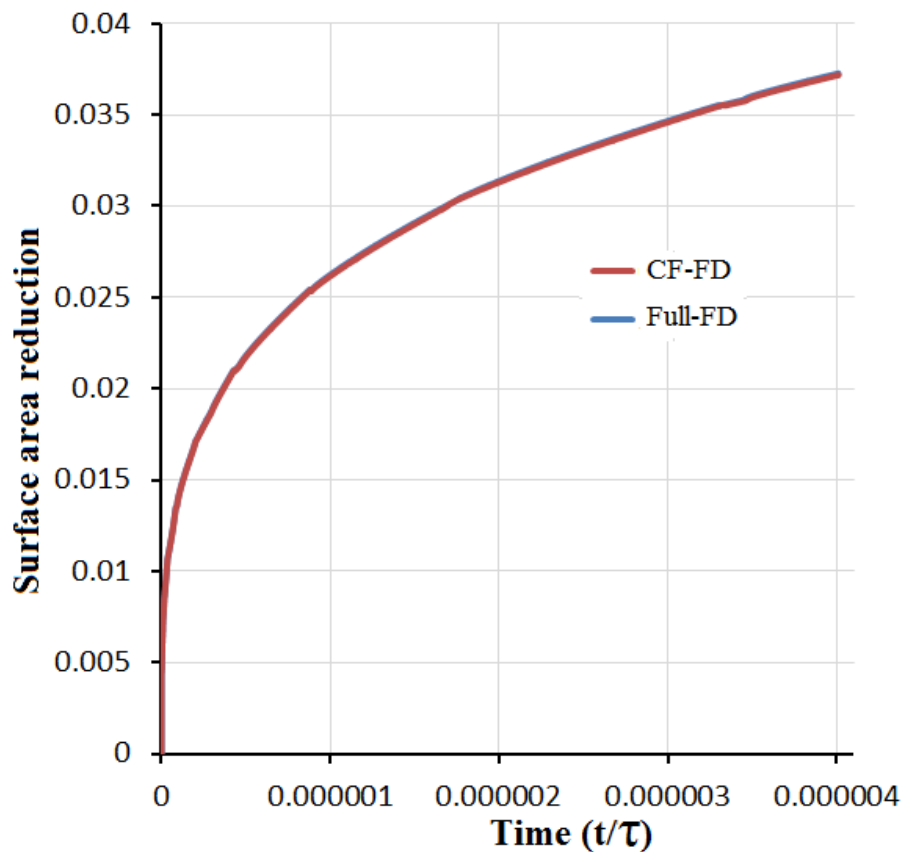


**Figure 3-24 Comparisons of the surface area reduction between curve fitting FD and full FD results at  $D_S/D_g = 1$ .**

Figure (3-25) shows a shrinkage ratio rate as a function of tip curvature,  $K_{tip}$ , for a diffusion coefficient of  $D_s/D_g = 1$  and a total sintering time  $t/\tau = 4 \times 10^{-6}$  using different applied stresses. Four different applied stresses,  $\sigma_s = 25, 50, 75,$  and  $100$  MPa, were used to investigate the effects of applied stress on the tip curvature,  $K_{tip}$ . Overall, it can be observed from the comparison that the shrinkage rate increases with increasing applied stress. This is because the grain boundary velocity increases due to the increase in the applied stress. In addition, the shrinkage rate increases with increasing tip curvature,  $K_{tip}$ , because  $K_{tip}$  depends on neck size ratio, and thus increases with decreasing neck size ratio; this in turn means that  $K_{tip}$  is larger at the beginning of the sintering stage but will decrease thereafter. In addition, all curves diverged at the beginning of the sintering process, but converged towards its final stages. Also, the maximum shrinkage rate at the first stage of the sintering process was 519206.8 at an applied stress of  $\sigma_s = 100$  MPa, while the minimum shrinkage rate was 221842.5 at an applied stress of  $\sigma_s = 25$  MPa.

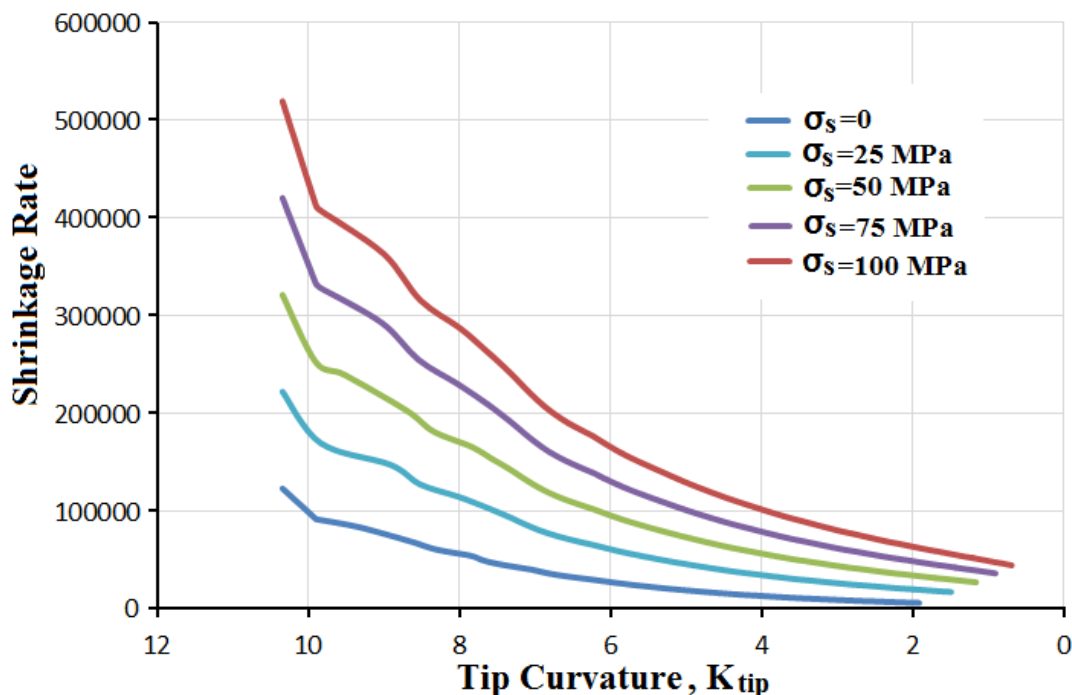
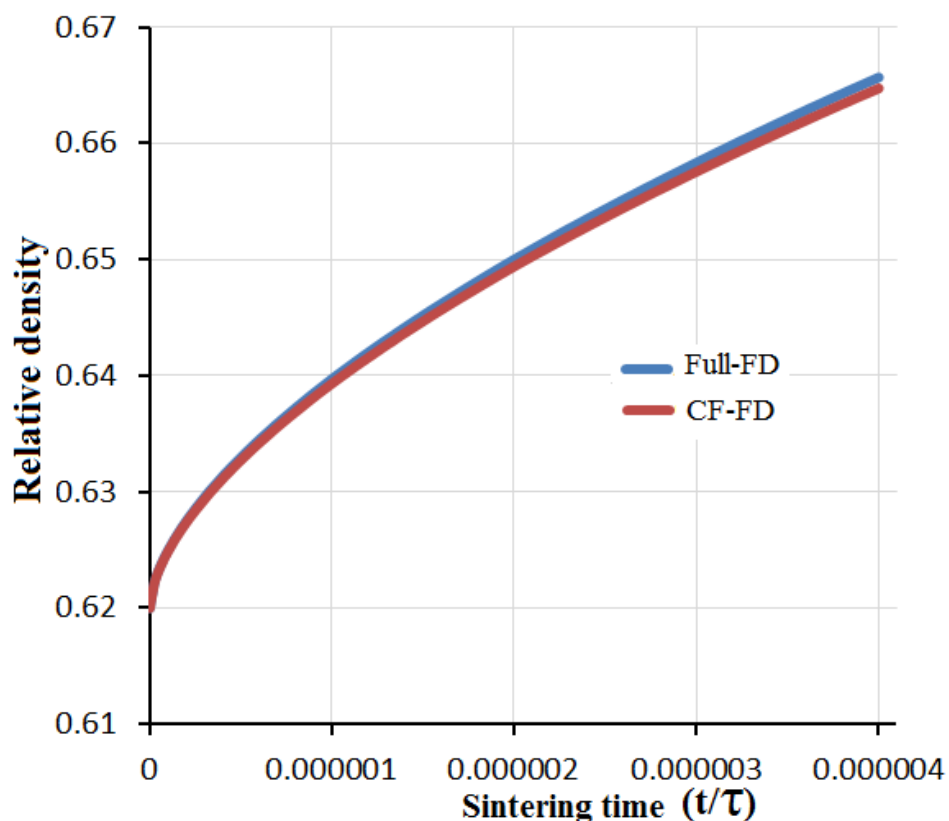


Figure 3-25 Shrinkage ratio rate as a function of tip curvature for different applied stresses.

Equation (3-20) was used in a numerical modelling program to determine the relative density of two particles, which depends on shrinkage ratio [59]. Figure (3-26) illustrates a comparison of the relative density between the curve-fitting FD and full FD results for a diffusion coefficient ratio  $D_S/D_g = 1$ . Overall, it can be seen from the figure that the relative density derived from the curve fitting FD method fully matched with the relative density of full FD; moreover, the relative densities found for the two methods increases with increasing sintering time. Lastly, the maximum relative density during the last stage of the sintering process was 0.665 while the minimum relative density was 0.62, which is the initial relative density used in the simulation.

$$\rho_r = \rho_0 \frac{1}{(1 - e)^3} \quad (3 - 20)$$



**Figure 3-26 Comparison of relative density between curve-fitting FD and full FD results at  $D_S/D_g = 1$ .**

Figure (3-27) shows the curvature of the node before tip formation between particles ( $K_{n-1}$ ) as a function of diffusion coefficient ratio ( $D_S/D_g = 0.01$  to 1) using four neck size ratios of 0.1, 0.2, 0.3 and 0.4 to determine the effect of neck size ratio on the curvature ( $K_{n-1}$ ). Overall, it can be seen that the curvature ( $K_{n-1}$ ) increases with the lowest neck size ratio, especially at  $D_S/D_g = 0.01$ ; this was because the curvatures between particles were not deformed at the beginning of the process. Table (3-2) shows the change in the curvatures with different neck size ratios. In addition, the curvature ( $K_{n-1}$ ) decreases with increasing diffusion coefficient ratio ( $D_S/D_g$ ), which means that all curves vary smoothly when increasing the diffusion coefficient ratio. This is because the curvature depends on two radii ( $K_{n-1} = 1/r_1 + 1/r_2$ ), where  $r_1$  is collected from a circle passing through three nodes: node n-1, node n-2, and the junction point, while  $r_2$  is the distance between the vertical axis and node n-1; thus, the two radii increase during the sintering process because of neck growth; moreover, the curvature  $K_{n-1}$  decreases due to the increasing neck radius.

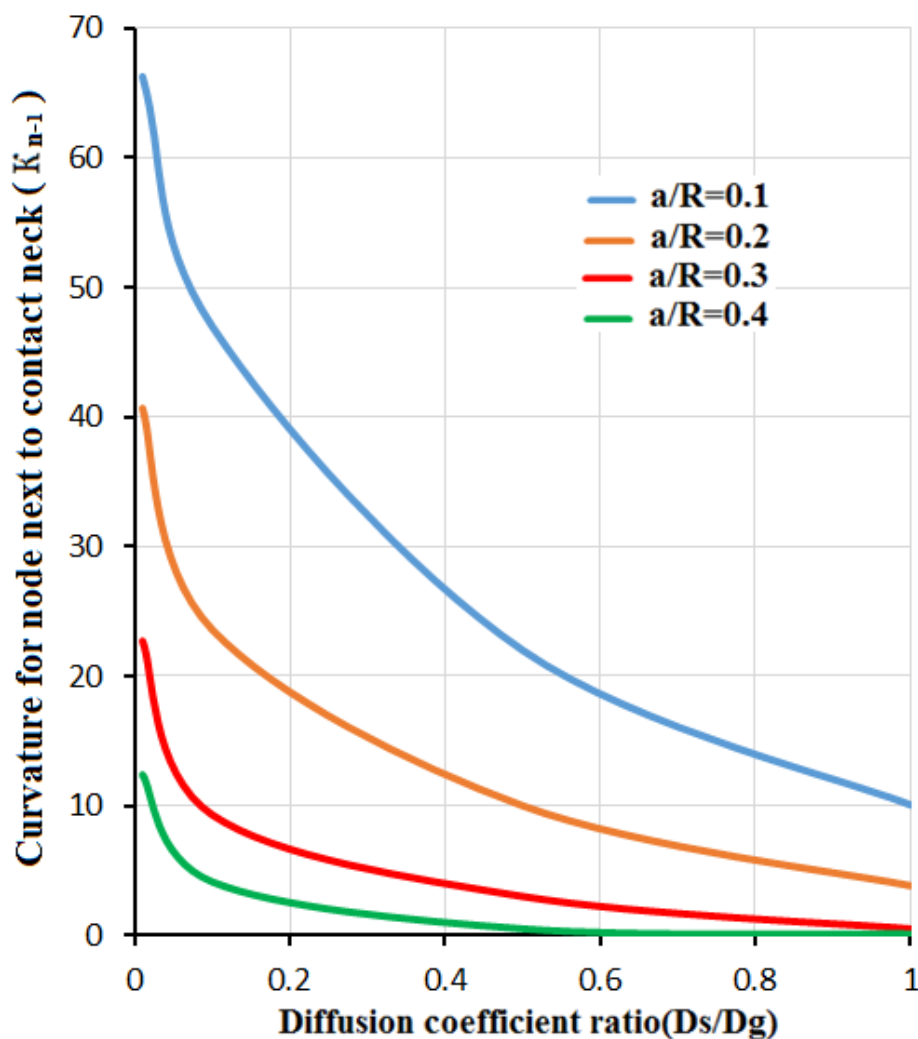


Figure 3-27 Curvature  $K_{n-1}$  as a function of diffusion coefficient ratio for different neck size ratios.

### 3.4.4 Additional results

These results were obtained from an MSc thesis under my supervision, and the MSc student in question used my curve-fitting FD model to collect sintering results. These results focus on the curvature between two particles during the sintering process, moreover, including the parameters' effects on tip curvature between particles during

sintering, namely due to surface energy, diffusion coefficient ratios, applied stresses.

#### 3.4.4.1 Factors effecting on Tip curvature between particles

Diffusion coefficient ratio and applied stress are utilized in a new finite differences method to simulate the tip curvature between particles during the sintering process. Figure (3-28) illustrates a comparison of the tip curvature,  $K_{tip}$ , for different applied stresses at a diffusion coefficient ratio of  $D_S/D_g = 1$ . Four different applied stresses,  $\sigma_s = 25, 50, 75,$  and  $100$  MPa were used to understand the effect of applied stress on the curvature between particles during the sintering process. Overall, it can be seen that  $K_{tip}$  decreases with increasing applied stress, especially in the final stage of the sintering process. However, all the above curves were convergent at the beginning of the sintering process, which is because the change in tip curvature is more flattened due to the increase of the applied stress, as shown in equation (3-18). Also, the minimum  $K_{tip}$  in the last step of the sintering process is 0.85 at an applied stress of  $\sigma_s = 100$  MPa, while the maximum  $K_{tip}$  is 1.7 at an applied stress of  $\sigma_s = 25$  MPa. Lastly, all curves started at  $K_{tip} = 10.5$ , reducing to  $K_{tip} = 0.85$  at an applied stress of  $\sigma_s = 100$  MPa in the final stage of the sintering process.

Figure (3-29) shows a comparison of the tip curvature,  $K_{tip}$ , for different diffusion coefficients under free sintering conditions. Four different diffusion coefficient ratios,  $D_S/D_g = 0.1, 1, 50,$  and  $100$ , were used to study the effects of diffusion coefficient ratio on the curvature between particles during the neck growth process. Overall, it can be observed that  $K_{tip}$  increases with increasing diffusion coefficient ratio, especially at the beginning of the sintering process, but all the associated curves converged towards the end of the process. The curve associated with a diffusion coefficient ratio of 100 matched that associated with a diffusion coefficient ratio of 50, which meant that the effect of diffusion coefficient ratio was essentially negligible when the diffusion coefficient ratio  $D_S/D_g > 50$ . Also, the maximum  $K_{tip}$  was 12.9 over a range of diffusion coefficient ratios of  $D_S/D_g = 50-100$ , while the minimum  $K_{tip}$  was 4.8 at a diffusion

coefficient ratio  $D_s/D_g = 0.1$  during the first stage of the sintering process.

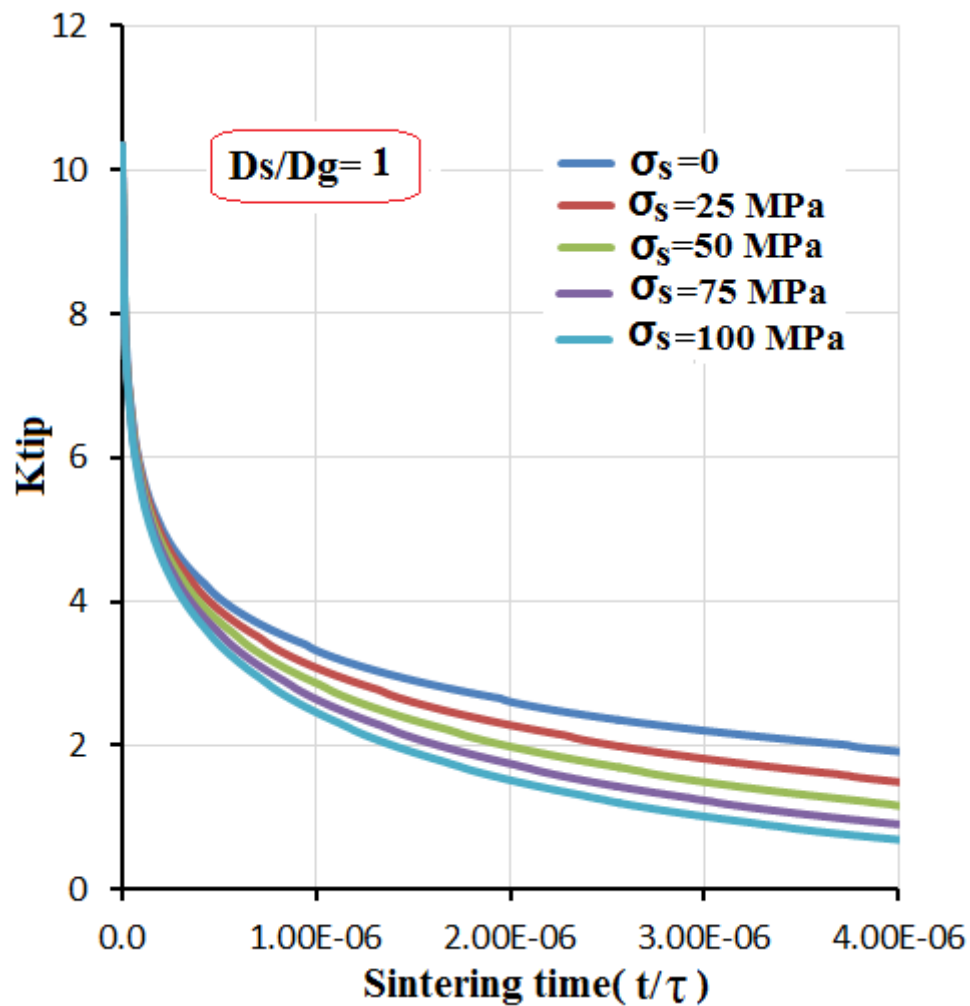
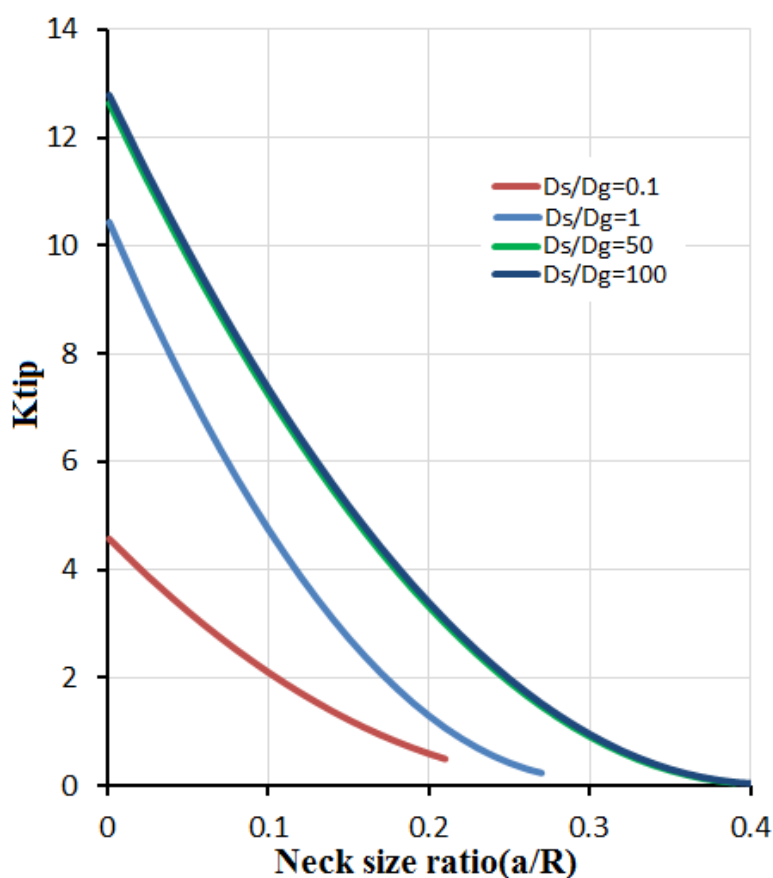


Figure 3-28 A comparison of tip curvature  $K_{tip}$  at  $D_s/D_g = 1$  for different applied stresses.



**Figure 3-29. Tip curvature as a function of neck size ratio for different diffusion coefficient ratios.**

Figure (3-30) shows a comparison of the tip curvature,  $K_{tip}$ , for different applied stresses at a diffusion coefficient ratio of  $D_s/D_g = 0.1$ . Four different applied stresses;  $\sigma_s = 25, 50, 75,$  and  $100$  MPa were used to understand the effects of the applied stress in the curvature between particles during the densification process. It can be observed that  $K_{tip}$  decreases with increasing shrinkage ratio while the shrinkage ratio increases with increasing applied stress, this is because the activation of the densification process is dependent on two factors: The first being the grain boundary diffusion mechanism and the second being the applied stress. All curves after the application of stress are close together; further, the applied stress led to the increase in  $K_{tip}$  and

an increase in shrinkage ratio compared with curve at a stress of  $\sigma_s = 0$ . Figure (3-31) compares the tip curvature,  $K_{tip}$ , for different applied stresses at a diffusion coefficient ratio of  $D_s/D_g = 1$ . It can be seen from all of the curves at a diffusion coefficient ratio of  $D_s/D_g = 1$  started at  $K_{tip} = 10.5$ , while the curves for a diffusion coefficient ratio of  $D_s/D_g = 0.1$  is 4.1; moreover, all curves at  $D_s/D_g = 1$  have larger gaps between each other than the curves for  $D_s/D_g = 0.1$ . In addition, all curves showed a lower shrinkage ratio compared with the curves found for  $D_s/D_g = 0.1$ , this is because the grain boundary diffusion coefficient decreases from 10 to 1. Also, the maximum shrinkage ratio in the final stage at 100 MPa was 0.17, while the minimum shrinkage ratio at 25 MPa was 0.07.

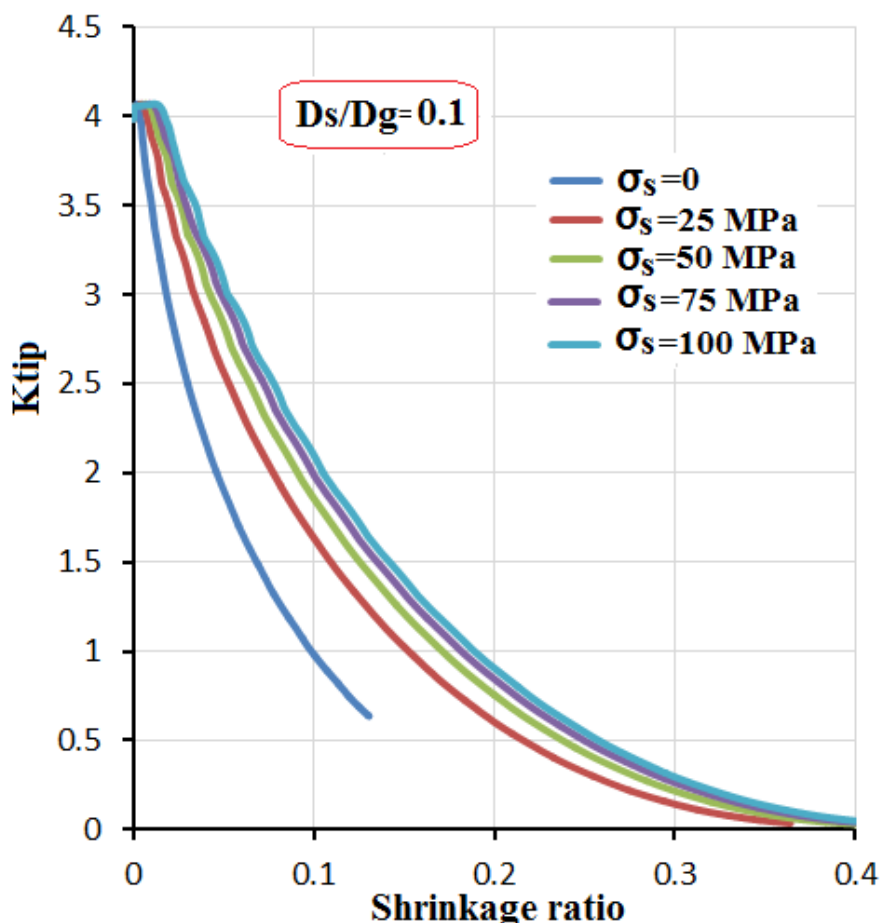


Figure 3-30 A comparison of  $K_{tip}$  at  $D_s/D_g = 0.1$  for different applied stresses.

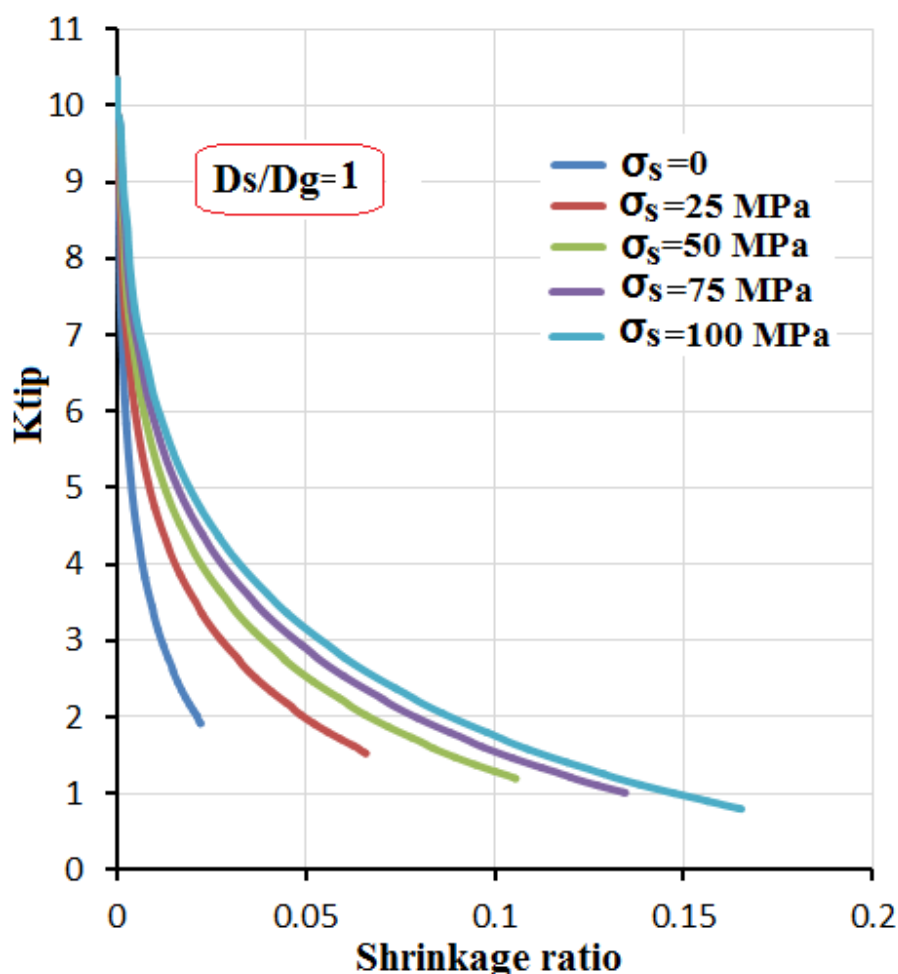


Figure 3-31 A comparison of  $K_{tip}$  at  $D_S/D_g = 1$  for different applied stresses.

Figure (3-32) shows a comparison of the tip curvature,  $K_{tip}$ , for different applied stresses at a diffusion coefficient ratio of  $D_S/D_g = 50$ . It can be observed that all curves for a diffusion coefficient ratio of  $D_S/D_g = 50$  started at  $K_{tip} = 12.4$ , while the curves for a diffusion coefficient ratio of  $D_S/D_g = 1$  started at 10.5; moreover, all curves for  $D_S/D_g = 50$  had larger gaps between each other than those at  $D_S/D_g = 1$ . In addition, all curves showed a decrease in shrinkage ratio compared with the curves for  $D_S/D_g = 1$ . Also, the maximum shrinkage ratio in the final stage at 100 MPa is 0.0045, while the minimum shrinkage ratio at 25 MPa is 0.0015.

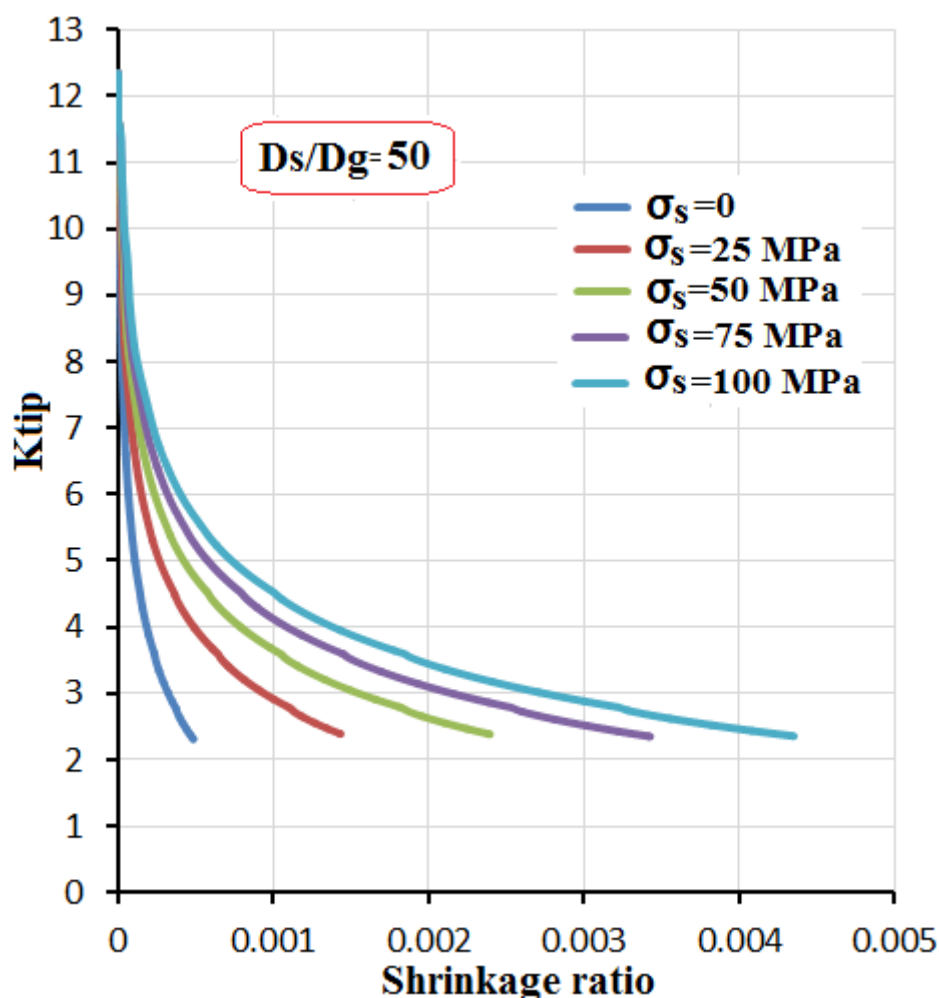


Figure 3-32 A comparison of  $K_{tip}$  at  $D_s/D_g = 50$  for different applied stresses.

Figure (3-33) shows a comparison of the tip curvature,  $K_{tip}$ , at different applied stresses and a diffusion coefficient ratio of  $D_s/D_g = 100$ . The vertical axis represents  $K_{tip}$  and the horizontal axis represents the shrinkage ratio. Overall, it can be seen that all curves showed a decrease in shrinkage ratio compared with the equivalent curves at  $D_s/D_g = 50$ , this is because of an increase in surface diffusion coefficient. Also, the maximum shrinkage ratio in the final stage at 100 MPa is 0.00225, while the minimum shrinkage ratio at 25 MPa is 0.0007.

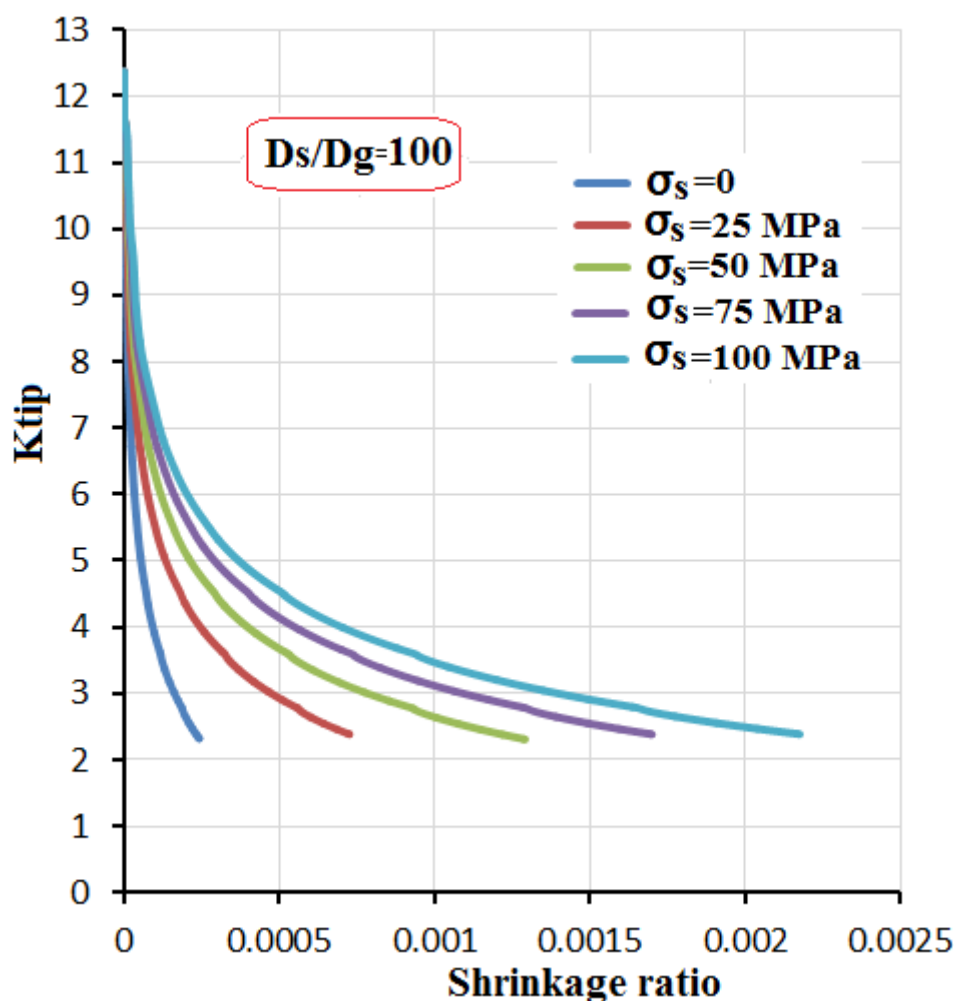


Figure 3-33 A comparison of  $K_{tip}$  at  $D_s/D_g = 100$  for different applied stresses.

Figure (3-34) compares the tip curvature,  $K_{tip}$ , for different surface energies at a diffusion coefficient ratio of  $D_s/D_g = 1$ . Six different surface energies, 1, 2, 3, 4, 6, and 8 J/m<sup>2</sup>, were used to investigate the effects of surface energy on the curvatures between particles. Overall, it can be observed that  $K_{tip}$  decreases with increasing shrinkage ratio, whilst the shrinkage ratio increases with increasing surface energy. This is due to the grain boundary velocity strongly depends on the surface energy, and the activation of the shrinkage between particles happening due to the increase in the

grain boundary velocity. The maximum shrinkage ratio is 0.121 at a surface energy of 8 J/m<sup>2</sup>, whilst the minimum shrinkage ratio is 0.023 at a surface energy of 1 J/m<sup>2</sup>.

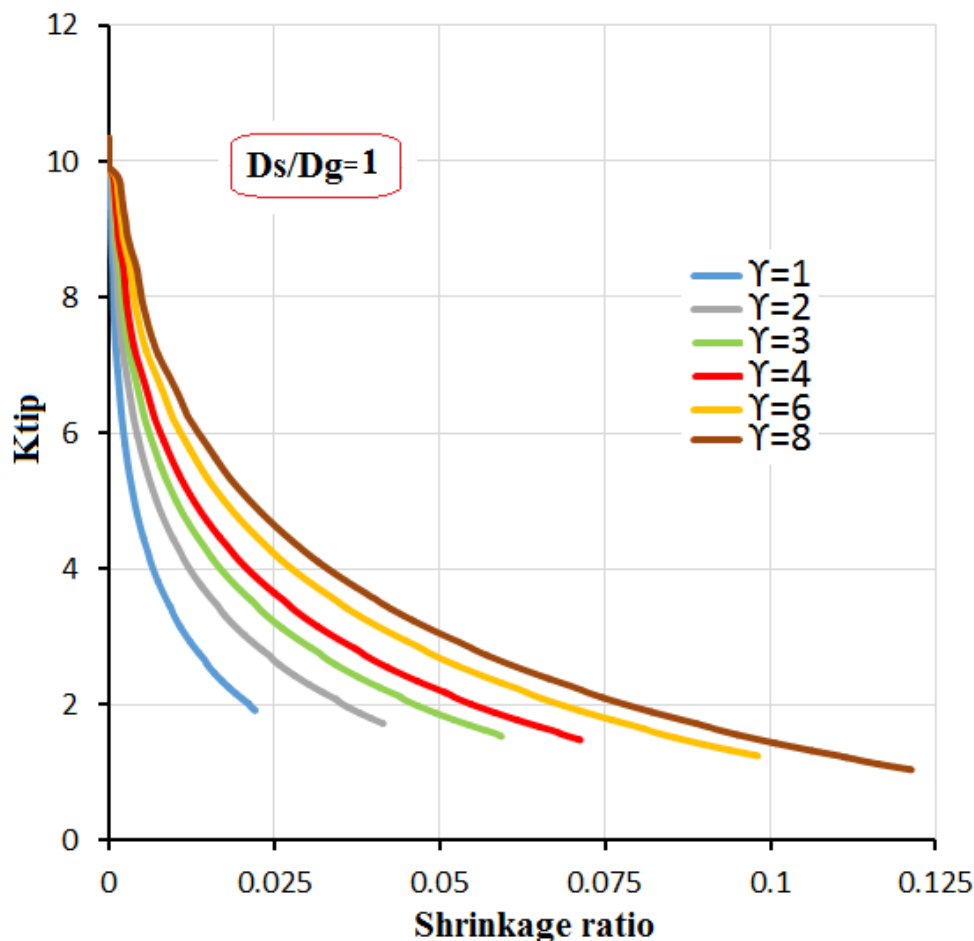


Figure 3-34 A comparison of  $K_{tip}$  at  $D_s/D_g = 1$  for different surface energies.

### 3.5 Summary

Chapter three focusses on the creation of a new, simple method of modelling the sintering between particles which depends on the creation of a curve-fitting equation for the curvatures of the particle surfaces for three diffusion coefficient ratios, and which are applied in the tip curvature  $K_{tip}$  equation for use in the finite difference code

to represent the two spherical particles, and to determine the effects of parameters such as diffusion coefficient ratio and applied stress. The summary of chapter three clarified the following points:

- 1- A curve fitting method for modelling the sintering process was created by performing three curve fittings for the curvature  $K_{n-1}$  for three diffusion coefficient ratios,  $D_S/D_g = 1, 0.1, 0.01$ , where  $K_{n-1} = 127.24\left(\frac{a}{R}\right)^2 - 100.57\left(\frac{a}{R}\right) + 18.846$  for  $D_S/D_g \geq 1$ , and where all these equations were applied in the tip curvature equation to form a new FD model to help understand sintering between particles.
- 2- The curve fitting equation for diffusion coefficient ratios  $D_S/D_g = 1, 5, 50, 100$  are the same curve fitting equation after comparing all diffusion coefficient ratios, and the curve fitting for curvature with  $D_S/D_g = 1$  will be used for  $D_S/D_g = 1, 5, 50, 100$ .
- 3- The curve fitting FD results precisely matched those of the full FD analysis for different diffusion coefficient ratios, especially at  $D_S/D_g = 5, 50$  and  $100$ , using two sintering parameters, namely neck size and shrinkage ratios.
- 4- The simulation results for the curve-fitting FD model showed only a slight match with the analytical Coblenz model.
- 5- Four applied stresses ( $\sigma_s = 25, 50, 75, 100$  MPa) were used in the simulations for the different diffusion coefficient ratios to compare the curve-fitting FD and full FD methods. The curve-fitting FD were in good agreement with the full FD results, especially at  $D_S/D_g = 5, 50$  and  $100$ , using the two sintering parameters of neck size and shrinkage ratios which means that the curve-fitting FD model will be appropriate for use in both free and forced sintering.
- 6- The curve-fitting FD for relative density results were in good agreement with the full FD method for a diffusion coefficient ratio of  $D_S/D_g = 1$ .
- 7- The effect of applied stress on shrinkage rate and tip curvature are significant in the sintering process, where shrinkage rate increases with increasing applied stress.

- 8- The surface area reduction obtained from the curve-fitting FD method was in good agreement with the full FD method for a diffusion coefficient ratio of  $D_S/D_g = 1$ .
- 9- Tip curvature,  $K_{tip}$ , decreases with increasing sintering time, applied stress, diffusion coefficient ratio, and shrinkage ratio during the sintering process.

### 3.6 Conclusions

The surface curvature of a particle plays an important role in the solid-state sintering process. The new curve-fitting method depends on the change of curvature of the particle's surface during the sintering process. The conclusions of chapter three clarified the following points:

1. A curve fitting method of modelling the sintering process was demonstrated to be the best method with which to model solid-state sintering using grain boundary diffusion without surface diffusion, as determined by comparison with a full finite difference method for different diffusion coefficients.
2. A curve fitting method of modelling the sintering process was proved to be a good method with which to model the force sintering process when validates with full FD model using difference applied stresses.
3. The relative density obtained from the new curve fitting method shows a complete match with the full finite difference method at a diffusion coefficient ratio equal to one.
4. The larger value of surface diffusion improved the matching between the curve fitting FD method and the full FD method.
5. The surface area reduction obtained from the new curve fitting method shows a complete match with the full finite difference method at a diffusion coefficient ratio equal to one.

## **4 CHAPTER FOUR: Application of curvature fitting equation to SLS**

Chapter four has two parts describing the sintering model: the first presents the variational model (VM) using curve fitting equations to model two copper particles. Neck size and shrinkage ratio for the variational model results are compared with the curve-fitting FD to show the variational model is appropriate for use in modelling the sintering process.

The second model presents the selective laser sintering of multiple copper particles using the variational model. This model has three layers, where each layer has nine particles. The behaviour of these 27 particles in the SLS process is explained by deriving equations for the model. The laser beam speed, laser power, and temperature distribution of the particles will be obtained via the COMSOL software using a thermal model of a laser beam during its movement above each particle in the layer, where each layer has nine particles. The neck formation and shrinkage between particles will be calculated during the SLS process using the variational model, and the last stage will be to compare these results with the curve-fitting FD.

### **4.1 Sintering of two particles based on the variational principle**

The variational model is used to describe changes in microstructure between particles using solid-state diffusion, thus this method is ideal for modelling the development of the geometry inside particles, and the movement of the curvature of the surface between particles. The variational method was used in simulations considering grain boundary diffusion by Needleman et al. (1983) [108], and extending research of VM using surface diffusion was developed by Suo et al.(1994) [109]. Cocks et al. (1996) [110] utilized the variational method to simulate two-dimensional grain boundary migration. Sun et al. (1996) [111] used the variational principle to couple surface and grain boundary diffusion. The numerical solution for sintering is enabled through the variational model, which represents a group of spherical particles contacting and affecting one another.

### 4.1.1 Governing equations of the variational model for sintering two particles:

A set of energy equations are derived for solid-state diffusion between particles to model the change in microstructure in particles during the sintering process, and this derivative begins with the free energy balance of the sintering process for neck growth to describe the meeting of grain boundaries with the free surfaces of particles. The sintering process between particles depends on the concept of the reduction in the total free energy between particles and the rate of reduction of free energy when adding the rate of the energy dissipation to balance the energy equation. The final equation describing this energy balance is shown in equation (4-1).

$$\dot{E} + \int_{\Omega} (\vec{F} \cdot \vec{x}) dV + \int_{\Omega} \frac{1}{\Omega} \mu_{tip} j_g d\Gamma = 0 \quad (4-1)$$

Where  $\vec{x}$  is atom velocity during diffusion, and  $\vec{F}$  is driving force of  $\vec{x}$

Applying the principle of virtual variation in energy balance equation by

$$\delta \dot{E} + \int_{\Omega} (\vec{F} \cdot \delta \vec{x}) dV + \int_{\Omega} \frac{1}{\Omega} \mu_{tip} \delta j_g d\Gamma = 0 \quad (4-2)$$

$$\vec{F} = \frac{\vec{x}}{M_g} \quad (4-3)$$

Where  $M_g$  is grain boundary mobility

$$\vec{x} = \frac{j_g}{h_g} \quad (4-4)$$

Where  $j_g$  is grain boundary flux and  $h_g$  is the grain boundary thickness.

Substitute equation (4-3) into equation (4-2):

$$\delta \dot{E} + \int_{\Omega} \left( \frac{1}{M_g} \vec{x} \cdot \delta \vec{x} \right) dV + \int_{\Omega} \frac{1}{\Omega} \mu_{tip} \delta j_g d\Gamma = 0 \quad (4-5)$$

Substitute equation (4-4) into equation (4-5):

$$\delta\dot{E} + \int \left(\frac{1}{M_g h_g} \cdot j_g \cdot \delta j_g\right) dA + \int \frac{1}{\Omega} \mu_{tip} \delta j_g d\Gamma = 0 \quad (4-6)$$

$$M_g = \frac{D_g}{h_g} \quad (4-7)$$

Substitute equation (4-7) into equation (4-6):

$$\delta\dot{E} + \frac{1}{D_g} \int_{gb} j_g \delta j_g dA + \int \frac{1}{\Omega} \mu_{tip} \delta j_g d\Gamma = 0 \quad (4-8)$$

The variational principle of initial contact between two spherical particles are derived starting from of energy balance of sintering which is shown in Figure (4-1).

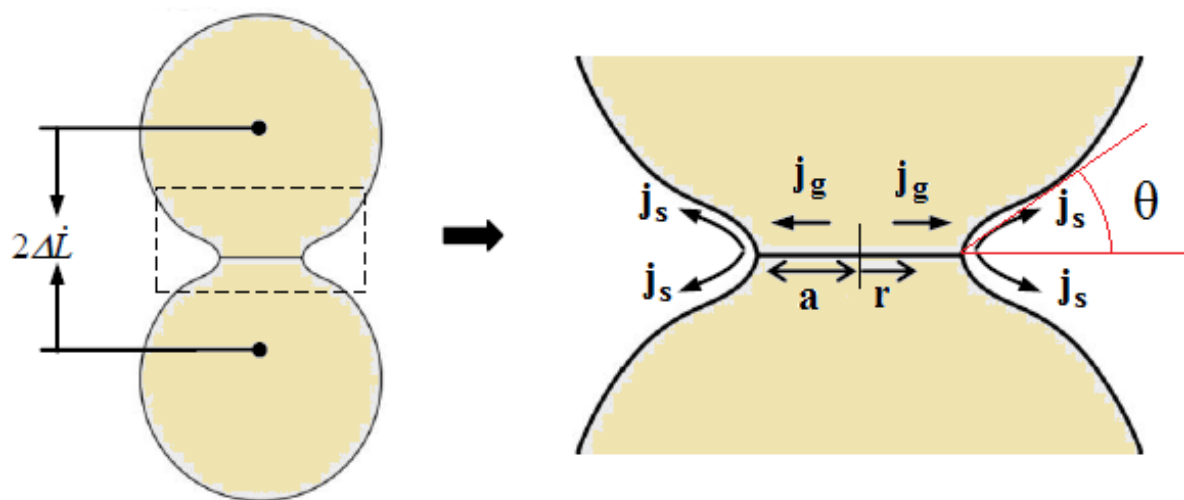


Figure 4-1 Geometry of two particles during the sintering process [26].

The energy dissipation equation is used in the energy balance:

$$R_S = \int_{gb} \frac{1}{D_g} j_g j_g dA \quad (4 - 9)$$

And:

$$V_g = \frac{a\dot{a}}{R} \quad (4 - 10)$$

$$j_g = -r\Delta\dot{L} = -r\frac{V_g}{2} \quad (4 - 11)$$

Substitute equation (4-10) into equation (4-11):

$$j_g = -r\frac{a\dot{a}}{2R} \quad (4 - 12)$$

And:

$$dA = 2\pi r dr \quad (4 - 13)$$

Where  $dA$  is the derivative of neck area between particles, and  $r$  is the neck radius.

Equation (4-14) represents the rate of change of free energy:

$$\dot{E} = -(2\gamma_s - \gamma_g)\dot{A} - 2\pi\frac{a\dot{a}}{R}a\gamma_s \sin\theta + F_a V_g \quad (4 - 14)$$

Substitute equation (4-13) into equation (4-14):

$$\dot{E} = -(2\gamma_s - \gamma_g)2\pi a\dot{a} - 2\pi\frac{a\dot{a}}{R}a\gamma_s \sin\theta + F_a V_g \quad (4 - 15)$$

The rate of neck growth between two contacting particles is represented by  $\dot{a}$ , and the variational principle of the change of free energy can be written with the virtual variation of the rate of neck radius, after substituting equation (4-10) into equation (4-15).

$$\delta \dot{E} = -(2\gamma_s - \gamma_g)2\pi a \delta \dot{a} - 2\pi a \gamma_s \sin \theta \frac{a \delta \dot{a}}{R} + F_a \frac{a \delta \dot{a}}{R} \quad (4-16)$$

And:

$$\delta \dot{E} = -4\gamma_s \pi a \delta \dot{a} + 2\pi a \gamma_{gb} \delta \dot{a} - 2\pi a \gamma_s \sin \theta \frac{a \delta \dot{a}}{R} + F_a \frac{a \delta \dot{a}}{R} \quad (4-17)$$

The applied force depends on neck area and stress, which is shown in equation (4-18)

$$\therefore F_a = \sigma \pi a^2 \quad (4-18)$$

Substitute equation (4-18) into equation (4-17):

$$\delta \dot{E} = -4\gamma_s \pi a \delta \dot{a} + 2\pi a \gamma_{gb} \delta \dot{a} - 2\pi a \gamma_s \sin \theta \frac{a \delta \dot{a}}{R} + \sigma \pi a^2 \frac{\delta \dot{a}}{R} \quad (4-19)$$

Rewriting the energy dissipation equation, after substitute equation (4-12) into equation (4-9):

$$R_S = \int_{gb} \frac{2\pi a^2 \dot{a} \delta \dot{a}}{4R^2 D_g} r^3 dr \quad (4-20)$$

And:

$$R_S = \frac{\pi a^2 \dot{a} \delta \dot{a}}{2R^2 D_{gb}} \int_0^a r^3 dr \quad (4-21)$$

Rewriting equation (4-8), after substitute equation (4-21), and equation (4-19):

$$\begin{aligned} -4Y_S \pi a \delta \dot{a} + 2\pi a Y_g \delta \dot{a} - 2\pi a Y_S \sin \theta \frac{a \delta \dot{a}}{R} + \sigma \pi a^3 \frac{\delta \dot{a}}{R} + \frac{\pi a^2 \dot{a} \delta \dot{a}}{2R^2 D_g} \int_0^a r^3 dr \\ + \int \frac{1}{\Omega} \mu_{tip} r \frac{a \delta \dot{a}}{2R} d\Gamma = 0 \end{aligned} \quad (4-22)$$

$$\begin{aligned} -4Y_S a \delta \dot{a} + 2a Y_g \delta \dot{a} - 2a Y_S \sin \theta \frac{a \delta \dot{a}}{R} + \sigma a^3 \frac{\delta \dot{a}}{R} + \frac{a^2 \dot{a} \delta \dot{a}}{2R^2 D_{gb}} \left[ \frac{r^4}{4} \right]_0^a + \int \frac{1}{\Omega} \mu_{tip} r \frac{a \delta \dot{a}}{2R} d\Gamma \\ = 0 \end{aligned} \quad (4-23)$$

$$\therefore d\Gamma = 2\pi dr \quad (4-24)$$

Substitute equation (4-24) into equation (4-23):

$$-4Y_S a \delta \dot{a} + 2a Y_{gb} \delta \dot{a} - 2a Y_S \sin \theta \frac{a \delta \dot{a}}{R} + \sigma a^3 \frac{\delta \dot{a}}{R} + \frac{a^6 \dot{a} \delta \dot{a}}{8R^2 D_g} + \frac{1}{\Omega} \mu_{tip} \frac{a^3 \delta \dot{a}}{2R} = 0 \quad (4-22)$$

$$\therefore (A) \delta \dot{a} = 0$$

$$\text{and } A = 0$$

$$-4Y_S a + 2a Y_g - 2Y_S \sin \theta \frac{a^2}{R} + \frac{\sigma a^3}{R} + \frac{a^6 \dot{a}}{8R^2 D_g} + \frac{1}{\Omega} \mu_{tip} \frac{a^3}{2R} = 0 \quad (4-23)$$

And:

$$\dot{a} = \frac{8R^2D_g}{a^6} \left( 4\gamma_s a - 2a\gamma_g + \frac{2a^2}{R} \gamma_s \sin \theta - \frac{\sigma a^3}{R} - \frac{1}{\Omega} \mu_{tip} \frac{a^3}{2R} \right) \quad (4-24)$$

$$\therefore \gamma_g = 2\gamma_s \cos \theta \quad (4-25)$$

The chemical potential in the tip between the two particles is given in equation (4-26)

$$\mu_{tip} = -\Omega\gamma_s K_{tip} \quad (4-26)$$

Substitute equation (4-25) and equation (4-26) into equation (4-24):

$$\dot{a} = \frac{8R^2D_g}{a^6} \left( 4\gamma_s a - 4a\gamma_s \cos \theta + 2 \frac{a^2}{R} \gamma_s \sin \theta - \frac{\sigma a^3}{R} + \gamma_s K_{tip} \frac{a^3}{2R} \right) \quad (4-26)$$

Rewriting equation (4-26):

$$\dot{a} = \frac{32\gamma_s R^2 D_g}{a^5} - \frac{32R^2 D_g \gamma_s \cos \theta}{a^5} + \frac{16R D_g \gamma_s \sin \theta}{a^4} - \frac{8R \sigma D_g}{a^3} + \frac{8\gamma_s K_{tip} R D_g}{2a^3} \quad (4-27)$$

The final equation for the rate of neck growth and velocity in sintering is given by:

$$\dot{a} = \frac{32\gamma_s R^2 D_g}{a^5} (1 - \cos \theta) + \frac{16R D_g \gamma_s \sin \theta}{a^4} - \frac{8R \sigma D_g}{a^3} + \frac{8\gamma_s K_{tip} R D_g}{2a^3} \quad (4-28)$$

Substitute equation (4-10) into equation (4-28):

$$V_g = \frac{32\gamma_s R D_g}{a^4} (1 - \cos \theta) + \frac{16D_g \gamma_s \sin \theta}{a^3} - \frac{8\sigma D_g}{a^2} + \frac{8\gamma_s K_{tip} D_g}{2a^2} \quad (4-29)$$

Lastly,  $K_{tip}$ , equation (3-18), can be substituted into equation (4-29), which is used in the VM simulation.

### 4.1.2 Variational model code

The Microsoft Visual Studio 10 software was employed to write the code using the variational model (VM) to model the behaviour between particles during the sintering process such as neck growth and densification processes. A flowchart describing the sintering simulation as depicted using the variational method is shown in figure (4-2).

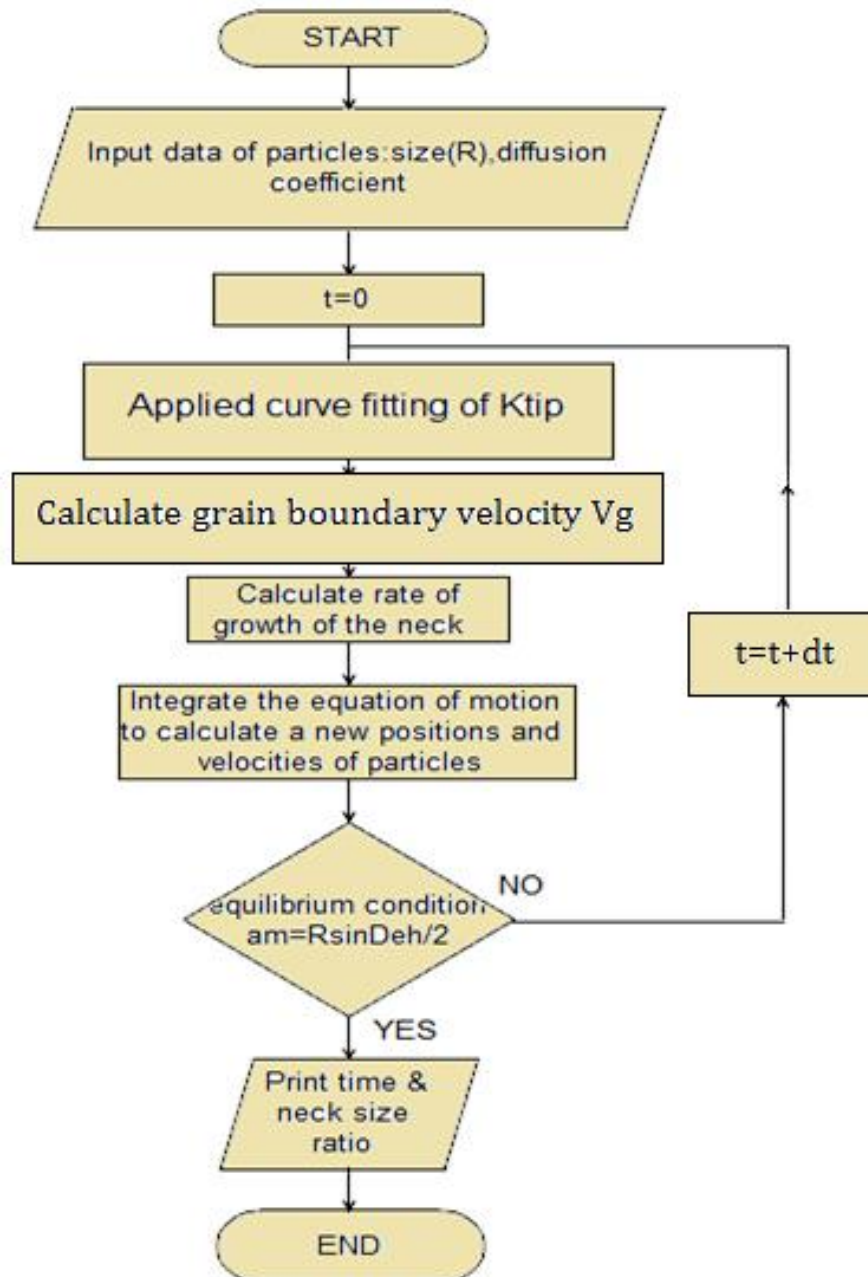


Figure 4-2 Flowchart of the variational model describing the sintering process.

### 4.1.3 Validation of the VM curve fitting

Firstly, the curve-fitting equation is applied using the variational method and validated against the FD curve-fitting results to demonstrate that the variational method of curve fitting is suitable for use in modelling the sintering process; neck size is used in this instance for the purposes of validation. The general condition for the sintering simulation using the VM model is free sintering, which means that the applied stress is equal to zero. Copper powder was utilized in the numerical simulation.

The  $K_{tip}$  equation (3-18) was used in the variational model to calculate the sintering parameters. The results of the variational method of curve fitting were validated against the FD curve-fitting method using neck size ratio between the two particles as the means of validation. Figure (4-3) shows a comparison of neck size ratio between the VM curve-fitting and FD curve-fitting of copper particles with a particle size of 20  $\mu\text{m}$  and a sintering temperature of 1300 K. It can be seen that the curve for the FD curve-fitting method showed an excellent match with the VM curve-fitting curve, which means that the curve-fitting method for the  $K_{tip}$  equation (equation (3-18)) is valid in the variational model for modelling the sintering process between particles, especially during the initial stage of the sintering process, and it will be used without the finite difference method in modelling the neck growth process.

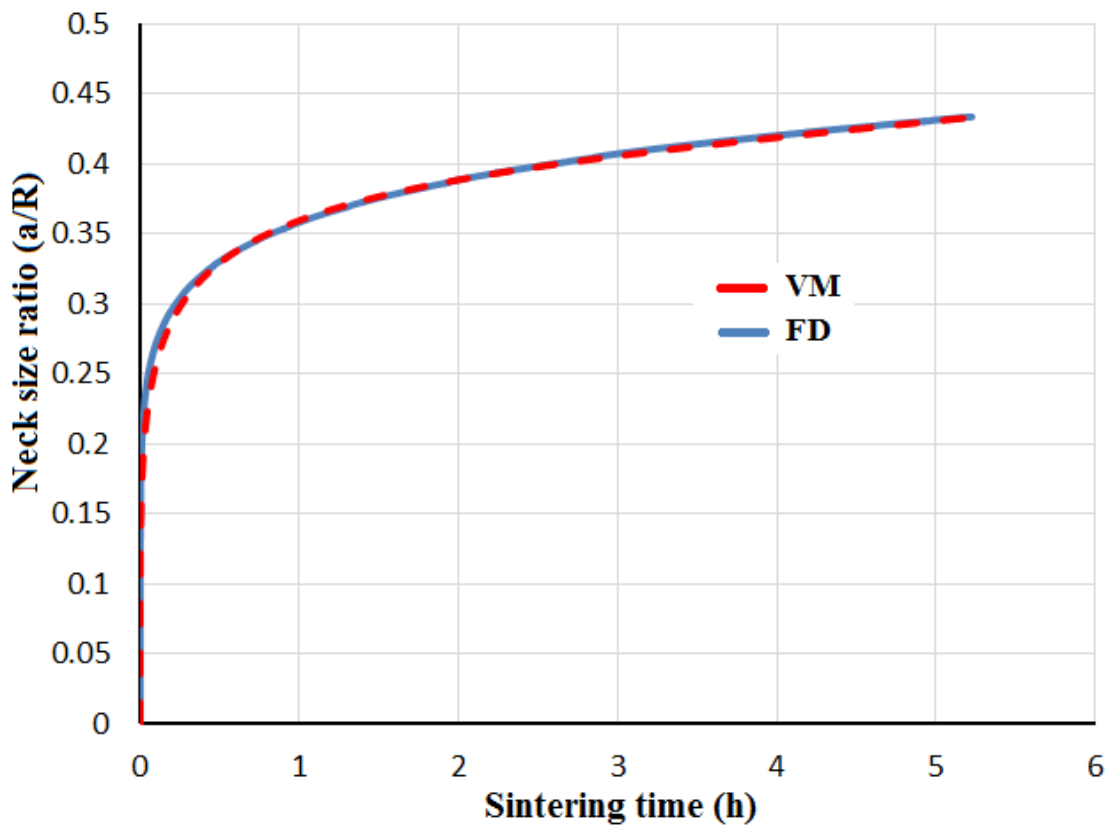


Figure 4-3 Comparison of the neck size ratio between the FD curve-fitting and VM curve-fitting models.

## 4.2 A Model for Selective Laser Sintering of Multi-particles

Selective laser sintering (SLS) is one of the more effective technologies used for manufacturing and producing complex parts from powdered materials. Here, the particles experience rapid heating and cooling due to the high intensity of the laser beam, during which these particles sinter and bond together. Laser power, scan speed, and powder layer thickness are significant parameters in SLS, and are dependent on the type of material and required geometry. There have been few theoretical studies conducted in order to understand how these parameters affect sintering kinetics. In this chapter, we present a particle-scale model for SLS using the variational framework to model sintering. A three-dimensional numerical model consisting of individual

particles is used to study the sintering kinetics as heat is applied over a short period of time. The model takes matter transportation mechanisms into account, including such effects as grain-boundary diffusion and surface diffusion. The coupling between the two diffusion processes is efficiently addressed using a novel approach in which the curvature of the contact neck is approximated from full numerical solutions performed outside the multi-particle model. Our purpose is to present a theoretical understanding on how the material and processing parameters can affect sintering kinetics, which can subsequently be used to guide the practical SLS process.

### 4.2.1 SLS numerical model

The SLS numerical model requires two numerical solution stages: the first is the thermal numerical model using the COMSOL FE software to find the particles' temperature due to the laser beam during the SLS process; the second is the sintering model, which uses the variational method to find neck growth size and densification between particles. Figure (4-4) shows the steps used to model selective laser sintering.

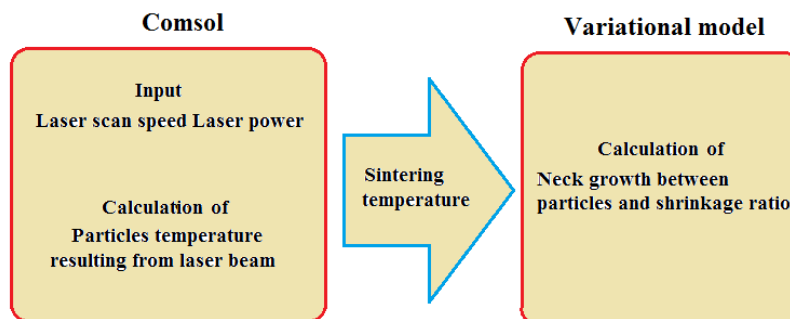


Figure 4-4 Diagram of the steps used in SLS modelling.

### 4.2.2 Governing equations for the sintering model

The model uses three layers, where each layer has nine particles. The behaviour of these 27 particles during the SLS process can be explained by the equations derived

to model this process, as shown in figure (4-5). Figures (4-6, 4-7 and 4-8) shows the laser routes and particle layers.

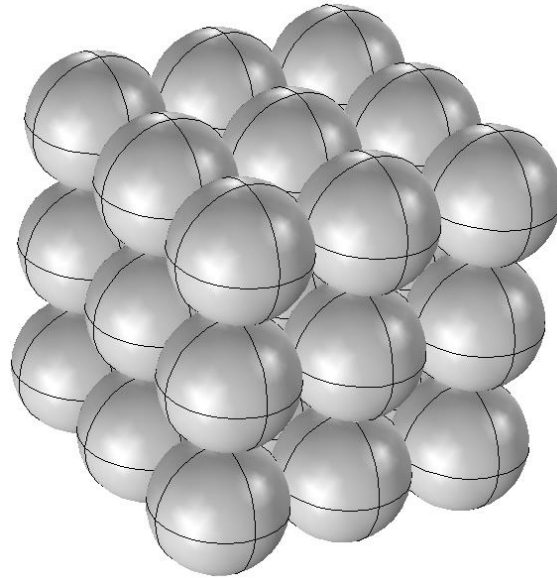


Figure 4-5. 27 Copper particle arrangement in three layers for use in the SLS model.

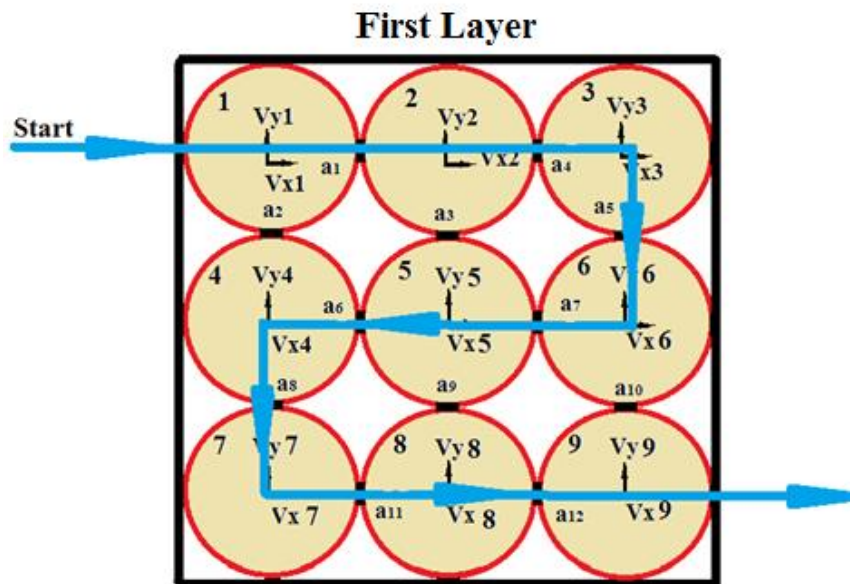


Figure 4-6 First layer for SLS model.

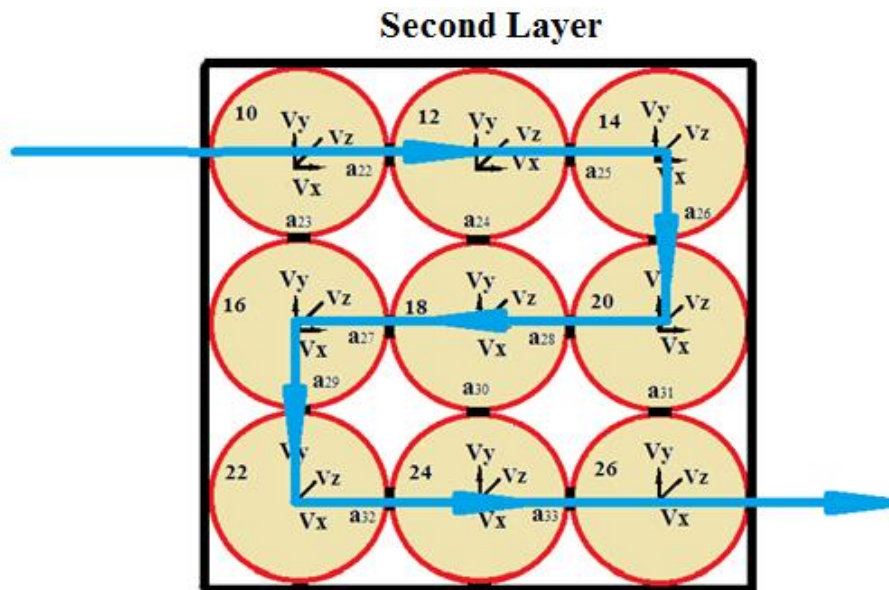


Figure 4-7 Second layer of the SLS model.

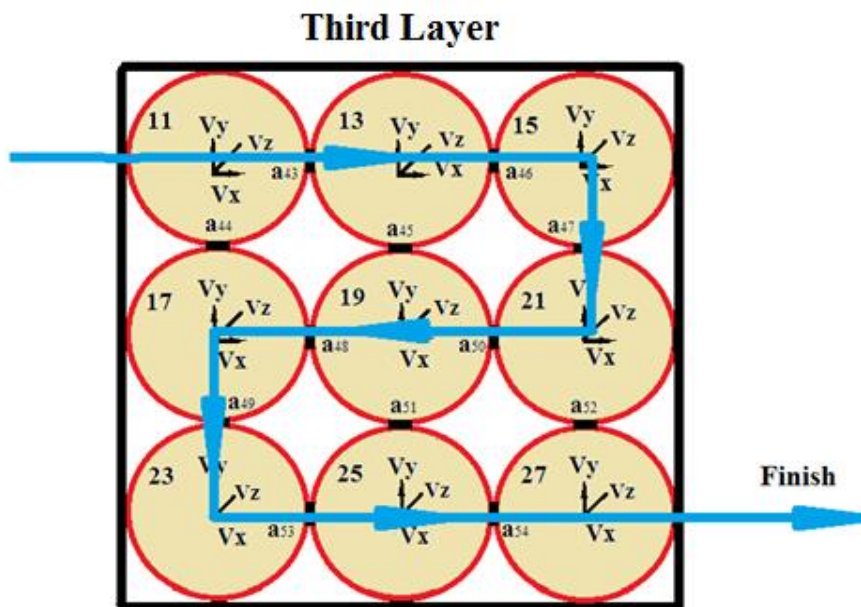


Figure 4-8 Third layer of the SLS model.

The general equations for the solid-state sintering process are shown below. Figures (4-6), (4-7), and (4-8) show the three layers of copper particles, and the direction of the laser beam during the SLS process for each of the three stages.

The function ( $\Pi$ ) is shown below

$$\Pi = R_S + \dot{E} + C_h \quad (4 - 30)$$

Where  $R_S$  is energy dissipation,  $\dot{E}$  is rate of change in free energy, and  $C_h$  is energy changing due to atoms movement.

Energy dissipation equation is shown in equation (4-31).

$$R_S = \frac{1}{D_g} \int_{gb} j_g^2 dA \quad (4 - 31)$$

Also

$$dA = 2\pi r dr \quad (4 - 32)$$

Where  $dA$  is a derivative of neck area between particles, while  $r$  is neck radius.

The grain boundary flux between particles is shown in equation (4-33)

$$j_g = -\frac{V_g r}{2} \quad (4 - 33)$$

Rewriting the Energy dissipation equation in virtual variational after substituting equations (4-32), (4-33), in equation (4-31).

$$\delta R_S = \frac{\pi}{2D_g} \int_{gb} V_g \delta V_g r^3 dr = \frac{\pi a^4}{8D_g} V_g \delta V_g \quad (4 - 34)$$

Energy changing due to atoms movement equation is shown in equation (4-35).

$$C_h = - \int_{\Gamma} \frac{1}{\Omega} \mu_{tip} \cdot j_g d\Gamma \quad (4-35)$$

$$d\Gamma = 2\pi dr \quad (4-36)$$

Where  $d\Gamma$  is derivative of circumference of neck which is located between particles.

The chemical potential depends on  $K_{tip}$  and surface energy, which is shown in equation (4-37)

$$\mu_{tip} = -\gamma_s \Omega K_{tip} \quad (4-37)$$

Rewriting Energy changing due to atoms movement equation in virtual variational after substituting equations (4-36), (4-33), and (4-37) in equation (4-35)

$$\delta C_h = - \int_{\Gamma} \pi \gamma_s \kappa_{tip} \cdot r dr \delta V_g = - \frac{\pi a^2}{2} \gamma_s \kappa_{tip} \cdot \delta V_g \quad (4-38)$$

Rate of change of free energy is clear in equation (4-39).

$$\dot{E} = -(2\gamma_s - \gamma_g) dA - 2\pi V_g a \gamma_s \sin \theta \quad (4-39)$$

The grain boundary energy  $\gamma_g$  depends on surface energy and dihedral angle which is shown in equation (4-40).

$$\gamma_g = 2\gamma_s \cos \theta \quad (4-40)$$

Rewriting rate of change of free energy equation in virtual variational after substituting equations (4-32) and (4-40), into equation (4-39).

$$\delta \dot{E} = -4\pi \gamma_s R(1 - \cos \theta) \delta V_g - 2\pi a \gamma_s \sin \theta \delta V_g \quad (4-41)$$

Rewriting the function ( $\Pi$ ) equation in virtual variational after substituting equations (4-41), (4-34), and (4-38) into equation (4-30)

$$\delta\Pi_i = \frac{\pi a^4}{8D_g} V_g \delta V_g - 4\pi\gamma_s R(1 - \cos\theta)\delta V_g - 2\pi a\gamma_s \sin\theta \delta V_g - \frac{\pi a^2}{2} \gamma_s \kappa_{tip} \delta V_g \quad (4-42)$$

Simplicity of equation (4-42)

$$\delta\Pi_i = \frac{\pi a^4}{8D_g} V_g \delta V_g + [F_i]\delta V_g \quad (4-43)$$

Applying virtual variational of function ( $\Pi$ ) for all particles in three axes X,Y,Z for three layers depending on figures(4-36)(4-37)(4-38):

$$\begin{aligned} \delta\Pi_X = & \delta\Pi_1 + \delta\Pi_4 + \delta\Pi_6 + \delta\Pi_7 + \delta\Pi_{11} + \delta\Pi_{12} + \delta\Pi_{22} + \delta\Pi_{25} + \delta\Pi_{27} + \delta\Pi_{28} + \delta\Pi_{32} \\ & + \delta\Pi_{33} + \delta\Pi_{43} + \delta\Pi_{46} + \delta\Pi_{48} + \delta\Pi_{50} + \delta\Pi_{53} + \delta\Pi_{54} \end{aligned} \quad (4-44)$$

$$\begin{aligned} \delta\Pi_Y = & \delta\Pi_2 + \delta\Pi_3 + \delta\Pi_5 + \delta\Pi_8 + \delta\Pi_9 + \delta\Pi_{10} + \delta\Pi_{23} + \delta\Pi_{24} + \delta\Pi_{26} + \delta\Pi_{29} + \delta\Pi_{30} \\ & + \delta\Pi_{31} + \delta\Pi_{44} + \delta\Pi_{45} + \delta\Pi_{47} + \delta\Pi_{49} + \delta\Pi_{51} + \delta\Pi_{52} = 0 \end{aligned} \quad (4-45)$$

$$\begin{aligned} \delta\Pi_Z = & \delta\Pi_{13} + \delta\Pi_{14} + \delta\Pi_{15} + \delta\Pi_{16} + \delta\Pi_{17} + \delta\Pi_{18} + \delta\Pi_{19} + \delta\Pi_{20} + \delta\Pi_{21} + \delta\Pi_{34} \\ & + \delta\Pi_{35} + \delta\Pi_{36} + \delta\Pi_{37} + \delta\Pi_{38} + \delta\Pi_{39} + \delta\Pi_{40} + \delta\Pi_{41} + \delta\Pi_{42} \\ = & 0 \end{aligned} \quad (4-46)$$

Where the number in this item  $\delta\Pi_1$  refers to number of grain boundary contacting between particles in the same axis.

Rewriting equation (4-43) to be show the grain boundary velocity for first row of layer one.

$$\begin{aligned} \delta\Pi_1 + \delta\Pi_4 = & \frac{\pi a_1^4}{8D_g} (V_{X2} - V_{X1})\delta(V_{X2} - V_{X1}) + \frac{\pi a_4^4}{8D_g} (V_{X3} - V_{X2})\delta(V_{X3} - V_{X2}) \\ & + F_1\delta(V_{X2} - V_{X1}) + F_2\delta(V_{X3} - V_{X2}) = 0 \end{aligned} \quad (4-47)$$

For boundary condition that the velocity of particle one equal zero,  $V_{X1} = 0$

Rewriting equation (4-47) after applying condition for velocities in x direction.

$$\begin{aligned}\delta\Pi_1 + \delta\Pi_4 &= \frac{\pi a_1^4}{8D_g} V_{X2} \delta V_{X2} + \frac{\pi a_4^4}{8D_g} (V_{X3} - V_{X2}) \delta(V_{X3} - V_{X2}) + F_1 \delta V_{X2} + F_4 \delta(V_{X3} - V_{X2}) \\ &= 0\end{aligned}\quad (4-48)$$

And

$$\begin{aligned}\left[ \frac{\pi a_1^4}{8D_g} V_{X2} - \frac{\pi a_4^4}{8D_g} (V_{X3} - V_{X2}) + (F_1 - F_4) \right] \delta V_{X2} + \left[ \frac{\pi a_4^4}{8D_g} (V_{X3} - V_{X2}) + F_4 \right] \delta V_{X3} \\ = 0\end{aligned}\quad (4-49)$$

$$A. \delta V_{X2} = 0$$

$$B. \delta V_{X3} = 0$$

$$\frac{\pi a_1^4}{8D_g} V_{X2} - \frac{\pi a_4^4}{8D_g} (V_{X3} - V_{X2}) + (F_1 - F_4) = 0 \quad (4-50)$$

$$\frac{\pi a_4^4}{8D_g} (V_{X3} - V_{X2}) + F_4 = 0 \quad (4-51)$$

Also substituting equations (4-51) into equation (4-50) to find  $V_{X2}$  and  $V_{X3}$ .

$$V_{X2} = -\frac{8D_g}{\pi a_1^4} F_1 \quad (4-52)$$

$$V_{X3} = -\frac{8D_g}{\pi a_1^4} F_1 - \frac{8D_g}{\pi a_4^4} F_4 \quad (4-53)$$

For particles velocities in y direction.

Rewriting equation (4-43) to be show the grain boundary velocity for first column of layer one

$$\begin{aligned}\delta\Pi_2 + \delta\Pi_8 &= \frac{\pi a_2^4}{8D_g} (V_{Y4} - V_{Y1}) \delta(V_{Y4} - V_{Y1}) + \frac{\pi a_8^4}{8D_g} (V_{Y7} - V_{Y4}) \delta(V_{Y7} - V_{Y4}) \\ &\quad + F_2 \delta(V_{Y4} - V_{Y1}) + F_8 \delta(V_{Y7} - V_{Y4}) = 0\end{aligned}\quad (4-54)$$

For boundary condition that the velocity of particle one equal zero,  $V_{Y1} = 0$

Rewriting equation (4-54) after applying condition.

$$\begin{aligned}\delta\Pi_2 + \delta\Pi_8 &= \frac{\pi a_2^4}{8D_g} V_{Y4} \delta V_{Y4} + \frac{\pi a_8^4}{8D_g} (V_{Y7} - V_{Y4}) \delta(V_{Y7} - V_{Y4}) + F_2 \delta V_{Y4} + F_8 \delta(V_{Y7} - V_{Y4}) \\ &= 0\end{aligned}\quad (4-55)$$

$$\begin{aligned}\left[ \frac{\pi a_2^4}{8D_g} V_{Y4} - \frac{\pi a_8^4}{8D_g} (V_{Y7} - V_{Y4}) + (F_2 - F_8) \right] \delta V_{Y4} + \left[ \frac{\pi a_8^4}{8D_g} (V_{Y7} - V_{Y4}) + F_8 \right] \delta V_{Y7} \\ = 0\end{aligned}\quad (4-56)$$

$$C. \delta V_{Y4} = 0$$

$$D. \delta V_{Y7} = 0$$

$$\frac{\pi a_2^4}{8D_g} V_{Y4} - \frac{\pi a_8^4}{8D_g} (V_{Y7} - V_{Y4}) + (F_2 - F_8) = 0 \quad (4-57)$$

$$\frac{\pi a_8^4}{8D_g} (V_{Y7} - V_{Y4}) + F_8 = 0 \quad (4-58)$$

Also substituting equations (4-58) into equation (4-57) to find  $V_{Y4}$  and  $V_{Y7}$ .

$$V_{Y4} = -\frac{8D_g}{\pi a_2^4} F_2 \quad (4-59)$$

$$V_{Y7} = -\frac{8D_g}{\pi a_2^4} F_2 - \frac{8D_g}{\pi a_8^4} F_8 \quad (4-60)$$

And all equations for all particles in different layer will be shown in appendix A.

### 4.2.3 Numerical model of sintering

A numerical model is used to describe the behavior of particles during the selective laser sintering process. The variational method was used to determine the sintering mechanisms between particles. The numerical model of selective laser sintering for 27 particles has been performed using the code for each particle in each layer; in this technique, the laser scan route is used as code steps for all particles for this time

period, and then to verify that all particles had the same neck size ratio. In this research, the function of the new technique is to validate the SLS process, the results of which showed that the SLS code is correct by demonstrating that the neck size ratio is the same for all 27 particles. The flowchart in figure (4-9) shows the numerical model used for the SLS process which represents the route taken by the laser beam.

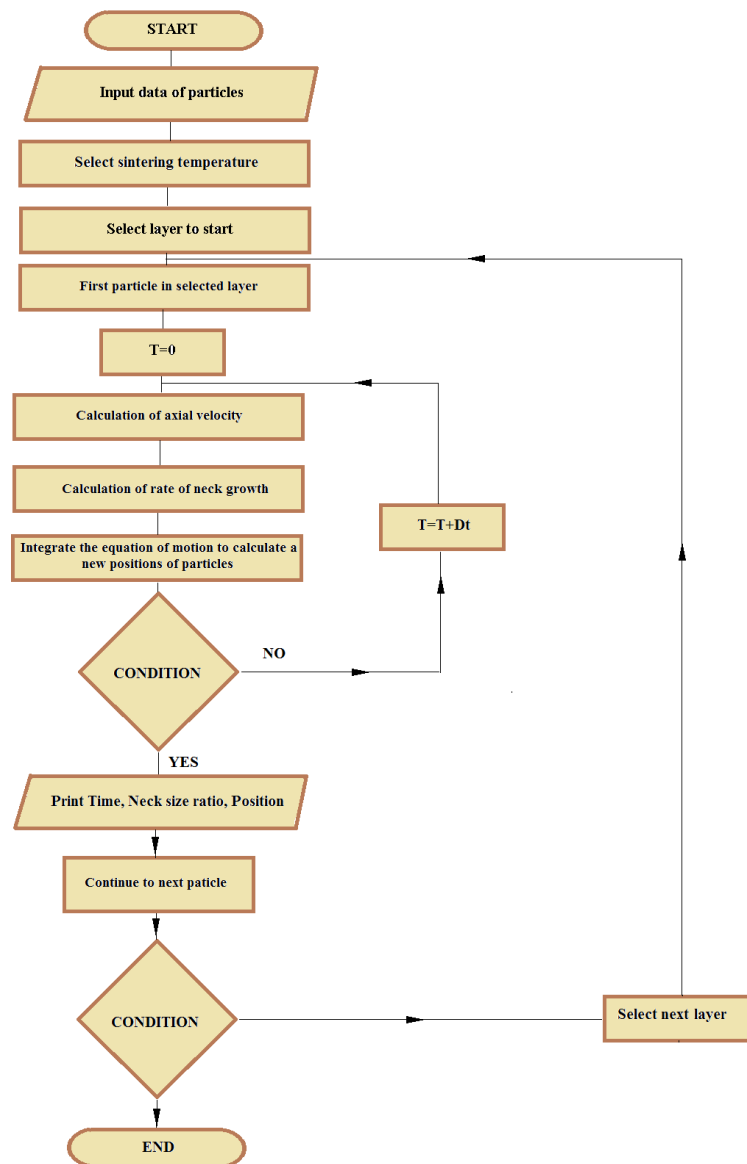


**Figure 4-9** Flow chart describing the numerical model for the selective laser sintering process.

#### 4.2.4 Governing equations of thermal model in the COMSOL software

The COMSOL software offers a thermal model by which to solve the temperature distribution across the copper particles with the movement of the laser beam over them. The temperature distribution is an important parameter in selective laser sintering, and many researchers have focussed on this field in order to understand the temperature distribution across the material surface or into the material bulk [112-114]. The SLS process has been modelled by many researchers [115-118] using the finite differences method, though using different parameters. The Fourier heat conduction formula is most frequently used to model the heat transfer in SLS to represent the attendant thermal processes. Equation (4-61) describes the heat conduction in the powder due to the laser beam, which is used in the COMSOL software to calculate the temperature of the particles.

$$\lambda \left( \frac{\partial^2 T}{\partial x^2} + \frac{\partial^2 T}{\partial y^2} + \frac{\partial^2 T}{\partial z^2} \right) + q = \rho C_p \frac{\partial T}{\partial t} \quad (4 - 61)$$

Where  $\rho$  is the powder density,  $q$  is external heat flux from the laser beam,  $C_p$  is specific heat, and  $\lambda$  is the heat conductivity.

Particles were represented in terms of the emission of surface radiation and convection during the SLS process, where equation (4-62) can be used to represent the boundary conditions for these two thermal effects.

$$-\lambda \frac{\partial T}{\partial t} = \varepsilon_e B(T^4 - T_e^4) + h_c(T - T_e) \quad (4 - 62)$$

Where  $B$  is the Stefan Boltzmann constant,  $\varepsilon_e$  is surface emissivity of the powder, and  $h_c$  is the convective coefficient.

Assuming no heat loss from the bottom:

$$-\lambda \frac{\partial T}{\partial t} = 0 \quad (4 - 63)$$

### 4.2.5 Governing equations for the laser beam in the COMSOL software

COMSOL offers a laser beam model to solve for the increase in heat during the movement of the laser beam over the copper particles. Most researchers use a Gaussian function to describe the profile of the laser beam in SLS. Indeed, the intensity distribution across the beam profile is approximately Gaussian, as shown in equation (4-64).

$$I(r) = I_o \exp \left[ \frac{-2r^2}{w_d^2} \right] \quad (4 - 64)$$

Where  $r$  is the radial distance from the centre of the laser beam.  $w_d$  is the laser beam waist radius, at which laser intensity is equal to 0.135 times the peak intensity, and hence the laser beam waist radius  $w_d$  is given by equation (4-65) [75].

$$w_d = \frac{\frac{d}{2}}{2.146} \quad (4 - 65)$$

The maximum laser beam intensity ( $I_o$ ) is the laser intensity at the centre of the axis of the laser beam, where equation (4-66) gives the maximum intensity [75].

$$I_o = \frac{2P}{\pi w_d^2} \quad (4 - 66)$$

The heat flux from the laser beam is given by equation (4-67) [75]:

$$q(r) = q_o \exp \left[ \frac{-2r^2}{w_d^2} \right] \quad (4 - 67)$$

### 4.2.6 Materials used in this study

Different powder materials have different impacts on SLS process which is dependent on powder parameters. Copper powders have been selected for use in the simulation model. Table (4.1) shows the input data for these powders.

**Table 4.1 Input parameters for copper powders used in the numerical model [30].**

Parameter	Value
Specific surface energy, $\gamma_s$	1.72 J/m <sup>2</sup>
Specific grain-boundary energy, $\gamma_g$	1 J/m <sup>2</sup>
Grain-boundary thickness pre-exponential grain-boundary diffusion coefficient, $\delta_g D_{go}$	$5.12 \times 10^{-19}$ m <sup>3</sup> /s
Gas constant, $R_r$	8.3144621 J/(mol K)
Boltzmann's constant, k	$1.3806503 \times 10^{-23}$ m <sup>2</sup> kg/(s <sup>2</sup> K)
Initial particle radius, R	$22.5 \times 10^{-6}$ m
Atomic volume, $\Omega$	$1.18 \times 10^{-29}$ m <sup>3</sup>
Dihedral angle, $\Psi$	146°
Sintering temperature, T	1027°C
Activation energy for grain boundary diffusion, $Q_g$	$1.05 \times 10^5$ J/mol

### 4.2.7 COMSOL software for laser beam and temperature distribution

Thermal SLS modelling includes two operations: the effect of the laser beam on the copper particles, and the heat transfer generated between particles. The laser beam equations are used in the COMSOL simulation to describe the laser beam speed and power during the sintering process, while the heat transfer equations are used to describe the heat transfer between particles. The aim of the thermal calculation is to determine the temperature of the particles during the SLS process. The temperature distribution across the particles can be solved via a finite element model using heat generation equations.

The thermal operation of the SLS process is represented by a finite element simulation using the COMSOL software to simulate a laser beam, where this process includes convective heat transfer, conductive heat transfer, and surface radiation. The model geometry used for the thermal simulations contains three layers, where layer thickness depends on particle size. Table (4-2) shows the laser parameters used as input to COMSOL. The finite element mesh of 27 copper particles applied in the COMSOL simulation contains 910,626 tetrahedral elements to give a particle size of 20  $\mu\text{m}$ , as shown in figure (4-10).

**Table 4.2 Laser parameters used as input to the COMSOL simulation**

Parameter	Value
Laser power (P)	5-25 W
Thermal conductivity ( $\lambda$ )	401 W/mK
Diffusivity (K)	$1.11 \times 10^{-4}$
Scan speed (V)	40-350 mm/s

Stefan Boltzmann constant	$5.670367 \times 10^{-8} \text{ kg/s}^3 \text{ K}^4$
Surface emissivity	0.07
Particle size	1-45 $\mu\text{m}$
Density( $\rho$ )	$8700 \text{ kg/m}^3$
Melting temperature	1358 K
Initial temperature	293.5 K

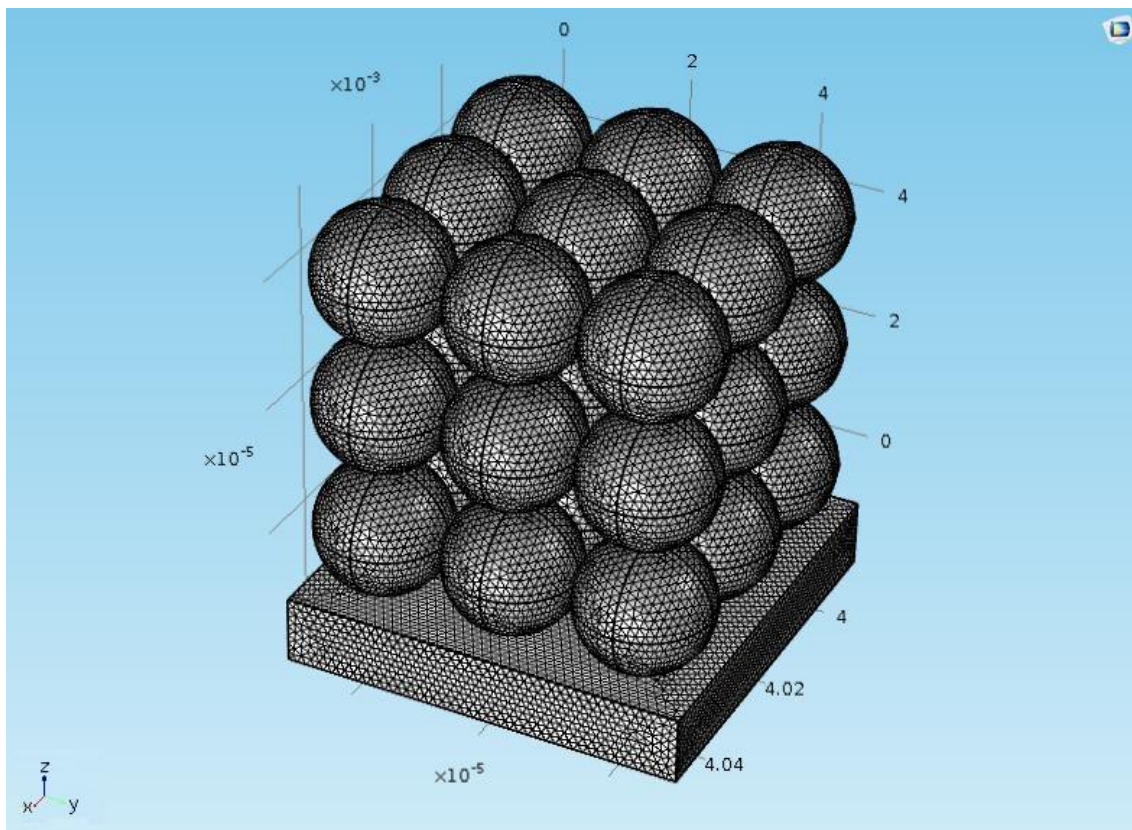


**Figure 4-10 Snapshot of the FE mesh for the 27 copper particles.**

Figure (4-11) shows a snapshot of nine particles in order to illustrate the surface temperature of the particles in first layer, as obtained from the COMSOL simulation. Here, a laser power of 8 W, a particle size of 1  $\mu\text{m}$ , and a laser scan speed of 250 mm/s were used in the COMSOL simulation. The maximum temperature was found to be 848 K, whereas the minimum temperature was 296 K. It can be seen from the snapshot that the first particle has the highest temperature (yellow particle), while the second particle has an intermediate temperature of 400 K, and all other particles were 296 K. As shown in this figure, the connection between the first particle and second particle is yellow in colour, which it means the highest temperature is in the neck between these particles.

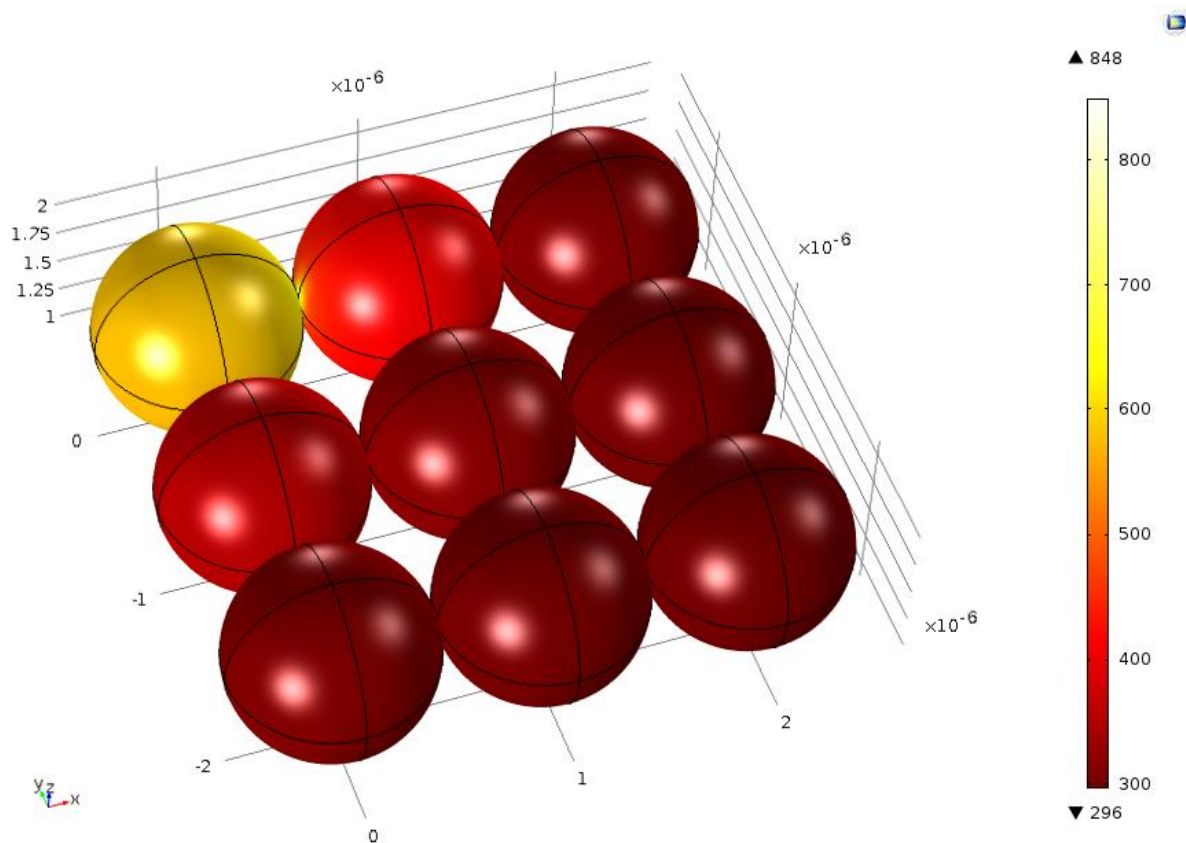


**Figure 4-11 Snapshot of the nine particles in the first layer.**

### 4.2.8 Validation of the sintering model

The validation of the selective laser sintering of 27 particles has completed using the same SLS code but utilizing a different technique, and in this technique is used laser scan for all particles for period of time, after which it was verified that all particles had the same neck size ratio. In this research, the new technique is used to validation the SLS process, the results of which demonstrated that the SLS code is correct through the neck size ratio being the same for all 27 particles, and flow chart of validation technique is shown in figure (4-12).

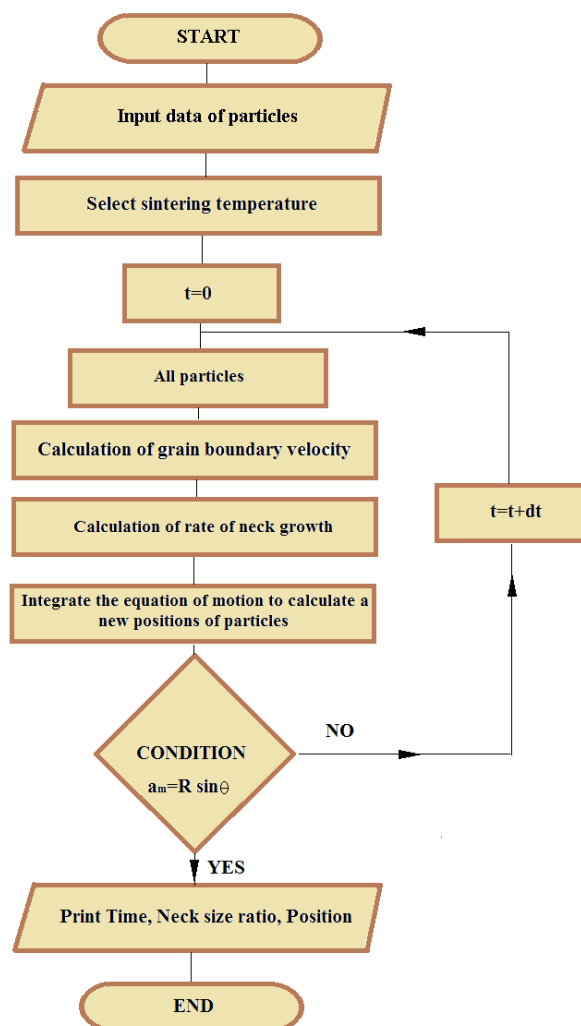


Figure 4-12 Flow chart showing the validation method used for all particles.

### 4.2.9 Results and discussion

The shrinkage ratio determined from the simulation of the SLS model is shown in Figure (4-13), which shows a plot of shrinkage ratio as a function of sintering time between particle 1 and particle 2. Shrinkage represents movements of particles during the SLS process, such as the movement of particle 2 to particle 1, and also the direction of movement of particle 2 towards particle 1; a particle size of  $1\ \mu\text{m}$ , and an average sintering temperature of 1300 K were used in the simulation in this instance. Overall, as one can see, the shrinkage ratio between particles increases with increased sintering time; this is because the grain boundary velocity increases due to the increase in grain boundary diffusion which results from an increased sintering temperature. Also, the maximum shrinkage ratio is 0.088 at a sintering time of 2 s after completing a layer.

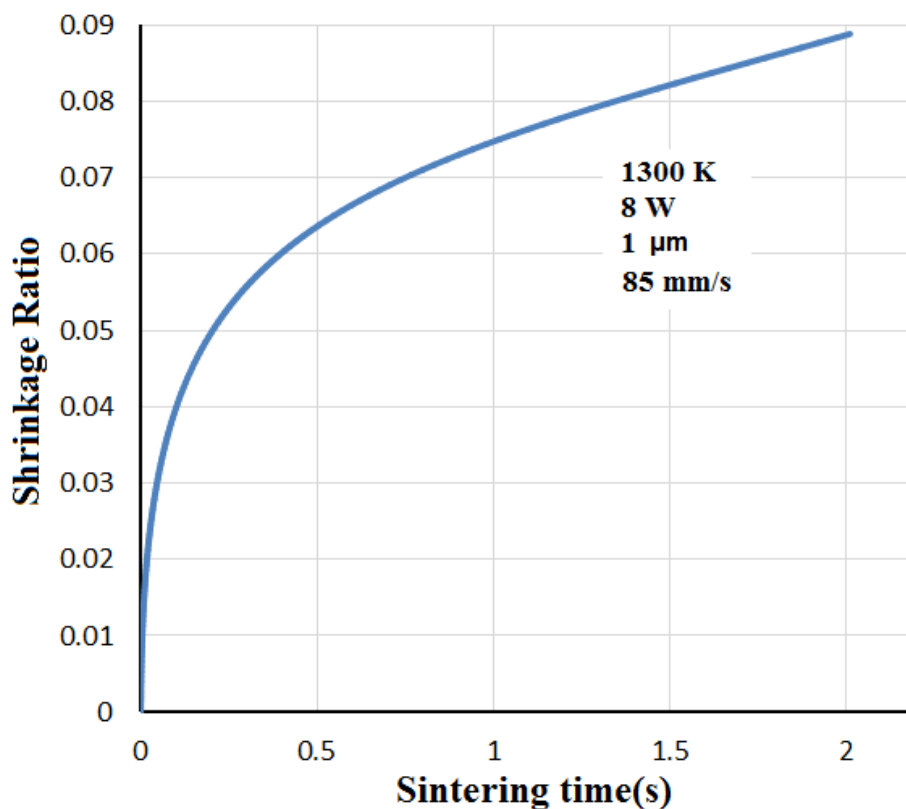


Figure 4-13 Shrinkage ratio as a function of sintering time.

Figure (4-14) shows the neck size ratio of the neck between particle 1 and particle 2 using a particle size of 1  $\mu\text{m}$  and an average sintering temperature of 1300 K. It can be seen from diagram that the initial neck size ratio changes very rapidly at the beginning of the SLS process, where each neck has two laser beam stages during the SLS process. In addition, the neck size ratio between particles increases with increasing sintering time because the neck growth rate depends on the grain boundary velocity, which increases due to the increase in grain boundary diffusion that results from an increased sintering temperature. Also, the maximum of neck size ratio is 0.433 at a sintering time of 2 s after completing a layer.

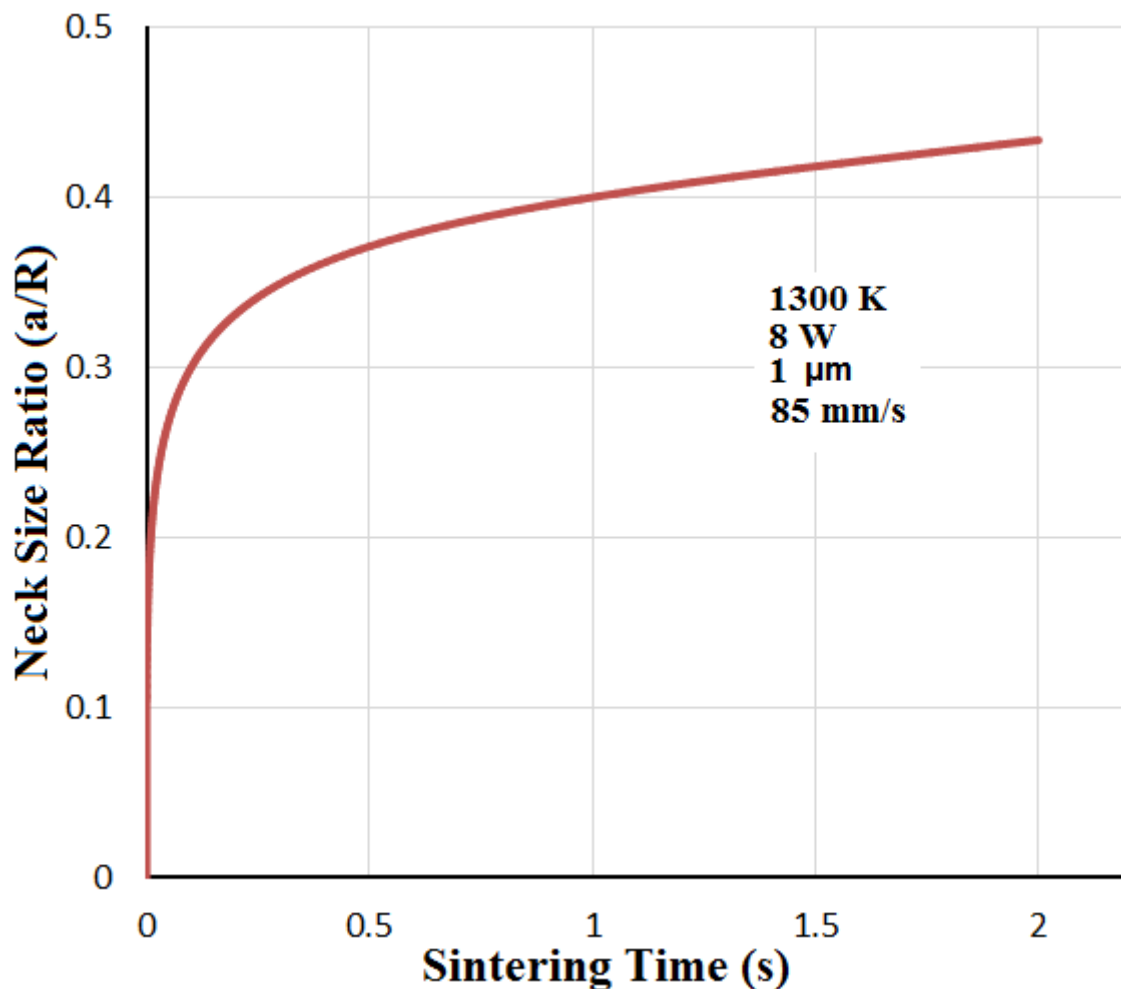


Figure 4-14 Neck size ratio as a function of sintering time.

#### 4.2.9.1 Validation of variational model:

The curve-fitting FD model was used to validate the SLS model for a particle size of 1  $\mu\text{m}$  via neck size ratio, which is a significant parameter in the sintering process. Figure (4-15) shows a comparison of the neck size ratios determined for the finite difference model and variational model. Overall, it was found that the FD curve was in good agreement with the VM curve.

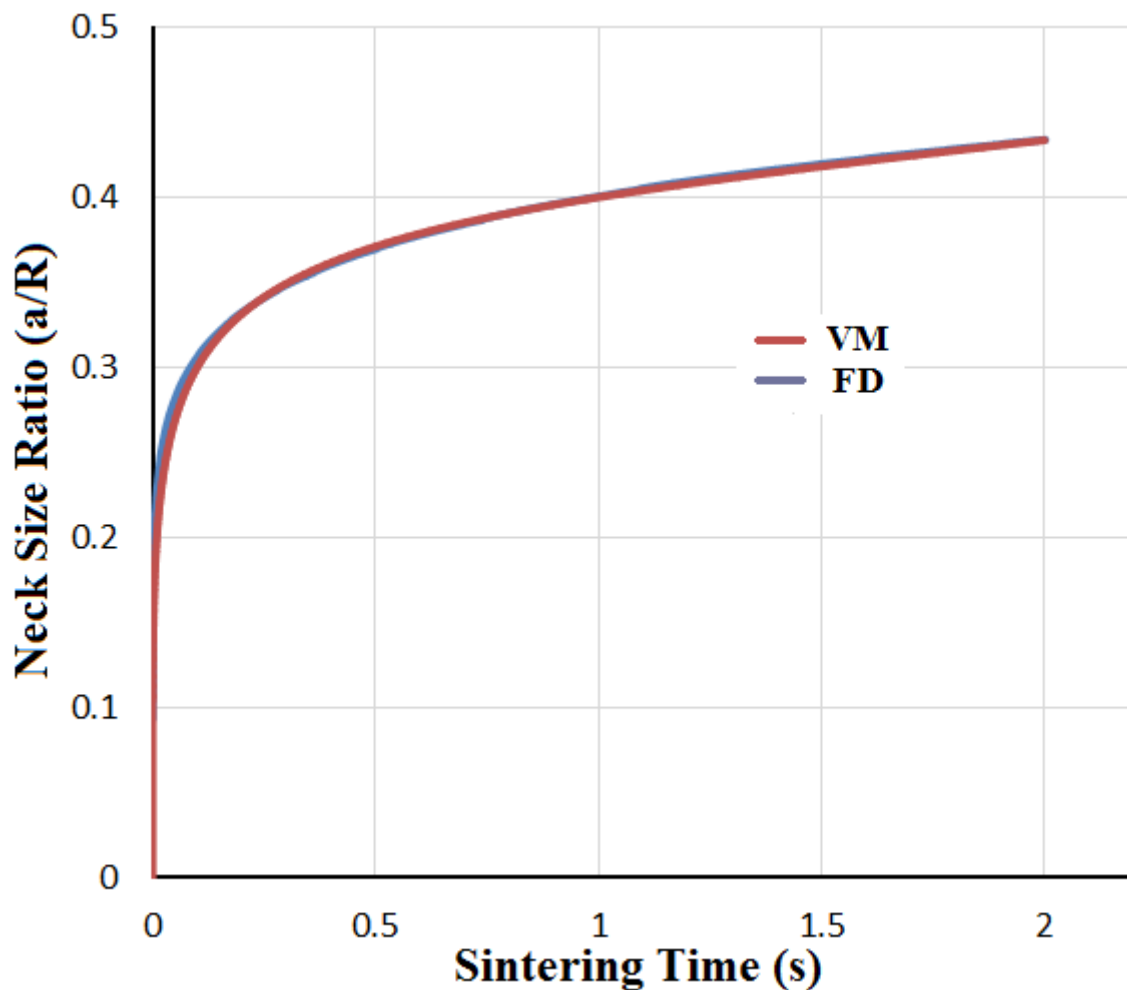


Figure 4-15 A comparison between the two numerical models in terms of neck size ratio for a particle size of 1  $\mu\text{m}$ .

#### 4.2.9.2 The effect of laser scan speed and laser power in the SLS process

The laser scan speed and laser power are the control process parameters that have a direct impact on the SLS process. Also, the laser scan speed and laser power are determined in the COMSOL software, after which these results are used in the variational method code to calculate the sintering parameters.

Figure (4-16) shows the sintering temperatures for all particles using three laser powers as applied to copper particles of 1  $\mu\text{m}$  in size. Three different laser powers, 5, 8 and 10 W, were used in this study to investigate the effects of laser power on the sintering temperature of the particles. It can be seen from this figure that the sintering temperature decreases with increasing laser scan speed, which means that the SLS process is more efficient when the temperature is higher. In addition, the sintering temperature increases with increasing laser power, especially at the final stage of the SLS process, because the laser energy increases due to the increase of laser power and decreasing laser scan speed. This is shown in equation (4-68) [119]. The temperature of the particles due to the laser, as determined from the COMSOL software, are utilized in the sintering model using grain boundary and surface diffusion coefficient equations (3-13) and (3-14), respectively. From these equations, one can change the sintering temperature of particles in the sintering simulation, thus the neck and shrinkage ratios are changed by adjusting laser power and laser scan speed, which affect the temperature of the particles.

$$E_L = \frac{P}{D_L S_L} \quad (4 - 68)$$

Where  $E_L$  is the laser energy,  $P$  is the laser power, and  $S_L$  is the laser scan speed. Lastly  $D_L$  is the diameter of the laser beam[119].

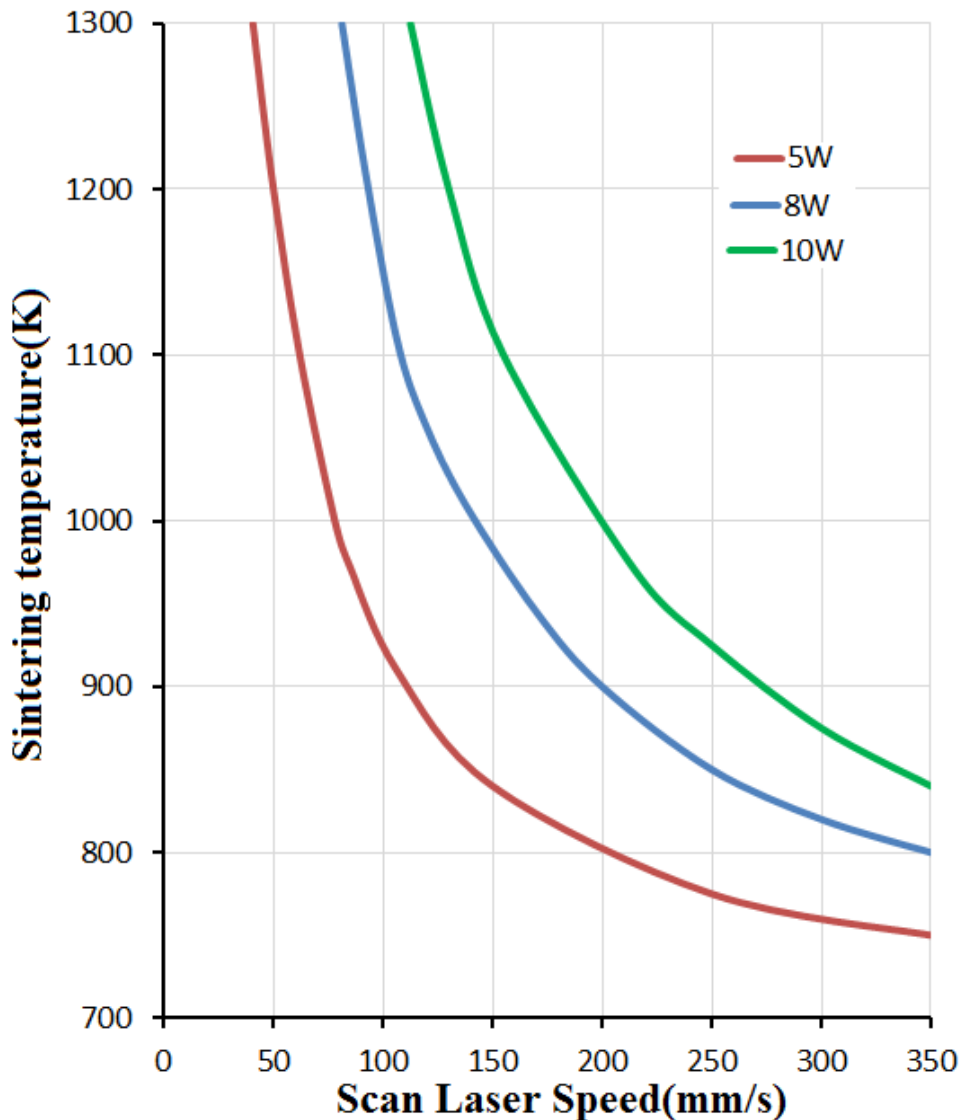


**Figure 4-16 Sintering temperature as a function of laser scan speed for a particle size of  $1\mu\text{m}$ .**

Figure (4-17) shows the neck size ratio between particles for three laser powers using a particle size of  $1\mu\text{m}$ . Three different laser powers, 5, 8 and 10 W, were used in this study to investigate the effect of laser power on the SLS process. It can be seen from the diagram that the neck size ratio decreases with increasing laser scan speed, which means that the SLS process is more efficiency when the scan speed is low, and further that the sintering temperature increases with decreasing laser scan speed. As shown in figure (4-17), the neck size ratio increases with increasing laser power, especially

in the final stage of the SLS process, which means that the SLS process itself is improved with increased laser power. Also, the minimum scan speed is 40 mm/s at a laser power of 5 W at the beginning of the SLS process, while the maximum scan speed is 350 mm/s, which is the same used for all laser powers. In addition, the maximum neck size ratio is 0.433, which is the same for all laser powers at the beginning of the SLS process while the maximum neck size ratio is 0.17 at a laser power of 10 W for the final stage.

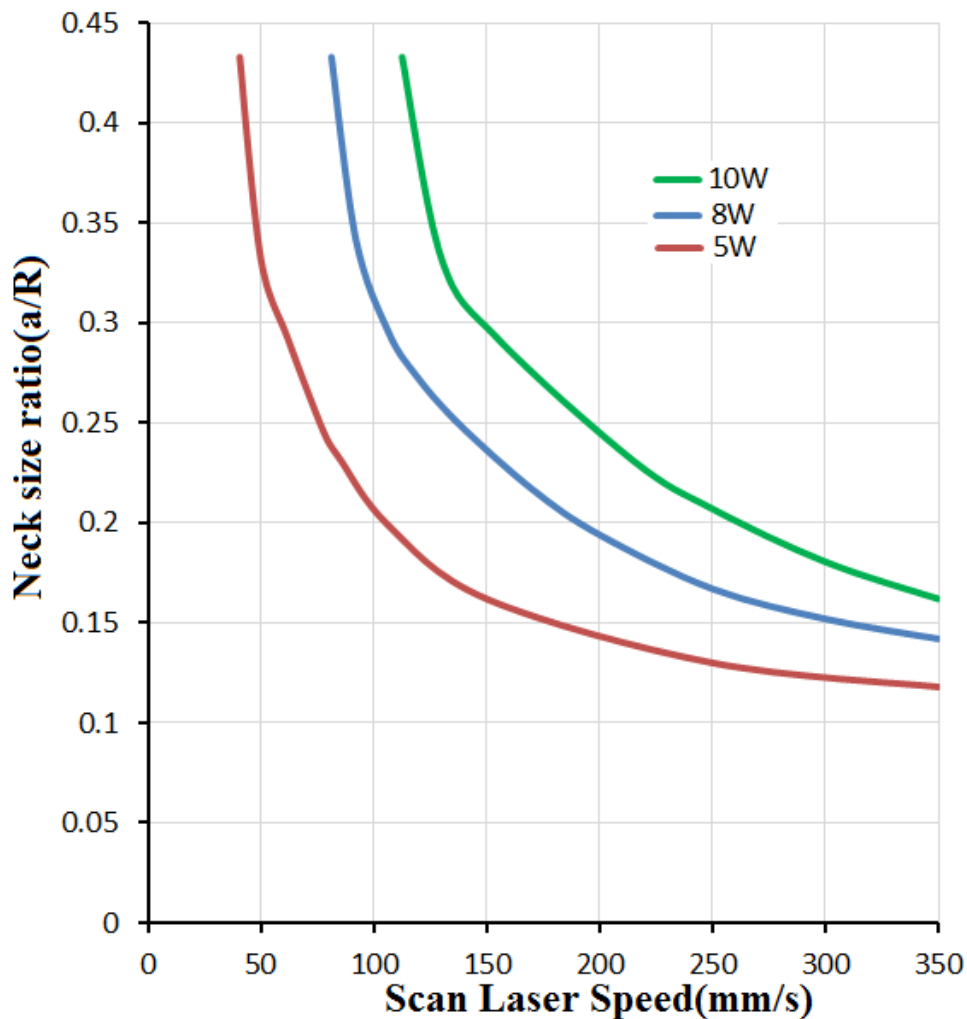


**Figure 4-17 Neck size ratio as a function of laser scan speed for three different laser powers and a particle size of 1  $\mu\text{m}$ .**

Figure (4-18) shows the shrinkage ratio between particles for three laser powers using a particle size of 1  $\mu\text{m}$ . Three different laser powers, 5, 8 and 10 W, were used in this study to investigate the effects of laser power on densification between particles during the SLS process. It can be seen from the diagram that the shrinkage ratio decreases with increasing laser scan speed, which means that the SLS process leads to greater densification when the scan speed decreases. As shown in figure (4-18), the shrinkage ratio increases with increasing laser power, especially in the final stage of the SLS process, which means that there was an improvement in shrinkage ratio due to the increase in temperature with laser power. Also, the maximum shrinkage ratio was 0.088, which was the same for all laser powers at the beginning of the SLS process, while the maximum shrinkage ratio was 0.013 at a laser power of 10 W for the final stage of the SLS process.

Figure (4-19) illustrates laser power as a function of laser scan speed for copper particles with a particle size of 1  $\mu\text{m}$ . Overall, it can be seen from diagram that the laser power increases with increasing laser scan speed, which is because equation (4-68) shows the laser power dependence on laser scan speed for the same size. Also, the maximum laser power was 25 W at a scan speed of 220 mm/s, while the minimum laser power was 5 W at a scan speed of 40 mm/s.

As shown in figure (4-19), the laser power and laser scan speed are two important factors in the SLS process. These factors can control the process, but the problem is in the specification of the powder. The sintering temperature increases due to the increase of laser power with increasing laser energy, and so the sintering temperature may reach powder melting temperature, which will be out of condition for the SLS process. The same is true for laser scan speed, where the sintering temperature increases due to the decrease of laser scan speed, and hence the importance of this factor.

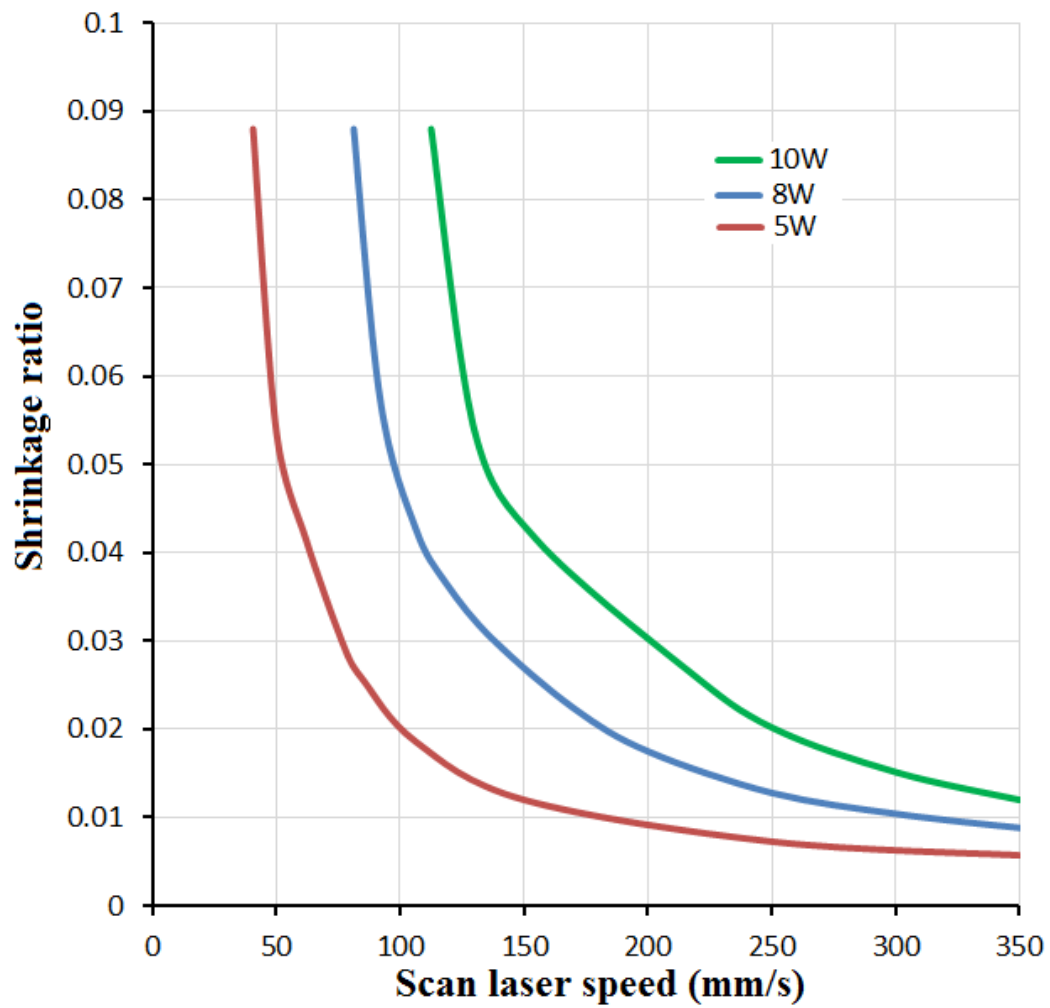
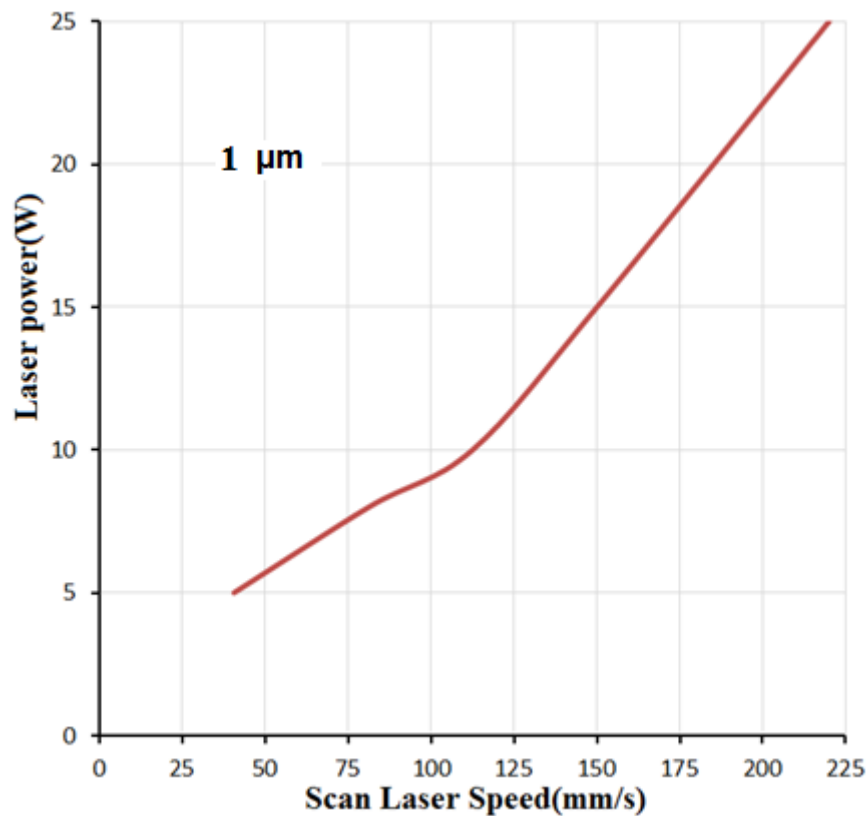
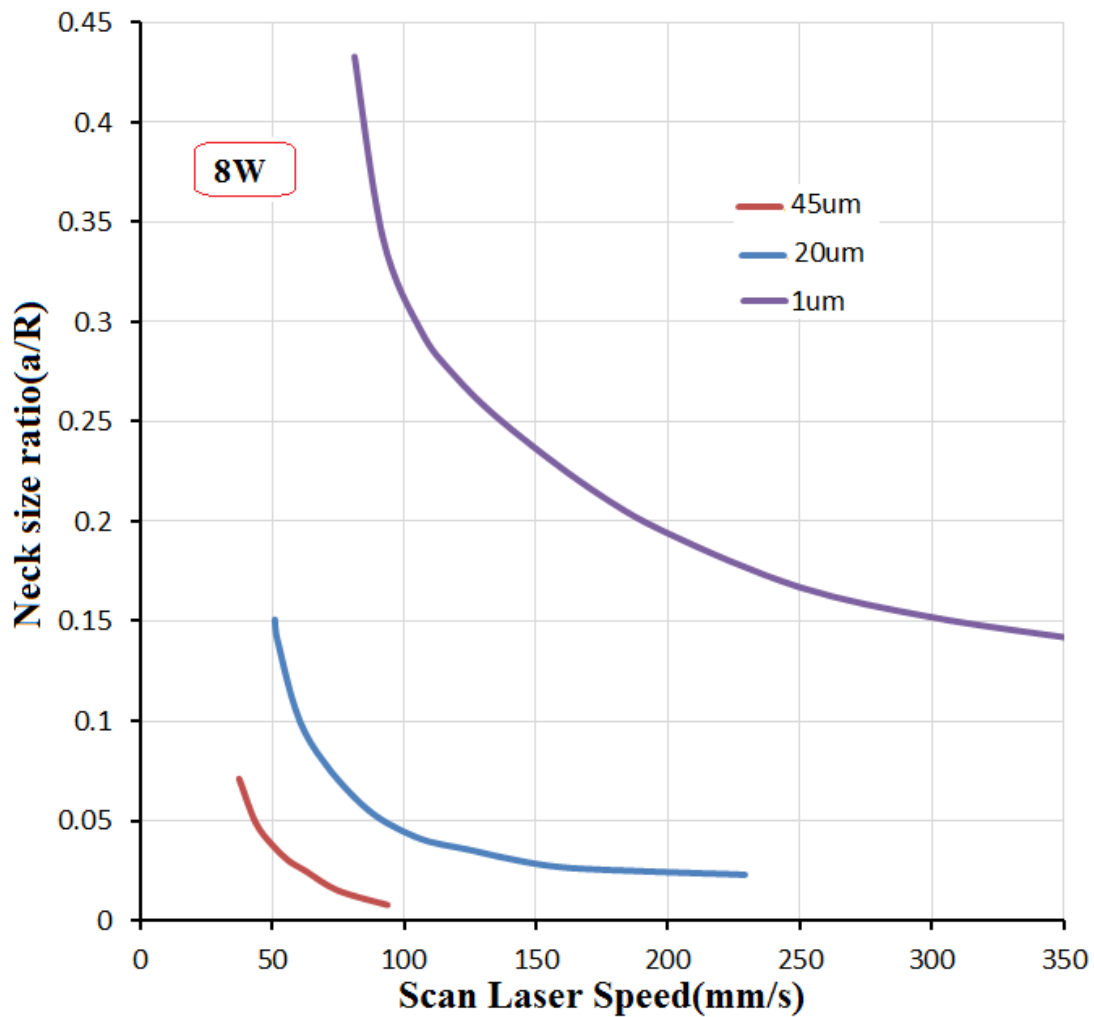


Figure 4-18 Shrinkage ratio as a function of scan laser speed for three different laser powers and particle size 1  $\mu\text{m}$ .



**Figure 4-19 Laser power as a function of laser scan speed for copper particles and a particle size of 1  $\mu\text{m}$ .**

Figure (4-20) illustrates a neck size ratio between particles for two steps of the laser scan using different particle sizes. Three different particle sizes, 1, 20, and 45  $\mu\text{m}$ , were used to investigate the effect of particle size on the SLS process; moreover, a laser power of 8 W was used to calculate the neck size ratio with different particle sizes. Overall, it can be seen from the figure that the neck size ratio decreases with increasing laser scan speed, which means that the SLS process is more efficient when the scan speed is reduced. Also, the maximum neck size ratio is 0.433 for a particle size of 1  $\mu\text{m}$  at a laser scan speed of 85 mm/s, while the maximum neck size ratio is 0.0726 for a particle size of 45  $\mu\text{m}$  at a laser scan speed of 43 mm/s at the beginning of the SLS process.



**Figure 4-20 Neck size ratio between particles for four different particle sizes and a laser power of 8 W.**

Figure (4-21) illustrates the maximum and minimum laser scan speeds for copper particles. A laser power of 8 W was used in the model to calculate the effects of different particle sizes on the SLS process. Overall, it can be seen from the figure that the laser scan speed increases with decreasing particle size. Also, the difference between the maximum and minimum laser scan speed for a particle size of 1  $\mu\text{m}$  is greater than for a particle size of 45  $\mu\text{m}$ , which means that the scan speed for a 1  $\mu\text{m}$  particle size is the most efficient. In addition, the difference between the maximum and minimum laser speeds converges when particle size increases. The maximum

difference between the curves was 269 mm/s at a particle size of 1  $\mu\text{m}$ , while the minimum difference between the curves was 55 mm/s at a particle size of 45  $\mu\text{m}$ .

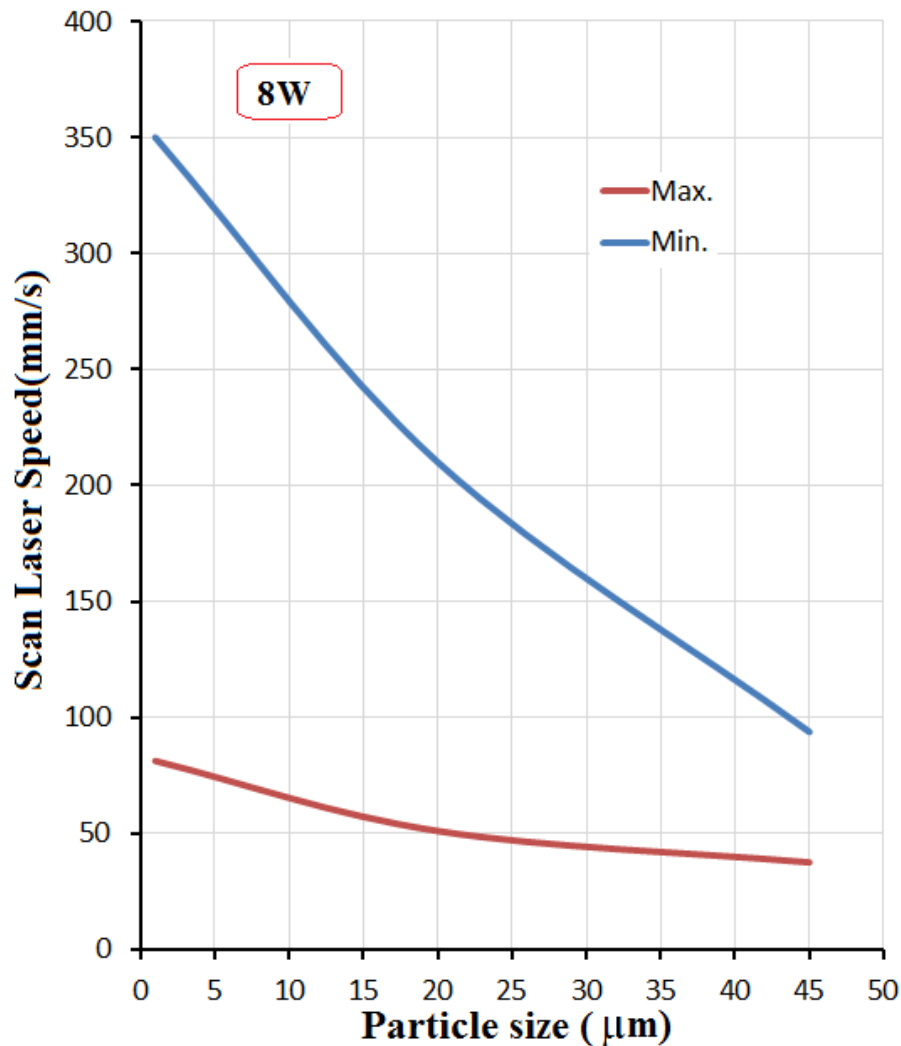


Figure 4-21 Laser scan speed as a function of particle size for a laser power of 8 W.

Figure (4-22) shows the maximum and minimum neck size ratios for copper powder using different particle sizes for a laser power of 8 W. As shown in the figure, the maximum neck size ratio was 0.433 at a particle size of 1  $\mu\text{m}$ , while the minimum neck size ratio was 0.142 at a particle size of 1  $\mu\text{m}$ . In addition, the maximum difference

between the curves was 0.291 at a particle size of 1  $\mu\text{m}$ , while the minimum difference between the curves was 0.0632 at a particle size of 45  $\mu\text{m}$ .

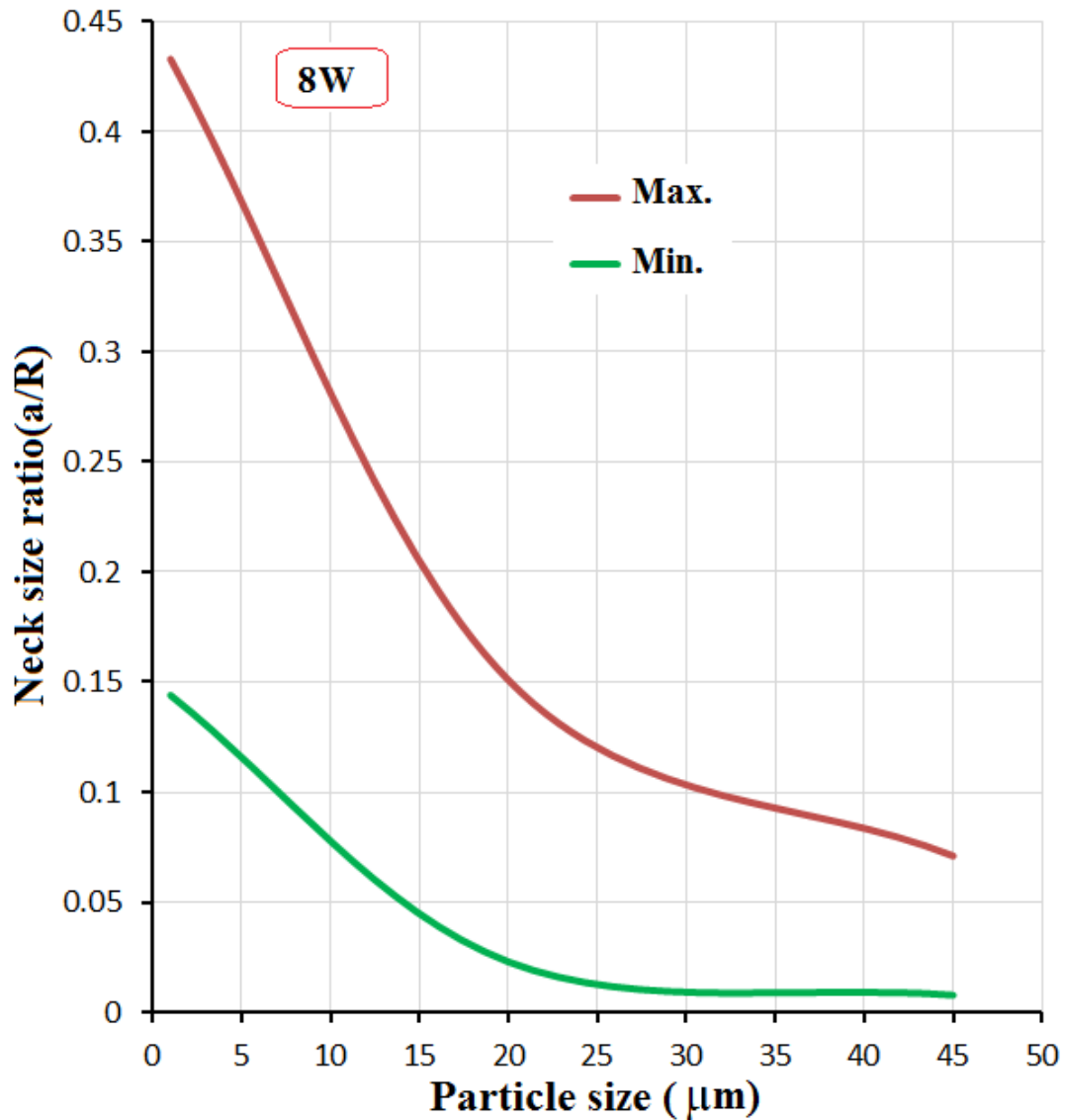


Figure 4-22 Neck size ratio as a function of particle size for a laser power of 8 W.

The relative density of the particles is calculated using the VM code in order to determine the densification between particles during the SLS process. Equation (3-20) was used in the VM model to determine the relative density, where the initial relative

density was calculated to be 0.523234, which was used as input to the numerical code. Figure (4-23) shows the relative density as a function of sintering time, where this curve was obtained from the VM simulation. A laser scan speed of 85 mm/s, a laser power of 8 W and a particle size of 1  $\mu\text{m}$  were used as inputs to the numerical simulation. It can be seen that there was a relative density increase with increasing sintering time, which means that the increase in relative density leads to an increase in densification in the SLS process, and a decrease in the porosity. This is because the densification process depends on the neck radius between particles which increases due to the increase in grain boundary diffusion. Also, the maximum relative density was 0.69 at 2 s, while the initial relative density was 0.5233 at the initial stage of the SLS process.

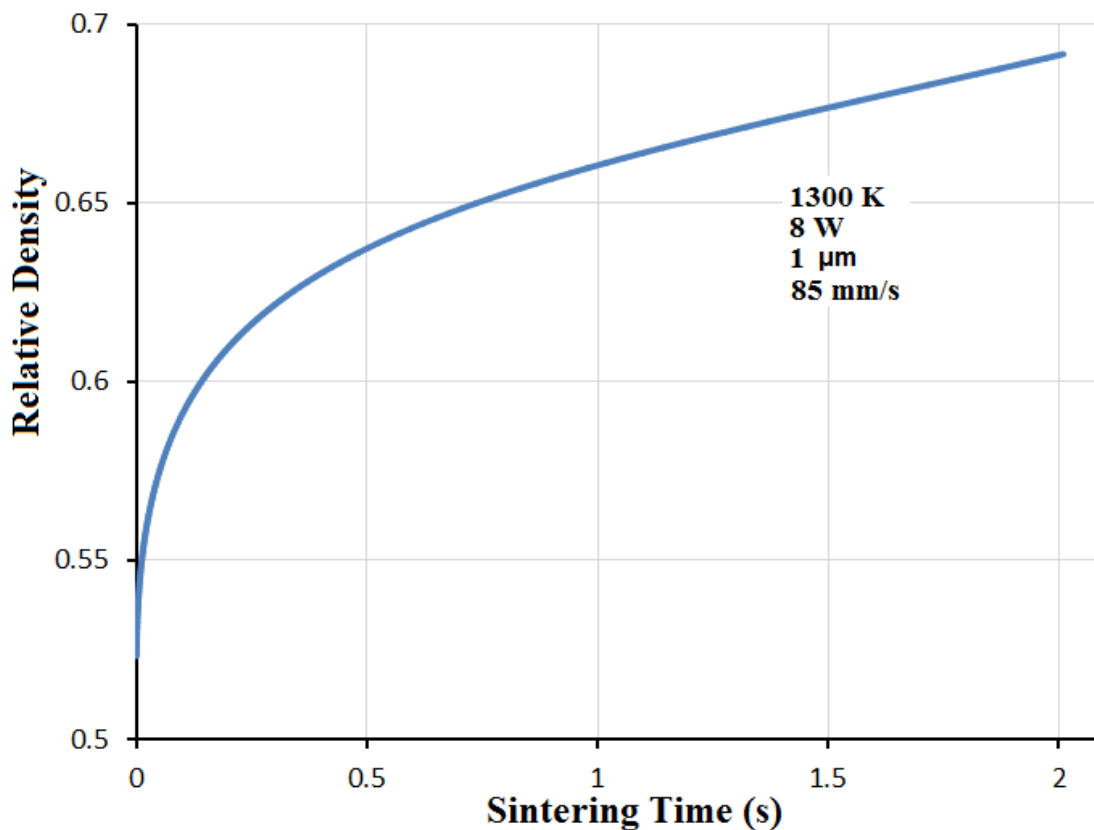


Figure 4-23 Relative density as a function of sintering time.

Figure (4-24) shows relative density as a function of neck size ratio between particles, where this curve was obtained from the numerical simulation. A laser scan speed of 85 mm/s, a laser power of 8 W, and a particle size of 1  $\mu\text{m}$  were used as input to the numerical simulation. Overall, it was found that the relative density increased with increasing neck size ratio, which means that increases in relative density depend on an associated increase in neck growth. Also, the maximum relative density was 0.69 at a neck size ratio of 0.433, while the initial relative density was 0.5233 at the initial stage of the SLS process.

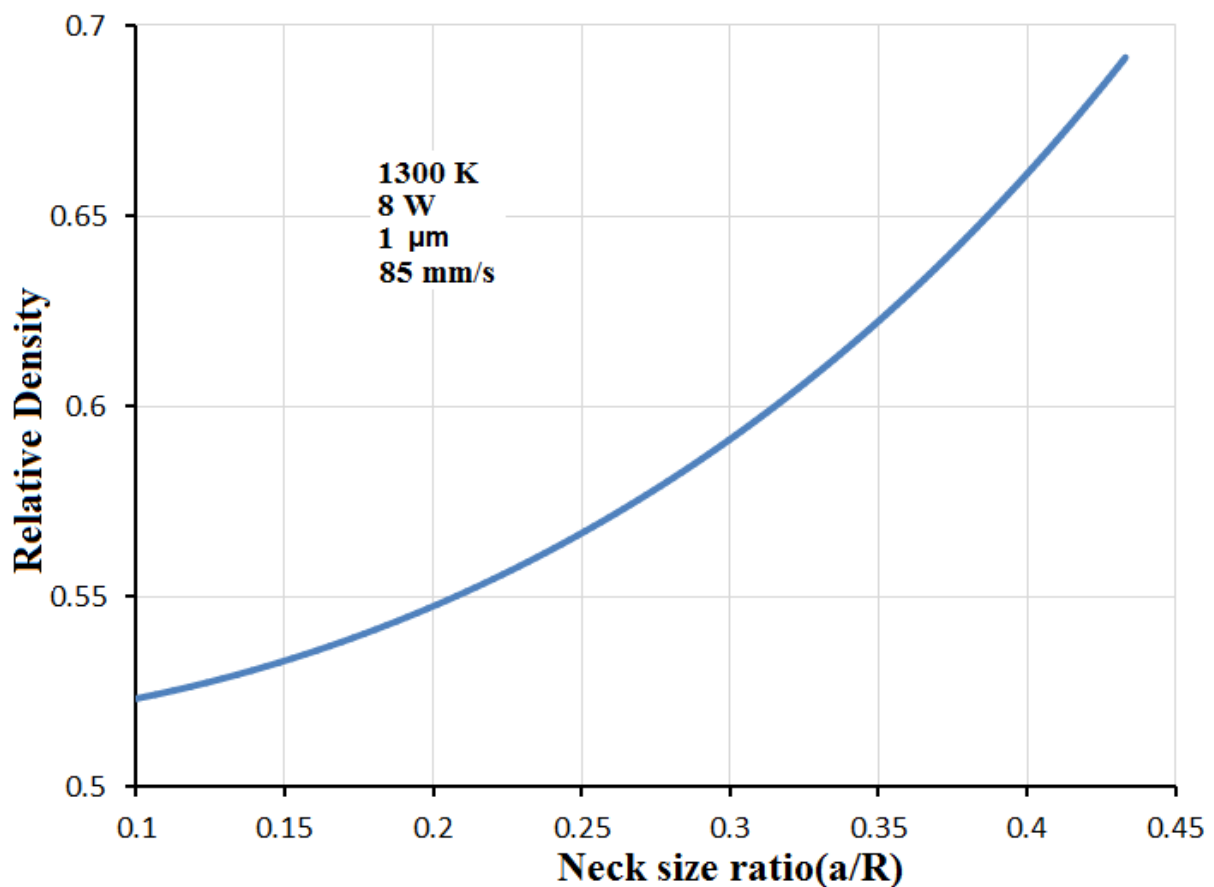
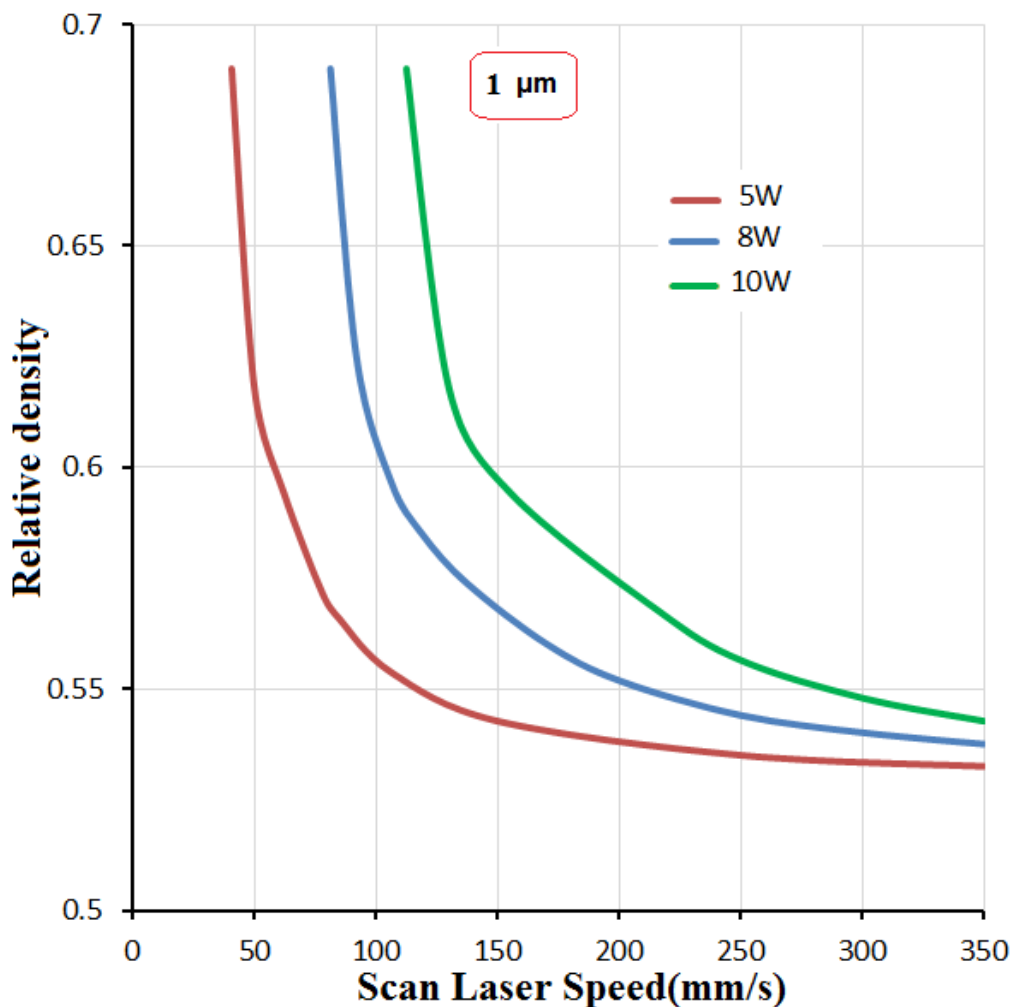


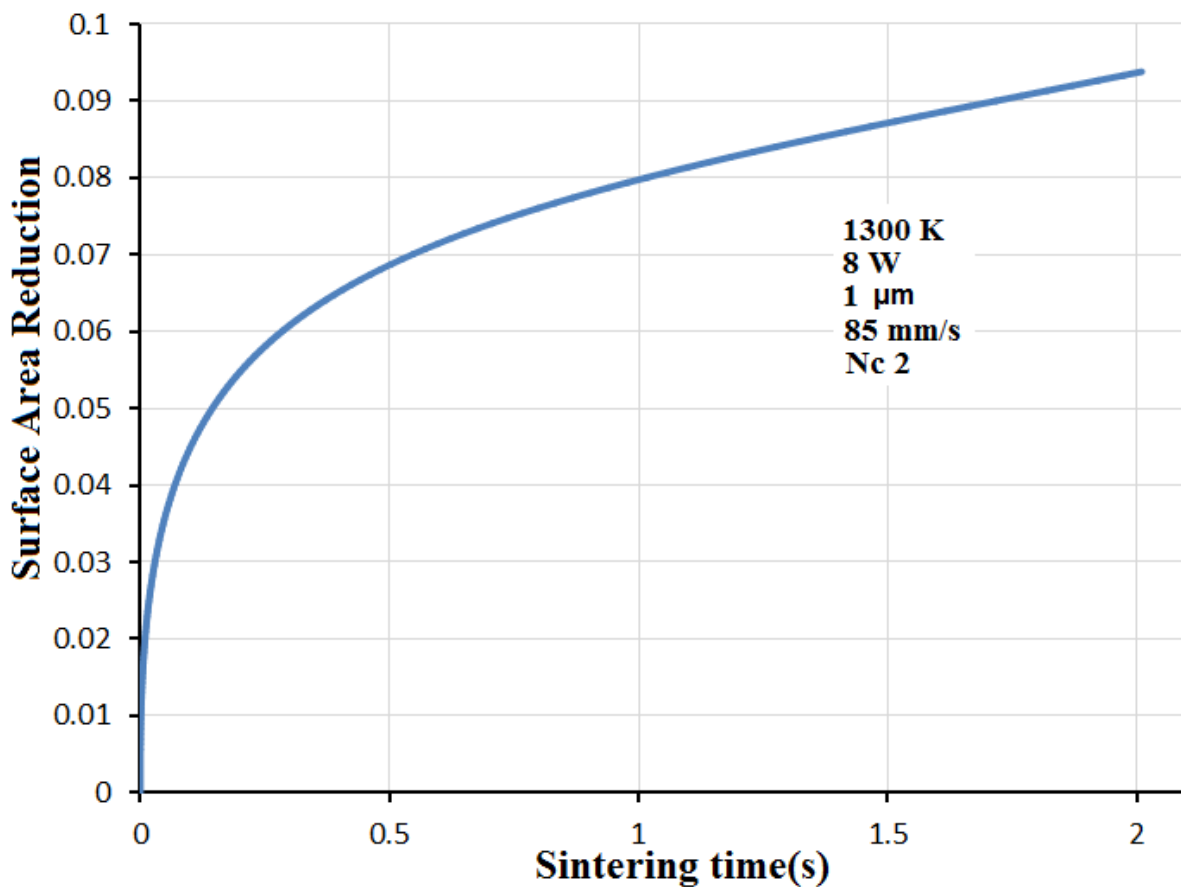
Figure 4-24 Relative density as a function of neck size ratio.

Figure (4-25) illustrates the relative density between particles after completion of the SLS process using different laser powers at a particle size of 1  $\mu\text{m}$ . Three different laser powers, 5, 8 and 10 W, were used to investigate the effects of laser power on the SLS process. Overall, it can be seen from this figure that relative density decreases with increasing laser scan speed. In addition, the relative density increases with increasing laser power, especially during the final stage. Also, the maximum relative density was 0.69, which was the same for all laser powers at the beginning of the SLS process, while the maximum relative density was 0.54 at a laser power of 10 W for the final stage of the SLS process.



**Figure 4-25 Relative density as a function of a laser scan speed for different laser powers and a particle size of 1  $\mu\text{m}$ .**

Figure (4-26) shows the reduction in surface area as a function of sintering time for copper particles, where this result was obtained from the VM numerical model. Equation (3-19) was used in the numerical modelling program to determine the surface area reduction and particle coordination number,  $N_c$ , which was used as input to the VM code [107]. It may be noted that the reduction in surface area increases with increasing sintering time, which is because the reduction in surface area becomes greater due to the increase in neck radius, which itself increases due to the increase in sintering temperature. Moreover, the surface area reduction increases sharply in the initial stage of sintering, then slows down during the final stage.



**Figure 4-26 Surface area reduction as a function of sintering time.**

Figure (4-27) shows the surface area reduction as a function of neck size ratio for multiple contact numbers, which is one of the results obtained from the VM model. Overall, it may be noted that the surface area reduction increased with increasing neck

size ratio; moreover, the reduction in surface area ratio increased slightly in the initial stages of sintering, while sharply increasing in the final stage. Also, the surface area reduction increased with increasing particle contact; for example, the particle at the centre of the model has six contacts with other particles, and thus undergoes a greater reduction in surface area than for other particles with less than six contacts.

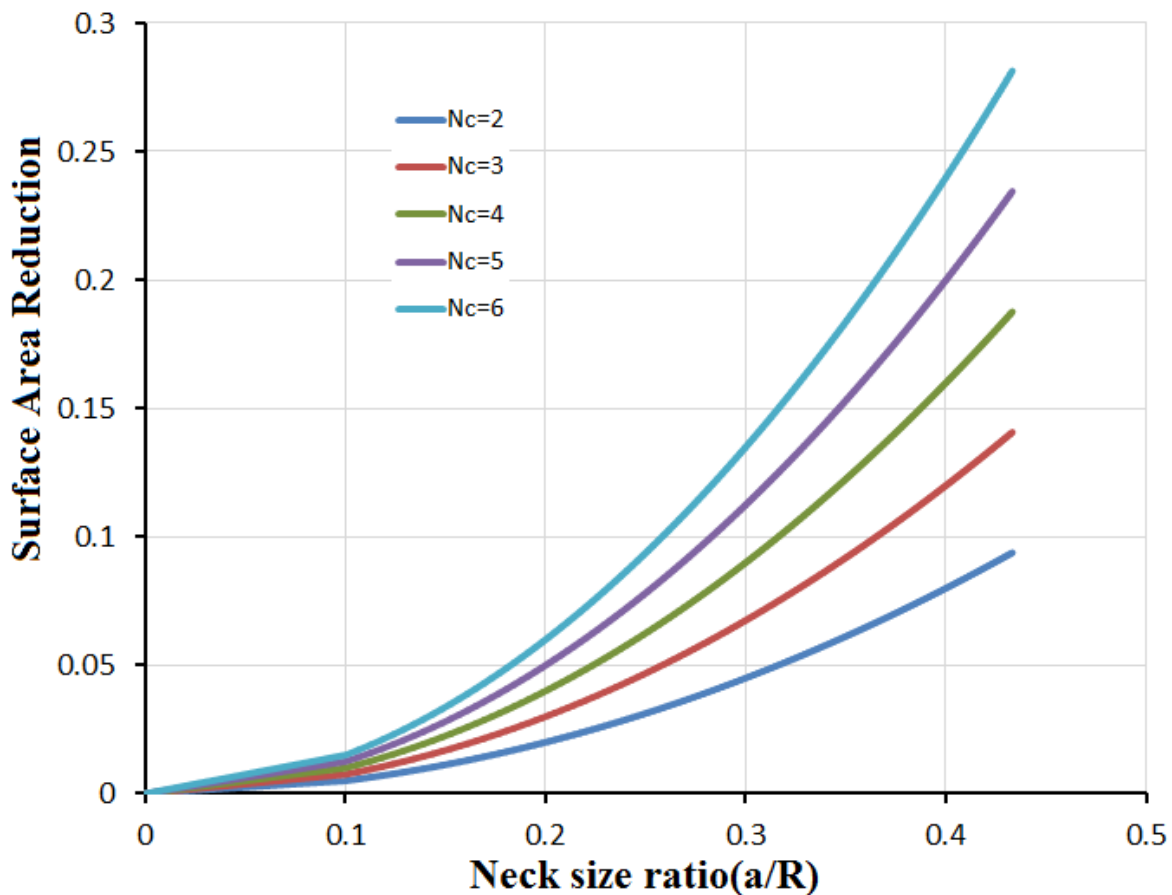


**Figure 4-27** Surface area reduction as a function of neck size ratio for different contact numbers, with a laser power of 8W, and a particle size of 1  $\mu\text{m}$ .

Figure (4-28) shows a reduction in surface area between particles using three different laser powers. Three different laser powers, 5, 8 and 10 W, were used to investigate the effects of laser power on reduction in surface area of the particles. It can be seen

from the diagram that the reduction in surface area decreased with increasing laser scan speed, which means that the SLS process is more efficient when there is an increase in temperature. In addition, each of the curves decreases sharply during the initial stage of the SLS process. Also, the maximum surface area reduction was 0.0937, which is the same for all laser powers at the beginning of the SLS process, while the maximum surface area reduction was 0.014 at a laser power of 10 W for the final stage of the SLS process.

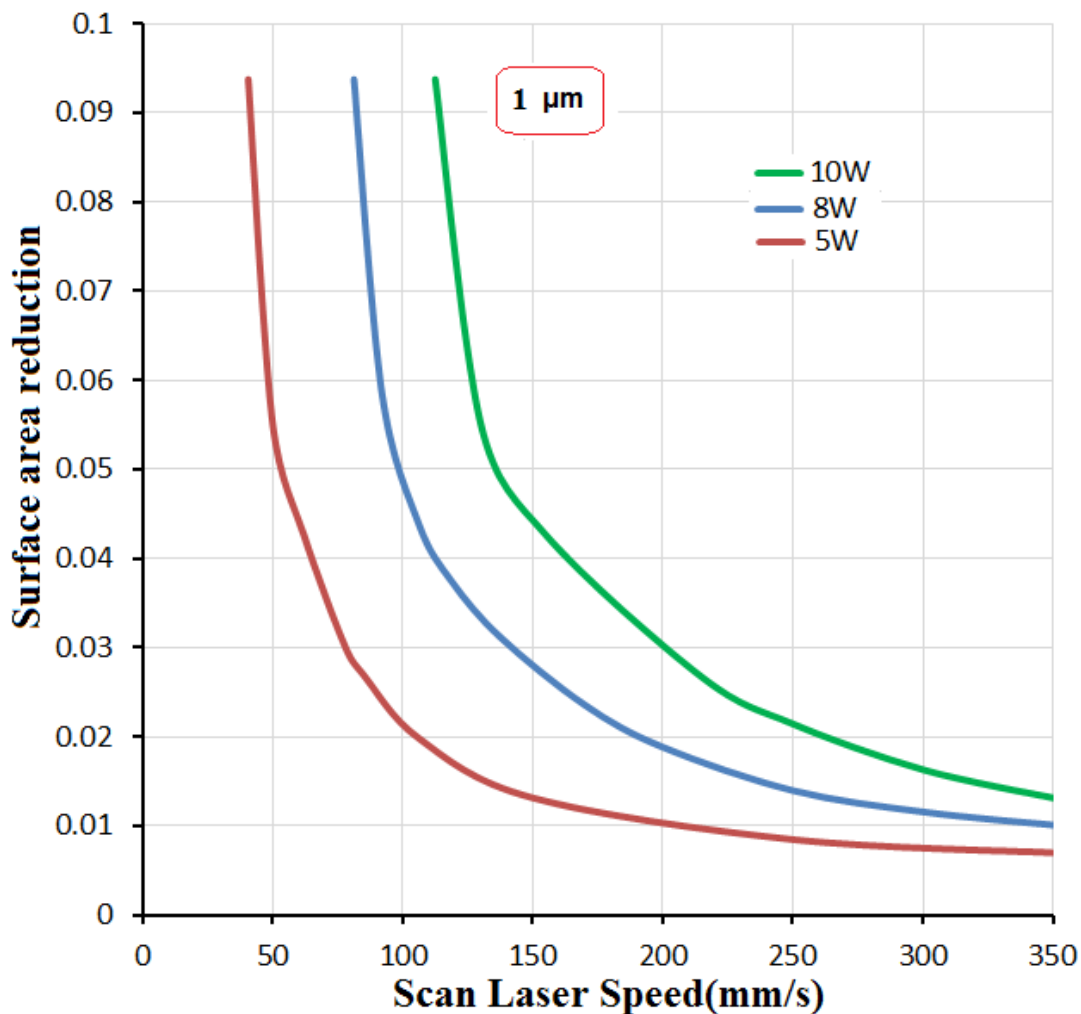


**Figure 4-28** Surface area reduction as a function of laser scan speed for a particle size of  $1 \mu\text{m}$ .

Figure (4-29) illustrates the three curves showing neck size ratio between particles. The highest curve represents the maximum neck size ratio, while the lowest curve

represents the minimum neck size ratio at constant sintering temperature. A particle size of 1  $\mu\text{m}$  and a laser power of 8 W were used in the SLS process. Overall, it can be seen from the figure that the maximum and average neck size ratios decreased with increasing scan speed, while the minimum curve stabilized in the final stage of the SLS process which means that the SLS process is more efficient when the sintering temperature is increased.

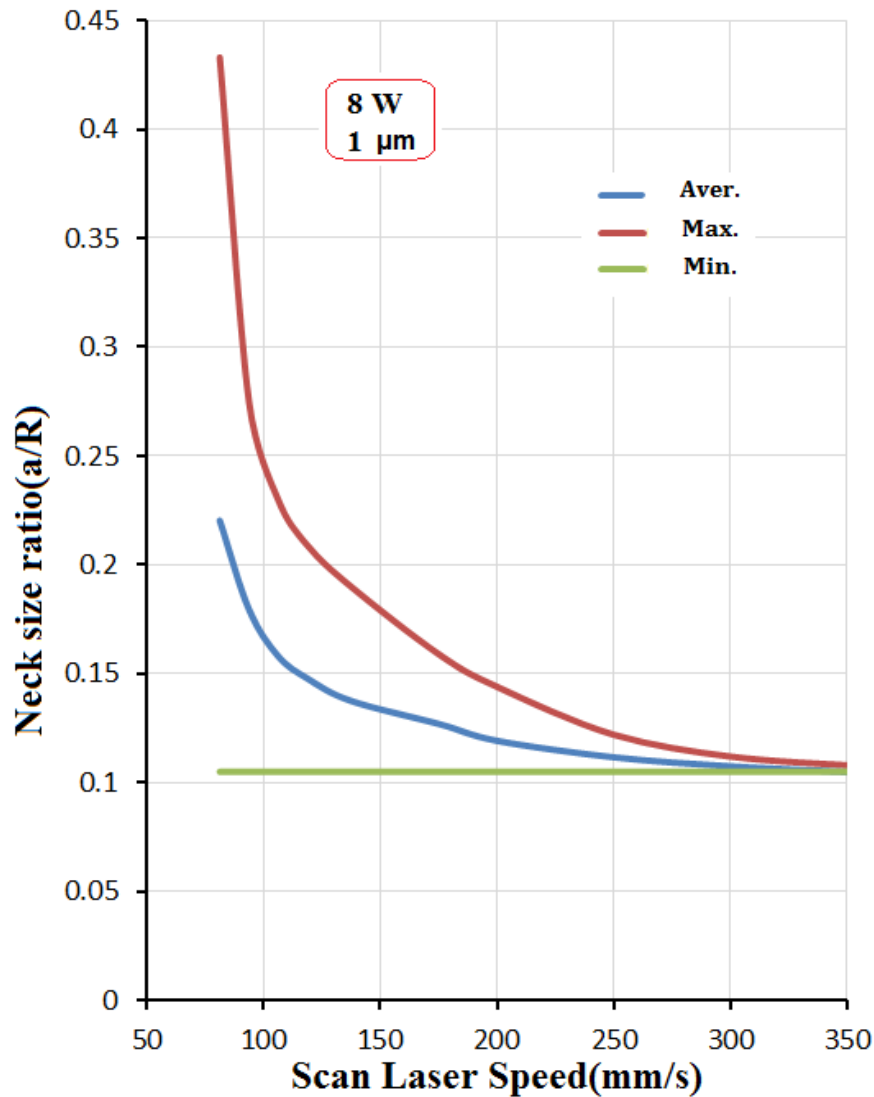


Figure 4-29 Neck size ratio as a function of laser scan speed for a particle size of 1  $\mu\text{m}$ .

Figure (4-30) illustrates the three curves showing the shrinkage ratio between particles. The highest curve represents the maximum shrinkage ratio, while the lowest curve represents the minimum shrinkage ratio at constant sintering temperature. A particle size of 1  $\mu\text{m}$  and a laser power of 8 W were used in the SLS process. Overall, it can be seen from the figure that the maximum and average shrinkage ratios decreased with increasing scan speed while the minimum curve stabilized until the final stage of the SLS process, which means that the SLS process is more efficient when the sintering temperature is increased.

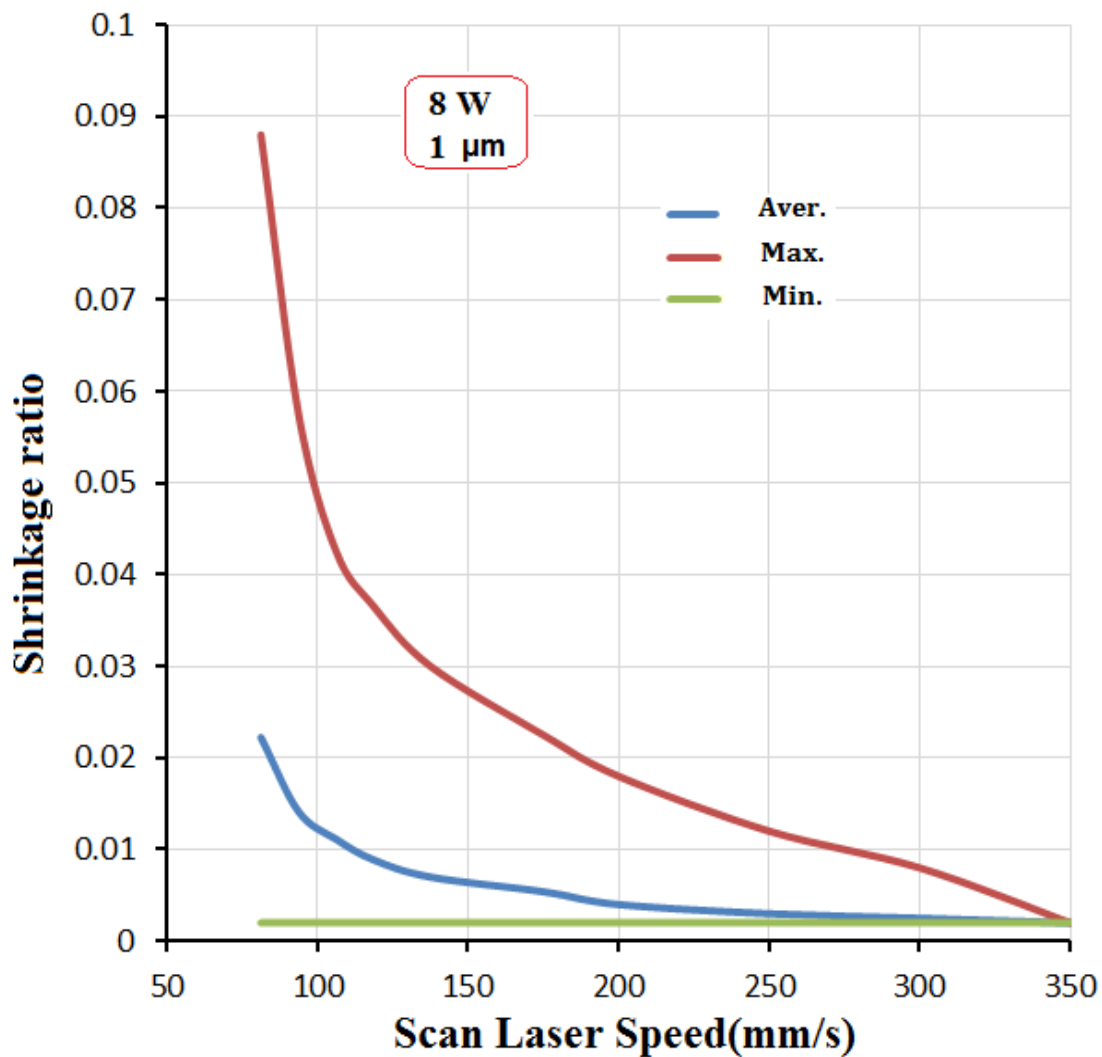
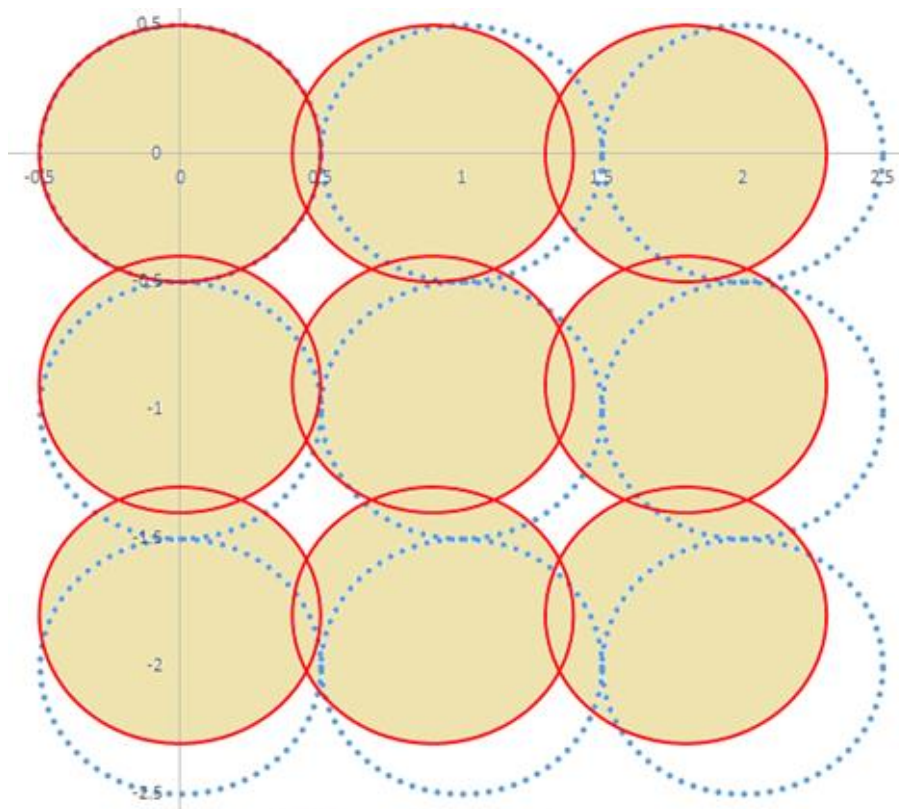


Figure 4-30 Shrinkage ratio as a function of scan laser speed for a particle size of 1  $\mu\text{m}$ .

The densification of the nine particles was obtained from the VM simulation for the route taken by the laser beam in the SLS model, as shown in Figure (4-31). Also figure (4-31) shows the movement of nine particles during the SLS process with a particle size of 1  $\mu\text{m}$ . Thus, the blue circles represent the particles before the SLS process, whilst the red circles demonstrate the particles after the process. Overall, it can be seen that the neck and movement between particles are changed by the laser beam route, as shown in the figure.



**Figure 4-31** The movements of the nine particles in the first layer for a particle size of 1  $\mu\text{m}$ . All dimensions are in microns.

#### 4.2.9.3 Changing particle size:

The effect of particle size on the SLS process is important. This was obtained from the simulation of copper particles, as shown in figure (4-32), which illustrates a plot of

different particle sizes as a function of shrinkage ratio, using a sintering temperature 1300 K and a laser power of 8 W. Different particle sizes (1-45  $\mu\text{m}$ ) were used in this study to investigate the effect of particle size on the SLS process. Overall, it was found that the shrinkage ratio decreased with increasing particle size, which means that SLS is extremely fast with a small particle size. Also, the maximum shrinkage ratio was 0.088 for a particle size of 1  $\mu\text{m}$ , while the minimum shrinkage ratio was 0.00337 for a particle size of 45  $\mu\text{m}$ .

Figure (4-33) shows relative density as a function of particle size. A range of particle sizes were used in the simulation at a fixed laser power of 8 W. Overall, it can be seen that the relative density decreased with increasing particle size which means that the SLS process is more efficient when the particle size was small. Also, the maximum relative density is 0.69 for a particle size of 1  $\mu\text{m}$ , while the minimum relative density was 0.53 for a particle size of 45  $\mu\text{m}$ .

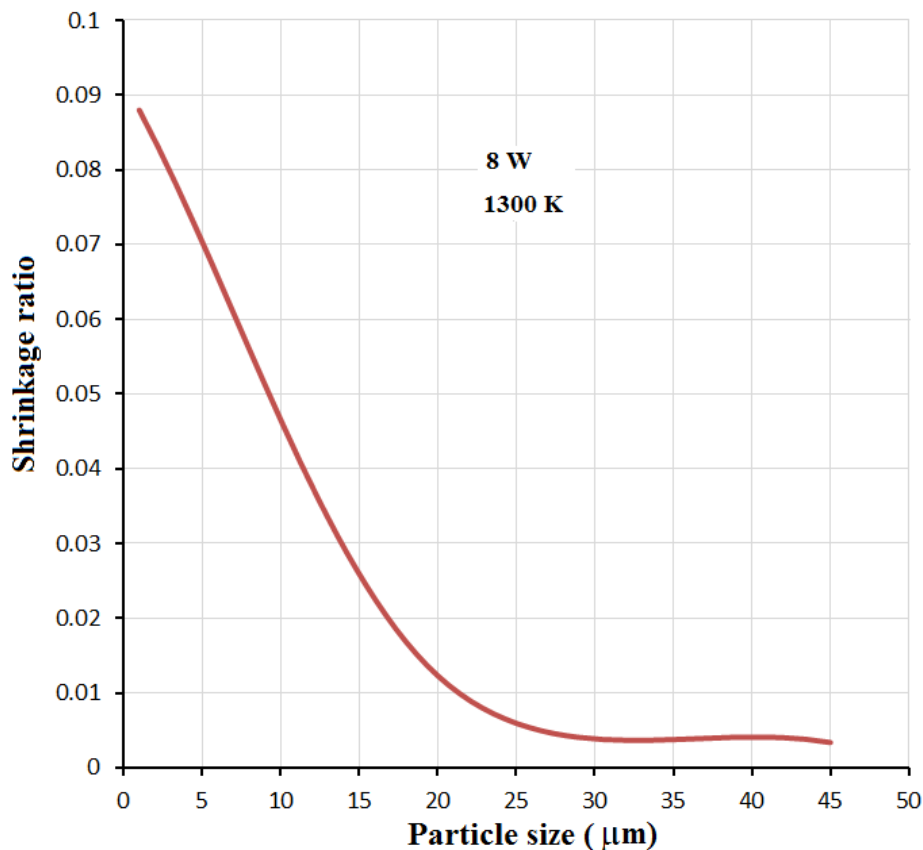


**Figure 4-32 Shrinkage ratio as a function of particle size.**

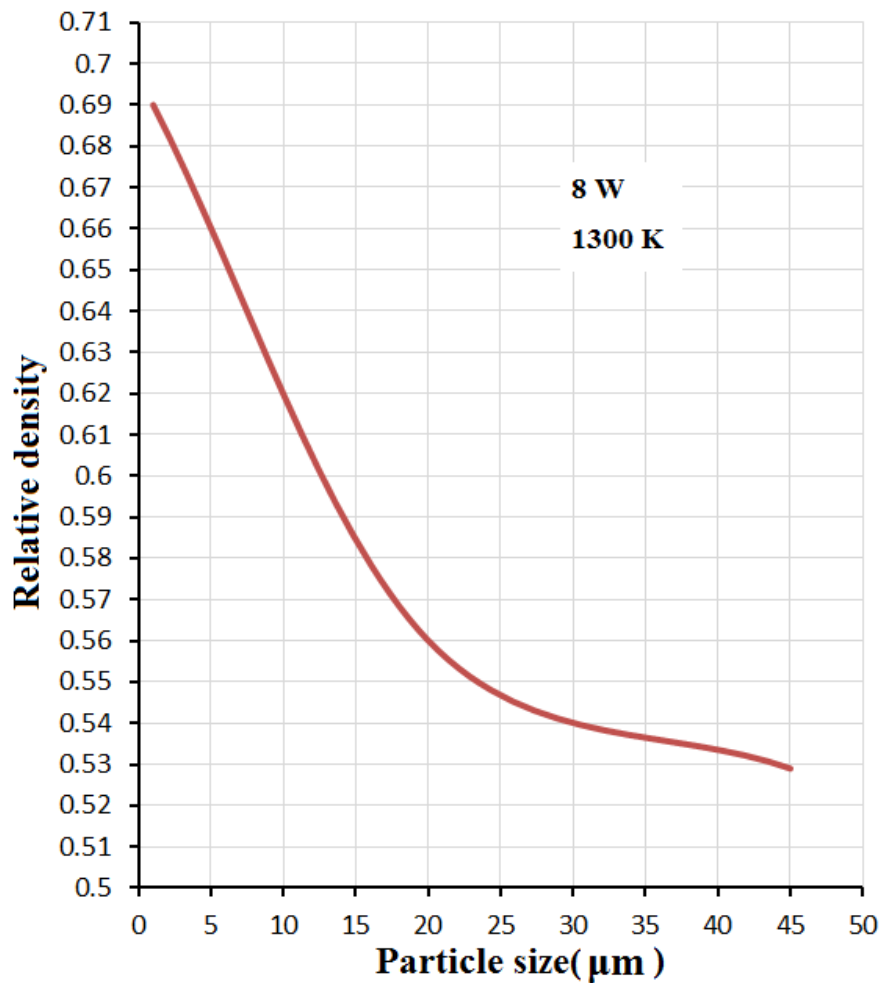


**Figure 4-33 Relative density as a function of particle size.**

Figure (4-34) illustrates surface area reduction as a function of particle size. A range of particle sizes were used in the simulation for a sintering time of 2 s for copper particles using a laser power of 8 W. Overall, it can be seen from the diagram that the surface area reduction decreases with increasing particle size. Also, the maximum surface area reduction is 0.0937 for a particle size of 1 µm, while the minimum surface area reduction is 0.0025 for a particle size of 45 µm.

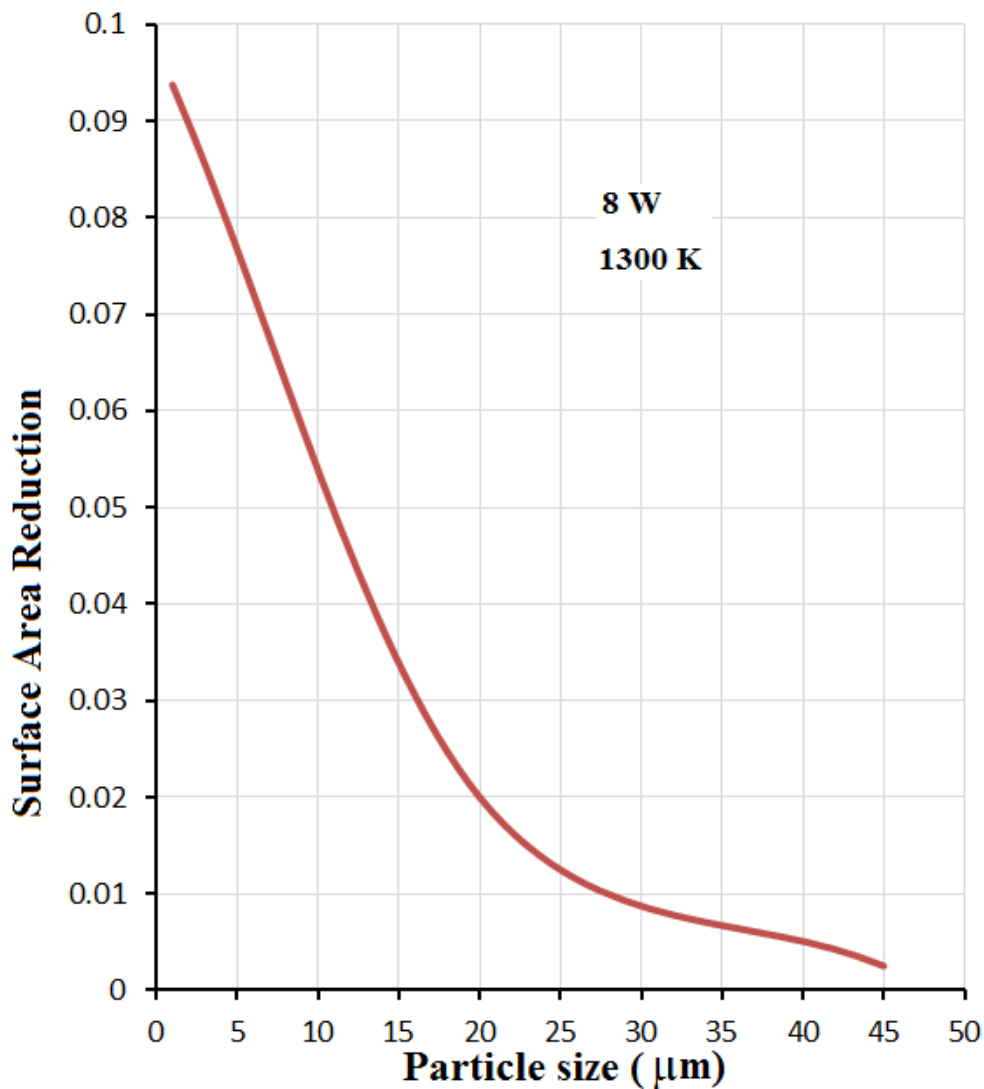


Figure 4-34 Neck size ratio as a function of particle size.

#### 4.2.10 Grain boundary diffusion coefficient as affecting the movement of particles:

Grain boundary diffusion plays an essential role in the sintering process, especially in the densification and the neck growth between particles; the densification increases due to the increase in grain boundary diffusion coefficient, because the increase in the size of the neck radius between particles. Figure (4-35) shows the movement of

particles for the second layer of a particle size of  $6\mu\text{m}$  at a sintering time of 40 s. It was found that the movement of particles was inward, even when the effect of the grain boundary diffusion mechanism is not taken into account in the SLS process.

#### **4.2.10.1 The effect of two connections:**

The SLS model of 27 particles was applied to find the effects of the diffusion coefficient on particle 18 in order to show the behavior of this particle with regards to the others. Thus, figure (4-36) shows the movement of particles for the second layer, as for the movement of particle number 18. It can be seen to acting differently compared to the other particles when a high initial diffusion coefficient is used ( $D_{go} = 100$ ). The particle moves diagonally to right and front side, because of this movement the particle doesn't have any contact with particles 16 and 24 and so particle 18 leaves those two particles without connection, and happened at 40 s.

#### **4.2.10.2 The effect of one connection:**

The movements of particles in the single layer were obtained through numerical methods. Figure (4-37) shows the movement of particles in the second layer with regards to the movement of particle number 18. The movement changes when a higher initial diffusion coefficient is used ( $D_{go} = 100$ ), this time particle 18 moves to the left hand side. Because of this movement the particle does not have contact with the particle to the right of it, this happened at 40 s.

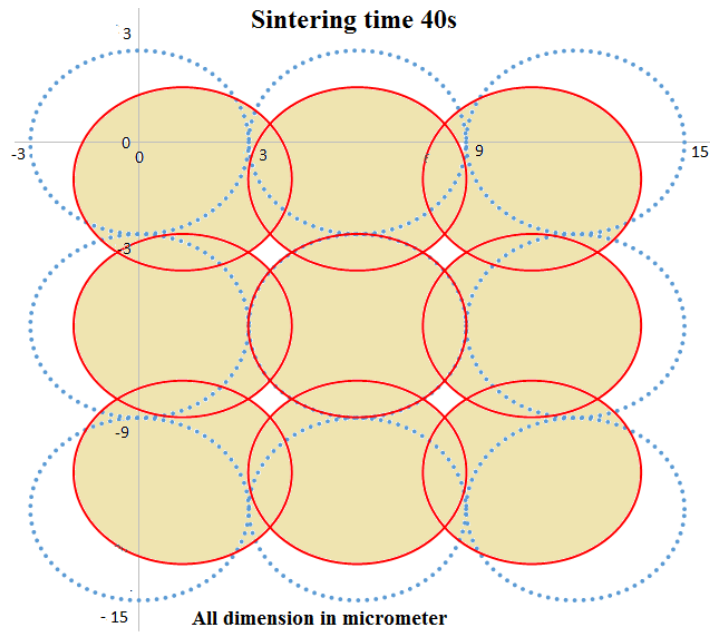


**Figure 4-35** The movement of the nine particles in the second layer.

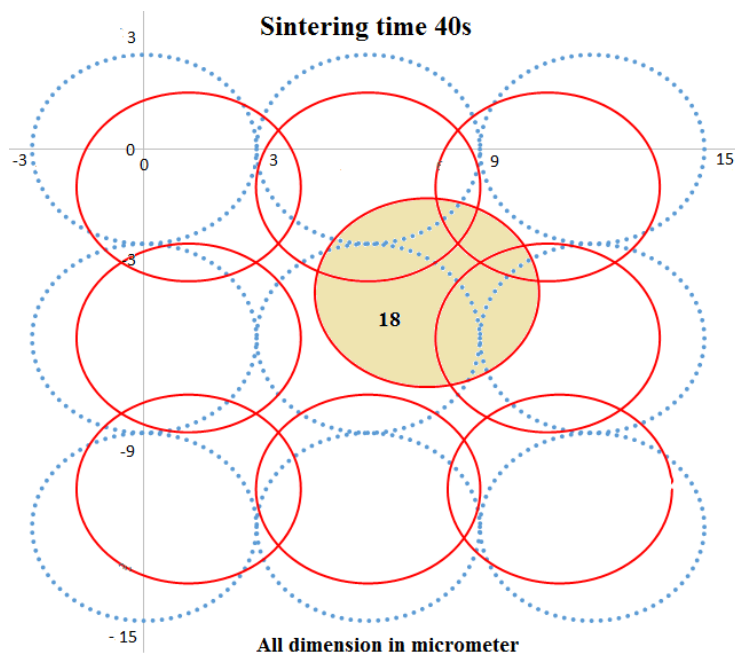


**Figure 4-36** The movement of particle 18 to the front right due to the effects of grain boundary diffusion.

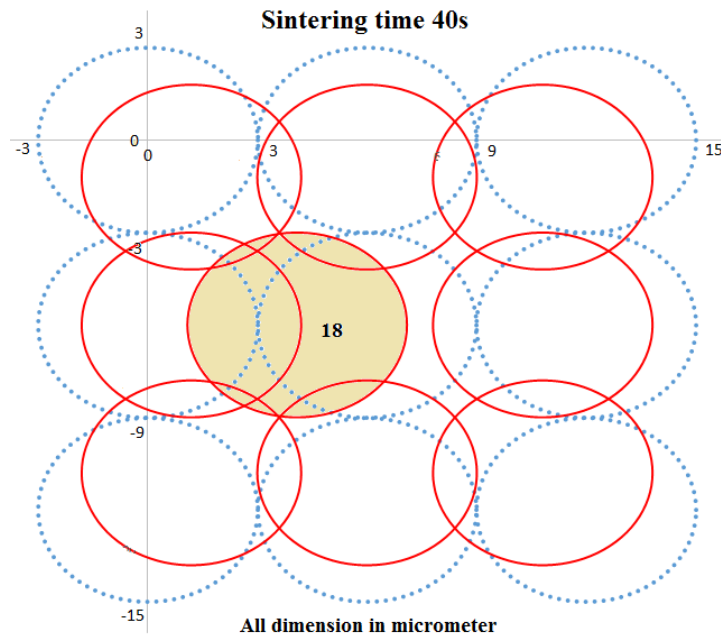


**Figure 4-37 The movement of particle 18 to the left.**

Figure (4-38) shows the movement of the particles in the second layer with respect to the movement of particle number 18. The movement changes when a higher initial diffusion coefficient is used ( $D_{go} = 100$ ), this time particle 18 moved forwards. Because of this movement the particle does not have contact with the particle to the behind it, this happened at 40 s.

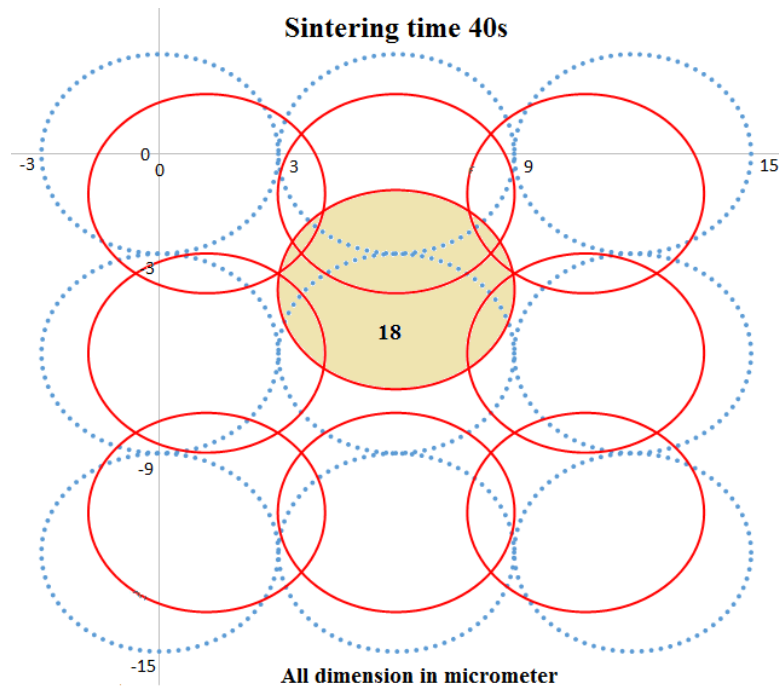


**Figure 4-38 Shows the movement of particle 18 to the front.**

### 4.3 Summary

Firstly, the summary for the first part of chapter four focus on the comparison for neck growth ratio for the FD curve-fitting and VM curve-fitting models to show the variational model is appropriate for use in describing the sintering process, as modelled using two copper powders. The VM curve fitting results using copper powder were in good agreement with the FD curve fitting results for the neck size.

Secondly, the summary for the second part of chapter four focus on the modelling of selective laser sintering process for 27 identical particles using the variational model for sintering between particles and a thermal model of the COMSOL software describing a laser beam and particle temperatures. Overall, the numerical code models the movement of laser beam over all spherical copper particles. Thus, the summary of the second part of chapter four clarified the following points:

- 1- A copper particle size of 1  $\mu\text{m}$  gave a higher neck growth ratio of 0.43, a relative density of 0.69 and a densification of 0.088 during the SLS process than large particle size, such as, 45  $\mu\text{m}$ .
- 2- The curve of neck size ratio of (VM curve fitting) model matched with the (FD curve-fitting) model.
- 3- A slow laser scan speed during the SLS process gave a high sintering temperature, neck growth, and relative density and densification.
- 4- The roughness of the product obtained from SLS process is high because the connection between particles is half size which is equal to  $\text{NR}=0.43$ .

#### **4.4 Conclusions**

Chapter four focussed on the application of a new curve fitting method, using the variational principal to proof that a new method can be used in another numerical method. Neck size ratio was used as sintering parameter for validation with curve fitting FD method. The conclusions to chapter four clarified the following points:

- 1- The VM curve fitting model was determined to be the best method with which to represent the sintering process between particles.
- 2- Powder size has obvious effects on selective laser sintering. Fine powders offer high contact area between powder particulates.
- 3- Laser power and laser scan speed are significant parameters in the selective laser sintering, the process of which can effectively be controlled by these two parameters.
- 4- Sintering temperature is an important parameter in selective laser sintering. High sintering temperatures show improved selective laser sintering.
- 5- The number of contacts between particles is a significant parameter in the selective laser sintering process. High contact between copper powders shows a greater reduction in surface area.

## 5 CHAPTER FIVE: Molecular Dynamics model for nanoparticles sintering

Chapter five is presented in five parts: the first focuses on the calculation of nanoparticle melting temperature using molecular dynamics, specifically the LAMMPS code, where changes to potential energy for each atom and nanoparticle size are used to calculate melting temperatures; the results will be compared with an analytical model. The second part presents the modelling of nanoparticle sintering using the LAMMPS code for two copper nanoparticles. The neck size and shrinkage ratio for the nanoparticles will be calculated for different sintering temperatures and compared with the analytical model. Finally, different nanoparticle sizes will be used in the molecular dynamics model to calculate size-related nanoparticle parameters.

The third part models hollow nanoparticles using the LAMMPS code for two copper nanoparticles. Neck sizes and shrinkage ratios for nanoparticles will be calculated and compared with solid nanoparticle results. The fourth part presents the modelling of multiple nanoparticles using the LAMMPS code for two distinct nanoparticle species: hollow and solid. Multiple nanoparticles will be used in the molecular dynamics model to show the effects of different nanoparticle groups on sintering parameters. The fifth part presents the simulation for the sintering process between two different sizes of nanoparticles using the LAMMPS code for two nanoparticle species: hollow and solid.

### 5.1 Introduction:

Nanoparticle sintering processes show unique behaviour compared to their microparticle sintering process; for example, nanoparticle sintering is a rapid process that only requires a low sintering temperature [120]. Copper plays an important role in electronics manufacturing because it has good electrical conductivity, is of comparatively low cost, and to achieve the best compatibility in inkjet, for instance, nano-copper is becoming increasingly used in copper ink [121, 122], which is used in

standard inkjet printers to print electronic circuits; in this application, the nano-copper is formed at a sintering temperature of only 523 K with a size of only 5 nm [123].

Previous researchers have not used numerical simulations to calculate the melting temperature of nanocopper; rather, they used MD to simulate nanoparticle sintering directly without performing any melting temperature calculations. In this chapter, melting temperatures for a range of nanoparticle sizes are calculated and compared with analytical formulae, whilst the initial solid-state sintering of nanocopper was studied using the LAMMPS code via the embedded atom method to investigate the initial sintering mechanism between copper nanoparticles; moreover, the effects of hollow nanoparticles on the sintering process are examined. The results collected from the molecular dynamics simulations will be compared with analytical models.

## **5.2 Methodology**

A molecular dynamics model was used to simulate copper nanoparticles of different sizes (5, 8, 10, 15, 20, 25, 30, 40, and 50 nm) at different temperatures using the LAMMPS code [124], which is an effective and efficient tool for examining nanoparticle processes. Many researchers used LAMMPS to describe the behaviour of nanoparticles during the sintering process, including the motion of atoms inside the nanoparticles themselves.

### **5.2.1 Computational methods:**

Molecular dynamics is a numerical method which is used to explore the motion of atoms in nanoparticles using Newton's Second Law and potential energies. Molecular dynamics depends on position, momentum, charge and atomic forces to determine the initial state, and time steps to continue the simulation until the last requested step of the program [125].

### 5.2.1.1 LAMMPS code

LAMMPS is an acronym for Large-scale Atomic/Molecular Massively Parallel Simulator. It is a classical numerical code derived from the molecular dynamics method. Sandia National Laboratories, under the United States Department of Energy, developed the LAMMPS code which is open source and can be downloaded for research purposes (<http://lammps.sandia.gov>) [124]; indeed, the code can be used as is or can be legitimately modified. The current version of LAMMPS is written in C++, but earlier versions were written in the Fortran F77 and F90 variants. The inputs to the LAMMPS code are:

1-Sintering temperature.

2-Initial potential energies of atoms inside nanoparticles.

3-Nanoparticle radius.

4-Unit types.

5-Nanoparticle shape.

6-Nanoparticle position.

7-The volume defining a group of nanoparticles.

8-Fixing the crystal orientation of the nanoparticles.

9-Fixing nanoparticle centres.

10-Fixing the maximum sintering time.

11-Fixing the time step.

12-Fixing the type of potential, for example a Lennard-Jones potential or the embedded atom method.

The outputs are:

1-Final potential energy of atoms.

2-Kinetic energy of atoms.

3-Total energy of atoms

4-Final position and velocity of atoms.

5-Final temperature.

6-Time for the process.

7-MSD, and shrinkage.

Figure (5-1) gives an overview of the LAMMPS code structure. The LAMMPS code proceeds in four steps: initialisation, atomic definition, force fields, and atomic simulation process. The initialization has three parts: atomic units, process boundary, and style of atom. The atomic definition step has three parts: nanoparticle style, nanoparticle positions and dimensions, and the creation of a volume for the group of nanoparticles. The force fields step has two parts: potential energy pair style and pair coefficient for the potential energy of the nanoparticle type. The final step is the atomic simulation process which has five steps: the time step to be used in the simulation, process parameters to show on-screen, initial atom velocities, a dump file for the output, and minimization of energy.

LAMMPS simulation results need visualization software to be displayed and analysed (for nanoparticles during the sintering process, in this instance). There are six high-quality visualization packages which are used to display such results and that allow the visualization of LAMMPS results, which are VMD, AtomEye, ParaView, PyMol, Ovito, Raster3d and RasMol [124]. These visualization packages are molecular graphics software packages designed for the presentation and analysis of molecular assemblies. These packages can offer animation facilities, allowing the display, and analysis, of atoms, ensembles or molecules using three-dimensional graphics. Further, these visualization packages are free, and any student is entitled to use them [126]. Ovito was considered the best software by which to visualize LAMMPS results in this thesis.

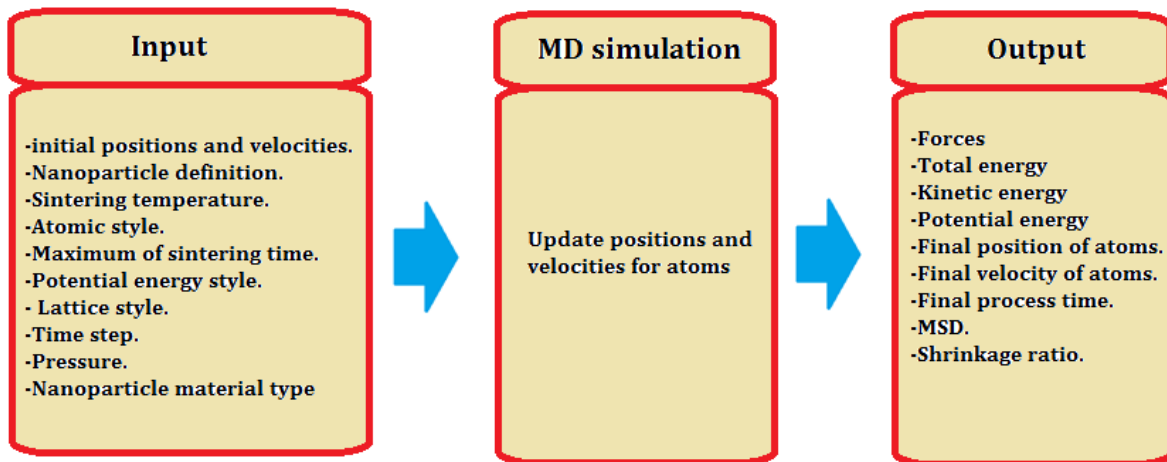


Figure 5-1 Structure of the LAMMPS code.

### 5.2.1.2 Embedded atom method (EAM)

The embedded atom method (EAM) potential for nanocopper was chosen as the force field in the MD-LAMMPS code through which to understand the behaviour of nanoparticles during the sintering process. Many researchers used the embedded atom method with MD to describe the atomic energy in the solution [102, 104, 127]. Thus, the embedded atom method (EAM) potential will be explained below.

The total potential energy is given by

$$E_{TP} = \sum_i E_i \quad (5 - 1)$$

where  $E_{TP}$  is a total potential energy, and  $E_i$  is the potential energy associated with atom  $i$  [128].

The embedded atom method (EAM) can be represented by two parameters which give:

$$E_i = \frac{1}{2} \sum_j \beta(r_{ij}) + \Gamma(\rho_i) \quad (5 - 2)$$

where  $\beta(r_{ij})$  is the two-body central interaction energy between atoms  $i$  and  $j$  which are separated by a distance  $r_{ij}$ , and  $\Gamma(\rho_i)$  is the embedded energy of atom  $i$  which is a function of electron density ( $\rho_i$ ) [128].

Also

$$r_{ij} = |r_i - r_j| \quad (5 - 3)$$

$$\Gamma(\rho_i) = D \rho_i \ln \rho_i \quad (5 - 4)$$

Where  $D$  is an analytical formula, and  $\rho_i$  is the electron density of atom  $i$ .

$$\rho_i = D \sum_j v(r_{ij}) \quad (5 - 5)$$

$$\beta(r_{ij}) = B_1 (r_{c1} - r_{ij})^2 \exp(-c_1 r_{ij}) \quad (5 - 6)$$

$$v(r_{ij}) = B_2 (r_{c2} - r_{ij})^2 \exp(-c_2 r_{ij}) \quad (5 - 7)$$

Where  $r_{c1}$  was selected to be  $1.65 r_{ij}$ , and  $r_{c2}$  was selected to be  $1.95 r_{ij}$  [128].

Copper powder parameters for EAM were obtained from Mishin et al. [129] which are used in the LAMMPS simulation to solve the sintering between nanoparticles.

### 5.2.2 Analytical model

Firstly, the diffusion coefficients of copper nanoparticles were calculated using equation (5-8), which is dependent on two parameters: temperature (T) and radius of nanoparticle ( $r$ ) [130].

$$D(r, T) = D_o(\infty) \exp \left[ \frac{-E}{RT} \exp \left[ \frac{-2S_{vib}(\infty)}{3R \left( \frac{r}{r_o} - 1 \right)} \right] \right] \quad (5 - 8)$$

Where  $E$  is the bulk activation energy, and table (5.1) shows the activation energies of different sintering mechanisms [103].  $S_{vib}(\infty)$  is a vibrational factor of the melting entropy and is equal to 8.06 J/mol.K for bulk copper [131].  $R$  is the gas constant (8.314 J/mol.K) and  $r$  is the radius of the nanoparticle while  $r_o$  is the radius of the nanoparticle for atoms located at the nanoparticle surface;  $r_o$  is dependent on the value of  $h$ , defined as the height of a monolayer of atoms;  $h = a/2$  for fcc materials, where  $a$  is the lattice constant, which is equal to 0.362 nm for copper [103], and  $r_o = 3h$  which is equal to 0.543 nm for copper.  $D_o(\infty)$  is the bulk initial diffusion coefficient, where table (5.2) displays the initial diffusion coefficient for different mechanisms [132].

**Table 5.1 Bulk activation energy for different diffusion coefficients [103].**

Sintering mechanism	Activation energy $E$ (KJmol <sup>-1</sup> )
Grain boundary diffusion	168.85
Surface diffusion	203.70
Lattice diffusion	145.18
Plastic flow	63.97
Evaporation-condensation	86.91

Table 5.2 Initial diffusion coefficients [132].

Sintering mechanism	Initial diffusion coefficient $D_0(\infty)$ ( $m^2/s$ )
Grain boundary diffusion	$20 \times 10^{-5}$
Surface diffusion	$2.6 \times 10^{-5}$
Lattice diffusion	$7.8 \times 10^{-5}$

Table (5.3) shows diffusion coefficients for different mechanisms at 600 K, as collected from equation (5-8), where these values will be used in the analytical equations to model the nanosintering process.

Table 5.3 Diffusion coefficients at 600 K [132].

Sintering mechanism	Diffusion coefficient $D(r,T)$ ( $m^2/s$ ) at $r = 5nm$ and $T = 600 K$
Grain boundary diffusion	$5.17474 \times 10^{-19}$
Surface diffusion	$1.05559 \times 10^{-23}$
Lattice diffusion	$1.62049 \times 10^{-17}$

An analytical model was used to validate MD simulation results, where this model had two parameters, such as neck and shrinkage ratio. Thus equation (2-1) for neck size ratio was used in this validation.

Figure (5-2) shows the validation of molecular dynamics simulation results with the analytical model via a comparison between four neck size ratio curves, one representing molecular dynamics simulation curves, and the others representing analytical diffusion mechanisms. The vertical axis represents the neck size ratio while the horizontal axis represents sintering time. Overall, the neck size ratio in the molecular dynamics simulation curve is closer to the surface diffusion curve than other analytical diffusion mechanisms, which means that the sintering mechanism for nano-copper is controlled by surface diffusion rather than other diffusion mechanisms. Also, the lattice diffusion curve is higher than the curves found for other mechanisms, while the grain boundary mechanism curve shows a greater difference with the MD curve than the surface mechanism curve. Lastly, the molecular dynamics curve has a different appearance from all the other curves, because the MD curve fluctuated and stabilized when compared with any of the other analytical mechanism curves. Also, the maximum neck size ratio from the molecular dynamics simulation was 0.46, whilst the minimum neck size ratio for the surface mechanism was 0.35.

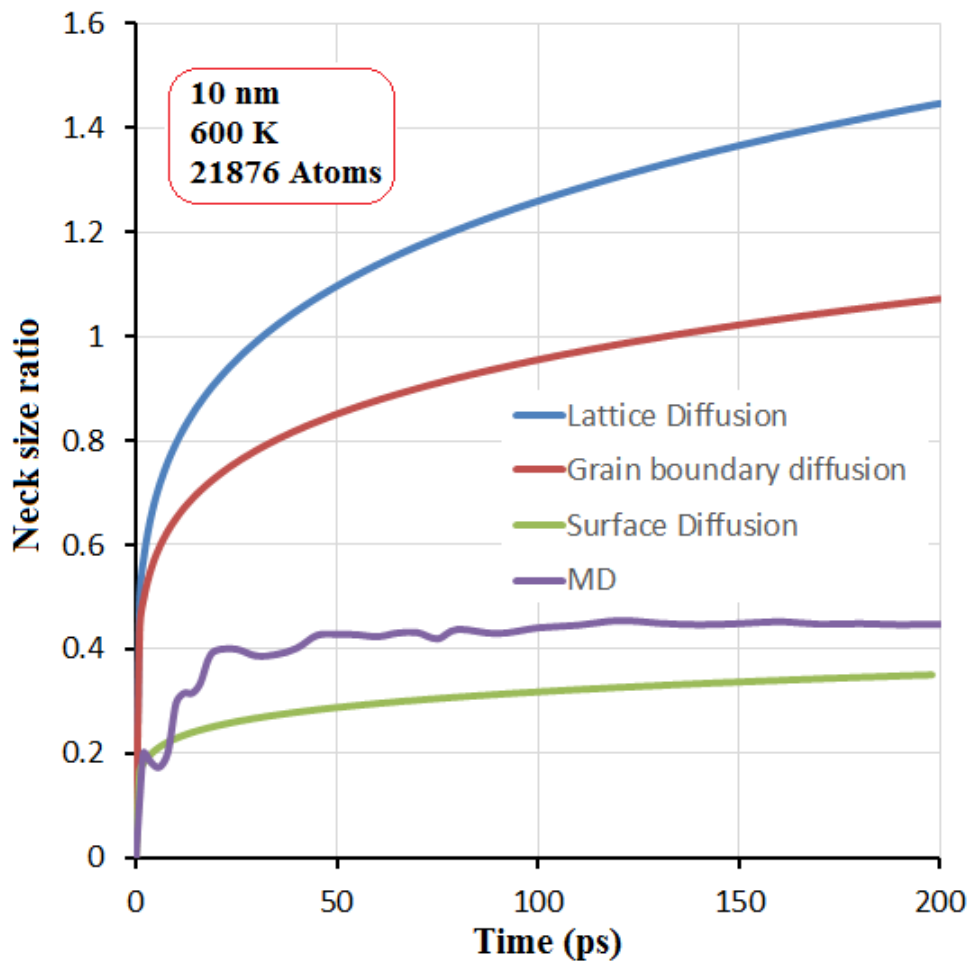


Figure 5-2 Neck size ratio compared with different diffusion mechanisms.

### 5.3 Calculation of nano-copper melting temperature

The melting temperature of nano-copper has a significant influence on the solid-state nanosintering process due to its dependence on nanoparticle size, which changes with nanosize. Also, the sintering process depends on the sintering temperature which is 0.95 times the melting temperature; thus, the melting temperature of a given nanoparticle varies depending on nanoparticle size, whereas for a microparticle the temperature is fixed. Melting temperatures of nanoparticles can be predicted experimentally by various experimental methods depending on nanosize, for instance,

electron diffraction has been used to calculate the melting temperature of thin layers of nanoparticles such as Sn [133], Au [134], and In and Pb [135].

### 5.3.1 Analytical models of nanoparticle melting temperature

Analytical models of melting temperature are the easiest methods by which to calculate material melting temperatures from analytical formulae, but sometimes the analytical model does not match with the experimental data because some parameters did not appear in these formulas. In this chapter, different analytical models have been utilized to compare with molecular dynamics simulation results of nano-copper.

#### 5.3.1.1 Pawlow model

In 1909, Pawlow was the first to construct a melting temperature model related to nanoparticle size, thus the related equation depends on parameters such as densities and surface energies, and is particularly popular and useful in this application. The Pawlow formula for melting temperature is shown below:

$$\frac{T_m}{T_B} = 1 - \frac{2}{\rho_S L_o r} \left( \gamma_S - \gamma_l \left( \frac{\rho_S}{\rho_l} \right)^{\frac{2}{3}} \right) \quad (5 - 9)$$

Where  $T_m$ ,  $T_B$ ,  $\rho_S$ ,  $\rho_l$ ,  $\gamma_S$ ,  $\gamma_l$  and  $L_o$  are parameters as denoted in table (5.4) which shows all parameters for copper used in the melting temperature equations [136].

**Table 5.4 Parameters for copper nanoparticles**

Parameter	Value
Melting temperature $T_B$ (K)	1357.77
Solid Density $\rho_s$ (kg/m <sup>3</sup> )	8960

Liquid Density $\rho_l$ (kg/m <sup>3</sup> )	7998
Solid Surface energy $\gamma_s$ (J/m <sup>2</sup> )	1.72
Liquid Surface energy $\gamma_l$ (J/m <sup>2</sup> )	1.1
Enthalpy of fusion $L_o$ (J/g)	205
Thickness of the liquid over layer $\delta$ (Å)	15.36
solid–liquid interface energy $\gamma_{sl}$ (J/m <sup>2</sup> )	0.177

### 5.3.1.2 Hanszen model

Hanszen (1960) proposed a new model for melting temperature as a function of nanoparticle size. The model is a modification of the Pawlow model, with the modification achieved by adding a new parameter, liquid overlayer solid energy, the equation for which is shown below [137].

$$\frac{T_m}{T_B} = 1 - \frac{2}{\rho_s L_o} \left( \frac{\gamma_{sl}}{r - \delta_l} - \frac{\gamma_l}{r} \left( 1 - \frac{\rho_s}{\rho_l} \right) \right) \quad (5 - 10)$$

### 5.3.1.3 Gibbs–Thomson model G-T

Gibbs–Thomson provided a theoretical equation for melting temperature as a function of nanoparticle size using thermodynamic parameters [138, 139]. The Gibbs–Thomson equation is shown below.

$$\frac{T_m}{T_B} = 1 - \frac{4\gamma_{sl}}{\rho_s L_o D} \quad (5 - 11)$$

### 5.3.1.4 Liquid drop model LDM

The liquid drop model assumes that nanoparticles transfer from solid state to liquid state at a fixed temperature. The calculation of melting temperature is essentially dependent on surface tension and the cohesive energy of the nanoparticle. Thus, the equation for the liquid drop model is shown below.

$$T_m = T_B \left( 1 - \frac{\beta}{d} \right) \quad (5 - 12)$$

Where  $d$  is the diameter of the nanoparticle, and  $\beta$  is a parameter that depends on the type of material, which is 0.9 nm for copper [140].

### 5.3.2 Numerical calculation of melting temperature of copper powder

The melting temperature of nano-copper has a significant influence on solid-state nanosintering due to (as previously mentioned) nanoparticle melting temperature depending on nanoparticle size. Nanoparticle melting temperatures are collected from MD-LAMMPS simulations through the determination of the change in potential energy of the nanoparticles over a wide range of temperatures. Figure (5-3) shows potential energy per atom as a function of temperature. It can be seen from this figure that potential energy increases with increasing temperature; furthermore, potential energy increases with decreasing nanoparticle size. Also, all potential energy curves are stepped, which indicates the melting temperatures of the surface and centre of the nano-copper. These temperatures have different values, the difference in which is dependent on nanoparticle diameter. In addition, there are three stages of potential energy for each nanoparticle size which change depending on nanoparticle size; for example, the three stages can be distinguished for each nanoparticle size. As shown in figure (5-3), each curve had three stages, the first stage of the curve represents increasing with potential energy due to the increase in temperature with the same slope, while the second stage is known as the abrupt jumping zone (to another stage) which means that the second stage represents the transition stage between first and

third stages. The third stage is a continuous zone which increases due to the temperature but the rate of increase of the third stage is greater than the first stage. Overall, the first stage, second stage, and third stage represent the solid state, the melting transition, and the liquid state, respectively. All these curves converge with increasing nanoparticle size except for the three curves at nanosizes of 1, 2, and 3 nm.

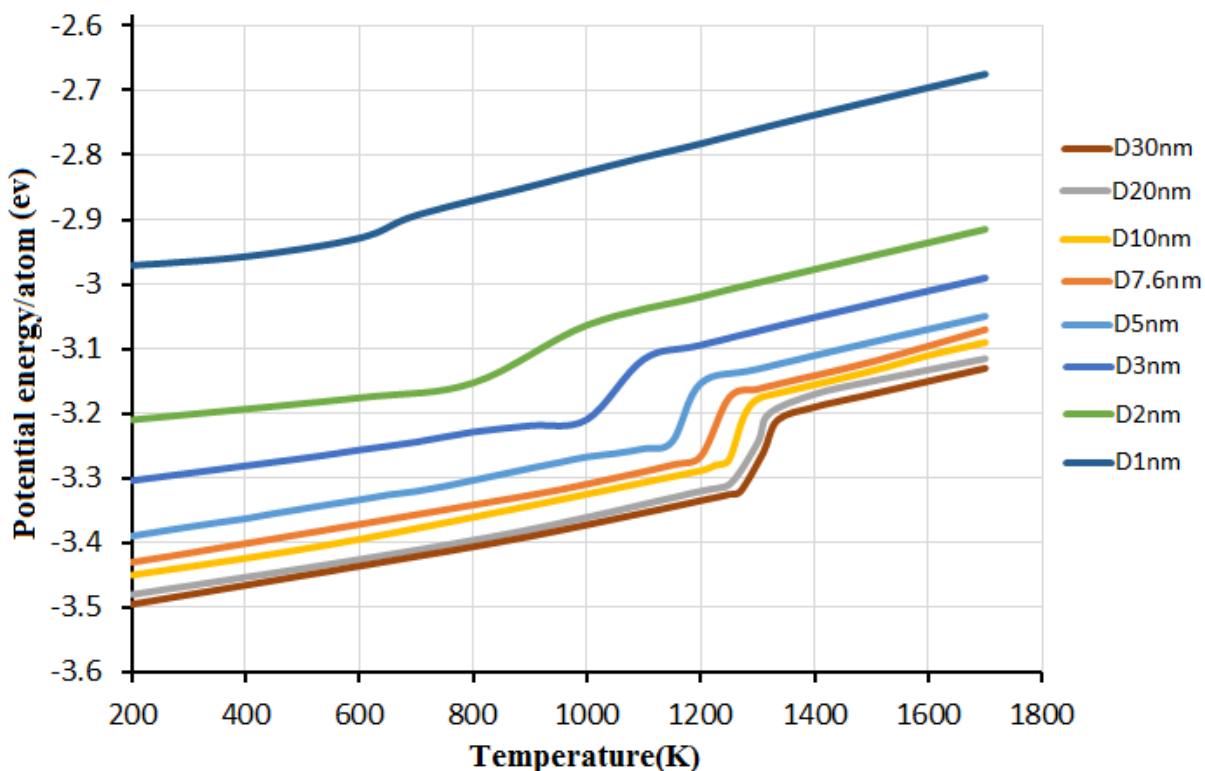


Figure 5-3 Potential energy/atom as a function of temperature for different nanocopper diameters.

Figure (5-4) illustrates the melting temperatures of nano-copper collected from the different stages of the curves of the figure (5-3). The orange curve represents the full melting temperatures, while the blue curve represents the surface melting temperatures. As shown in figure (5-4), there are three regions in the curves: the first region is when below the surface melting curve (blue curve), which represents the solid phase of the nanoparticle, while the second stage, between the two curves (blue

and orange) represents the unstable region between the solid and liquid phases. The third region, above the full melting curve, represents the liquid phase of the nanoparticle. It can be seen from figure (5-4) that there are two curves: the first represents the starting surface melting temperature whilst the second represents the full melting temperature of the nano-copper for each size, the data for which being collected from the second stage of each nanoparticle size from (figure (5-3)); for instance, the starting point of the second stage represents the surface melting point, whilst the end point of the second stage represents the full melting point. In addition, the full melting temperature for nano-copper is greater than the surface melting temperature curve; whilst the two curves started at the same temperature at a size of 1 nm, from this point both curves were seen to follow different trajectories.

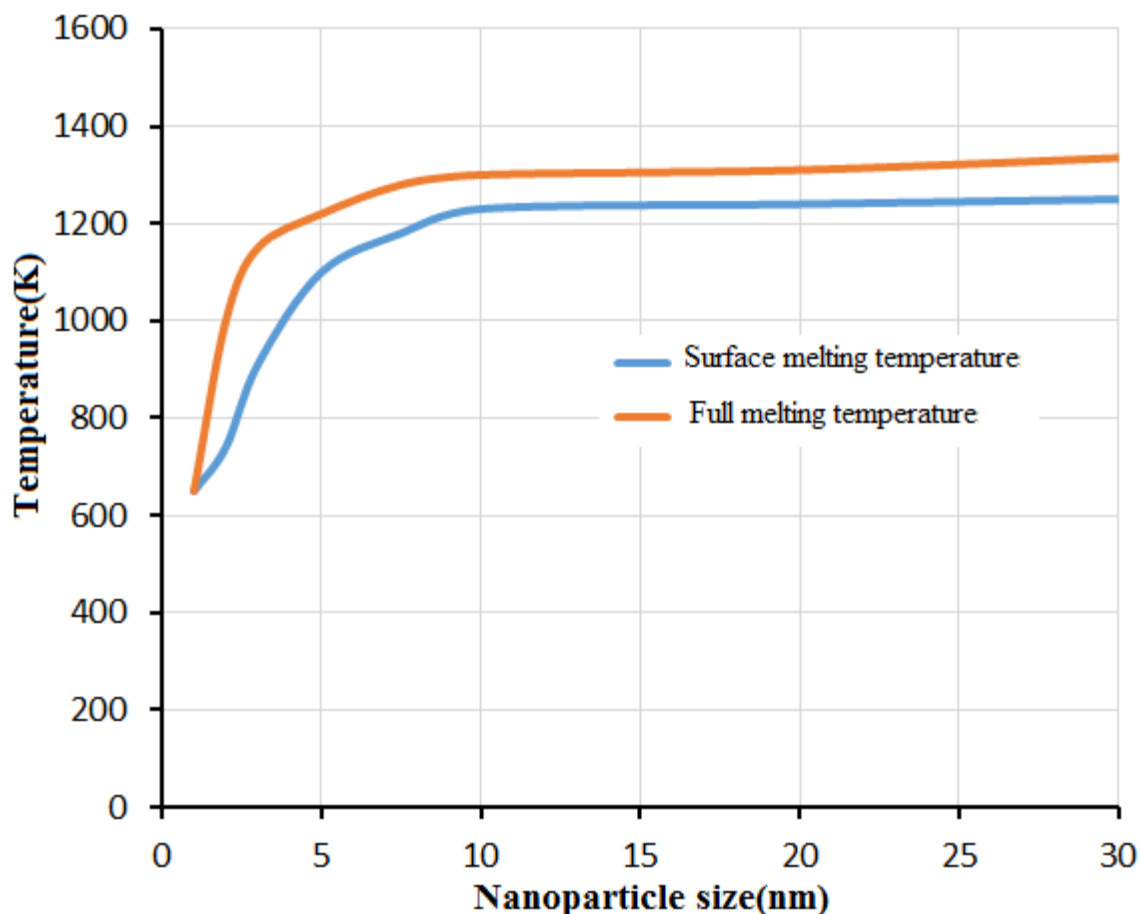


Figure 5-4 Full and surface melting temperatures.

### 5.3.3 Validation of melting temperature for nanocopper

The various nanocopper melting temperatures were determined from molecular dynamics simulations and compared with analytical models for a range of nanoparticle sizes (1-30 nm) in order to determine which model was closest to the molecular dynamics simulation results.

Figure (5-5) shows a comparison of full melting temperatures between the molecular dynamics simulation curve and the four analytical curves for nanocopper melting temperatures. The vertical axis represents the full melting temperature while the horizontal axis represents the nanoparticle size. Four analytical melting temperature formulae were compared with the molecular dynamics simulation melting temperatures, namely the Pawlow, Hanszen, Liquid drop method (LDM), and Gibbs-Thomson (G-T) models. There are two regions in the melting temperature curves, the first ranging in size from 1 to 14 nm, whilst the second ranges from 14 to 30 nm, as shown in figure (5-5). It can be observed that all the analytical curves are close to the MD simulation curve, this is seen in the second region, but did not match the MD simulation curve in the first region of the curves, except the Gibbs-Thomson curve, which was close to MD simulation curve, indicating that the Gibbs-Thomson model is suitable for determining the full melting temperatures for copper nanoparticles.

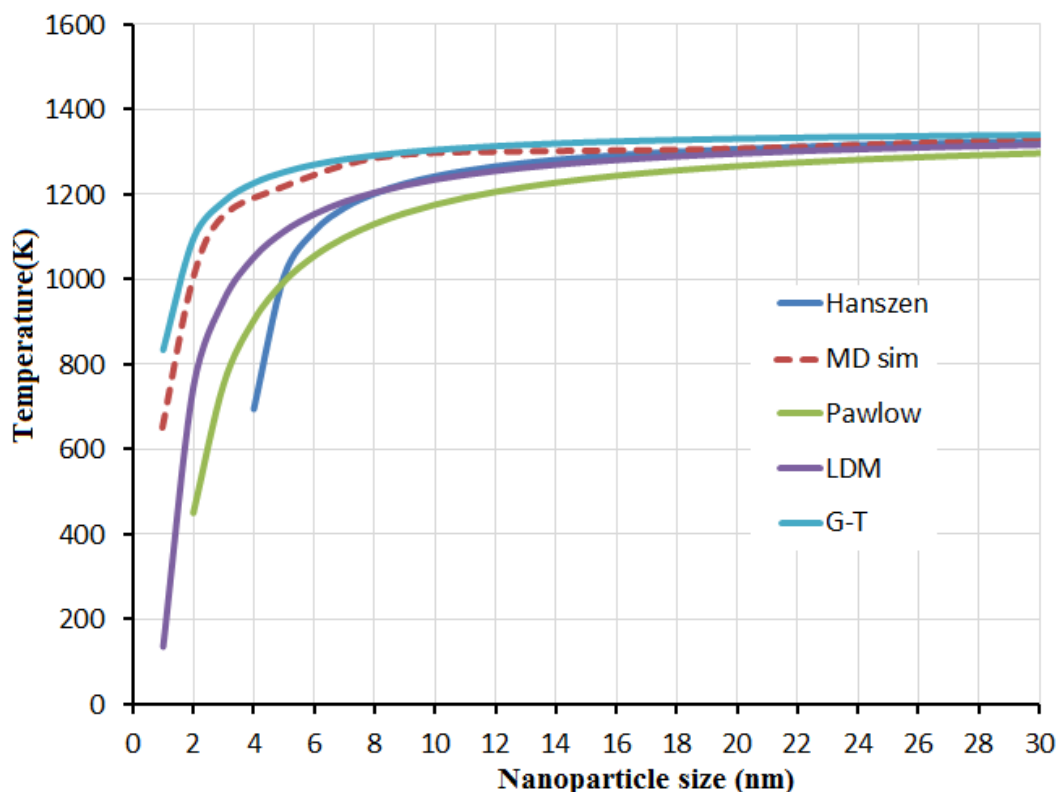


Figure 5-5 Melting temperature of nanocopper comparison with models.

#### 5.4 Molecular dynamics simulation of solid-state sintering of nanocopper

All results were determined from the molecular dynamics simulation using the LAMMPS code for different particle sizes and sintering temperatures of copper powders. It has been shown that neck growth and densification processes are significant factors in the nanosintering process. Figure (5-6) illustrates a comparison between eight curves of different nanoparticle sizes for two copper nanoparticles at a sintering temperature 600 K. The vertical axis represents the neck size ratio while the horizontal axis represents the sintering time in picoseconds. Eight different nanoparticle diameters, 5, 10, 15, 20, 25, 30, 40, and 50 nm were used in this study to investigate the effects of nanoparticle size on the solid-state sintering process. Generally, the neck size ratio increases with increased sintering time. It can be seen

from the figure that all the curves had two stages: in stage one, all curves increased with increasing sintering time until 20 ps, whilst in the second stage, all curves stabilise until the end of the sintering process. Lastly, the neck size ratio curves became close together when nanoparticle size increases, especially for diameters between 25-50 nm. In addition, the neck size ratio increases with decreasing of the nanoparticle size, this is due to the sintering process is very fast for the smaller nanoparticle with rapid sintering time.

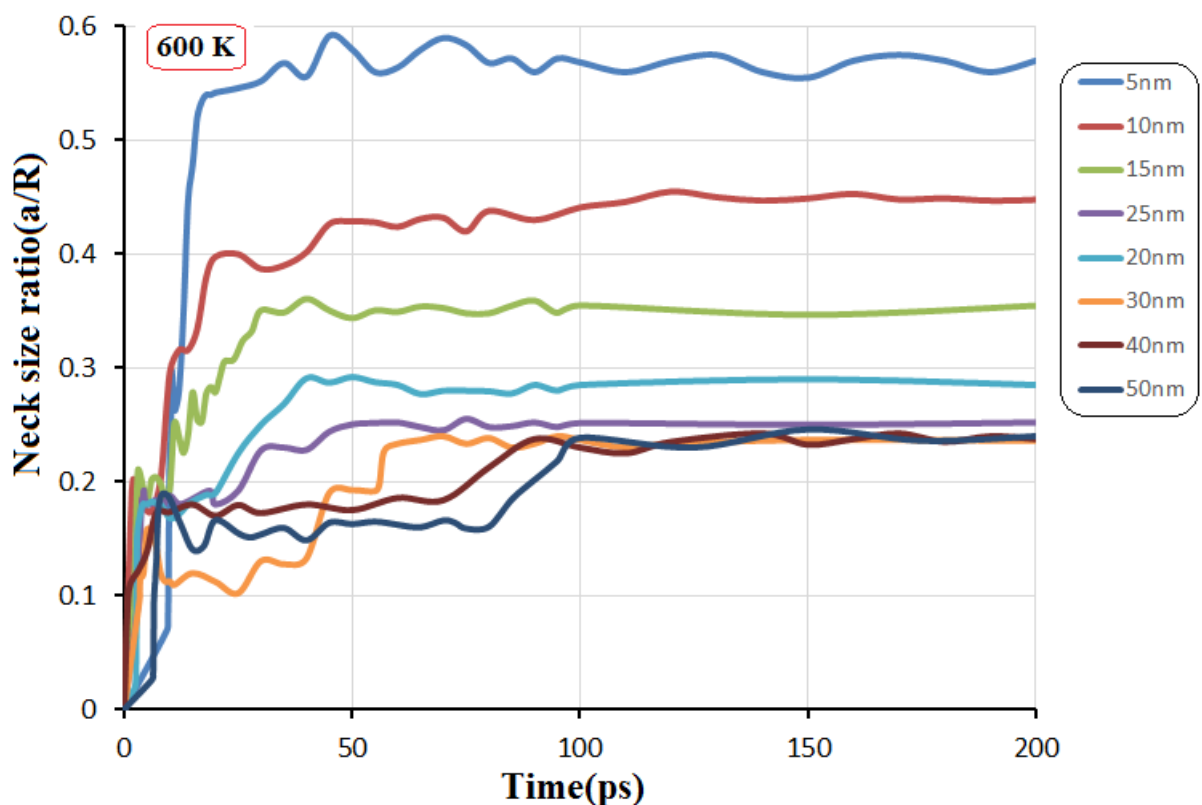
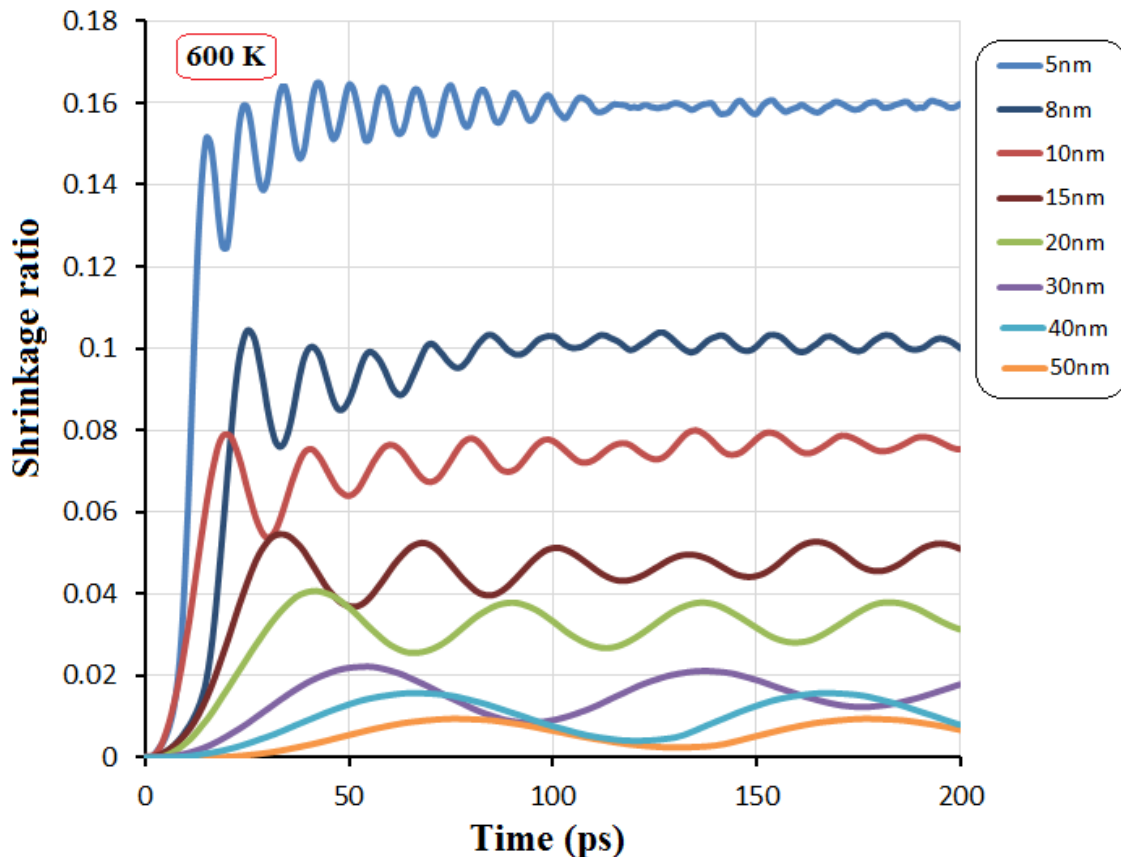


Figure 5-6 Neck size ratio for different nanoparticle sizes at a sintering temperature of 600 K.

Figure (5-7) shows a comparison between eight different nanoparticle sizes for two copper nanoparticles at a sintering temperature of 600 K. The vertical axis represents the shrinkage ratio while the horizontal axis represents the sintering time in picosecond. Eight different nanoparticle diameters, 5, 8, 10, 15, 20, 25, 30, 40, and 50 nm, were used in this study to investigate the effect of nanoparticle size on shrinkage ratio. Generally, the shrinkage ratio increases due to the increase in sintering time. It can be

seen that the shrinkage ratio decreases with increasing of the nanoparticle diameter, this is because the fine nanoparticles have a larger driving force for the sintering process as shown in equation (2.19) [10]. In addition, all curves have two stages: stage one, all the curves increase with increasing sintering time, until 20 ps. Whilst during the second stage, all the curves fluctuate starting at 20 ps until the end of the process, the fluctuation of the curves vary depending on nanoparticle size. For instance, the fluctuation of the curve for nanoparticle size 5 is different than the fluctuation of the curve for nanoparticle size 50, this means that the movement of nanoparticles inward depends on nanoparticle size. Lastly, the shrinkage ratio curves are closer together when nanoparticle sizes increase, this is especially seen for diameters between 30-50 nm.



**Figure 5-7 Shrinkage ratio for different nanoparticle sizes at a sintering temperature of 600 K.**

Figure (5-8) displays a snapshot of the half section of two copper nanoparticles with a diameter of 5 nm over a sintering time of 18 ps. It can be seen that a diamond geometry had been created in the coalescence between two copper nanoparticles, which means that recrystallization is occurring in the neck connection between the copper nanoparticles; moreover, the direction of movement of atoms inside the nano-copper is in the same direction, and it looks like a honeycomb geometry. This is because the movement of dislocation between nanoparticles during the sintering process.

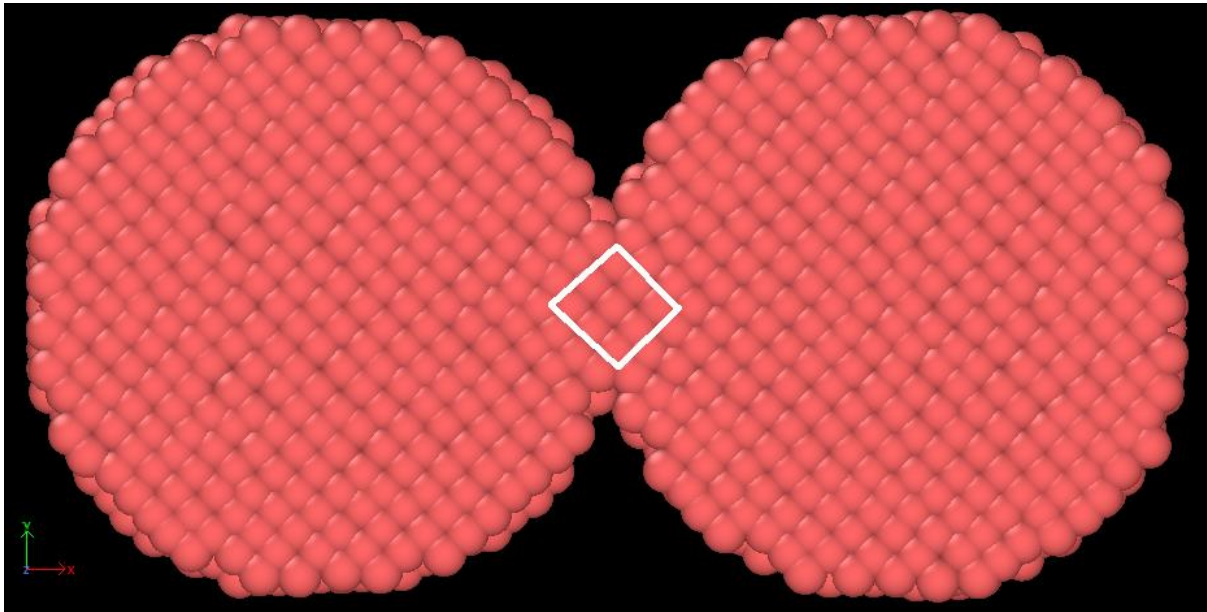


**Figure 5-8 Snapshot of two half copper nanoparticles for crystal lattice (100-100) for a size of 5 nm and sintering temperature 600 K.**

Figure (5-9) shows a comparison of the relative densities of different particle sizes for two copper nanoparticles at a sintering temperature of 600 K. Seven different nanoparticle diameters, 5, 10, 15, 20, 30, 40, and 50 nm, were used to study the effect of nanoparticle size on relative density. The initial relative density is 0.64, which was used as an input in the molecular dynamics simulation [39]. Generally, the relative density increases with increasing sintering time, this is because the relative density depends on the shrinkage ratio as shown in equation (3-20). As shown in the figure, relative density decreases with increasing nanoparticle diameter. In addition, the

maximum relative density is 1.08 for a nanoparticle size of 5 nm and a sintering time of 200 ps, while the minimum relative density is 0.66 for a nanoparticle size of 50 nm. An increase of nanoparticle size impacts the stability of curves which means that an increase of nanoparticle size leads to the stabilization of the curve without any particular fluctuation; for example, a relative density of 50 nm compared with 5 nm. Also, the relative densities of nano-copper at size 30, 40, 50 nm are closer together than other nanoparticle sizes which means that the relative density did not change due to the increase in nanoparticle size. This is seen for nanoparticle sizes 30, 40, and 50 nm.

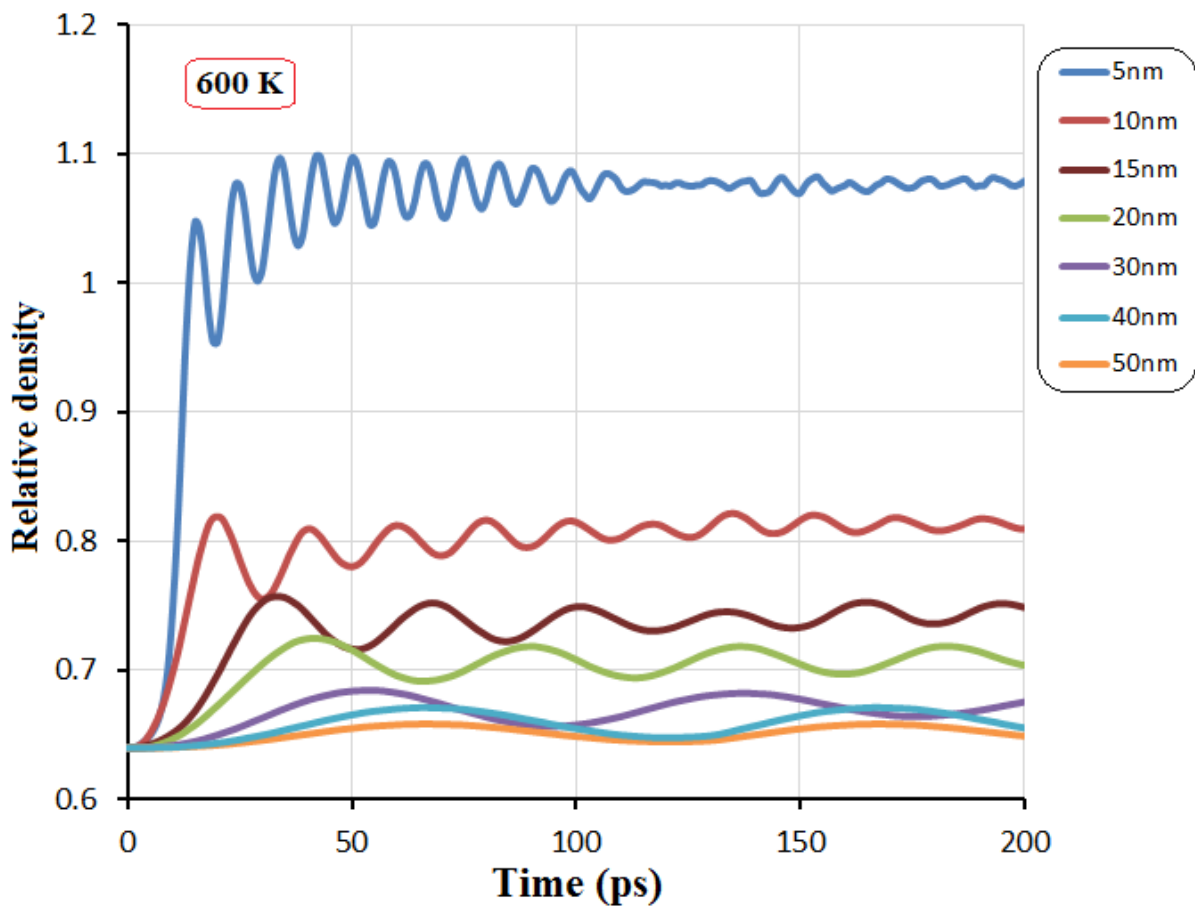
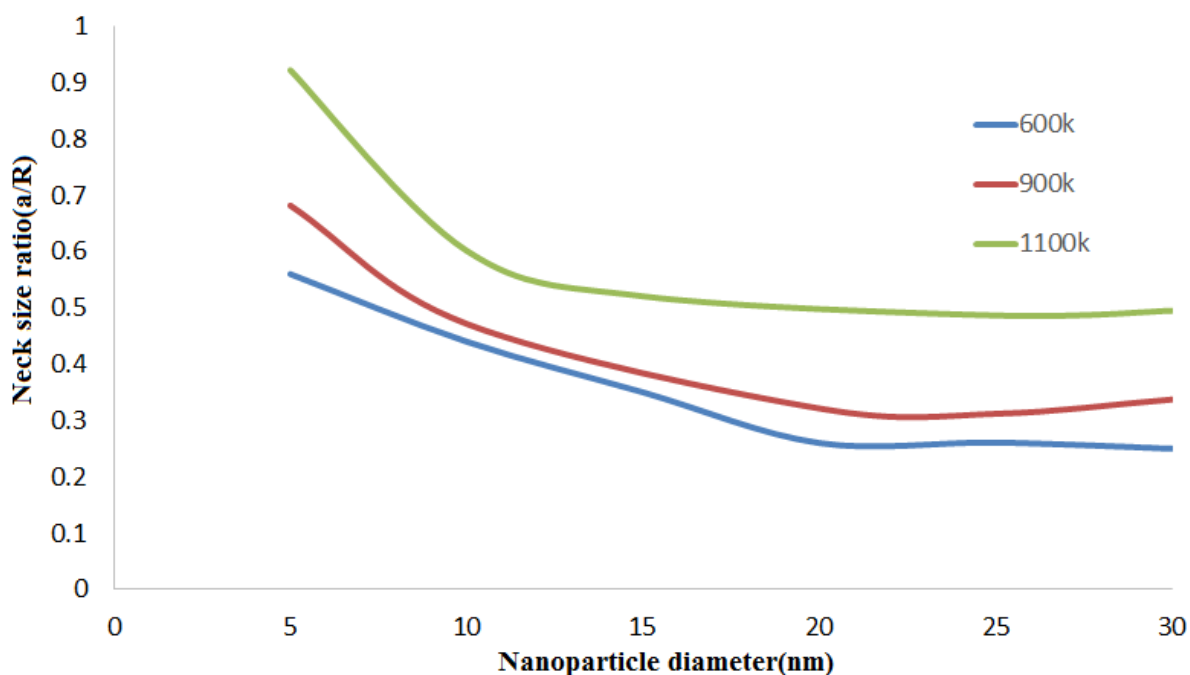


Figure 5-9 “Relative density” for different nanoparticle sizes at a sintering temperature of 600 K.

Figure (5-10) illustrates a comparison of neck size ratio for different sintering temperatures of two copper nanoparticles. Three different sintering temperatures, 600,

900 and 1100 K, were used in this study to investigate the effects of sintering temperature on the nanosintering process. Generally the neck size ratio decreases with increasing nanoparticle size, and the effect of sintering temperature is clear from figure (5-10); sintering temperature increases with increasing neck size ratio for different nanoparticles sizes, but the difference between curves are not the same, for instance, the two curves of 600 K and 900 K are closer to each other than the curve of 1100 K. In addition, all curves had two stages: the first stage had a decreasing gradient and then the second stage consists of this gradient then stabilising. The first stage ended at different nanoparticle sizes for different sintering temperatures. The second stage for the 1100 K sintering temperature started at  $d = 13$  nm while the other two sintering temperatures 600, 900 K, started at  $d = 20$  nm.



**Figure 5-10 Neck size ratio with copper nanoparticle size for different sintering temperature.**

The shrinkage ratio was used in the LAMMPS code to determine the shrinkage between nanoparticles. Figure (5-11) shows a comparison of shrinkage ratio between

three curves at different sintering temperatures for two copper nanoparticles. Three different sintering temperatures, 600, 900 and 1100 K, were used in this study to investigate the effect of sintering temperature on the nanodensification process. The vertical axis represents shrinkage ratio while the horizontal axis represents the nanoparticle diameters. As shown in the figure, generally the shrinkage ratio decreases with increasing nanoparticle size and increases with increasing sintering temperature for each nanoparticle size. The maximum shrinkage ratio was found to be 0.3 for a nanoparticle size of 5 nm, while the minimum of shrinkage ratio was found to be 0.024 for a nanoparticle size of 30 nm.

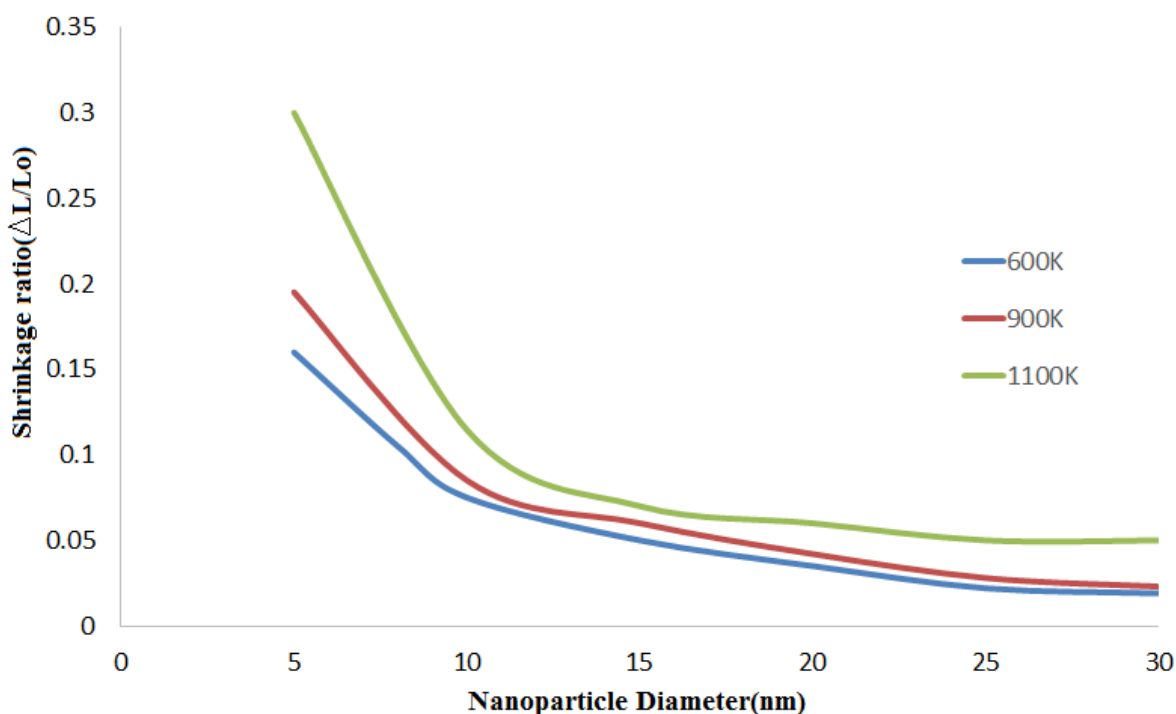


**Figure 5-11 Shrinkage ratio with copper nanoparticle size for different sintering temperatures.**

#### 5.4.1 Effect of crystal orientation on copper nanoparticle sintering

Crystal orientation is defined as the rotation of the crystal lattice in different directions, for example normal in the x direction (100), in two directions, x and y (110) and in three

directions, x, y and z (111). Figure (5-12) shows the effect of crystal orientation on the nano-copper sintering process at a sintering temperature of 600 K and nanoparticle size of 5 nm. It can be seen from the figure that the curve of crystal orientation (100-111) is higher than the normal curve (100-100), this is because the connection between two different nanoparticle (100-111) crystal orientations build a new grain boundary between nanoparticles, which improves neck growth by making atoms to move and increase neck size. The curve of (100-111) shift to right than the curve of (100-100). The maximum neck size ratio is 0.62 for sintering of a 100-111 crystal lattice for a sintering time of 100 ps, while the maximum of neck size ratio is 0.51 for sintering a 100-100 crystal lattice for a sintering time of 100 ps.

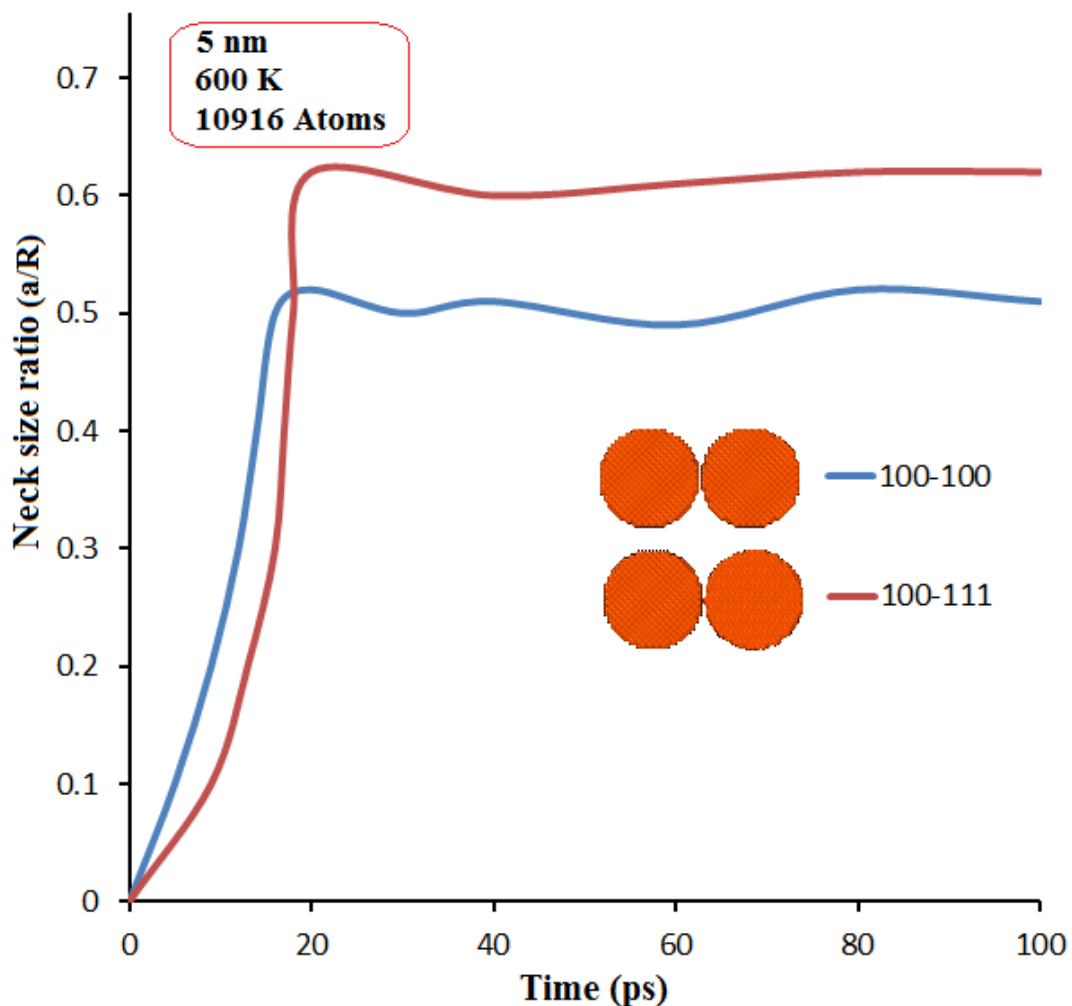


Figure 5-12 Neck size ratio with time for different crystal orientations at 600 K.

Figure (5-13) illustrates a comparison of neck size ratio between for two crystal orientations of two copper nanoparticles at a sintering temperature of 1100 K. The vertical axis represents neck size ratio while the horizontal axis represents the sintering time in picosecond. Overall, it can be clearly seen that the effects of sintering temperature in crystal orientation (100-111) is desirable as it improves the bonding between nanoparticles. Also, the maximum neck size ratio is 0.9 when sintering a 100-111 crystal lattice while a maximum of neck size ratio of 0.72 was found when sintering a 100-100 crystal lattice.

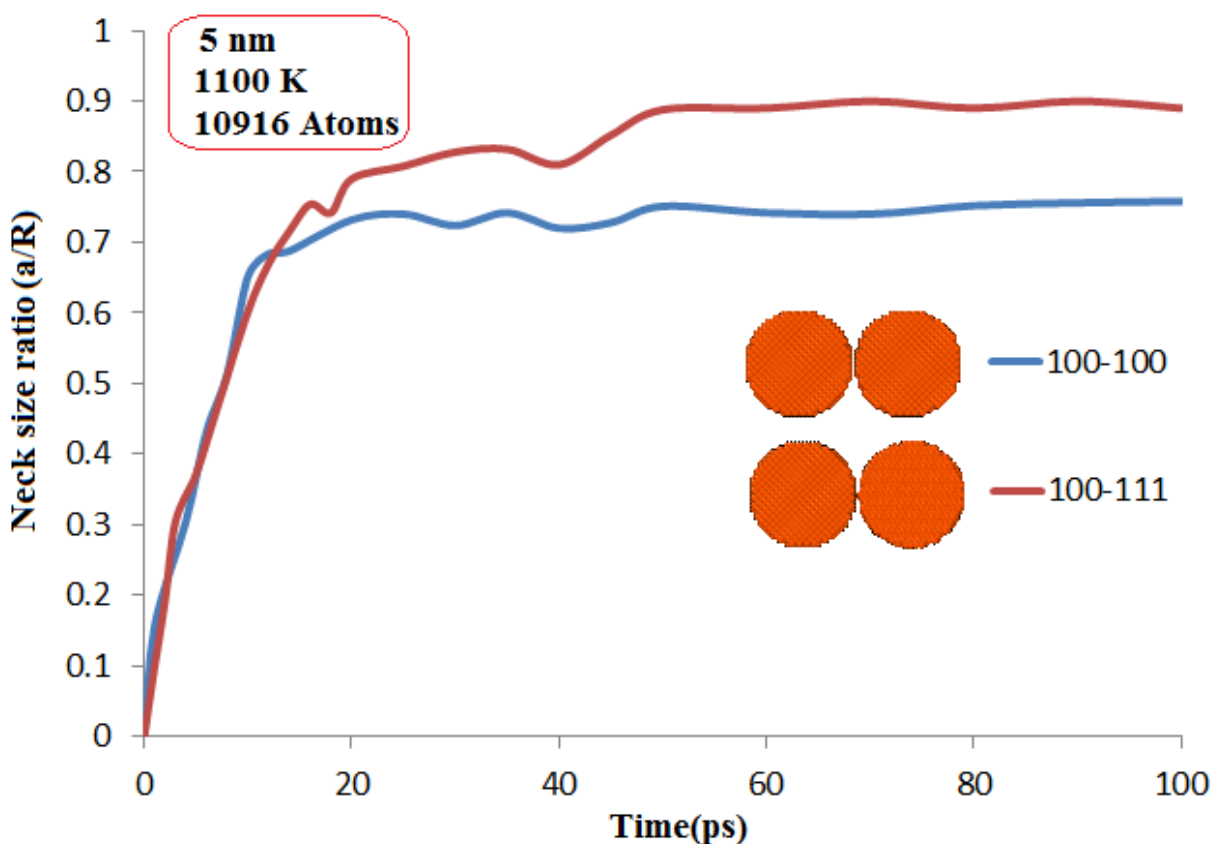
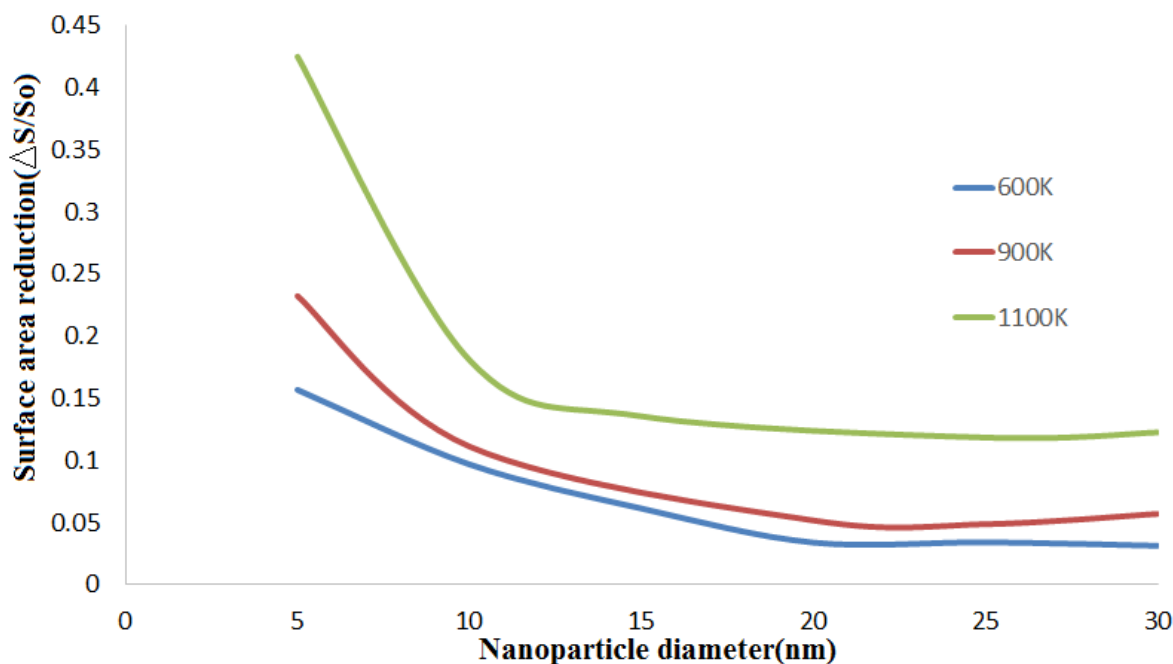


Figure 5-13 Neck size ratio with time for different crystal orientations at 1100 K.

### 5.4.2 Surface area reduction

The surface area reduction was used to show the effects of this parameter in the nano-copper sintering process. Figure (5-14) gives a comparison of surface area reduction at different sintering temperatures for two copper nanoparticles. Three different sintering temperatures, 600, 900 and 1100 K were used in this study to investigate the effects of sintering temperature on surface area reduction, as determined by a LAMMPS numerical model. Equation (3-19) was used in the numerical model program to determine the surface area reduction, where the particle coordination number  $N_C$  was equal to 2. It can be seen that the surface area reduction increases with decreasing nanoparticle size, this is because the fine nanoparticles have higher neck radius between nano-copper. In addition, the effects of sintering temperature are clear, for example, the sintering temperature increases with increasing surface area reduction, especially for smaller nanoparticle sizes (5 nm), while it is only slightly increased for larger nanoparticle sizes.



**Figure 5-14 Surface area reduction with nanoparticle sizes for difference sintering temperatures.**

### 5.4.3 Mean square displacement (MSD)

MSD is defined as the average distance of molecular transports in nanoparticles during the sintering process. It is an important parameter in nanosintering process collected from molecular dynamics simulations because it can provide a better approximation of the diffusion coefficient of atoms. Equation (5-13) shows the formula of MSD in molecular dynamics simulations.

$$MSD = r^2(t) = \frac{1}{N} \sum_{i=0}^N (r_i(t) - r_i(0))^2 \quad (5 - 13)$$

The diffusion coefficient ( $D(T)$ ) can be calculated using equation (5-14), which is related to the Einstein diffusion formula (which itself depends on MSD).

$$D(T) = \frac{r^2}{2f_d t} \quad (5 - 14)$$

Where  $r^2$  is the MSD of the atoms,  $f_d = 3$  for three-dimensional bulk diffusion and  $t$  is the sintering time. Figure (5-15) shows a comparison of the MSDs for different sintering temperatures of two copper nanoparticles with diameters of 5 nm. Three different sintering temperatures, 600, 900, and 1100 K were used in this study to investigate the effects of sintering temperature on MSD for the nanosintering process. It can be seen from this diagram that the mean square displacement increases due to increasing sintering temperature. In addition, it is clear that the effects of sintering temperature are particularly significant at 1100 K. Also, the maximum MSD is  $90 \text{ \AA}^2$  for a sintering temperature of 1100 K and sintering time of 400 ps, while the minimum MSD of  $18.55 \text{ \AA}^2$  was found for a sintering temperature of 600 K at the final stage of the nanosintering process.

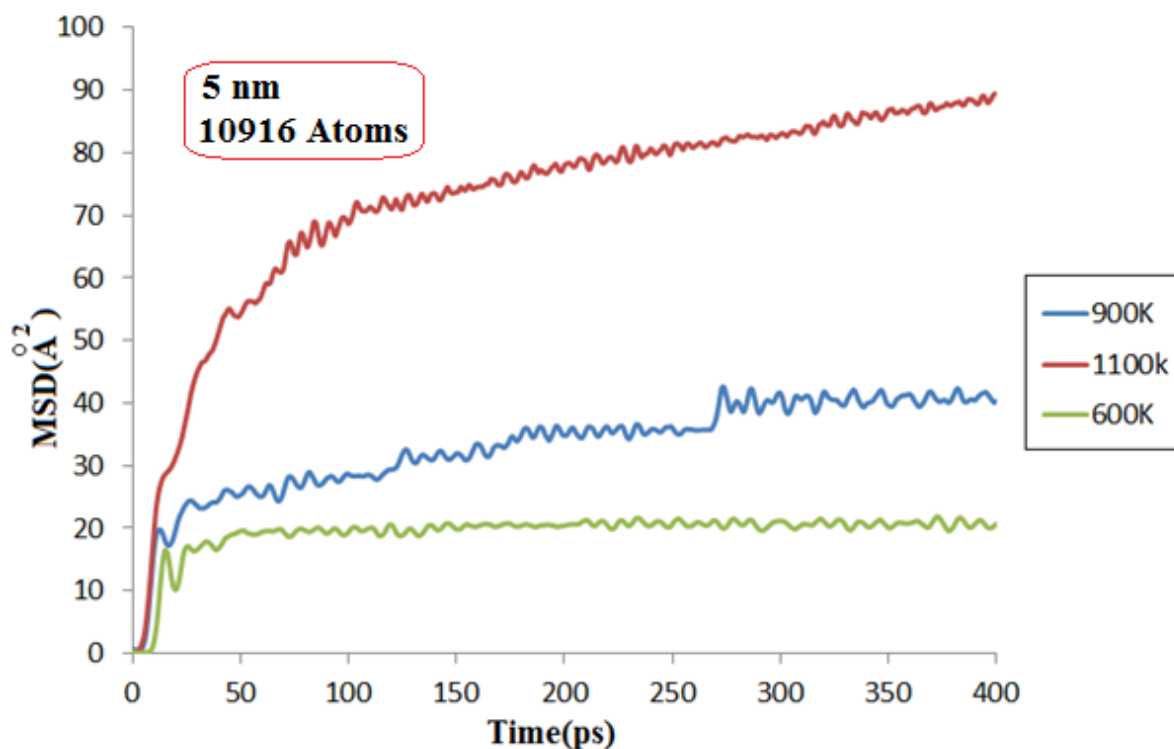


**Figure 5-15 Mean square displacement of 5 nm for different sintering temperatures.**

Figure (5-16) gives a comparison of the diffusion coefficients for different sintering temperatures of two copper nanoparticles with diameters of 5 nm. Three different sintering temperatures, 600, 900, and 1100 K were used in this study to investigate the effects of the sintering temperature on the diffusion coefficient for the nanosintering process. Overall, it can be seen from this diagram that the diffusion coefficient increases due to increasing sintering temperature; moreover, the diffusion coefficient decreases with increased sintering time. Also, the maximum diffusion coefficient of 0.35 was observed for a sintering temperature of 1100 K for a sintering time of 21 ps, while the minimum diffusion coefficient of 0.01 was observed for a sintering temperature of 600 K during the final stage of the nanosintering process.

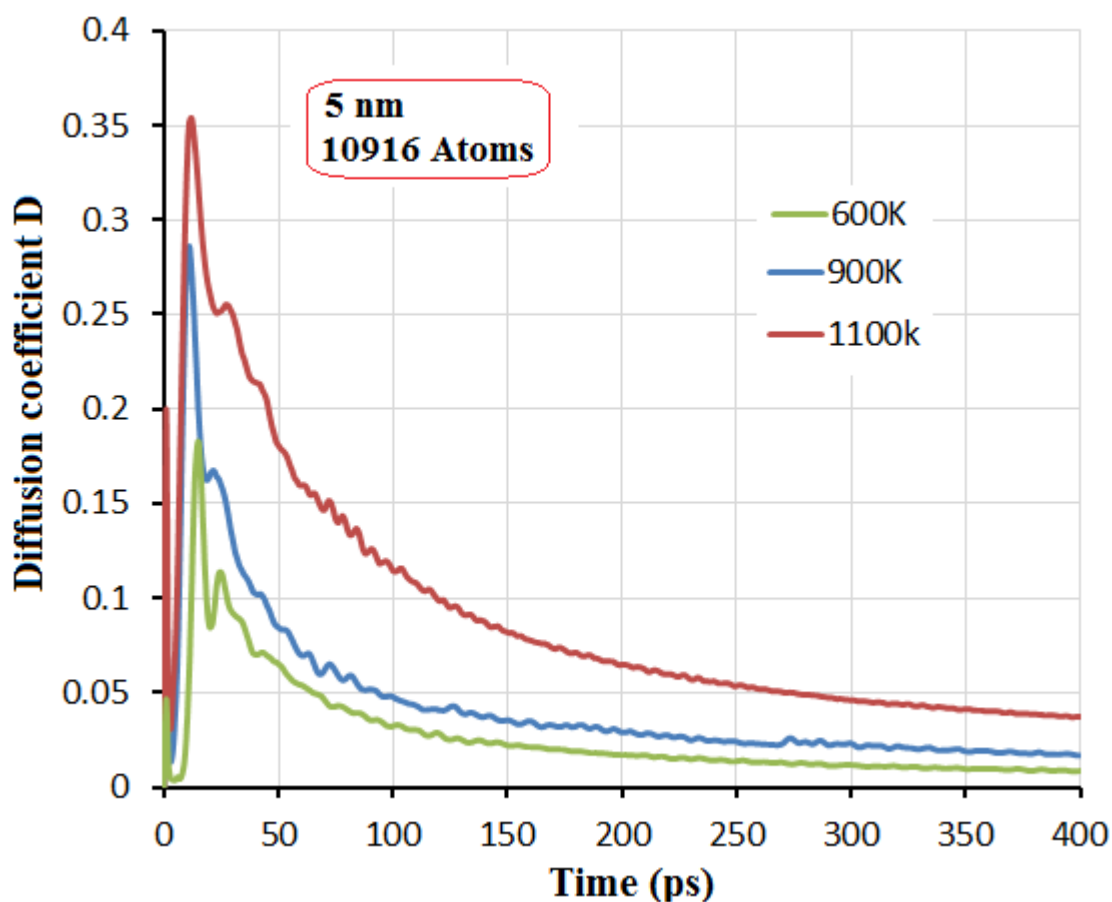


Figure 5-16 Diffusion coefficient for difference sintering temperature.

#### 5.4.4 Hollow nanocopper sintering

Hollow copper nanoparticles were created to study the effects of hollow nano-copper on the solid-state sintering process at the same sintering temperature are used before. The hollow nano-copper has two diameters, the outer and inner diameters, which were 10 and 7.5 nm, respectively. Figure (5-17) illustrates a comparison of neck size ratio between the solid and hollow nano-coppers at a fixed sintering temperature (600 K) using an outer diameter of 10 nm for the solid nanoparticles. Overall, it can be clearly seen that the neck size ratio of the hollow nano-copper is larger than that of the solid nano-copper, this is because the hollow nano-copper creates plastic deformation

mechanism which accelerates the sliding of dislocations from the hollow surface to the neck region. This means that a lot of atoms move to the neck region (two dislocation paths for each nano-copper), thereby improving the neck size between nanoparticles. Also, the maximum neck size ratio is 0.615 for hollow nanoparticles for a sintering time of 400 ps, while the minimum of neck size ratio is 0.452 for solid nanoparticles at the final stage of the sintering process.

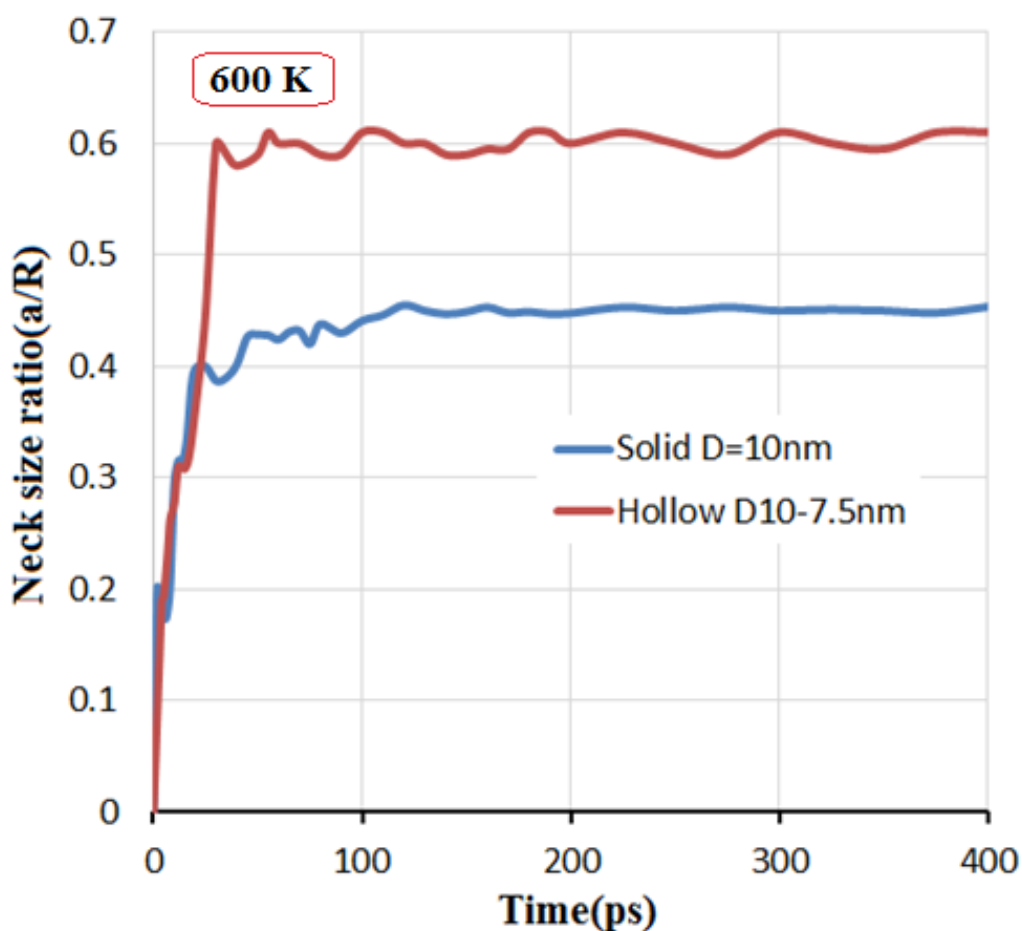
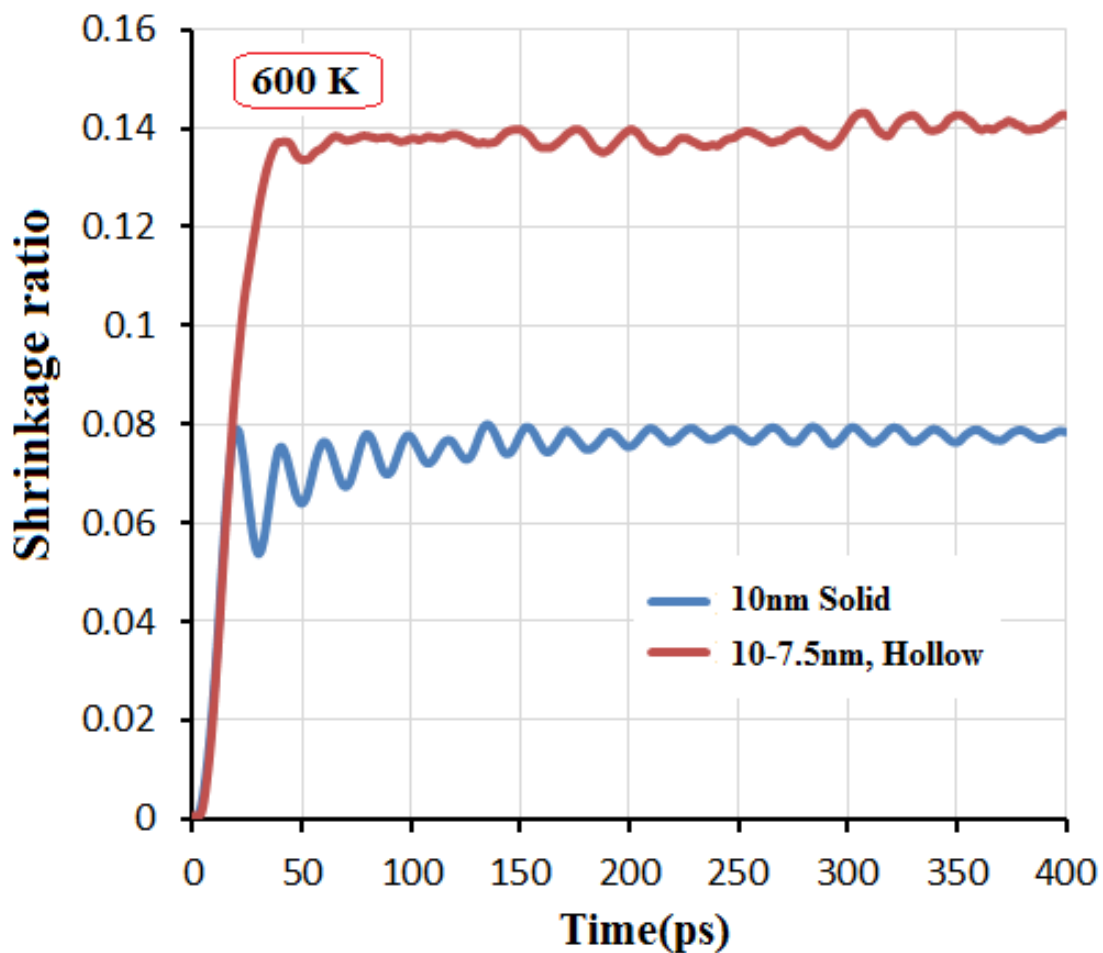


Figure 5-17 A comparison of neck size ratio between solid and hollow nano-copper at 600 K.

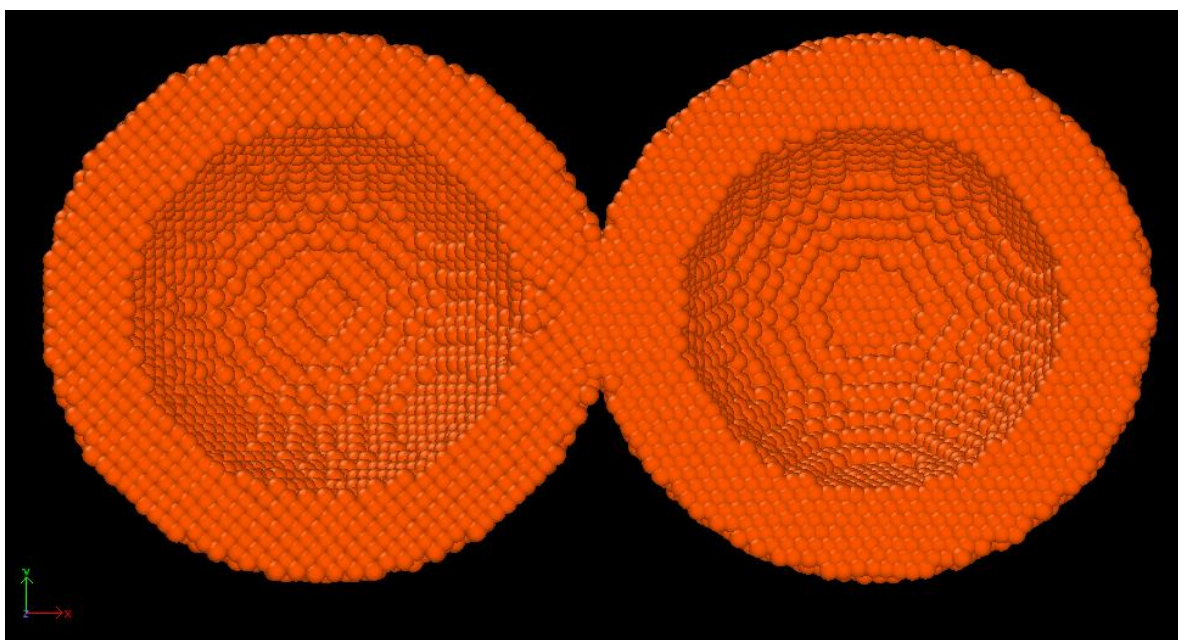
Figure (5-18) shows a comparison of the shrinkage ratio of a solid and hollow nanoparticle for two copper nanoparticles at a sintering temperature of 600 K. Overall, it can be seen that the shrinkage ratio of hollow nano-copper is greater than that of solid nano-copper. The maximum shrinkage ratio was 0.14 for hollow nanoparticles, for a sintering time of 400 ps. While the minimum shrinkage ratio was 0.0785 for solid nanoparticles at the final stage of the sintering process.



**Figure 5-18 Shrinkage ratio with time for solid and hollow copper nanoparticles at 600 K.**

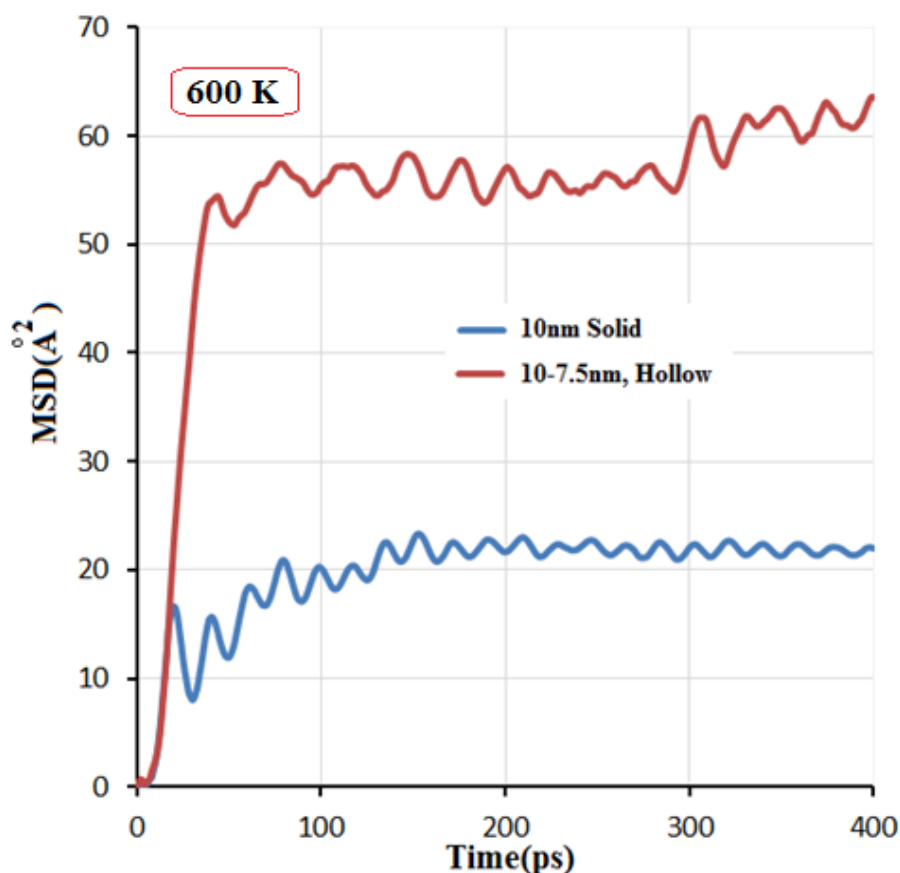
Figure (5-19) shows a snapshot of a half section through two hollow nano-coppers with outer and inner diameters of 10 nm and 7.5 nm, for a sintering time of 10 ps. It

can be seen that neck begins to growth between the two hollow particles and the shape of the neck has the appearance of a diamond, which represents the movement of atoms inside the two nanoparticles which create the neck region. Also, figure (5-19) illustrates the movement of dislocations inside hollow nano-copper particles during the nanosintering process.



**Figure 5-19 Snapshot of two hollow copper nanoparticles.**

Figure (5-20) compares the MSD between two solid and hollow copper nanoparticles at a sintering temperature of 600 K. Overall, it can be clearly seen that the MSD of hollow nano-copper is higher than that of for solid nano-copper. Also, the maximum MSD was  $62.5 \text{ \AA}^2$  for the hollow nanoparticles for a sintering time of 400 ps. While the minimum MSD of  $22.35 \text{ \AA}^2$  was found for solid nanoparticles at the final stage of the sintering process. Lastly, the effect of hollow nanoparticles on the shrinkage ratio and MSD was greater than in the neck size ratio. That means the effect of grain boundary diffusion is greater than all other diffusion mechanisms in nano-copper sintering.

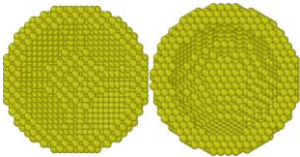
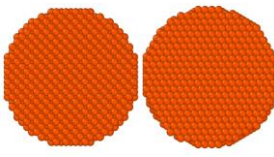
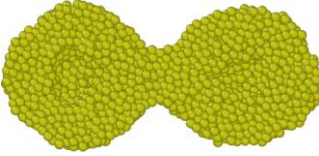
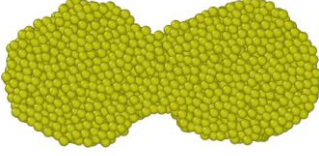
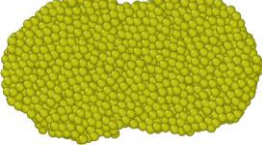
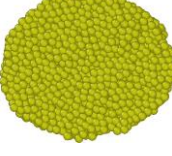
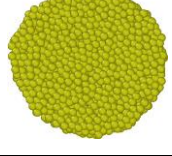


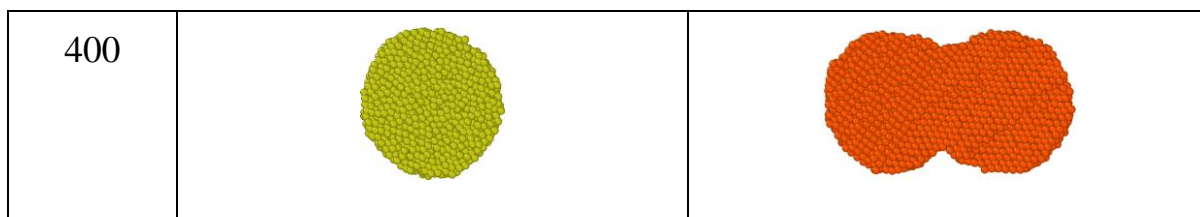
**Figure 5-20** MSD for solid and hollow copper nanoparticles at 600 K.

Table (5.5) shows snapshots of a half section of two solid and hollow copper nanoparticles with initial sizes of 5 nm for solid nanoparticles, and 5-3.75 nm for the hollow nanoparticles; this table also compares hollow and solid nanoparticles at a sintering temperature of 1000 K. The first column in table represents sintering time in picosecond while the second, third columns represent snapshots of hollow and solid nanoparticle respectively. Overall, it can be seen that the hollow nanoparticles have become one large nanoparticle, while the two solid nano-coppers remained two nanoparticles at the end of the sintering process, this is because the hollow nano-copper creates plastic deformation mechanism which accelerates the sliding of dislocations from the hollow surface to the neck region. This means that a lot of atoms

move to the neck region (two dislocation paths for each nano-copper), thereby improving the neck size between nanoparticles.

**Table 5.5 Comparison between hollow and solid nanoparticles at a sintering temperature of 1000 K and nanoparticle size 5nm.**

Sintering time(ps)	Hollow	Solid
0		
5		
10		
20		
50		
100		



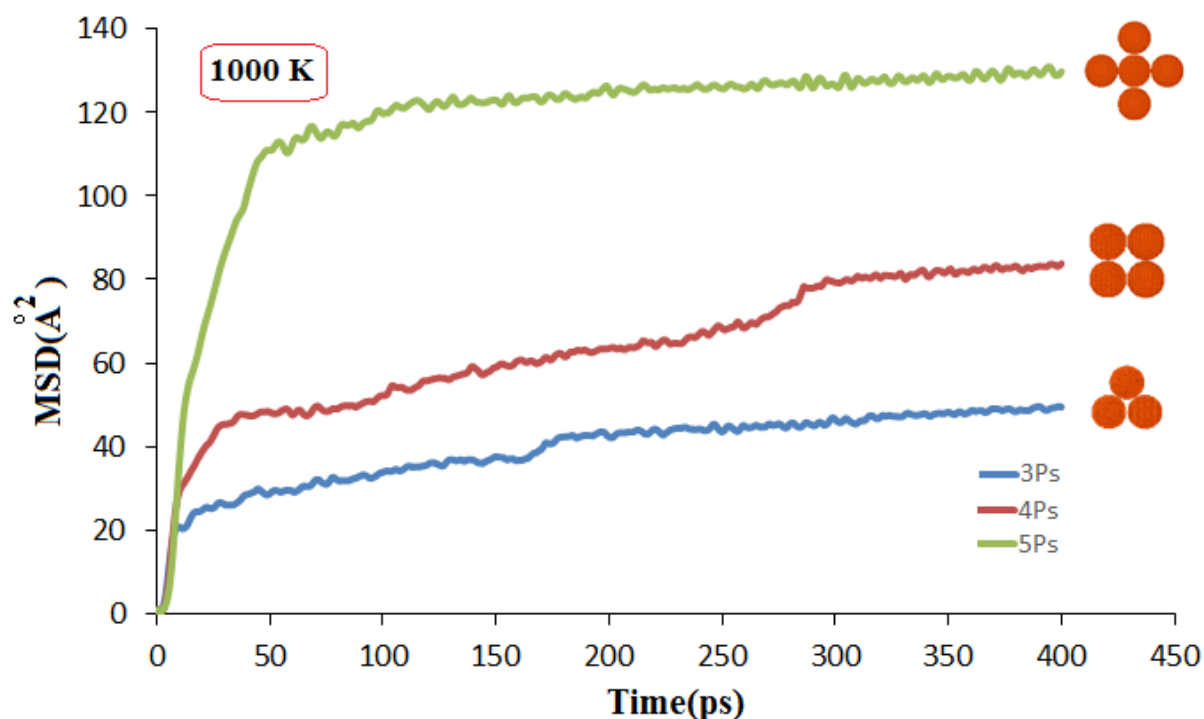
### 5.4.5 Multiple copper nanoparticle sintering

The behaviour of multiple nanoparticles can be examined in the sintering process when applying heat to such a system. Solid and hollow nanoparticles are used in simulations whilst using different numbers of particles, i.e., three, four and five nanoparticles, and of different crystallographic orientations. Finally, the solid nanoparticle results are compared with those for hollow nanoparticles at different sintering temperatures. This is achieved using MSD and potential energy to show the effect of sintering temperature in the two varieties of nanoparticles (Solid and Hollow). The numbers of atoms inside each system are given in table (5.6). Yousefi [106] used molecular dynamics to simulate 27 nickel nanoparticles at a sintering temperature of 300 K, concluding that surface diffusion is the dominant mechanism in the sintering process.

**Table 5.6 The number of atoms inside nanoparticles.**

Number of nanoparticles at a size of 5 nm	Number of Atoms
Two solid nanoparticles	10916
Three solid nanoparticles	16342
Four solid nanoparticles	21782
Five solid nanoparticles	27294
Two hollow nanoparticles	6820
Three hollow nanoparticles	9423
Four hollow nanoparticles	12571
Five hollow nanoparticles	15778

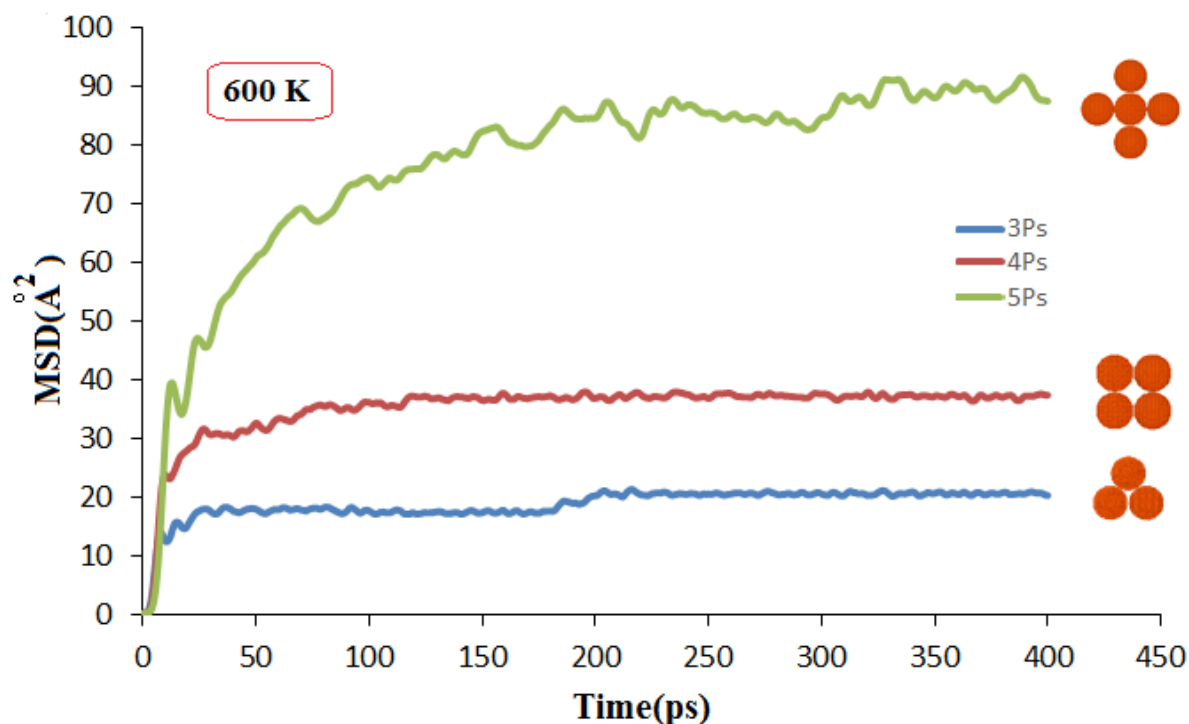
Figure (5-21) compares the MSD of three different nanoparticle systems with diameters of 5 nm and a sintering temperature of 1000 K. Three different systems of copper nanoparticle with diameters of 5 nm were used in order to investigate the effects of the number of nanoparticles present in the sintering process. Generally, the curve of five nanoparticles system has the highest MSD of all, this is because the movement of atoms of the five nanoparticles is higher than all the other systems. Also, the maximum MSD was  $120 \text{ \AA}^2$  for the five nanoparticles with a sintering time of 400 ps, while the minimum MSD was  $48 \text{ \AA}^2$  for three nanoparticles during the final stage of the sintering process.



**Figure 5-21 Comparison of MSDs for three solid types of particles at a fixed particle size of 5 nm at sintering temperature of 1000K.**

Figure (5-22) compares the MSDs of different systems of nanoparticle with diameters of 5 nm at a sintering temperature of 600 K. It was found that the MSD for five nanoparticles has higher than all systems, which it means the MSD increases due to

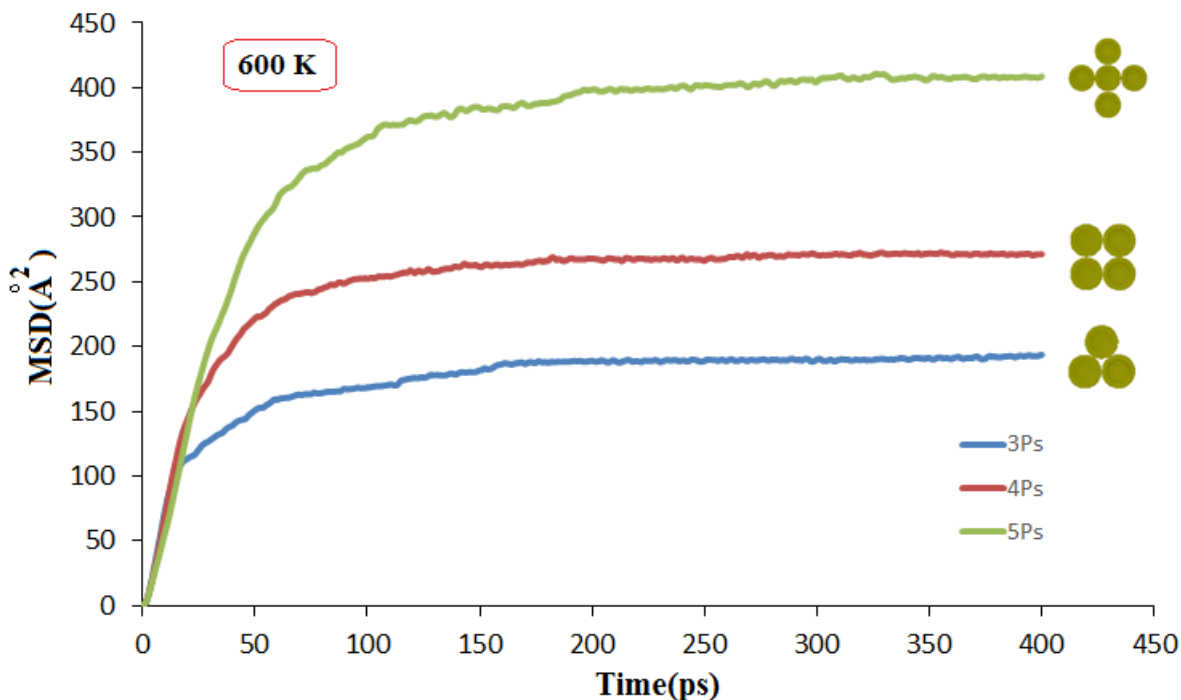
the increase in the number of nanoparticles. In addition, the curve of five nanoparticle system has a difference than all curves which means that the movement of atoms for five nanoparticle system is not the same of three and four nanoparticle system. Also, the maximum MSD was  $90 \text{ \AA}^2$  for five nanoparticles, while the minimum MSD was  $19 \text{ \AA}^2$  for three nanoparticles at the final stage of the sintering process.



**Figure 5-22 Comparison of MSDs for three solid types of particles at a fixed particle size of 5 nm at sintering temperature of 600 K.**

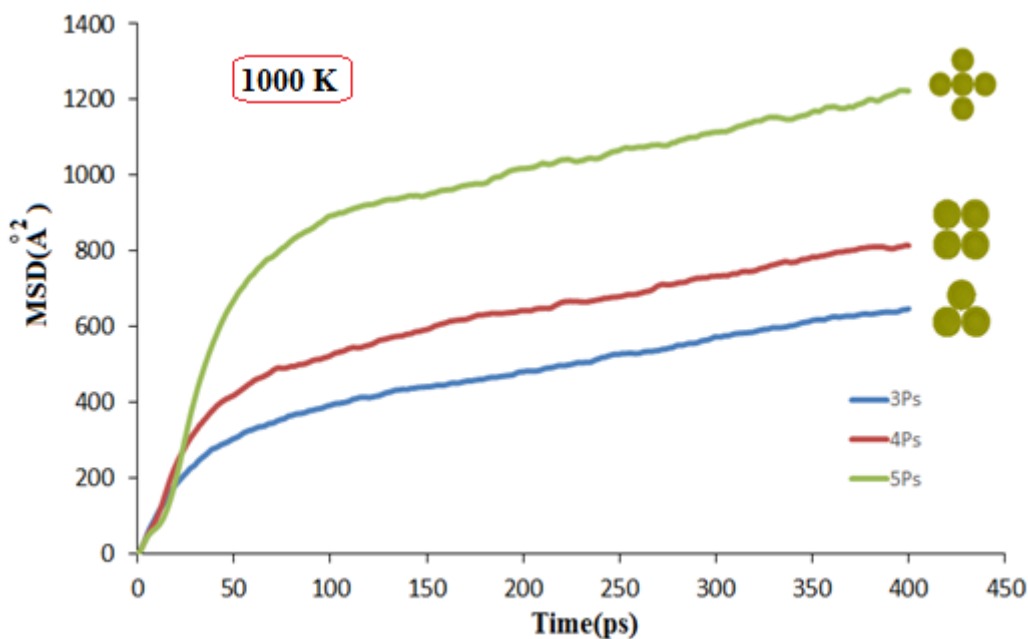
Figure (5-23) gives a comparison of the MSD between the three different hollow particle systems, at a sintering temperature of 600 K. Three different hollow copper nano-particle systems with fixed diameters of 5 nm were used to investigate the effects of multiple hollow nanoparticle types on the sintering process. Generally, the system of the five hollow nanoparticles had the highest MSD compared to all the other systems. This is because the movement of atoms at five nanoparticles system had a position

more than the other systems. Also, the maximum MSD was 403 Å<sup>2</sup> for five hollow nanoparticles while the minimum MSD was 175 Å<sup>2</sup> for the three hollow nanoparticles for a sintering time of 400 ps.



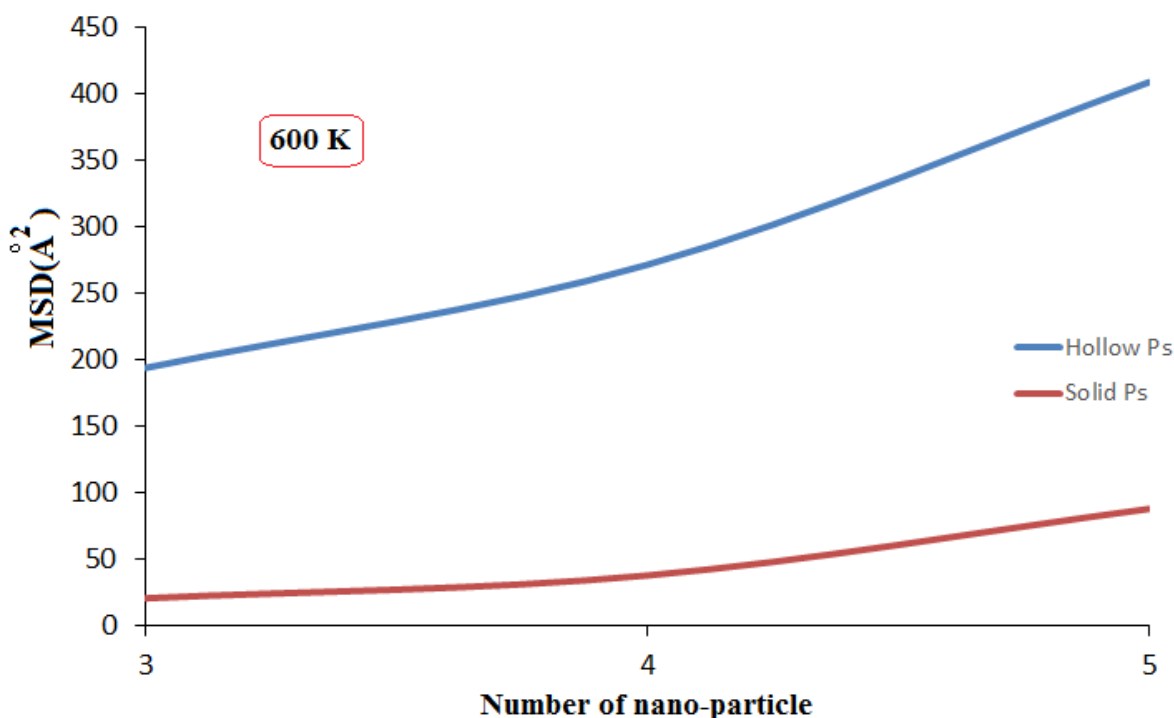
**Figure 5-23 Comparison of MSDs for three hollow nanoparticles types at a sintering temperature of 600 K.**

The comparison between the different hollow nanoparticle systems at a sintering temperature of 1000 K are shown in figure (5-24). It can be seen that the curves in figure (5-24) increase in two stages, while the curves in figure (5-23) increase just during the first stage. The MSD of the five nanoparticles system in figure (5-24) is higher than in figure (5-23), this is because of the increase in sintering temperature. Also, the maximum MSD was 1220 Å<sup>2</sup> for five hollow nanoparticles while the minimum MSD was 602 Å<sup>2</sup> for three hollow nanoparticles for a sintering time of 400 ps.



**Figure 5-24 Comparison of MSDs for three hollow types of nanoparticles at a sintering temperature of 1000 K.**

Figure (5-25) gives a comparison of the MSD between hollow and solid nanoparticles for different systems of nanoparticles at a sintering temperature of 600 K. As shown in figure (5-25), the maximum MSD is  $410 \text{ \AA}^2$  for the five hollow nanoparticles while the minimum MSD is  $80 \text{ \AA}^2$  at time 400ps. Overall, it can be observed that the hollow nanoparticles have a higher MSD than the solid nanoparticles, and the highest MSD was found for the system with the five hollow nanoparticles, while the system with three solid nanoparticles showed the lowest MSD. The gradient of the hollow nanoparticle curve increased at a faster rate compared to the curve of the solid nanoparticle curve.

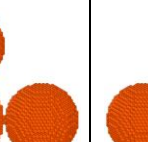
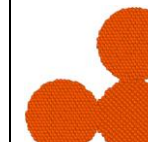
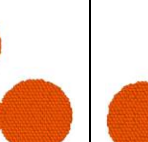
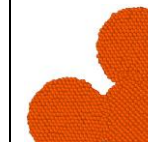
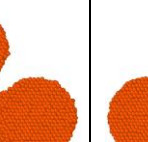


**Figure 5-25 Comparison of MSDs for hollow and solid nanoparticles at 600 K.**

Table (5.7) shows a number of snapshots of the evolution of the different systems of solid nanoparticle shapes for different sintering temperatures (600 and 1000 K) and for different sintering times. The first column represents the sintering time in picoseconds while the second, third, fourth, fifth and sixth represent snapshots of different solid nanoparticle systems; the top row represents the sintering temperature in Kelvin. It may be noted that the difference between the six cases are shown in the table (5.7); for example, the hole between the three nanoparticles at 1000 K has vanished at a time of 5 ps, whilst for the three nanoparticle system are seen to be more united (shrink together at 1000 K more than at 600 K). In addition, it may be noted that the third nanoparticle at 1000 K has a different movement because the crystal orientation is (111), so its movement is more inline towards the centre of other nanoparticles, giving a flush fit. For four nanoparticles, however, it can be seen in table (5.7) that the hole between them at 1000 K has vanished at a time of 20 ps, they can

also be seen to be better unified than the nanoparticles at 600 K; furthermore, four nanoparticles at 600 K showed the least shrinkage (because shrinkage between nanoparticles depends on sintering temperature). Lastly, for five nanoparticles, it was found that the geometry at 1000 K showed greater alteration than at 600 K. This was because the middle nanoparticle in the sintering process at 1000 K vanished at 50 ps. The geometry had the appearance of a connection between four nanoparticles.

Table 5.7 Different systems of nanoparticles at various different temperatures.

Temp. \ Time	600K	1000K	600K	1000K	600K	1000K
0						
5						
10						

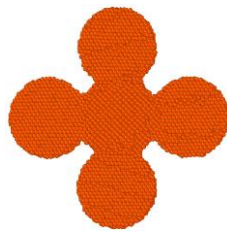
20						
50						
100						
400						

Table (5.8) compares different hollow nanoparticle shapes at different sintering temperatures (600 and 1000 K), for different sintering times. Overall, the sintering temperature and hollow nanoparticles improved the sintering process; for example, the geometry of the three hollow nanoparticles at a temperature of 1000 K changed to a spherical shape at a sintering time of 50 ps. 600 K and 1000 K were used to show the behaviour of hollow nanoparticles during the sintering process, whereas for four hollow nanoparticles, it can be seen from table (5-8) that their final shape at 1000 K

was spherical, which means that the sintering process at a temperature of 1000K completed the final stage of the sintering process when compared with the nanoparticles at a temperature of 600K. Lastly, for five hollow nanoparticles, it was shown that the final geometry at 1000 K was spherical, which means that all of the nanoparticles moved inward together, this resulted in full densification.

**Table 5.8 Different systems of hollow nanoparticles at different temperatures.**

Temp. \ Time	600K	1000K	600K	1000K	600K	1000K
0						
50						
100						

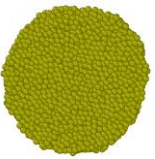
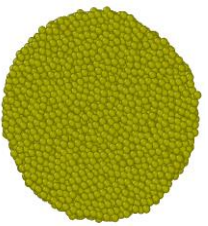
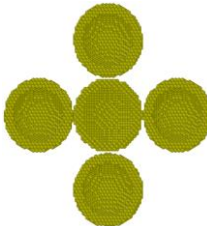
<b>400</b>						
------------	---	---	---	--	---	---

Table (5.9) shows a comparison between hollow and solid nanoparticle systems for a sintering temperature of 600 K with different sintering times. Overall, it can be seen that all the gaps inside and between the nanoparticles collapsed and modified to form solid structures, while the gaps between solid nanoparticles remained, which means that the densification of the hollow nanoparticles was greater than for solid nanoparticles.

**Table 5.9 Comparison between hollow and solid nanoparticles at a sintering temperature of 600 K.**

Style Time	Hollow	Solid	Hollow	Solid	Hollow	Solid
0						
50						

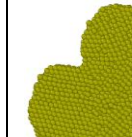
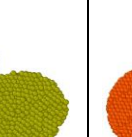
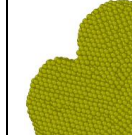
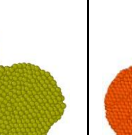
100						
400						

Figure (5-26) compares different types of hollow and solid nanoparticles at a sintering temperature of 1000 K. Overall, it can be seen that the potential energy of the solid nanoparticles is lower than for the hollow nanoparticles, which means that the hollow nanoparticles were more favorable for the nanosintering process than solid nanoparticles, this is because the hollow nano-copper accelerates the sliding of dislocation inside the nanoparticle during the nanosintering process, thus the movement of atoms, from inside of nanoparticles to the neck region, increases due to the sliding dislocation, and lastly the potential energy increases due to the movement of atoms. In addition, three nanoparticles had a higher potential energy than five for both solid and hollow nanoparticle types. The minimum potential energy/atom is -3.21 eV for hollow nanoparticle at style 5 NPs while the minimum potential energy/atom is -3.29 eV for solid nanoparticle at style 5 NPs at the final stage of the sintering process.

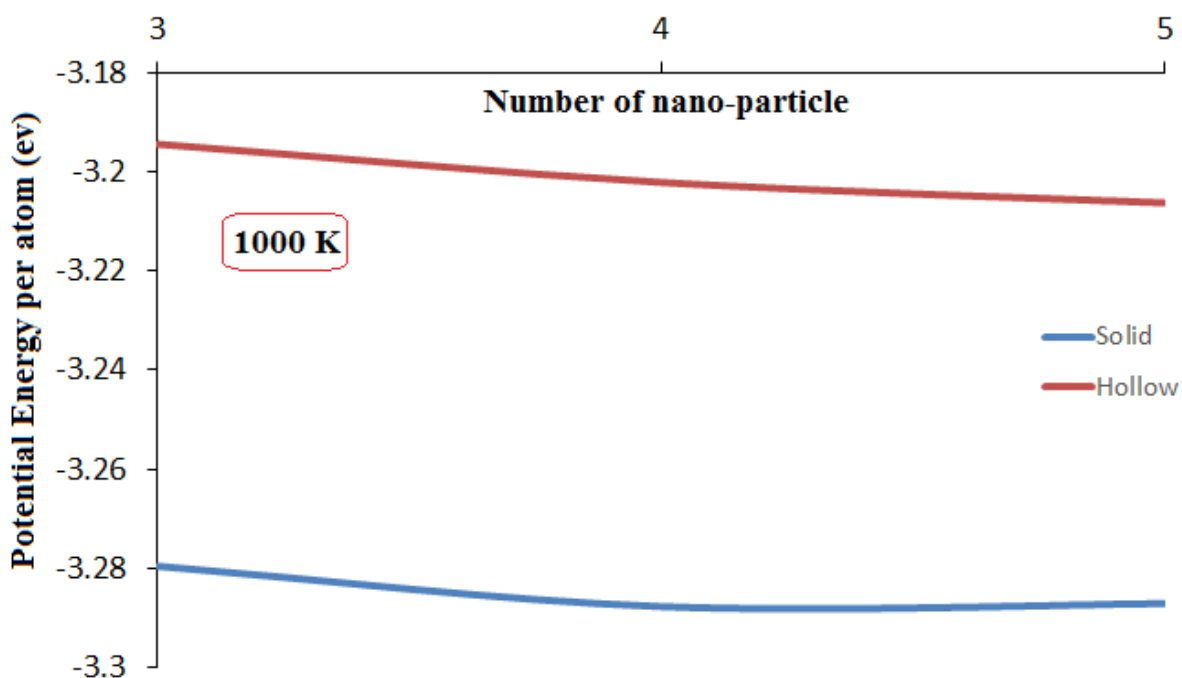
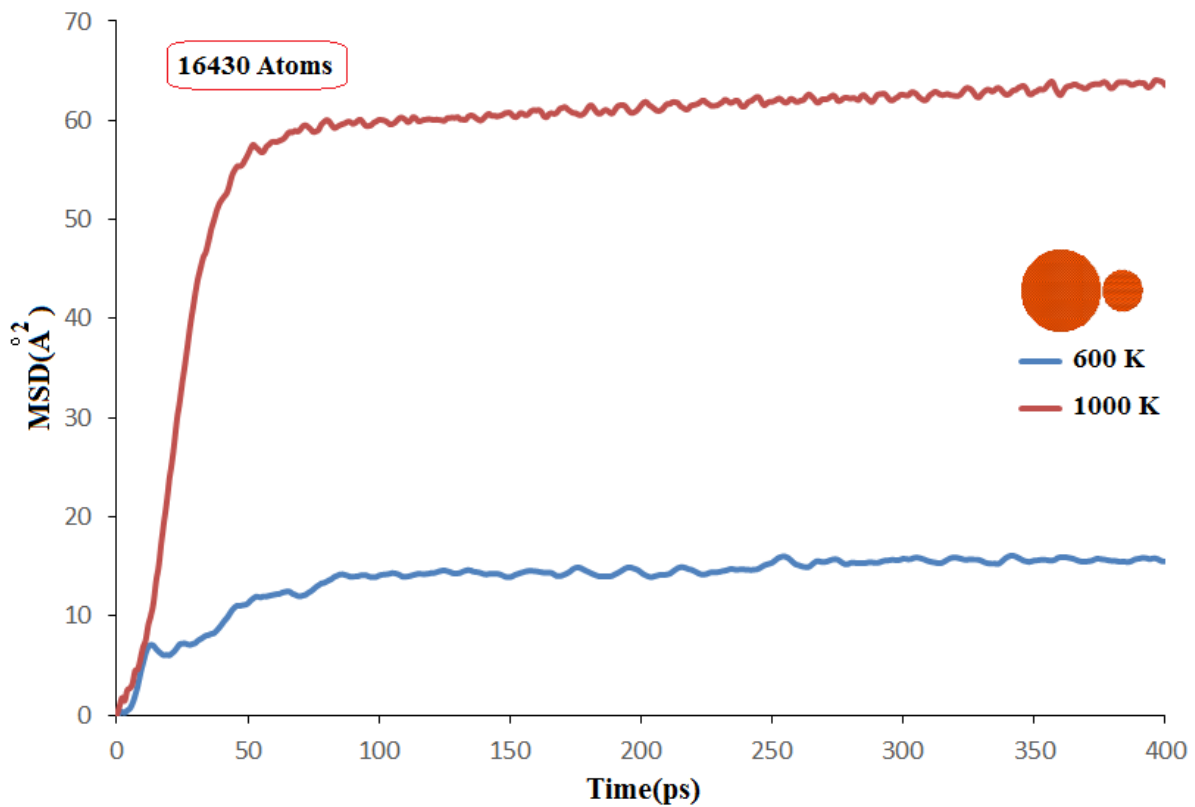


Figure 5-26 Potential energies per atom for hollow and solid nanoparticles at 1000 K.

#### 5.4.6 Sintering of different nanoparticle sizes:

The two curves in figure (5-27) compare MSDs for a couple of nanoparticles (10 and 5 nm) at sintering temperatures of 600 and 1000 K. As can be seen, there are two stages, the first being extremely rapid between 0 to 50 ps, while the second stage stabilizes between 50 to 400 ps. The MSD for nanoparticle sintering at a temperature of 1000 K is greater than that at 600 K. Also, the maximum MSD is  $62 \text{ \AA}^2$  at a sintering temperature of 1000 K, while the minimum shrinkage ratio is  $14 \text{ \AA}^2$  at 600 K for the final sintering process. Thus, the effect of temperature gives a higher MSD between nanoparticles.



**Figure 5-27 MSD for two different nanoparticle sizes for different sintering temperatures.**

The two curves in figure (5-28) give a comparison of the shrinkage ratio for a couple of nanoparticles (10-5 nm) for sintering temperatures of 600 and 1000 K. Overall, it can be seen that the densification for a couple of nanoparticles at a sintering temperature of 1000 K is greater than for nanoparticles at 600 K; for example, the two snapshots at 50 ps in figure (5-28) show the difference between the two nanoparticles for different sintering temperatures. Also, the maximum shrinkage ratio is 0.27 at a sintering temperature of 1000 K, while the maximum shrinkage ratio is 0.12 at 600 K.

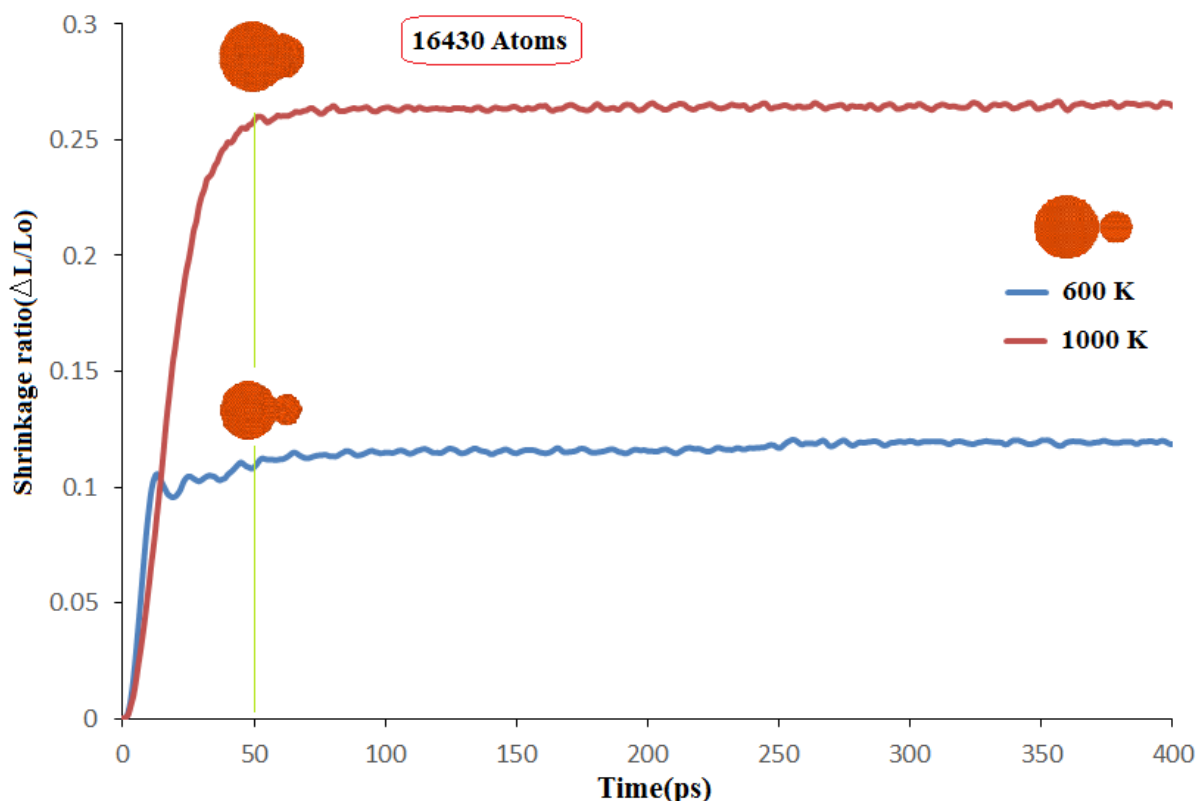
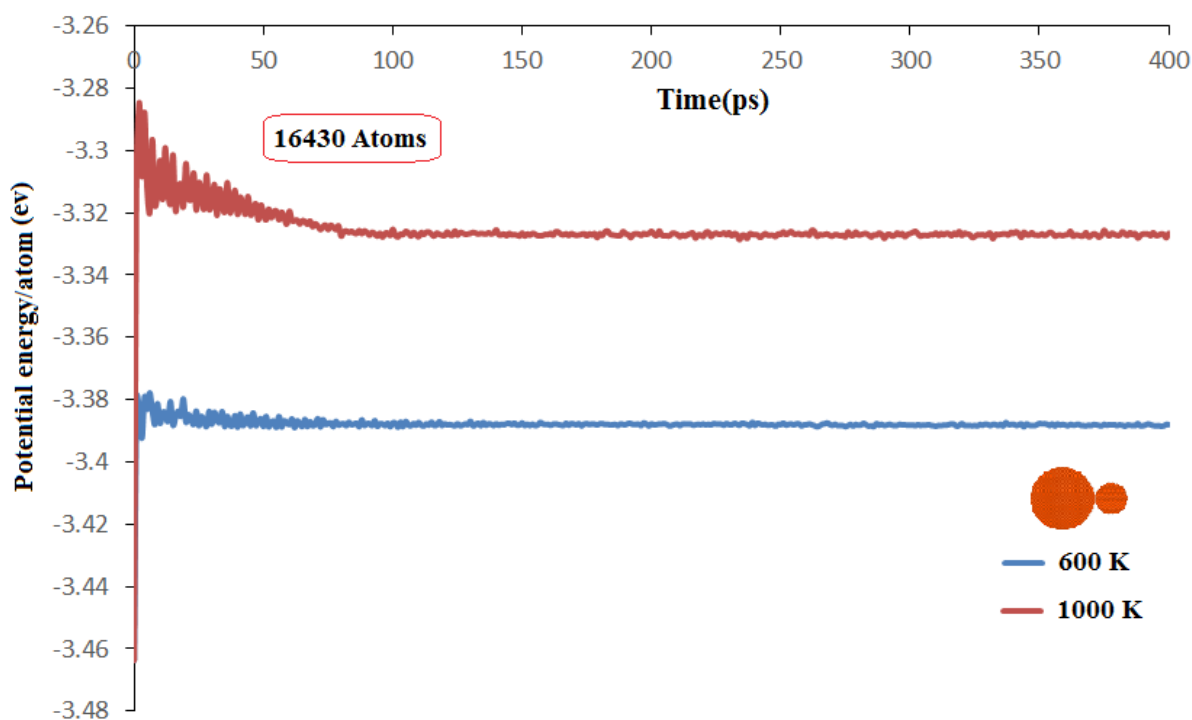


Figure 5-28 Shrinkage ratio for a couple of different nanoparticles at different sintering temperatures.

The two curves in figure (5-29) compare the potential energy for a couple of nanoparticles (10-5 nm) at sintering temperatures of 600 and 1000 K. Overall, it is clear that the potential energy for sintering at 1000 K is higher than at 600 K; the potential energy increases due to the increase in sintering temperature, this is because the effect of sintering temperature plays an important role in the nanosintering process. The nanoparticles sizes 10 and 5 nm used in the simulation have two different melting temperatures, the smaller having a lower melting temperature. Thus at higher sintering temperatures the activated grain boundary and surface diffusion mechanisms between nanoparticles causes the finer nanoparticles to be absorbed by the larger nanoparticles. Also, the minimum potential energy/atom is -3.32 eV at a sintering temperature of 1000 K while the minimum potential energy/atom is -3.38 eV for solid

nanoparticles at a sintering temperature of 600 K for the final stage of the sintering process. Lastly, the curve at 600 K started to stabilize after sintering time 25 ps while the curve at 1000 K started to stabilize after sintering time 100 ps because of sintering temperature.



**Figure 5-29 Potential energies for a couple of different nanoparticles at different sintering temperatures.**

Table (5.10) shows snapshots of comparisons of two solid and hollow nanoparticle types at different sintering temperatures of 600 and 1000 K. Overall, it can be seen that the sintering of hollow nanoparticles at 1000 K shows more densification than sintering at 600 K, especially at a time of 400 ps; moreover, the neck growth between nanoparticles at 1000 K for hollow nanoparticles is greater than for nanoparticles at 600 K, especially at a time of 5 ps. Lastly, the collapse in nanoparticle sintering at 1000 K for hollow nanoparticles is greater than at 600 K, especially from 50 ps until the final stage.

Table 5.10 Solid and hollow nanoparticles at different sintering temperatures.

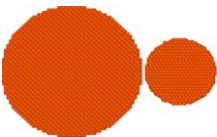
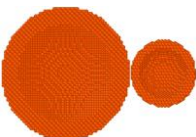
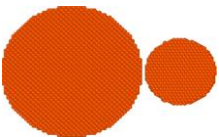
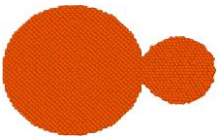
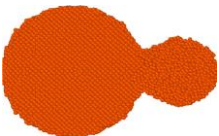
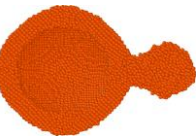
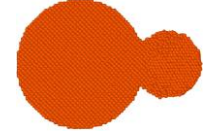
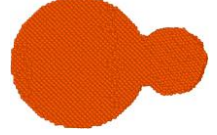
Style & Temp. Time	Solid 600K	Hollow 600K	Solid 1000K	Hollow 1000K
	0			
5				
10				
20				
50				
100				
400				

Figure (5-30) shows a comparison of neck size ratio for the hollow and solid nanoparticles at a sintering temperature of 600 K. Overall, it was seen that the neck between the hollow nanoparticles is greater than that of solid nanoparticles, this is because the hollow nanoparticles accelerate the sliding of dislocations for plastic deformation of the atoms, thus, it improved the neck growth process. In addition, the two curves are matched in the beginning but after, the curves were seen to separate after 20 ps. Also, the maximum neck radius is 50.51 Å for hollow nanoparticles while the maximum neck radius is 37.5 Å for solid nanoparticles at the final stage of the sintering process.

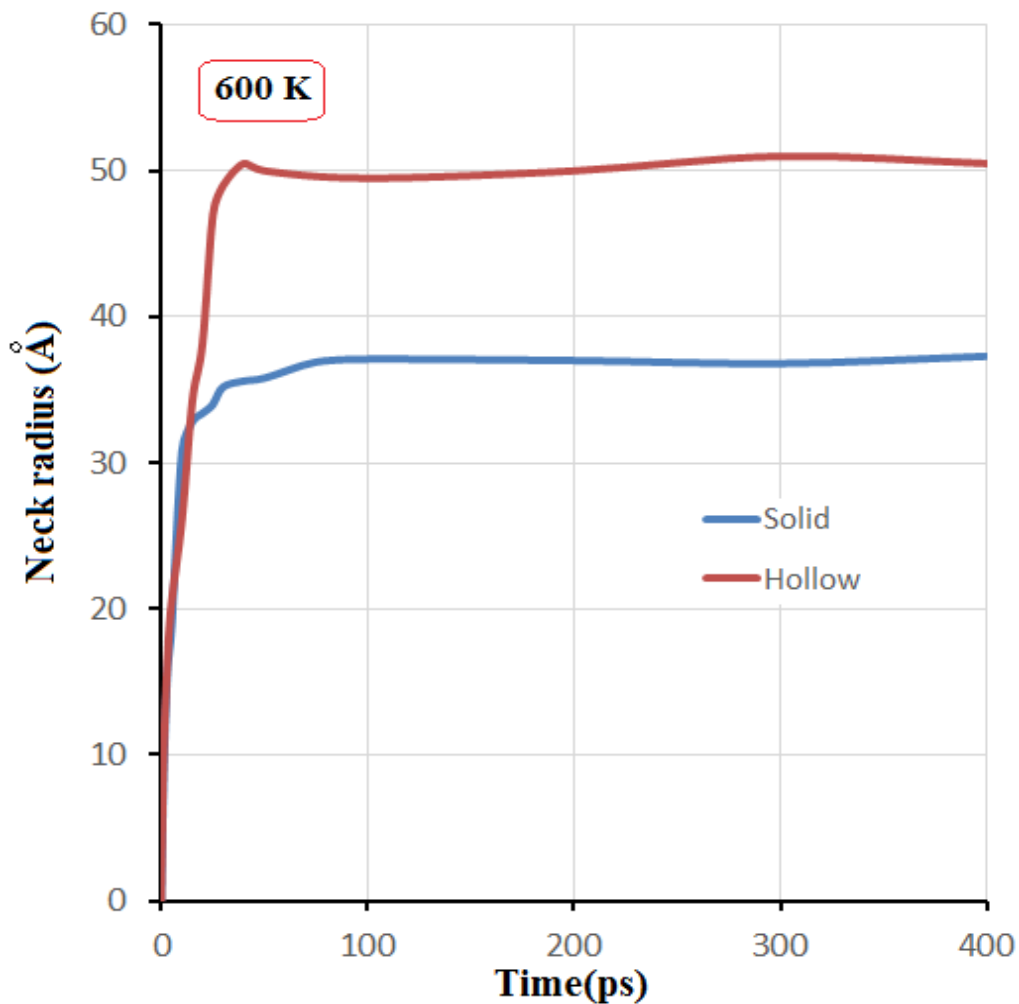


Figure 5-30 Neck radii of solid and hollow nanoparticles at sintering temperature 600 K.

Figure (5-31) gives a comparison of neck size for two solid nanoparticles of different sizes at different sintering temperatures. Two sintering temperatures, 600 and 1000 K, were used in the simulations in order to show the neck growth during the sintering of the nanoparticles at different temperatures. Overall, it can be seen that the neck size for each of the different sizes of nanoparticles at a sintering temperature of 1000 K was larger than the nanosintering at 600 K, which means that the sintering temperature impacts the nanosintering process. Also, the maximum neck radius is 62 Å for sintering temperature 1000 K while the maximum neck radius is 37.2 Å for a sintering temperature of 600 K at the final stage of the sintering process. Lastly, the green line at 50 ps in figure (5-31) shows the difference between the two snapshots at two different temperatures.

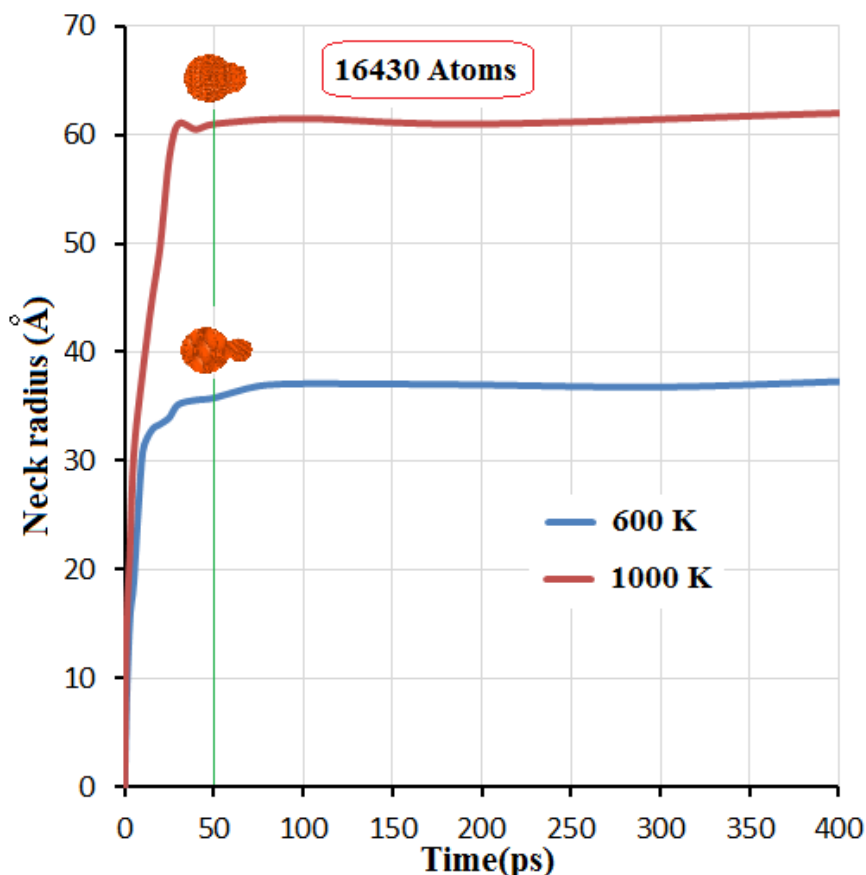


Figure 5-31 Neck size radius for the solid nanoparticles at different sintering temperatures.

A comparison between hollow and solid nanoparticles of different nanoparticle types, and at a sintering temperature of 600 K, is shown in figure (5-32). Overall, it can be seen that the shrinkage ratio for the hollow nanoparticles is higher than the solid nanoparticles, this is because the hollow nanoparticles accelerate the sliding of dislocations for plastic deformation of the atoms, and it improved the densification process between particles. In addition, the two curves look like one curve in the beginning, but later the curves diverged after time 20 ps. Also, the maximum shrinkage ratio is 0.215 for hollow nanoparticles, and 0.125 for solid nanoparticles at the final stage of the sintering process.

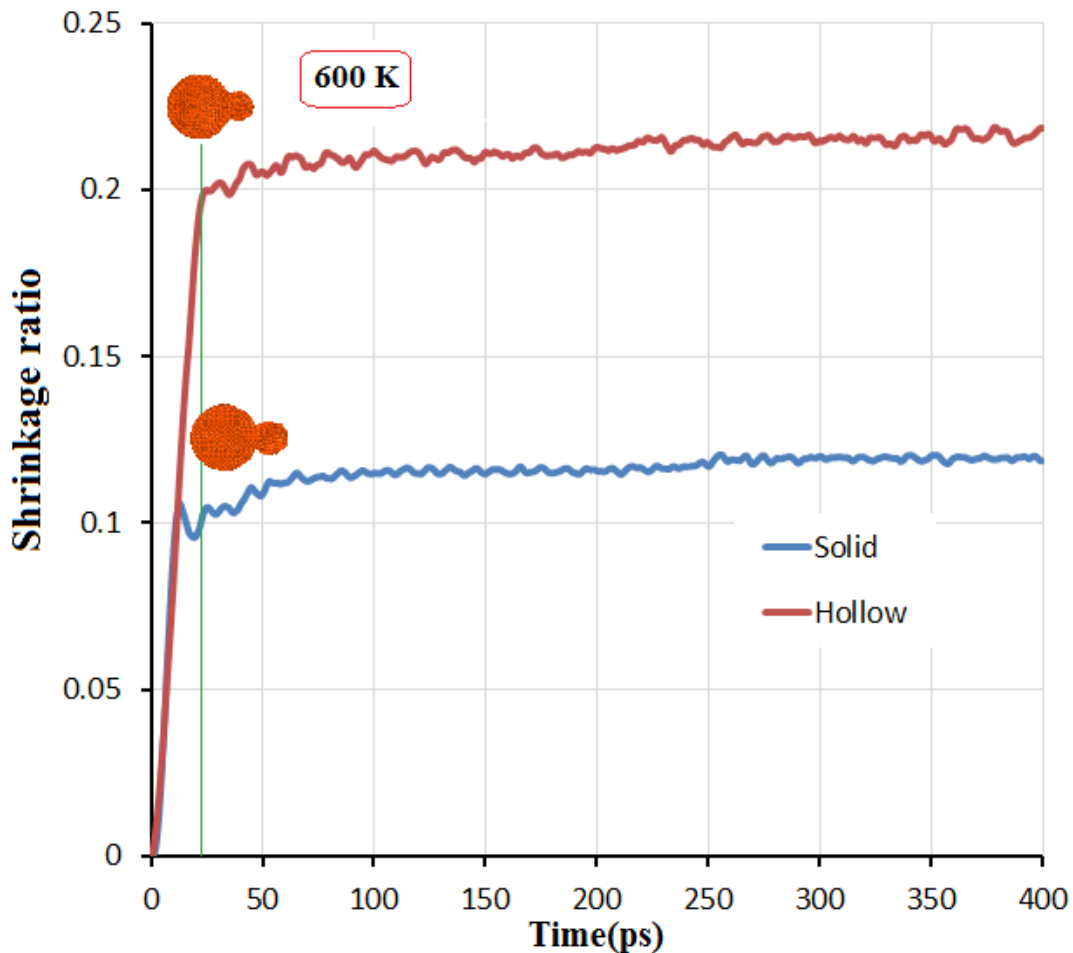


Figure 5-32 Shrinkage ratio of two solid and hollow nanoparticles of differing size at 600 K.

## 5.5 Summary

Chapter five focuses on the mechanisms of the solid-state nanosintering process between copper nanoparticles using molecular dynamics simulations as found using the LAMMPS code to simulate coalescence between copper nanoparticles during sintering. Chapter five clarified the following points:

- 1- The full melting temperature of nanocopper was obtained from molecular dynamics simulations, using potential energy functions, was in good agreement with the G-T analytical model, while other models were in good agreement with larger nanocopper sizes, in particular ranging from 16 to 30 nm.
- 2- The neck size ratio had two stages of change: the first represented an increasing of neck size ratio due to the increased sintering time and continued up to 20 ps, while the second stage represents the stabilization of the neck size ratio, which continued from 30 ps until the final stage of the sintering process.
- 3- Neck growth and densification process between nanoparticles was increased by hollow nanoparticles of copper (30.43% for the neck size ratio, and 78.34% for the shrinkage ratio).
- 4- The neck growth between nanoparticles of copper was increased by using 100-111 crystal lattice (17.74% comparing with a 100-100 lattice).
- 5- Five hollow nanoparticles produced the highest MSD than different types of multiple nanoparticles.
- 6- Neck growth and densification between nanoparticles was increased by using hollow mix nanoparticles (33.34% for neck size ratio, and 83.34% for the shrinkage ratio compared with the mixed solid nanoparticles), this is because there are two effects: the first effect is hollow nanoparticles mentioned before, and the second effect is sintering between two different nanoparticles size. Thus the effect of sintering is larger in smaller nanoparticle this is because the melting temperature of the small nanoparticle is lower than the big nanoparticle.
- 7- The nanosintering process is faster than, and different to, the microsintering process; for instance, the full neck growth between the copper nanoparticles of 5 nm diameters was 0.95 at a sintering time of 200 ps, while the full neck growth

for microcopper of 1  $\mu\text{m}$  diameters is 0.945 at a sintering time of 8 s. In addition, the nanosintering process occurred in two distinct stages, while the microsintering process proceeded in one stage that continued with increasing sintering time.

## 5.6 Conclusions

The behaviour of nanocopper during the sintering process has been investigated using molecular dynamics via the LAMMPS code. The conclusion of chapter five clarified the following points.

- 1- Powder size has a significant effect on the nanosintering process. Fine copper nanoparticles improved the nanosintering process.
- 2- The nanosintering and microsintering processes are different. Nanosintering is rapid and different stages than microsintering process.
- 3- The sintering temperature improved sintering between nanoparticles in terms of three sintering parameters: neck size ratio, shrinkage ratio, and mean square displacement.
- 4- Crystal orientation has an important effect on the neck growth process. A 100-111 crystal lattice shows an enhanced nanosintering process.
- 5- Hollow nanoparticles improved sintering process for copper nanoparticles.
- 6- The smaller copper nanoparticles merged during nanosintering process.

## 6 CHAPTER SIX: Conclusions

### 6.1 Overall Conclusions:

Chapter six displays the major conclusions for the sintering modelling. There are three conclusions for this thesis.

#### 6.1.1 Chemical potential at triple junction conclusions

The following conclusions were drawn for chemical potential at triple junction:

1. The optimal method with which to model solid-state sintering using grain boundary diffusion without surface diffusion is the curve fitting method. This was shown when comparing with a full FD method for different diffusion coefficients.
2. The best method with which to model the force sintering process is the curve fitting method. This was shown when validates with a full FD method using difference applied stresses.
3. A relative density at a diffusion coefficient ratio equal to one obtained from the new curve fitting model shows a complete match with the full FD method.
4. The higher value of surface diffusion improved the matching between the curve fitting FD method and the full FD method.
5. A surface area reduction at a diffusion coefficient ratio equal to one obtained from the new curve fitting method shows a complete match with the full finite difference method.

#### 6.1.2 Application of curvature fitting equation to SLS Conclusions

The following conclusions can be drawn for curvature fitting equation to SLS:

1. Modelling of the SLS process using VM-curve fitting was demonstrated to be the optimal method with which to represent the SLS process between particles, as determined by comparison with the FD curve fitting method.
2. Powder size has obvious effects on selective laser sintering. Fine powders offer a large contact area between powder particulates.
3. The selective laser sintering was affected by particle size. Fine powders in the SLS process have high neck size ratio for copper powders.
4. Laser scan speed and laser power are important parameters in the selective laser sintering process, the process of which can efficiently be controlled by these two parameters.
5. The sintering temperature is a significant parameter in selective laser sintering. High sintering temperatures show improved the contact between powders.
6. Selective laser sintering was affected by the number of contacts between powders. A high number of contacts between copper powders show a greater reduction in surface area.

### **6.1.3 Molecular Dynamics model for nanoparticles sintering**

#### **Conclusions**

The following conclusions can be drawn from the work on the nanosintering process:

- 1- The nanosintering process was significantly affected by powder size. Fine copper nanoparticles improved the nanosintering process.
- 2- The nanosintering process is different to the microsintering process. The nanosintering is more rapid and proceeds via different stages than the microsintering process.
- 3- The sintering temperature improved the sintering between nanoparticles in terms of three sintering parameters: neck size ratio, shrinkage ratio, and mean square displacement.

- 4- The neck growth and densification process were improved depending on crystal orientation. A 100-111 crystal lattice orientation enhances the nanosintering process.
- 5- The nanosintering process was improved by the use of hollow nanoparticles, because of the dislocation movements inside nanoparticles.
- 6- The smaller nanocopper particles merged with the larger nanocopper particles during the nanosintering process when using a mix of nanoparticle sizes

**REFERENCES:**

- [1] Groover MP. Fundamentals of modern manufacturing: materials processes, and systems: John Wiley & Sons; 2007.
- [2] Narasimhan K. Sintering of powder mixtures and the growth of ferrous powder metallurgy. *Materials Chemistry and Physics*. 2001;67:56-65.
- [3] German R. Sintering: from empirical observations to scientific principles: Butterworth-Heinemann; 2014.
- [4] Kang S-JL. Sintering: densification, grain growth and microstructure: Butterworth-Heinemann; 2004.
- [5] Pan J, Cocks A. A numerical technique for the analysis of coupled surface and grain-boundary diffusion. *Acta metallurgica et materialia*. 1995;43:1395-406.
- [6] Hitchcock D, Livingston R, Liebenberg D. Improved understanding of the spark plasma sintering process. *Journal of Applied Physics*. 2015;117:174505.
- [7] Agrawal D. Microwave sintering of ceramics, composites and metallic materials, and melting of glasses. *Transactions of the Indian ceramic society*. 2006;65:129-44.
- [8] Francis JSC. A study on the phenomena of flash-sintering with tetragonal zirconia: University of Colorado at Boulder; 2013.
- [9] Ganeriwala R, Zohdi TI. A coupled discrete element-finite difference model of selective laser sintering. *Granular Matter*. 2016;18:21.
- [10] Pan J. Solid-state diffusion under a large driving force and the sintering of nanosized particles. *Philosophical magazine letters*. 2004;84:303-10.
- [11] Fang ZZ. Sintering of advanced materials: Elsevier; 2010.
- [12] Herring C. Effect of change of scale on sintering phenomena. *Journal of Applied Physics*. 1950;21:301-3.
- [13] Coblenz W, Dynys J, Cannon R, Coble R. Initial stage solid state sintering models. A critical analysis and assessment. *Sintering Processes Materials Science Research*. 1980;13:141-57.
- [14] Frenkel J. Viscous flow of crystalline bodies. *Zhurnal Eksperimentalnoi i Teoreticheskoi Fiziki*. 1946;16:29-38.
- [15] Coble R. Initial sintering of alumina and hematite. *Journal of the American Ceramic Society*. 1958;41:55-62.
- [16] Kuczynski GC. Self-diffusion in sintering of metallic particles. *Trans AiME*. 1949;185:169-78.
- [17] Ashby M. A first report on sintering diagrams. *Acta Metallurgica*. 1974;22:275-89.

- [18] Swinkels F, Ashby M. A second report on sintering diagrams. *Acta Metallurgica*. 1981;29:259-81.
- [19] Cannon RM, Carter WC. Interplay of sintering microstructures, driving forces, and mass transport mechanisms. *Journal of the American Ceramic Society*. 1989;72:1550-5.
- [20] Lippmann H, Iankov R. Mathematical modeling of sintering during powder forming processes. *International journal of mechanical sciences*. 1997;39:585-96.
- [21] Shima S, Oyane M. Plasticity theory for porous metals. *International Journal of Mechanical Sciences*. 1976;18:285-91.
- [22] Mori K, Ohashi M, Osakada K. Simulation of microscopic shrinkage behaviour in sintering of powder compact. *International journal of mechanical sciences*. 1998;40:989-99.
- [23] Svoboda J, Riedel H. New solutions describing the formation of interparticle necks in solid-state sintering. *Acta Metallurgica et Materialia*. 1995;43:1-10.
- [24] Zhang W, Schneibel J. The sintering of two particles by surface and grain boundary diffusion—a two-dimensional numerical study. *Acta metallurgica et materialia*. 1995;43:4377-86.
- [25] Bouvard D, McMeeking R. Deformation of Interparticle Necks by Diffusion - Controlled Creep. *Journal of the American Ceramic Society*. 1996;79:666-72.
- [26] Pan J, Cocks A, Kucherenko S. Finite element formulation of coupled grain-boundary and surface diffusion with grain-boundary migration. *Proceedings of the Royal Society of London A: Mathematical, Physical and Engineering Sciences: The Royal Society*; 1997. p. 2161-84.
- [27] Kryuchkov YN. Evaluation of the efficiency of sintering of porous ceramic materials. *Refractories and industrial ceramics*. 1997;38:164-7.
- [28] Zhang W, Gladwell I. Sintering of two particles by surface and grain boundary diffusion—a three-dimensional model and a numerical study. *Computational materials science*. 1998;12:84-104.
- [29] Pan J, Le H, Kucherenko S, Yeomans J. A model for the sintering of spherical particles of different sizes by solid state diffusion. *Acta materialia*. 1998;46:4671-90.
- [30] Parhami F, McMeeking R, Cocks A, Suo Z. A model for the sintering and coarsening of rows of spherical particles. *Mechanics of Materials*. 1999;31:43-61.
- [31] Hooper R, Macosko CW, Derby JJ. Assessing a flow-based finite element model for the sintering of viscoelastic particles. *Chemical engineering science*. 2000;55:5733-46.
- [32] Martin C, Bouvard D, Shima S. Study of particle rearrangement during powder compaction by the discrete element method. *Journal of the Mechanics and Physics of Solids*. 2003;51:667-93.
- [33] Pan J, Ch'ng H, Cocks A. Sintering kinetics of large pores. *Mechanics of materials*. 2005;37:705-21.
- [34] Ma J. Constitutive modelling of the densification of porous ceramic components: University of Cambridge; 1997.

- [35] Martin C, Schneider L, Olmos L, Bouvard D. Discrete element modeling of metallic powder sintering. *Scripta materialia*. 2006;55:425-8.
- [36] Hwang K-S, German R, Lenel F. Analysis of initial stage sintering through computer simulation. *PMI Powder metallurgy international*. 1991;23:86-91.
- [37] Ch'ng H, Pan J. Sintering of particles of different sizes. *Acta Materialia*. 2007;55:813-24.
- [38] Chen P, Ni J. Discrete element modeling of micro-feature hot compaction process. *Transactions of the North American Manufacturing Research Institution/SME*.36.
- [39] Exner HE. Principles of single-phase sintering. *Rev Powder Metall Phys Ceram* 1,(1/4), 1979. 1979.
- [40] Henrich B, Wonisch A, Kraft T, Moseler M, Riedel H. Simulations of the influence of rearrangement during sintering. *Acta Materialia*. 2007;55:753-62.
- [41] Olmos L, Martin CL, Bouvard D. Sintering of mixtures of powders: Experiments and modelling. *Powder Technology*. 2009;190:134-40.
- [42] Olevsky E, Maximenko A, Van der Biest O. On-line sintering strength of ceramic composites. *International journal of mechanical sciences*. 2002;44:755-71.
- [43] Tikare V, Braginsky M, Olevsky EA. Numerical Simulation of Solid - State Sintering: I, Sintering of Three Particles. *Journal of the American Ceramic Society*. 2003;86:49-53.
- [44] Demirskyi D, Agrawal D, Ragulya A. Neck growth kinetics during microwave sintering of copper. *Scripta Materialia*. 2010;62:552-5.
- [45] Kiani S, Pan J, Yeomans JA, Barriere M, Blanchart P. Finite element analysis of sintering deformation using densification data instead of a constitutive law. *Journal of the European Ceramic Society*. 2007;27:2377-83.
- [46] Maximenko AL, Olevsky EA. Effective diffusion coefficients in solid-state sintering. *Acta materialia*. 2004;52:2953-63.
- [47] Wakai F, Yoshida M, Shinoda Y, Akatsu T. Coarsening and grain growth in sintering of two particles of different sizes. *Acta materialia*. 2005;53:1361-71.
- [48] Olmos L, Martin CL, Bouvard D, Bellet D, Di Michiel M. Investigation of the sintering of heterogeneous powder systems by synchrotron microtomography and discrete element simulation. *Journal of the American Ceramic Society*. 2009;92:1492-9.
- [49] Martin CL, Camacho - Montes H, Olmos L, Bouvard D, Bordia RK. Evolution of defects during sintering: Discrete element simulations. *Journal of the American Ceramic Society*. 2009;92:1435-41.
- [50] Olevsky EA, Tikare V, Garino T. Multi - Scale Study of Sintering: A Review. *Journal of the American Ceramic Society*. 2006;89:1914-22.
- [51] Martin C, Bordia R. The effect of a substrate on the sintering of constrained films. *Acta Materialia*. 2009;57:549-58.
- [52] Galakhov A. Numerical method for simulating sintering. *Refractories and Industrial Ceramics*. 2009;50:191-7.

- [53] Olevsky E, Molla TT, Frandsen HL, Bjørk R, Esposito V, Ni DW et al. Sintering of Multilayered Porous Structures: Part I - Constitutive Models. *Journal of the American Ceramic Society*. 2013;96:2657-65.
- [54] Wakai F, Fukutome H, Kobayashi N, Misaki T, Shinoda Y, Akatsu T et al. Direct observation of sintering mechanics of a single grain boundary. *Acta Materialia*. 2012;60:507-16.
- [55] Yan Z, Martin CL, Guillon O, Bouvard D. Effect of size and homogeneity of rigid inclusions on the sintering of composites. *Scripta Materialia*. 2013;69:327-30.
- [56] Wang C, Chen S-H. The effect of agglomerate on micro-structural evolution in solid-state sintering. *Acta Mechanica Sinica*. 2012:1-8.
- [57] Wang C, Chen S. Application of the complex network method in solid-state sintering. *Computational Materials Science*. 2013;69:14-21.
- [58] Wakai F, Brakke K. Mechanics of sintering for coupled grain boundary and surface diffusion. *Acta materialia*. 2011;59:5379-87.
- [59] Nosewicz S, Rojek J, Pietrzak K, Chmielewski M. Viscoelastic discrete element model of powder sintering. *Powder technology*. 2013;246:157-68.
- [60] Martin S, Guessasma M, L chelle J, Fortin J, Saleh K, Adenot F. Simulation of sintering using a non smooth discrete element method. Application to the study of rearrangement. *Computational Materials Science*. 2014;84:31-9.
- [61] Ou H, Sahli M, Gelin J-C, Barri re T. Experimental analysis and finite element simulation of the co-sintering of bi-material components. *Powder Technology*. 2014;268:269-78.
- [62] Martin S, Parekh R, Guessasma M, L chelle J, Fortin J, Saleh K. Study of the sintering kinetics of bimodal powders. A parametric DEM study. *Powder Technology*. 2015;270:637-45.
- [63] Luo W, Pan J. Effects of Surface Diffusion and Heating Rate on First - Stage Sintering That Densifies by Grain - Boundary Diffusion. *Journal of the American Ceramic Society*. 2015;98:3483-9.
- [64] Martin CL, Yan Z, Jauffres D, Bouvard D, Bordia RK. Sintered ceramics with controlled microstructures: numerical investigations with the Discrete Element Method. *Journal of the Ceramic Society of Japan*. 2016;124:340-5.
- [65] Nosewicz S, Rojek J, Chmielewski M, Pietrzak K, Lumelskyj D. Application of the Hertz formulation in the discrete element model of pressure-assisted sintering. *Granular Matter*. 2017;19:16.
- [66] Rojek J, Nosewicz S, Ma dziarz M, Kowalczyk P, Wawrzyk K, Lumelskyj D. Modeling of a sintering process at various scales. *Procedia Engineering*. 2017;177:263-70.
- [67] Wang D, Yuan H, Qiang J. The Microstructure Evolution, Mechanical Properties and Densification Mechanism of TiAl-Based Alloys Prepared by Spark Plasma Sintering. *Metals*. 2017;7:201.

- [68] Zhao X, Li S, Zhang M, Liu Y, Sercombe TB, Wang S et al. Comparison of the microstructures and mechanical properties of Ti–6Al–4V fabricated by selective laser melting and electron beam melting. *Materials & Design*. 2016;95:21-31.
- [69] Zhu W, Yan C, Shi Y, Wen S, Liu J, Shi Y. Investigation into mechanical and microstructural properties of polypropylene manufactured by selective laser sintering in comparison with injection molding counterparts. *Materials & Design*. 2015;82:37-45.
- [70] Miranda R, Lopes G, Quintino L, Rodrigues J, Williams S. Rapid prototyping with high power fiber lasers. *Materials & Design*. 2008;29:2072-5.
- [71] Bakshi K, Mulay A. A Review on Selective Laser Sintering: A Rapid Prototyping Technology.
- [72] Steen WM. Background and General Applications. *Laser Material Processing: Springer*; 2003. p. 11-60.
- [73] Maeda K, Childs T. Laser sintering (SLS) of hard metal powders for abrasion resistant coatings. *Journal of Materials Processing Technology*. 2004;149:609-15.
- [74] Römer G, Meijer J. Metal surface temperature induced by moving laser beams. *Optical and quantum electronics*. 1995;27:1397-406.
- [75] Dong L, Makradi A, Ahzi S, Remond Y. Three-dimensional transient finite element analysis of the selective laser sintering process. *Journal of materials processing technology*. 2009;209:700-6.
- [76] Loh L-E, Chua C-K, Yeong W-Y, Song J, Mapar M, Sing S-L et al. Numerical investigation and an effective modelling on the Selective Laser Melting (SLM) process with aluminium alloy 6061. *International Journal of Heat and Mass Transfer*. 2015;80:288-300.
- [77] Ganeriwala R, Zohdi TI. Multiphysics modeling and simulation of selective laser sintering manufacturing processes. *Procedia CIRP*. 2014;14:299-304.
- [78] Ganci M, Zhu W, Buffa G, Fratini L, Bo S, Yan C. A macroscale FEM-based approach for selective laser sintering of thermoplastics. *The International Journal of Advanced Manufacturing Technology*. 2017:1-12.
- [79] Singh S, Sachdeva A, Sharma VS. Investigation of dimensional accuracy/mechanical properties of part produced by selective laser sintering. *International Journal of Applied Science and Engineering*. 2012;10:59-68.
- [80] Velu R, Singamneni S. Evaluation of the influences of process parameters while selective laser sintering PMMA powders. *Proceedings of the Institution of Mechanical Engineers, Part C: Journal of Mechanical Engineering Science*. 2015;229:603-13.
- [81] Peyre P, Rouchausse Y, Defauchy D, Régnier G. Experimental and numerical analysis of the selective laser sintering (SLS) of PA12 and PEKK semi-crystalline polymers. *Journal of Materials Processing Technology*. 2015;225:326-36.
- [82] Cheng C, Chen J. Femtosecond laser sintering of copper nanoparticles. *Applied Physics A*. 2016;122:289.
- [83] Moser D, Pannala S, Murthy J. Computation of effective thermal conductivity of powders for selective laser sintering simulations. *Journal of Heat Transfer*. 2016;138:082002.

- [84] Heires M. The International Organization for Standardization (ISO). *New Political Economy*. 2008;13:357-67.
- [85] Moriarty P. Nanostructured materials. *Reports on Progress in Physics*. 2001;64:297.
- [86] Link S, Mohamed M, El-Sayed M. Simulation of the optical absorption spectra of gold nanorods as a function of their aspect ratio and the effect of the medium dielectric constant. *The Journal of Physical Chemistry B*. 1999;103:3073-7.
- [87] Bhushan B. *Springer handbook of nanotechnology*: Springer Science & Business Media; 2010.
- [88] Sahoo SK, Labhasetwar V. Nanotech approaches to drug delivery and imaging. *Drug discovery today*. 2003;8:1112-20.
- [89] Silva GA. Introduction to nanotechnology and its applications to medicine. *Surgical neurology*. 2004;61:216-20.
- [90] Tsukagoshi K, Yoneya N, Uryu S, Aoyagi Y, Kanda A, Ootuka Y et al. Carbon nanotube devices for nanoelectronics. *Physica B: Condensed Matter*. 2002;323:107-14.
- [91] Gooding JJ. Nanostructuring electrodes with carbon nanotubes: A review on electrochemistry and applications for sensing. *Electrochimica Acta*. 2005;50:3049-60.
- [92] Koparde VN, Cummings PT. Sintering of titanium dioxide nanoparticles: a comparison between molecular dynamics and phenomenological modeling. *Journal of Nanoparticle Research*. 2008;10:1169-82.
- [93] Pan H, Ko SH, Grigoropoulos CP. The solid-state neck growth mechanisms in low energy laser sintering of gold nanoparticles: a molecular dynamics simulation study. *Journal of Heat Transfer*. 2008;130:092404.
- [94] Pan H, Ko SH, Grigoropoulos CP. The Neck Growth Mechanisms in Low Energy Laser Sintering of Gold Nanoparticles—A Molecular Dynamics Simulation Study. *Proc of SPIE Vol2007*. p. 64581J-1.
- [95] Mao Q, Luo K. Molecular Dynamics Simulation of Sintering Dynamics of Many TiO<sub>2</sub> Nanoparticles. *Journal of Statistical Physics*. 2015;160:1696-708.
- [96] Zhang Y, Wu L, Guo X, Jung Y-G, Zhang J. Molecular dynamics simulation of electrical resistivity in sintering process of nanoparticle silver inks. *Computational Materials Science*. 2016;125:105-9.
- [97] Hussain F, Hayat SS, Imran M, Ahmad S, Bouafia F. Sintering and deposition of nanoparticles on surface of metals: A molecular dynamics approach. *Computational Materials Science*. 2012;65:264-8.
- [98] Moitra A, Kim S, Kim S-G, Park SJ, German RM, Horstemeyer MF. Investigation on sintering mechanism of nanoscale tungsten powder based on atomistic simulation. *Acta Materialia*. 2010;58:3939-51.
- [99] Nakao K, Ishimoto T, Koyama M. Sintering simulation for porous material by integrating molecular dynamics and master sintering curve. *The Journal of Physical Chemistry C*. 2014;118:15766-72.

- [100] Ding L, Davidchack RL, Pan J. A molecular dynamics study of sintering between nanoparticles. *Computational Materials Science*. 2009;45:247-56.
- [101] Yang L, Gan Y, Zhang Y, Chen J. Molecular dynamics simulation of neck growth in laser sintering of different-sized gold nanoparticles under different heating rates. *Applied Physics A*. 2012;106:725-35.
- [102] Buesser B, Pratsinis SE. Morphology and crystallinity of coalescing nanosilver by molecular dynamics. *The Journal of Physical Chemistry C*. 2015;119:10116-22.
- [103] Seong Y, Hwang S, Kim SJ, Kim S, Kim S-G, Kim HJ et al. Atomistic Simulation of Sintering Mechanism for Copper Nano-Powders. *한국분말야금학회지*. 2015;22:247-53.
- [104] Wang J, Shin S, Hu A. Geometrical Effects on Sintering Dynamics of Cu–Ag Core–Shell Nanoparticles. *The Journal of Physical Chemistry C*. 2016;120:17791-800.
- [105] HA A, Atis M, Özdoğan C, Hu A, Yavuz M, Zhou Y. Molecular dynamics simulation of sintering and surface premelting of silver nanoparticles. *Materials Transactions*. 2013;54:884-9.
- [106] Yousefi M, Khoie MM. Molecular dynamics simulation of Ni/Cu-Ni nanoparticles sintering under various crystallographic, thermodynamic and multi-nanoparticles conditions. *The European Physical Journal D*. 2015;69:71.
- [107] García V, Schilling C. Ultrasonic velocity and reduction of surface area during solid-state sintering. *Materials Science and Engineering: A*. 1999;265:42-9.
- [108] Needleman A, Rice JR. OVERVIEW NO. 9 - PLASTIC CREEP FLOW EFFECTS IN THE DIFFUSIVE CAVITATION OF GRAIN BOUNDARIES. *Perspectives in Creep Fracture*: Pergamon; 1983. p. 107-24.
- [109] Suo Z, Wang W. Diffusive void bifurcation in stressed solid. *Journal of Applied Physics*. 1994;76:3410-21.
- [110] Cocks ACF, Gill SPA. A variational approach to two dimensional grain growth—I. Theory. *Acta Materialia*. 1996;44:4765-75.
- [111] Sun B, Suo, Z., & Cocks, A. C. F. a global view of structural evolution. *J Mech Phys Solids* 1996;44: 559-81.
- [112] Kumar S. Selective laser sintering: a qualitative and objective approach. *JOM Journal of the Minerals, Metals and Materials Society*. 2003;55:43-7.
- [113] Kruth J-P, Levy G, Klocke F, Childs T. Consolidation phenomena in laser and powder-bed based layered manufacturing. *CIRP Annals-Manufacturing Technology*. 2007;56:730-59.
- [114] Song B, Dong S, Liao H, Coddet C. Process parameter selection for selective laser melting of Ti6Al4V based on temperature distribution simulation and experimental sintering. *The International Journal of Advanced Manufacturing Technology*. 2012;61:967-74.
- [115] Yifu S, Dongdong G, Chenye Y. Simulation of temperature field in direct metal laser sintering processes. *Chinese Mechanical Engineering*. 2005;16:67-73.
- [116] Jian X, Xiaogang S. Simulation and testing of the transient temperature field of infrared laser sintering. *Journal of Harbin Engineering University*. 2011;32:965-8.

- [117] Shuai C, Feng P, Gao C, Zhou Y, Peng S. Simulation of dynamic temperature field during selective laser sintering of ceramic powder. *Mathematical and Computer Modelling of Dynamical Systems*. 2013;19:1-11.
- [118] Zhang D, Cai Q, Liu J, Zhang L, Li R. Select laser melting of W–Ni–Fe powders: simulation and experimental study. *The International Journal of Advanced Manufacturing Technology*. 2010;51:649-58.
- [119] Gu D. *Laser additive manufacturing of high-performance materials*: Springer; 2015.
- [120] Groza JR. Nanosintering. *Nanostructured Materials*. 1999;12:987-92.
- [121] Cook BS, Fang Y, Kim S, Le T, Goodwin WB, Sandhage KH et al. Inkjet catalyst printing and electroless copper deposition for low-cost patterned microwave passive devices on paper. *Electronic Materials Letters*. 2013;9:669-76.
- [122] Deng D, Qi T, Chen Y, Jin Y, Xiao F. Preparation of antioxidative nano copper pastes for printed electronics application. *Electronic Packaging Technology and High Density Packaging (ICEPT-HDP), 2012 13th International Conference on: IEEE; 2012*. p. 250-3.
- [123] Jang S, Seo Y, Choi J, Kim T, Cho J, Kim S et al. Sintering of inkjet printed copper nanoparticles for flexible electronics. *Scripta Materialia*. 2010;62:258-61.
- [124] Plimpton S. Fast Parallel Algorithms for Short-Range Molecular Dynamics. *Journal of Computational Physics*. 1995;117:1-19.
- [125] Gromov AA, Teipel U. *Metal nanopowders: production, characterization, and energetic applications*: John Wiley & Sons; 2014.
- [126] LAMMPS MD simulator. <http://lammps.sandia.gov/index.html>.
- [127] Goudeli E, Pratsinis SE. Crystallinity dynamics of gold nanoparticles during sintering or coalescence. *AIChE Journal*. 2016;62:589-98.
- [128] Doyama M, Kogure Y. Embedded atom potentials in fcc and bcc metals. *Computational materials science*. 1999;14:80-3.
- [129] Mishin Y, Mehl M, Papaconstantopoulos D, Voter A, Kress J. Structural stability and lattice defects in copper: Ab initio, tight-binding, and embedded-atom calculations. *Physical Review B*. 2001;63:224106.
- [130] Jiang Q, Zhang S, Li J. Grain size-dependent diffusion activation energy in nanomaterials. *Solid State Communications*. 2004;130:581-4.
- [131] Alarifi H. *Ag Nanoparticles and their Application in Low-Temperature Bonding of Cu*. 2014.
- [132] Butrymowicz DB, Manning JR, Read ME. Diffusion in copper and copper alloys. Part I. volume and surface self - diffusion in copper. *Journal of Physical and Chemical Reference Data*. 1973;2:643-56.
- [133] Wronski C. The size dependence of the melting point of small particles of tin. *British Journal of Applied Physics*. 1967;18:1731.
- [134] Buffat P, Borel JP. Size effect on the melting temperature of gold particles. *Physical review A*. 1976;13:2287.

- [135] Coombes C. The melting of small particles of lead and indium. *Journal of Physics F: Metal Physics*. 1972;2:441.
- [136] Kim H-S, Dhage SR, Shim D-E, Hahn HT. Intense pulsed light sintering of copper nanoink for printed electronics. *Applied Physics A: Materials Science & Processing*. 2009;97:791-8.
- [137] Hanszen K-J. Theoretische untersuchungen über den schmelzpunkt kleiner kügelchen. *Zeitschrift für Physik A Hadrons and Nuclei*. 1960;157:523-53.
- [138] Gibbs JW. *The collected works of J. Willard Gibbs*. Yale Univ. Press; 1948.
- [139] Makkonen L. On the methods to determine surface energies. *Langmuir*. 2000;16:7669-72.
- [140] Nanda K, Sahu S, Behera S. Liquid-drop model for the size-dependent melting of low-dimensional systems. *Physical review A*. 2002;66:013208.

## Appendix A:

Equations of all particles for SLS model.

### For first layer

Boundary condition:  $V_{x1}, V_{x4}, V_{x7}, V_{y1}, V_{y2}, V_{y3} = \text{zero}$ , and all velocities of axis Z in layer one = zero.

$$\delta\Pi_6 + \delta\Pi_7 = 0 \quad (A - 1)$$

$$V_{X5} = -\frac{8D_g}{\pi a_6^4} F_6 \quad (A - 2)$$

$$V_{X6} = -\frac{8D_g}{\pi a_6^4} F_6 - \frac{8D_g}{\pi a_7^4} F_7 \quad (A - 3)$$

$$\delta\Pi_{11} + \delta\Pi_{12} = 0 \quad (A - 4)$$

$$V_{X8} = -\frac{8D_g}{\pi a_{11}^4} F_{11} \quad (A - 5)$$

$$V_{X9} = -\frac{8D_g}{\pi a_{11}^4} F_{11} - \frac{8D_g}{\pi a_{12}^4} F_{12} \quad (A - 6)$$

$$\delta\Pi_3 + \delta\Pi_9 = 0 \quad (A - 7)$$

$$V_{Y5} = -\frac{8D_g}{\pi a_3^4} F_3 \quad (A - 8)$$

$$V_{Y8} = -\frac{8D_g}{\pi a_3^4} F_3 - \frac{8D_g}{\pi a_9^4} F_9 \quad (A - 9)$$

$$\delta\Pi_5 + \delta\Pi_{10} = 0 \quad (A - 10)$$

$$V_{Y6} = -\frac{8D_g}{\pi a_5^4} F_5 \quad (A - 11)$$

$$V_{Y9} = -\frac{8D_g}{\pi a_5^4} F_5 - \frac{8D_g}{\pi a_{10}^4} F_{10} \quad (A - 12)$$

**For second layer**

Boundary condition:  $V_{x10}, V_{x16}, V_{x22}, V_{y10}, V_{y12}, V_{y14}, = \text{zero}$ .

$$\delta\Pi_{22} + \delta\Pi_{25} = 0 \quad (A - 13)$$

$$V_{X12} = -\frac{8D_g}{\pi a_{22}^4} F_{22} \quad (A - 14)$$

$$V_{X14} = -\frac{8D_g}{\pi a_{22}^4} F_{22} - \frac{8D_g}{\pi a_{25}^4} F_{25} \quad (A - 15)$$

$$\delta\Pi_{27} + \delta\Pi_{28} = 0 \quad (A - 16)$$

$$V_{X18} = -\frac{8D_g}{\pi a_{27}^4} F_{27} \quad (A - 17)$$

$$V_{X20} = -\frac{8D_g}{\pi a_{27}^4} F_{27} - \frac{8D_g}{\pi a_{28}^4} F_{28} \quad (A - 18)$$

$$\delta\Pi_{32} + \delta\Pi_{33} = 0 \quad (A - 19)$$

$$V_{X24} = -\frac{8D_g}{\pi a_{32}^4} F_{32} \quad (A - 20)$$

$$V_{X26} = -\frac{8D_g}{\pi a_{32}^4} F_{32} - \frac{8D_g}{\pi a_{33}^4} F_{33} \quad (A - 21)$$

$$\delta\Pi_{23} + \delta\Pi_{29} = 0 \quad (A - 22)$$

$$V_{Y16} = -\frac{8D_g}{\pi a_{23}^4} F_{23} \quad (A - 23)$$

$$V_{Y22} = -\frac{8D_g}{\pi a_{23}^4} F_{23} - \frac{8D_g}{\pi a_{29}^4} F_{29} \quad (A - 24)$$

$$\delta\Pi_{24} + \delta\Pi_{30} = 0 \quad (A - 25)$$

$$V_{Y18} = -\frac{8D_g}{\pi a_{24}^4} F_{24} \quad (A - 26)$$

$$V_{Y24} = -\frac{8D_g}{\pi a_{24}^4} F_{24} - \frac{8D_g}{\pi a_{30}^4} F_{30} \quad (A - 27)$$

$$\delta\Pi_{25} + \delta\Pi_{31} = 0 \quad (A - 28)$$

$$V_{Y20} = -\frac{8D_g}{\pi a_{25}^4} F_{25} \quad (A - 29)$$

$$V_{Y26} = -\frac{8D_g}{\pi a_{25}^4} F_{25} - \frac{8D_g}{\pi a_{31}^4} F_{31} \quad (A - 30)$$

**For third layer**

Boundary condition:  $V_{x11}, V_{x17}, V_{x23}, V_{y11}, V_{y13}, V_{y15} = \text{zero}$ .

$$\delta\Pi_{43} + \delta\Pi_{46} = 0 \quad (A - 40)$$

$$V_{X13} = -\frac{8D_g}{\pi a_{43}^4} F_{43} \quad (A - 41)$$

$$V_{X15} = -\frac{8D_g}{\pi a_{43}^4} F_{43} - \frac{8D_g}{\pi a_{46}^4} F_{46} \quad (A - 42)$$

$$\delta\Pi_{48} + \delta\Pi_{50} = 0 \quad (A - 43)$$

$$V_{X19} = -\frac{8D_g}{\pi a_{48}^4} F_{48} \quad (A - 44)$$

$$V_{X21} = -\frac{8D_g}{\pi a_{48}^4} F_{48} - \frac{8D_g}{\pi a_{50}^4} F_{50} \quad (A - 45)$$

$$\delta\Pi_{53} + \delta\Pi_{54} = 0 \quad (A - 46)$$

$$V_{X25} = -\frac{8D_g}{\pi a_{53}^4} F_{53} \quad (A - 47)$$

$$V_{X27} = -\frac{8D_g}{\pi a_{53}^4} F_{53} - \frac{8D_g}{\pi a_{54}^4} F_{54} \quad (A - 48)$$

$$\delta\Pi_{44} + \delta\Pi_{49} = 0 \quad (A - 49)$$

$$V_{Y17} = -\frac{8D_g}{\pi a_{44}^4} F_{44} \quad (A - 50)$$

$$V_{Y23} = -\frac{8D_g}{\pi a_{44}^4} F_{44} - \frac{8D_g}{\pi a_{49}^4} F_{49} \quad (A - 51)$$

$$\delta\Pi_{45} + \delta\Pi_{51} = 0 \quad (A - 52)$$

$$V_{Y19} = -\frac{8D_g}{\pi a_{45}^4} F_{45} \quad (A - 53)$$

$$V_{Y25} = -\frac{8D_g}{\pi a_{45}^4} F_{45} - \frac{8D_g}{\pi a_{51}^4} F_{51} \quad (A - 54)$$

$$\delta\Pi_{47} + \delta\Pi_{52} = 0 \quad (A - 55)$$

$$V_{Y21} = -\frac{8D_g}{\pi a_{47}^4} F_{47} \quad (A - 56)$$

$$V_{Y27} = -\frac{8D_g}{\pi a_{47}^4} F_{47} - \frac{8D_g}{\pi a_{52}^4} F_{52} \quad (A - 57)$$

$$\delta\Pi_{13} + \delta\Pi_{34} = 0 \quad (A - 58)$$

$$V_{Z10} = -\frac{8D_g}{\pi a_{13}^4} F_{13} \quad (A - 59)$$

$$V_{Z11} = -\frac{8D_g}{\pi a_{34}^4} F_{34} - \frac{8D_g}{\pi a_{13}^4} F_{13} \quad (A - 60)$$

$$\delta\Pi_{14} + \delta\Pi_{35} = 0 \quad (A - 61)$$

$$V_{Z12} = -\frac{8D_g}{\pi a_{14}^4} F_{14} \quad (A - 62)$$

$$V_{Z13} = -\frac{8D_g}{\pi a_{35}^4} F_{35} - \frac{8D_g}{\pi a_{14}^4} F_{14} \quad (A - 63)$$

$$\delta\Pi_{15} + \delta\Pi_{36} = 0 \quad (A - 64)$$

$$V_{Z14} = -\frac{8D_g}{\pi a_{15}^4} F_{15} \quad (A - 65)$$

$$V_{Z15} = -\frac{8D_g}{\pi a_{36}^4} F_{36} - \frac{8D_g}{\pi a_{15}^4} F_{15} \quad (A - 66)$$

$$\delta\Pi_{16} + \delta\Pi_{37} = 0 \quad (A - 67)$$

$$V_{Z16} = -\frac{8D_g}{\pi a_{16}^4} F_{16} \quad (A - 68)$$

$$V_{Z17} = -\frac{8D_g}{\pi a_{37}^4} F_{37} - \frac{8D_g}{\pi a_{16}^4} F_{16} \quad (A - 69)$$

$$\delta\Pi_{17} + \delta\Pi_{38} = 0 \quad (A - 70)$$

$$V_{Z18} = -\frac{8D_g}{\pi a_{17}^4} F_{17} \quad (A - 71)$$

$$V_{Z19} = -\frac{8D_g}{\pi a_{38}^4} F_{38} - \frac{8D_g}{\pi a_{17}^4} F_{17} \quad (A - 72)$$

$$\delta\Pi_{18} + \delta\Pi_{39} = 0 \quad (A - 73)$$

$$V_{Z20} = -\frac{8D_g}{\pi a_{18}^4} F_{18} \quad (A - 74)$$

$$V_{Z21} = -\frac{8D_g}{\pi a_{39}^4} F_{39} - \frac{8D_g}{\pi a_{18}^4} F_{18} \quad (A - 75)$$

$$\delta\Pi_{19} + \delta\Pi_{40} = 0 \quad (A - 76)$$

$$V_{Z22} = -\frac{8D_g}{\pi a_{19}^4} F_{19} \quad (A - 77)$$

$$V_{Z23} = -\frac{8D_g}{\pi a_{40}^4} F_{40} - \frac{8D_g}{\pi a_{19}^4} F_{19} \quad (A - 78)$$

$$\delta\Pi_{20} + \delta\Pi_{41} = 0 \quad (A - 79)$$

$$V_{Z24} = -\frac{8D_g}{\pi a_{20}^4} F_{20} \quad (A - 80)$$

$$V_{Z25} = -\frac{8D_g}{\pi a_{41}^4} F_{41} - \frac{8D_g}{\pi a_{20}^4} F_{20} \quad (A - 81)$$

$$\delta\Pi_{21} + \delta\Pi_{42} = 0 \quad (A - 82)$$

$$V_{Z26} = -\frac{8D_g}{\pi a_{21}^4} F_{21} \quad (A - 83)$$

$$V_{Z27} = -\frac{8D_g}{\pi a_{42}^4} F_{42} - \frac{8D_g}{\pi a_{21}^4} F_{21} \quad (A - 84)$$

$$\delta\Pi_{20} + \delta\Pi_{41} = 0 \quad (A - 85)$$

$$V_{Z26} = -\frac{8D_g}{\pi a_{21}^4} F_{21} \quad (A - 86)$$

$$V_{Z27} = -\frac{8D_g}{\pi a_{42}^4} F_{42} - \frac{8D_g}{\pi a_{21}^4} F_{21} \quad (A - 87)$$